



universität
wien

DISSERTATION / DOCTORAL THESIS

Titel der Dissertation / Title of the Doctoral Thesis

Low-scaling algorithms for many-body exchange-like diagrams

verfasst von / submitted by

Tobias Schäfer, MSc BSc

angestrebter akademischer Grad / in partial fulfilment of the requirements for the degree of

Doktor der Naturwissenschaften (Dr. rer. nat.)

Wien / Vienna, 2018

Studienkennzahl lt. Studienblatt / degree programme code as it appears on the student record sheet: A 796 605 411

Dissertationsgebiet lt. Studienblatt / field of study as it appears on the student record sheet: Physik / Physics

Betreuer / Supervisor: Univ.-Prof. Dipl.Ing. Dr. Georg Kresse

Abstract

In this thesis we prove that developing low-scaling algorithms for many-body exchange-like contributions to the total energy is both possible and practical. Predicting materials properties from first principles requires efficient computer codes. Still, *ab-initio* materials physics is one of the most computationally demanding fields of all science. The key challenge is to calculate sufficiently accurate approximations to the many-electron Schrödinger equation, also known as the electronic structure problem. In particular correlations of the electrons play an important role in the determination of properties like the crystal structure, surface energies, or thermodynamic phase boundaries. In this work, we present new algorithms that substantially increase the efficiency of correlation energy calculations of large many-electron systems, beyond mean field approaches like density functional or Hartree-Fock theory, employing orbital-based many-body perturbation theory. Orbitals are simple and illustrative mathematical ingredients to construct approximations to the ground state energy of many-electron systems. But associating an orbital with an electron is wrong, since orbitals are distinguishable though electrons are not. Therefore in all proper theories so called exchange-like terms must appear, which correct exactly this error. Those exchange-like terms are taken into account by methods like second-order Møller-Plesset theory (MP2) or approximate by second-order screened exchange (SOSEX). However, the implementation of algorithms that calculate these exchange terms possess a very high computational complexity, leading to a very steep scaling of the computation time with respect to the system size. The main goal of this thesis is to show, that low-scaling implementations for exchange-like contributions to the correlation energy are indeed possible. We present three algorithms which reduce the scaling of MP2 and SOSEX calculations from the canonical quintic to a quartic or even cubic scaling, by pure analytical rearrangements, i.e. without sacrificing the accuracy. The reduced scaling allows for accurate correlation energy calculations that including exchange-like terms on systems which involve several hundreds of valence electrons. We also present three mutually different stochastic algorithms, which reduce the computational cost at the price of a statistical error. Those implementations make even larger systems accessible if only the error per electron is of interest. Furthermore, all implemented codes are highly parallelized and can be considered as high-performance codes. All considerations are based on the plane-wave basis, which is a suitable basis for periodic systems.

Zusammenfassung

Mit dieser Arbeit wird bewiesen, dass die Entwicklung von niedrig skalierenden Algorithmen zur Berechnung von austauschartigen Vielteilchen-Termen sowohl möglich als auch praktisch ist. Die Vorhersage von Materialeigenschaften mittels *ab initio* Methoden erfordert effiziente Computerprogramme. Nach wie vor ist die computergestützte Materialphysik eine der rechenintensivsten Wissenschaftszweige. Das zentrale Problem, auch bekannt als Problem der elektronischen Struktur, besteht in der Berechnung hinreichend genauer Näherungen zur Vielteilchen-Schrödingergleichung. Die Korrelation von Elektronen ist dabei von besonderer Bedeutung, bestimmt sie doch maßgeblich Eigenschaften wie die Kristallstruktur, Oberflächenenergien oder thermodynamische Phasengrenzen. In dieser Arbeit stellen wir neue Algorithmen vor, welche die Effizienz von Berechnungen der Korrelationsenergie großer Systeme erheblich verbessern. Wir setzen dabei auf Orbital-basierte Vielteilchen-Störungstheorie und gehen damit über Hartree-Fock oder Dichtefunktionaltheorie hinaus. Orbitale sind einfache und anschauliche mathematische Zutaten um Näherungen zur Grundzustandsenergie von Vielteilchensystemen zu konstruieren. Allerdings ist die Assoziation eines Orbitals mit einem Elektron falsch, da Elektronen ununterscheidbar sind, Orbitale dagegen unterscheidbar. Alle ordnungsgemäßen Theorien berücksichtigen daher sogenannte austauschartige Terme, die genau diesen Fehler korrigieren. Diese austauschartigen Terme werden von Methoden wie zweiter-Ordnung-Møller-Plesset-Störungstheorie (engl. second-order Møller-Plesset perturbation theory, MP2) oder näherungsweise durch zweiter-Ordnung-abgeschirmter-Austausch (engl. second-order screened exchange, SOSEX) berücksichtigt. Allerdings weisen diese austauschartigen Terme eine hohe algorithmische Komplexität auf, was sich wiederum oft in einem steilem Skalierungsverhalten der Rechenzeit gegenüber der Systemgröße äußert. Das Hauptziel dieser Arbeit besteht in dem Beweis, dass niedrigskalierende Algorithmen zur Berechnung der Austauschsterme jedoch sehr wohl möglich sind. Wir präsentieren drei Algorithmen, welche die Skalierung von MP2- und SOSEX-Rechnungen von einer quintischen auf eine quartische oder gar kubische Skalierung reduzieren. Dabei werden ausschließlich analytische Umformungen vorgenommen, sodass keinerlei Genauigkeit geopfert wird. Durch diese niedrigere Skalierung ist es möglich, die Korrelationsenergie mitsamt Austauschstermen für Systeme einiger hundert Valenzelektronen mit hoher Genauigkeit zu berechnen. Wir stellen ebenfalls drei grundlegend verschiedene stochastische Algorithmen vor, welche die Rechenkosten zum Preis von statistischen Ungenauigkeiten reduzieren. Diese Implementierungen erlauben es, Berechnungen an noch größeren Systemen vorzunehmen, wenn nur der relative Fehler pro Elek-

tron entscheidend ist. Des weiteren sind alle implementierten Algorithmen hochgradig parallelisiert und damit Hochleistungssoftware. Jegliche Betrachtungen verwenden ebenen Wellen, welche eine probate Basis für periodische Systeme darstelle.

Contents

1	Introduction	11
I	Theory	15
2	The many-body Hamiltonian and how we treat it	17
2.1	The Many-body Hamiltonian and the free energy	17
2.2	Comments on the mathematical notation	18
2.3	Born-Oppenheimer approximation for the free energy	19
2.4	Mean field approach and Bloch's theorem	22
2.5	What about the spin?	27
2.6	Pseudopotentials and the projector augmented wave method	28
2.7	Lattice vibrations: relaxing the frozen nuclei	32
3	The symmetry of the wave function for electrons	37
3.1	The symmetrization postulate for identical particles	37
3.2	Construction of N -electron states in mean field methods	38
3.3	Slater-Condon rules	40
3.4	Pauli exclusion	41
4	The Hartree-Fock mean field approach	43
4.1	General idea	43
4.2	The Hartree-Fock equation	44
4.3	Excited determinants: singles, doubles, triples,	47
4.4	Illustrative HF calculations for molecules and solids	48
5	Exchange and correlation	51
5.1	Exchange correlation of two non-interacting particles	51
5.2	Correlation energy and the cusp conditions	52
5.3	Dynamic and static correlation	54
5.4	Exchange-correlation holes in the density	55
5.5	Exact exchange	56

6	Density functional theory	57
6.1	The Hohenberg-Kohn theorems	57
6.2	The Kohn-Sham equations	60
6.3	Illustrative DFT calculations for molecules and solids	61
7	<i>Excursion: Green's functions and the quantum field theoretical view</i>	63
7.1	Green's function and self-energy	63
7.2	Hartree-Fock from the QFT perspective	66
7.3	Exchange from the QFT picture	70
8	Correlation energy methods	71
8.1	Second-order Møller-Plesset perturbation theory	71
8.1.1	Canonical formulation	71
8.1.2	MP2 for 3D periodic systems in the thermodynamic limit	75
8.1.3	Periodic MP2 in the PAW and the long-wavelength limit	78
8.1.4	Van der Waals interactions in HF and MP2	80
8.1.5	Laplace transformed formulation	82
8.1.6	Green's function formulation	83
8.2	Adiabatic connection and fluctuation-dissipation	87
8.3	The random phase approximation	90
8.4	RPA with exchange: second-order screened exchange	92
8.5	Illustrative MP2 and RPA calculations for molecules and solids	94
II	Low-complexity algorithms for the correlation energy	99
9	Overview of the developed algorithms	101
10	Deterministic algorithms	103
10.1	Quartic scaling MP2 for periodic systems	103
10.1.1	Reducing the computational cost	103
10.1.2	Exploiting the time reversal symmetry	106
10.1.3	Implementation	107
10.1.4	Benchmark calculations	111
10.1.5	Conclusion and Outlook	117
10.2	Quartic scaling SOSEX for periodic systems	118
10.3	Cubic scaling MP2: prospects and limitations	122
11	Stochastic algorithms	125
11.1	Real space Monte Carlo sampling of Feynman diagrams	126
11.1.1	Monte Carlo integration and importance sampling	126
11.1.2	Monte Carlo integration of the MP2 energy for periodic systems	129
11.1.3	Implementation of efficient importance sampling techniques	130
11.1.4	Measured system size scaling	136

11.1.5	Conclusion	137
11.2	Periodic MP2 with stochastic orbitals	139
11.2.1	Stochastic orbitals in the plane wave basis	139
11.2.2	Implementation	142
11.2.3	Benchmark calculations	148
11.2.4	Conclusion	155
11.3	Electron repulsion integrals in a random basis	156
11.3.1	The random basis	156
11.3.2	Implementation	157
11.3.3	Results	159
11.3.4	Conclusion and Outlook	162
12	Summary, Conclusion and Outlook	163
III	Application of the Random Phase Approximation	165
13	Ab initio phase diagram of PbSe crystals calculated with the RPA	167
13.1	Introduction	167
13.2	Theory and methods	169
13.3	Computational details	171
13.3.1	The crystal structures of B1, B33, and B2	171
13.3.2	Pseudopotentials, basis set and k-point meshes	171
13.3.3	Error estimates	172
13.4	Results	172
13.4.1	Comparison of DFT functionals with RPA	172
13.4.2	The temperature-pressure phase diagram	173
13.5	Discussion and Conclusion	175
IV	Appendices	179
14	Acknowledgments	181
15	List of publications and talks	183
15.1	Peer reviewed articles	183
15.2	Contributed Talks	183
15.3	Poster presentations	184
16	Bibliography	185

CHAPTER 1

Introduction

For this PhD thesis, the world consists only of electrons and atomic nuclei as well as their interactions. This drastically reduced world is sufficient to predict physical and chemical properties of known or unknown materials, hence, being a common approach in *computational materials physics*. How do the involved atoms arrange? Do they form a stable regular lattice? What is the impact of pressure and temperature? The answer to such questions are often sufficiently determined by the non-relativistic quantum theory. No additional empirical information is necessary. Therefore, we call this approach *ab initio*, meaning *from the beginning*. Whether the above questions can be answered in practice, depends on whether we can solve the many-body Schrödinger equation, the fundamental equation of quantum mechanics.

The practical experience of the last century, however, shows that exact solutions are available only for a very limited number of cases. Speaking of materials, molecules and atoms, only the hydrogen atom is an analytical solvable system. For all real materials, the known mathematical tools are insufficient to solve the Schrödinger equation exactly. Fortunately, this problem has been eased with the development of computers. However, even with modern supercomputers it is still not possible to numerically solve the Schrödinger equation directly. Alone the necessary memory to store the solution of a system that involves only few atoms, would quickly exceed the globally available storage. Thus, one of the main goals in *ab initio* computational materials physics is to develop efficient algorithms that can calculate sufficiently accurate approximations to the solution of the Schrödinger equation.

In this work, we are mainly interested in the development of algorithms to calculate the free energy of three dimensional periodic many-body systems like, for instance, crystalline solids or atoms on surfaces (illustrations can be found in Fig. 2.1 on p. 25). In contrast to molecules, these systems are in principle infinitely extended and we are interested in the free energy per unit cell, the periodically repeated building block of the system. Free energies are especially important to compute bond lengths, crystal structures, surface energies, or thermodynamic phase diagrams. In the following, we provide a brief and therefore incomplete description of the state of the art, which allows to describe one computational difficulty, being the main subject of this work: the computation of exchange-like terms in many-body perturbation theory.

Today, we can choose out of a large spectrum of techniques to approximate or simplify the Schrödinger equation. Many of those *ab initio* techniques were developed already between the late 1920s and the early 1970s, and the first software implementations (mostly restricted to finite systems like molecules) arose in the 1980s. A key anchor point is the *Born-Oppenheimer approximation* [1]. It states that a separate treatment of the electrons and atomic nuclei is possible due to the small ratio of their masses. Although they have the lower mass, the electrons are mainly responsible for the determination of the physical and chemical properties of materials. Therefore, research strongly focuses on approximations to the solution of the electronic part of the Schrödinger equation (also known as the *electronic structure problem*). Corner stones are, e.g., the *Hartree-Fock approximation* (HF), *Møller-Plesset perturbation theory* (MP), *density functional theory* (DFT), the *random phase approximation* (RPA), second-order screened exchange (SOSEX) or *coupled cluster theory* (CC). Some of them will be introduced in detail later in this work.

Since these methods are approximations, they can be classified by their accuracy and by their computational cost in memory and time. Today, the so called orbital-based or wavefunction-based methods as MP, RPA, or CC are becoming increasingly popular, since they allow for a systematic improvement of the approximation of the electronic Schrödinger equation. However, their computational cost is fairly high. A measure for the computational complexity is given by the scaling of the computation time and the scaling of the required memory with respect to the system size (e.g. the number of involved electrons). A steep scaling restricts the application of an algorithm to small systems with only a few electrons, if a result is required in a reasonably short time of a few hours or days. Hence, the development of low-complexity algorithms is a highly important task in *ab initio* computational materials physics.

At present, the RPA is among the most promising candidates to calculate reasonably accurate approximations of the electronic Schrödinger equation due to its low scaling compared to MP or CC. However, the RPA introduces a systematic error by neglecting the *Pauli exclusion principle* for electrons. This principle follows from the fact that electrons are indistinguishable particles, implying a certain mathematical property of the solution of the Schrödinger equation. This property is systematically violated by the RPA.

On the other hand, MP, SOSEX¹, and CC do not violate the Pauli exclusion principle. These corrections are particularly relevant when short-range interactions between electrons play an important role in the considered material. The correction terms are called *exchange terms* since they subtract all contributions that correspond to the situation if two arbitrary electrons were exchanged. Those parts are not allowed to contribute to the solution, since the electrons are indistinguishable, which implies that the exchange of two electrons is a meaningless notion.

Unfortunately, those exchange terms introduce additional computational complexity, making MP, SOSEX, and CC steep scaling and computationally very expensive methods. In this work we present new algorithms that significantly reduce the computational complexity of the exchange terms, such that larger systems are tractable. In particular

¹SOSEX does not fully account for the Pauli exclusion principle but approximately corrects the RPA.

we focus on MP2 and SOSEX, since the exchange terms are formally simple and directly accessible in these methods. In summary, the developed algorithms represent an important step towards the calculation of accurate correlation energies for large systems, involving several hundreds of valence electron. All algorithms are implemented in the Vienna *ab initio* simulation package (VASP). As our benchmark theory we employ second-order Møller-Plesset perturbation theory (MP2) since it is the simplest candidate that includes exchange terms. We also discuss how the new methods could be adapted for SOSEX.

The thesis is structured as follows. The first part provides an introduction to the theoretical basis on which *ab initio* computational materials physics is founded today. It is written in a pedagogical manner, aimed to everyone who has basic knowledge in quantum mechanics. The skilled reader can skip this part without hesitation, and may start directly from Chap. 7 or even from Part II. The main research work of this thesis follows in Part II. There, we introduce and discuss six newly developed algorithms to reduce the computational complexity of correlation energy calculations, with a particular attention to exchange-like contributions. We distinguish three deterministic and three stochastic algorithms. While the deterministic approaches maintain the numerical accuracy and achieve the lower scaling only by rearrangements of mathematical terms, the stochastic algorithms come at the price of a statistical error. We conclude Part II in Chap. 12. Separated from this, we present a research work on lead selenide (PbSe) in Part III. The RPA method was used to calculate the temperature-pressure phase diagram of three different crystal structures of PbSe. In this part, we resolved the inconsistency of previous DFT-based *ab initio* studies, and provide accurate data for the construction of force fields.

Part I

Theory

CHAPTER 2

The many-body Hamiltonian and how we treat it

2.1 The Many-body Hamiltonian and the free energy

In computational materials physics we aim to calculate materials properties under realistic conditions. In this thesis, we focus on systems in the thermodynamic equilibrium. For this purpose the canonical ensemble serves as a convenient starting point, since it allows to control the particle number, the volume, and the temperature of the considered system. The state of the considered system is then determined by the minimum of the free energy, defined by

$$F(T, V) = -k_B T \ln Z(T, V) , \quad (2.1)$$

in which

$$Z(T, V) = \sum_{k=0}^{\infty} e^{-\beta \mathcal{E}_k} , \quad (2.2)$$

is the canonical partition sum. Here, k_B is the Boltzmann constant¹, T is the temperature, $\beta = (k_B T)^{-1}$, and V is the volume of the considered system. The partition sum is calculated by the sum over all possible energetic states, where the energies \mathcal{E}_k implicitly depend on the volume V . Accurate calculations of $F(T, V)$ allow, e.g., for structure predictions, calculation of bond lengths, surface energies, or phase diagrams of real materials. The energies \mathcal{E}_k are determined by the eigenvalues of the many-body Hamilton operator H (see below) of the considered system,

$$H\Psi_k = \mathcal{E}_k\Psi_k . \quad (2.3)$$

This eigenvalue equation is also known as the *time-independent Schrödinger equation*, being a fundamental postulate of quantum mechanics. Its eigenvectors are square integrable functions, $\Psi_k(\mathbf{R}_1, \dots, \mathbf{R}_M, \mathbf{r}_1, \dots, \mathbf{r}_N)$, where \mathbf{R}_I and \mathbf{r}_i are understood as the eigenvalues of the position operators of the nuclei and electrons, respectively. If the quantum mechanical system is a real material, consisting of M atomic nuclei and N electrons, the Hamilton

¹ $k_B \approx 8.6173 \cdot 10^{-5} \text{ eV/K}$ or $1.3806 \cdot 10^{-23} \text{ J/K}$, K \equiv Kelvin, eV \equiv electronvolt, J \equiv Joule

operator takes the form,

$$H = T_n + T_e + V_{nn} + V_{ne} + V_{ee} \quad (2.4)$$

with

$$T_n = - \sum_{I=1}^M \frac{\hbar^2}{2M_I} \nabla_{\mathbf{R}_I}^2, \quad T_e = - \frac{\hbar^2}{2m} \sum_{i=1}^N \nabla_{\mathbf{r}_i}^2, \quad (2.5)$$

$$V_{nn} = \kappa_C \sum_{I < J}^M \frac{Z_I Z_J e^2}{|\mathbf{R}_I - \mathbf{R}_J|}, \quad V_{ne} = -\kappa_C \sum_I^M \sum_i^N \frac{Z_I e^2}{|\mathbf{R}_I - \mathbf{r}_i|}, \quad V_{ee} = \kappa_C \sum_{i < j}^N \frac{e^2}{|\mathbf{r}_i - \mathbf{r}_j|}. \quad (2.6)$$

Here, T_n and T_e are the kinetic energy operators of the atomic nuclei (n) with mass M_I and of the electrons (e) with mass $m \approx 9.1094 \cdot 10^{-31}$ kg, respectively. The Coulomb interaction is decomposed into the interaction between the nuclei, V_{nn} , the interaction between the nuclei and the electrons, V_{ne} , and the electron-electron interaction, V_{ee} . The position operators of the nuclei and electrons are termed as \mathbf{R}_I and \mathbf{r}_i , respectively. Each electron carries the negative elementary charge² $-e$, whereas the nuclei are oppositely charged by $Z_I e$. The expression $\kappa_C = (4\pi\epsilon_0)^{-1}$ is the Coulomb constant³. We will make use of the Hartree atomic units. Hence, we set $e = m = \hbar = \kappa_C = 1$ in order to keep the equations simple and clear.

As mentioned in the Introduction, exact analytical solutions of the time-independent many-body Schrödinger equation (2.3) are unattainable (except for $M = N = 1$, being the hydrogen atom). Therefore, all many-body considerations have to rely on approximation techniques. In the following, we introduce some of the important corner stones.

2.2 Comments on the mathematical notation

In this thesis we will make use of the bra-ket notation by Dirac [2]. This is particularly useful to distinguish between the abstract mathematical object, e.g. a vector in Hilbert space, $|\Phi\rangle$, and its representation in a certain basis, e.g. a wave function in real space, $\Phi(\mathbf{r})$. The relation of both objects, for this example, is given by the inner product,

$$\langle \mathbf{r} | \Phi \rangle = \Phi(\mathbf{r}). \quad (2.7)$$

This clear distinction avoids the "awkward jump in the flow of one's thoughts when one changes from one to the other." [2] If a clear distinction is not necessary, we also sometimes write Φ instead of $|\Phi\rangle$ for the general vector (as in Eq. 2.3). The same holds for operators. As used in the previous section, the momentum operator can be written in an abstract and in a real space notation. In the abstract notation the action of the momentum operator \mathbf{P} on a state vector $|\Phi\rangle$ is simply $\mathbf{P}|\Phi\rangle$. The relation to the real space representation is, again, given by an inner product,

$$\langle \mathbf{r} | \mathbf{P} | \mathbf{r}' \rangle = -i\hbar \nabla_{\mathbf{r}} \delta(\mathbf{r} - \mathbf{r}') = i\hbar \nabla_{\mathbf{r}'} \delta(\mathbf{r} - \mathbf{r}'), \quad (2.8)$$

² $e \approx 1.6022 \cdot 10^{-19}$ C, C \equiv Coulomb

³ $\epsilon_0 \approx 8.8542 \cdot 10^{-12}$ F/m, F \equiv Farad, m \equiv meter

where $\nabla_{\mathbf{r}}\delta(\mathbf{r} - \mathbf{r}')$ is understood as a distribution. One can conclude that

$$\langle \mathbf{r} | \mathbf{P} | \Phi \rangle = -i\hbar \nabla_{\mathbf{r}} \Phi(\mathbf{r}) . \quad (2.9)$$

Since this work is about many-electron systems, we introduce the following notation for many-electron states,

$$\dots \otimes |\varphi_i\rangle \otimes \dots \otimes |\varphi_j\rangle \otimes \dots = \dots |\varphi_i\rangle \dots |\varphi_j\rangle \dots = |\dots \varphi_i \dots \varphi_j \dots\rangle , \quad (2.10)$$

i.e. the tensor product of state vectors of a sub Hilbert space (left) is simply written as a single state vector of the entire Hilbert space (right), or, alternatively, as a sequence of state vectors (middle), neglecting the tensor product symbol. An N electron wave function, $|\Phi\rangle$, can thus be written in real space as

$$\langle \mathbf{r}_1 \dots \mathbf{r}_N | \Phi \rangle = \Phi(\mathbf{r}_1, \dots, \mathbf{r}_N) . \quad (2.11)$$

2.3 Born-Oppenheimer approximation for the free energy

Although the many-particle Hamiltonian (2.4) looks quite symmetric for interchanging n (nuclei) and e (electrons), they play a completely different role in molecules or solids at ambient conditions. The electrons act as a glue and bind the nuclei, giving the molecule or crystal its characteristic spatial structure, as the vibrating nuclei are mainly responsible for thermodynamic properties like the specific heat.

Born-Oppenheimer approximation

The different roles are a consequence of the small ratio of the masses m/\mathcal{M} , where \mathcal{M} is an average mass of the considered nuclei. Born and Oppenheimer [1] showed, that an expansion of the eigenenergies \mathcal{E}_k of the many-body Hamiltonian (2.3) in terms of $x = (m/\mathcal{M})^{1/4}$ reveals, as they write, the "natural ordering of the energy contributions". The lowest order, $\mathcal{O}(x^0)$, corresponds to "nailed" or frozen nuclei, where only the electron dynamics contribute. The lowest order corrections are the $\mathcal{O}(x^2)$ terms and include vibrations of the nuclei. Rotations are covered by the $\mathcal{O}(x^4)$ terms. All three types of energy contribution are independent of each other. Only at higher orders, the three types are coupled, including, e.g., interactions between the electrons and the vibrations of the nuclei. This is especially important for effects like the temperature dependence of electric conductivity, which, however, will not play a role in this thesis. Here, we restrict ourselves to the first two orders, the electron energy with frozen nuclei and the nucleus vibrations.

Employing this approximation, the independence of the two energy contributions can be incorporated into to the Schrödinger equation (2.3) in the following way,

$$\mathcal{E}_k \approx \Xi_l + E_m , \quad k = (l, m) , \quad (2.12)$$

$$\Psi_k(\mathbf{R}_1, \dots, \mathbf{R}_M, \mathbf{r}_1, \dots, \mathbf{r}_N) \approx \Lambda_l(\mathbf{R}_1, \dots, \mathbf{R}_M) \cdot \Phi_m(\mathbf{r}_1, \dots, \mathbf{r}_N) . \quad (2.13)$$

Here, the eigenvalues \mathcal{E}_k are splitted into the vibrational energies Ξ_l and into the electronic energies E_m . The index k is also splitted into the independent indices l and m . Furthermore, the eigenfunctions decompose into a product of a function describing only the nuclei, Λ_l , and into the electronic wave function, Φ_m . If we, furthermore, split the Hamiltonian into a part, H_n , which only acts on the nuclei, Λ_l , and another one, H_e , which only acts on the electrons, Φ_m , we can rewrite the Schrödinger equation (2.3) as,

$$\frac{H_n \Lambda_l}{\Lambda_l} + \frac{H_e \Phi_m}{\Phi_m} \approx \Xi_l + E_m . \quad (2.14)$$

This splitting can be achieved, if we define

$$H_e^{\{\mathbf{R}_l\}} = T_e + V_{nn}^{\{\mathbf{R}_l\}} + V_{ne}^{\{\mathbf{R}_l\}} + V_{ee} , \quad (2.15)$$

where the positions of the nuclei $\{\mathbf{R}_l\}$ only appear as parameters instead of operators. The electronic energies E_m are found by minimizing over a landscape of all possible configurations of frozen nuclei at $\{\mathbf{R}_l\}$,

$$E_m = \min_{\{\mathbf{R}_l\}} E_m^{\{\mathbf{R}_l\}} = E_m^{\{\mathbf{R}_l^0\}} , \quad (2.16)$$

where we denote the minimizing configuration as $\{\mathbf{R}_l^0\}$. The same holds for the wave-function of the electrons

$$\Phi_m(\mathbf{r}_1, \dots, \mathbf{r}_N) = \Phi_m^{\{\mathbf{R}_l^0\}}(\mathbf{r}_1, \dots, \mathbf{r}_N) , \quad (2.17)$$

which are related by the

electronic Schrödinger equation,

$$H_e^{\{\mathbf{R}_l\}} \Phi_m^{\{\mathbf{R}_l\}}(\mathbf{r}_1, \dots, \mathbf{r}_N) = E_m^{\{\mathbf{R}_l\}} \Phi_m^{\{\mathbf{R}_l\}}(\mathbf{r}_1, \dots, \mathbf{r}_N) . \quad (2.18)$$

The energy landscape, $E_m^{\{\mathbf{R}_l\}}$, then acts as an effective potential for the nuclei. However, to avoid any dependence of l from m we pick the electronic ground state, $m = 0$, for the effective potential, and find an expression for Hamiltonian of the nuclei,

$$H_n = T_n + E_{m=0}^{\{\mathbf{R}_l\}} , \quad (2.19)$$

wherein the \mathbf{R}_l now regain their previous purpose as operators. We thus arrive at the

Schrödinger equation for the nuclei,

$$H_n \Lambda_l(\mathbf{R}_1, \dots, \mathbf{R}_M) = \Xi_l \Lambda_l(\mathbf{R}_1, \dots, \mathbf{R}_M) . \quad (2.20)$$

The choice of $m = 0$ for the effective energy landscape can be justified in the following way. In the case of metals, it is known, that the electrons have a vanishing contribution to

the heat capacity at ambient conditions. This can be derived from the free electron model. Thus, the electronic ground state is a reasonable assumption for metals. For insulators with a finite band gap $E_g = E_1 - E_0$, the free electron model is no longer valid. But we can still expect the material to be in the ground state for temperatures $k_B T \ll E_g$. At room temperature this corresponds to $E_g \gg 0.026 \text{ eV}$, which includes even semiconductors.

Free energy in the Born-Oppenheimer approximation

If we apply the results of the Born-Oppenheimer approximation to the canonical partition function (2.2), we obtain

$$\begin{aligned} Z(T, V) &= \sum_{k=0}^{\infty} e^{-\beta \mathcal{E}_k} \approx \sum_{l,m=0}^{\infty} e^{-\beta(E_m + \Xi_l)} \\ &= e^{-\beta E_0} e^{-\beta \Xi_0} \sum_{m=0}^{\infty} e^{-\beta(E_m - E_0)} \sum_{l=0}^{\infty} e^{-\beta(\Xi_l - \Xi_0)}. \end{aligned} \quad (2.21)$$

As above, we assume that energy from the heat bath is not absorbed by the electrons if $k_B T \ll E_m - E_0$, such that $e^{-\beta(E_m - E_0)} \approx 0$ for $m \geq 1$. We conclude,

$$Z(T, V) \approx e^{-\beta E_0} e^{-\beta \Xi_0} \sum_{l=0}^{\infty} e^{-\beta(\Xi_l - \Xi_0)}. \quad (2.22)$$

The last assumption ($k_B T \ll E_m - E_0$) clearly excludes metals (systems with a vanishing band gap), which would require a special treatment. Since metals also pose many other numerical difficulties in the development of algorithms, which are not dealt with in this thesis, we will limit ourselves to materials with finite band gaps. For the free energy this results in

$$F(T, V) = -k_B T \ln Z(T, V) \approx E_0 + \Xi_0 - k_B T \ln \sum_{l=0}^{\infty} e^{-\beta(\Xi_l - \Xi_0)}. \quad (2.23)$$

If we define the

free energy of the vibrations (phonons) by

$$F_n(T, V) = \Xi_0 - k_B T \ln \sum_{l=0}^{\infty} e^{-\beta(\Xi_l - \Xi_0)}, \quad (2.24)$$

with the *zero point vibration energy* Ξ_0 , we can write

the free energy as

$$F(T, V) \approx E_0 + F_n(T, V), \quad (2.25)$$

where E_0 is simply the electronic ground state energy.

Again, this approximation only holds as long as the temperature has no effect on the electrons, leaving thermal properties solely to the vibrations of the nuclei.

Summary

In short, we found that it is sufficient to solve the electronic Schrödinger equation (2.18) only for the ground state $E_0^{\{\mathbf{R}_I\}}$ on a sufficiently large set of configurations $\{\mathbf{R}_I\}$ of the positions of the nuclei. The minimum of $E_0^{\{\mathbf{R}_I\}}$ then provides the desired electronic ground state E_0 . In order to include the vibrational energy, also the Schrödinger equation for the nuclei (2.20) has to be solved, but there, the full spectrum is required. The latter is usually achieved by the harmonic approximation, assuming that the nuclei, located at the equilibrium positions $\{\mathbf{R}_I^0\}$, are all connected by springs (this will be discussed in Sec. 2.7). The greatest difficulty in materials physics, however, remains to find the ground state energy of the electronic Schrödinger equation (2.18).

2.4 Mean field approach and Bloch's theorem

We are left with a many-electron Schrödinger equation (2.18), and it is still not possible to treat this equation for $N \geq 2$ electrons directly. The major difficulty arises from the combination of V_{ne} and V_{ee} , not only from the fact that N is large. For instance, the case $V_{ee} = 0$ leads to the independent electron model, and the case $V_{ne} = 0$ is called homogeneous electron gas. For both models, numerical and also special analytical solutions are available, even for large N . For many real materials, however, both interactions, V_{ne} and V_{ee} are crucial.

Mean field Hamiltonians

Nevertheless, one generally accepted approach is to replace the electronic Hamiltonian (2.15) by a *mean field* (MF) Hamiltonian H_e^{MF} , where the nucleus-electron and electron-electron interactions are replaced by a sum of effective one-electron potentials, $V_{ne} + V_{ee} \rightarrow V_{\text{eff}}$,

$$H_e \rightarrow H_e^{\text{MF}} = T_e + V_{nn} + V_{\text{eff}}, \quad V_{\text{eff}} = \sum_{i=1}^N \mathbb{1} \otimes \dots \otimes \underbrace{v_{\text{eff}}}_{i\text{'th position}} \otimes \dots \otimes \mathbb{1}. \quad (2.26)$$

From the mathematical perspective, this appears as a rather desperate attempt. However, in physics, we do not aim to solve mathematical equation exactly, but we often desire reasonable approximations that cover the considered physical phenomena sufficiently accurate. From the Drude model [3] or the Drude-Sommerfeld [4] model, for instance, we know already since the year 1900 that materials properties can, indeed, be predicted by models that replace the nucleus-electron and electron-electron interactions. Since the

mean field Hamiltonian is now a sum of one-electron operators,

$$H_e^{\text{MF}} = \sum_{i=1}^N \mathbb{1} \otimes \dots \otimes \underbrace{h^{\text{MF}}}_{i\text{'th position}} \otimes \dots \otimes \mathbb{1}, \quad h^{\text{MF}} = \frac{\mathbf{P}^2}{2} + V_{\text{nn}} + v_{\text{eff}}, \quad (2.27)$$

where V_{nn} is just a number (the interaction energy of the nuclei), its eigenstates decay into products of one-electron states. Those one-electron states are solutions of an effective one-electron Schrödinger equation,

$$h^{\text{MF}}|\varphi\rangle = \varepsilon|\varphi\rangle. \quad (2.28)$$

Usually, such mean field equations are derived from energy functionals of one-electron states, $E[\{\varphi\}]$, or energy functionals of the electron density, $E[\rho]$. The variation principle, $\delta E/\delta\varphi = \varepsilon\varphi$ or $\delta E/\delta\rho = 0$ then defines the mean field Hamiltonian. Clearly, the choice of the energy functionals determines if the resulting orbitals or densities are meaningful at all. As an illustration, one can consider the Hartree functional⁴,

$$E_{\text{Hartree}}[\{\varphi\}] = \sum_i^N \int d^3r \varphi_i^*(\mathbf{r}) \nabla^2 \varphi_i(\mathbf{r}) - \sum_I^M \sum_i^N \int d^3r \frac{Z_I |\varphi_i(\mathbf{r})|^2}{|\mathbf{R}_I - \mathbf{r}|} + \frac{1}{2} \sum_{ij}^N \int d^3r \int d^3r' \frac{|\varphi_i(\mathbf{r})|^2 |\varphi_j(\mathbf{r}')|^2}{|\mathbf{r} - \mathbf{r}'|} + V_{\text{nn}}^{\{\mathbf{R}_I\}}, \quad (2.29)$$

which, after applying the variational principle, results in the following mean field equation in order to determine the one-electron states $\varphi_i(\mathbf{r})$,

$$\underbrace{\left[-\frac{1}{2} \nabla^2 - \sum_I^M \frac{Z_I}{|\mathbf{R}_I - \mathbf{r}|} + \sum_j^N \int d^3r' \frac{|\varphi_j(\mathbf{r}')|^2}{|\mathbf{r} - \mathbf{r}'|} \right]}_{h_{\text{Hartree}}^{\text{MF}}} \varphi_i(\mathbf{r}) = \varepsilon_i \varphi_i(\mathbf{r}). \quad (2.30)$$

Thus, the effective potential of the Hartree functional reads,

$$v_{\text{eff}}(\mathbf{r}) = - \sum_I^M \frac{Z_I}{|\mathbf{R}_I - \mathbf{r}|} + \sum_j^N \int d^3r' \frac{|\varphi_j(\mathbf{r}')|^2}{|\mathbf{r} - \mathbf{r}'|}. \quad (2.31)$$

Although this approach appears reasonable, it disregards two crucial contributions to the ground state, namely *exchange* and *correlation*, two terms which will be clarified in Chap. 5. In Chap. 4 and 6 we will introduce two established mean field approaches, the Hartree-Fock method and density functional theory, that can predict physical properties of materials quite accurately.

⁴Note, that Hartree excluded the case $i = j$ in the ij sum. For simplicity we neglect this subtlety.

With mean field approaches, we eventually arrived at equations, that are tractable with modern computers. It is a one-particle differential equation and its solutions are functions of only one coordinate. If such a model can satisfactorily predict materials properties, depends on the construction of the effective potential v_{eff} . The resulting eigenstates of (2.28) are considered as the electron orbitals that are called *atomic orbitals* in the case of atoms which are described by the well-known quantum numbers (n, l, m, s) . They are called *molecular orbitals* in the case of molecules, and *Bloch orbitals* in the case of a periodic crystal. It is, however, important to keep in mind, that the exact solution of the electronic Schrödinger equation (2.18) is one single high dimensional wave function that covers all electrons whereas the concept of electron orbitals is only a mean field approximation. This approximation is also referred to as the *independent particle picture*.

Such mean field calculations are the foundation of today's ab initio computational physics. The resulting orbitals and eigenvalues serve as a basis to construct many-electron wave functions or to perform perturbation theory calculations in order to correct the error, introduced by the mean field approach.

Bloch's theorem

In the case of a crystal that has a periodic lattice structure, a mathematical part of the eigenstates of the mean field Hamiltonian (2.28) inherit the periodicity of the crystal lattice. This is known as Bloch's theorem [5] and can be derived as follows.

Let us assume that the crystal lattice of our material is a *Bravais lattice* which can be characterized by three *primitive lattice* vectors, $\mathbf{a}_1, \mathbf{a}_2, \mathbf{a}_3$. This implies that the nuclei are arranged in a regular lattice, such that any periodic repetition of each nucleus can be reached by linear combinations of the Bravais lattice vectors, $\mathbf{R} = n_1\mathbf{a}_1 + n_2\mathbf{a}_2 + n_3\mathbf{a}_3$. The cell spanned by these primitive lattice vectors and the nuclei it contains is summarized as *primitive unit cell*. An illustration of crystal structures is given in Fig. 2.1.

For each lattice vector \mathbf{R} , we can define a translation operator by $t_{\mathbf{R}} = e^{-i\mathbf{R}P}$, acting as $\langle \mathbf{r} | t_{\mathbf{R}} | f \rangle = f(\mathbf{r} + \mathbf{R})$ on any function f . The crystal lattice also defines a *reciprocal lattice* via $\mathbf{b}_i \mathbf{a}_j = 2\pi\delta_{ij}$, where the last equation defines the *reciprocal lattice vectors*, \mathbf{b}_i , $i = 1, 2, 3$. If we assume infinitely many repetitions in all three directions of the lattice (to avoid surface effects), one can show that the mean field Hamiltonian commutes with the translation operator, $[h^{\text{MF}}, t_{\mathbf{R}}] = 0$, for all lattice vectors \mathbf{R} . This implies that h^{MF} and $t_{\mathbf{R}}$ have a common set of eigenstates,

$$h^{\text{MF}}|\varphi\rangle = \varepsilon|\varphi\rangle, \quad (2.32)$$

$$t_{\mathbf{R}}|\varphi\rangle = c_{\mathbf{R}}|\varphi\rangle. \quad (2.33)$$

Since $t_{\mathbf{R}}$ is a unitary operator, its eigenvalues are of magnitude one, $|c_{\mathbf{R}}| = 1$. Furthermore, from $t_{\mathbf{R}}t_{\mathbf{R}'} = t_{\mathbf{R}+\mathbf{R}'}$, we can conclude, $c_{\mathbf{R}}c_{\mathbf{R}'} = c_{\mathbf{R}+\mathbf{R}'}$. This restricts the eigenvalues to exponential functions of the form $c_{\mathbf{R}} = e^{ig(\mathbf{R})}$, where $g : \mathbb{R}^3 \rightarrow \mathbb{R}$ is a linear function. If we define a vector \mathbf{k} in reciprocal space by $\mathbf{k} = k_1\mathbf{b}_1 + k_2\mathbf{b}_2 + k_3\mathbf{b}_3$ with the choice

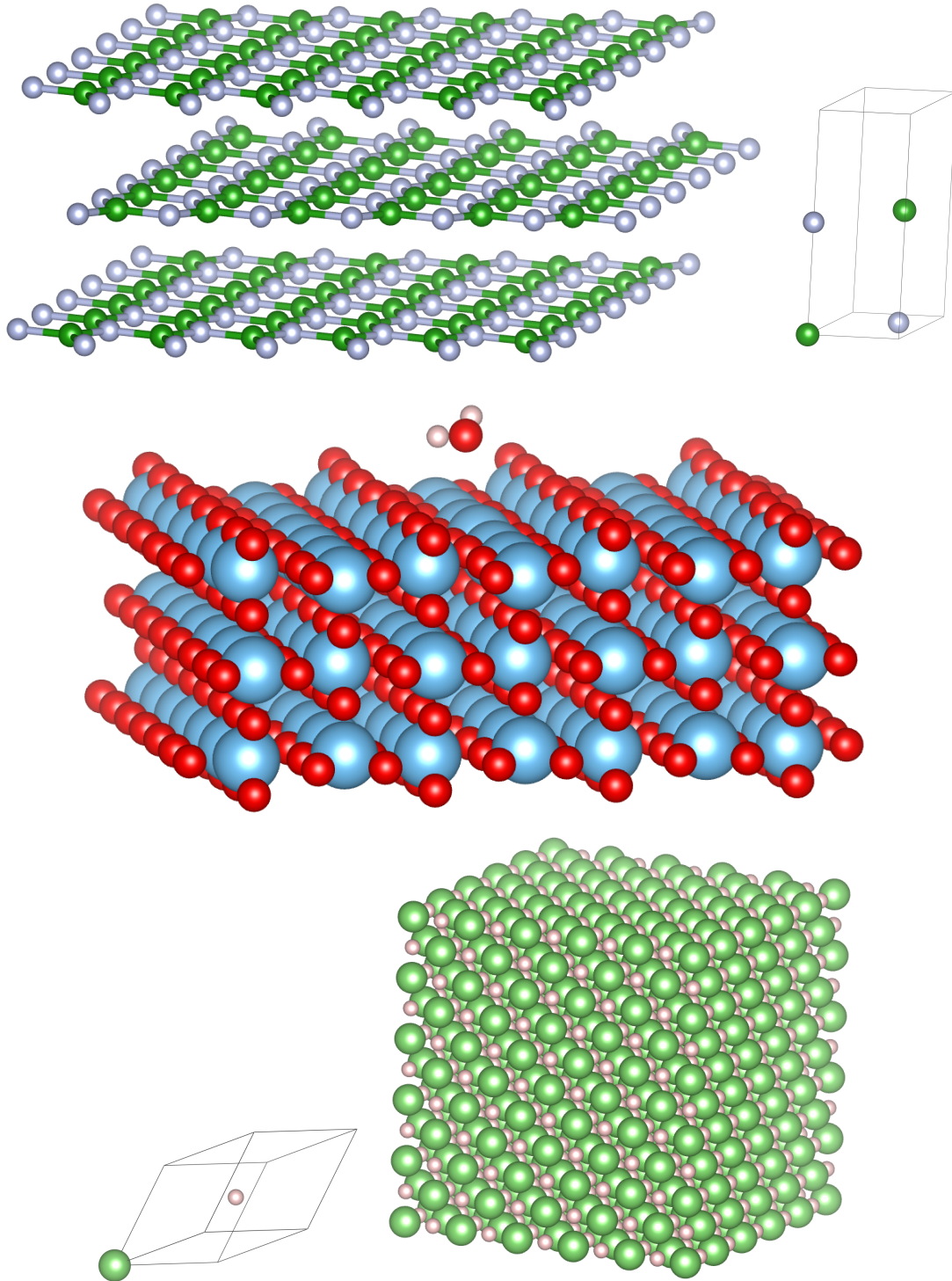


Figure 2.1: This figure shows examples of arrangements of the nuclei, as they are considered in materials physics, forming crystal structures or surfaces. Top: three layers of hexagonal boron nitride and the corresponding primitive cell. Middle: a water molecule on the surface of TiO_2 . Bottom: The crystal structure of lithium hydride and the corresponding primitive unit cell.

$k_i = g(\mathbf{a}_i)/2\pi$, then we can write for an eigenstate $|\varphi\rangle$,

$$t_{\mathbf{R}}|\varphi\rangle = c_{\mathbf{R}}|\varphi\rangle = e^{ig(\mathbf{R})}|\varphi\rangle = e^{i[n_1g(\mathbf{a}_1)+n_2g(\mathbf{a}_2)+n_3g(\mathbf{a}_3)]}|\varphi\rangle = e^{i\mathbf{k}\mathbf{R}}|\varphi\rangle . \quad (2.34)$$

Thus, each eigenstate $|\varphi\rangle$ determines the linear function g , and therefore, determines \mathbf{k} such that Eq. (2.34) holds. Accordingly we can assign to each eigenstate $|\varphi\rangle$ and each eigenvalue ε , its *Bloch vector* \mathbf{k} , $|\varphi\rangle \rightarrow |\varphi_{\mathbf{k}}\rangle$, $\varepsilon \rightarrow \varepsilon_{\mathbf{k}}$. The Bloch vector \mathbf{k} is also called *crystal momentum* or simply *wave vector*. Note that replacing $\mathbf{k} \rightarrow \mathbf{k} + \mathbf{G}$, where $\mathbf{G} = m_1\mathbf{b}_1 + m_2\mathbf{b}_2 + m_3\mathbf{b}_3$, $m_i \in \mathbb{Z}$, is a reciprocal lattice vector, leads to exactly the same equation, since $e^{i\mathbf{G}\mathbf{R}} = 1$. Thus we can restrict \mathbf{k} to the *first Brillouine zone* which is defined by the assumption that any \mathbf{k}' can be reached by $\mathbf{k}' = \mathbf{k} + \mathbf{G}$. Calculating the inner product of Eq. (2.34) with $\langle \mathbf{r} |$ yields the common formulation of Bloch's theorem, which states, that each eigenstate of the mean field Hamiltonian, h^{MF} , obeys the relation,

$$\varphi_{\mathbf{k}}(\mathbf{r} + \mathbf{R}) = e^{i\mathbf{k}\mathbf{R}}\varphi_{\mathbf{k}}(\mathbf{r}) . \quad (2.35)$$

A mathematically equivalent formulation is

$$\varphi_{\mathbf{k}}(\mathbf{r}) = \gamma \cdot e^{i\mathbf{k}\mathbf{r}}u_{\mathbf{k}}(\mathbf{r}) , \quad (2.36)$$

where γ is a normalization factor and $u_{\mathbf{k}}(\mathbf{r})$ is a periodic function: $u_{\mathbf{k}}(\mathbf{r} + \mathbf{R}) = u_{\mathbf{k}}(\mathbf{r})$.

Since h^{MF} commutes with $t_{\mathbf{R}}$, the wave vectors \mathbf{k} are good quantum numbers, but the energies $\varepsilon_{\mathbf{k}}$ can be degenerate. To fix this, another quantum number, the *band index* n , is introduced, $|\varphi_{\mathbf{k}}\rangle \rightarrow |\varphi_{n\mathbf{k}}\rangle$, $\varepsilon_{\mathbf{k}} \rightarrow \varepsilon_{n\mathbf{k}}$, such that $\varepsilon_{n\mathbf{k}} \leq \varepsilon_{n+1\mathbf{k}}$. The eigenvalues $\varepsilon_{n\mathbf{k}}$ therefore form the so called *band structure* of the corresponding material. In this independent particle picture, the lowest N states are called *occupied states* whereas all remaining ones are called *unoccupied states* or *virtual states*. The upper bound for the eigenvalues $\varepsilon_{n\mathbf{k}}$ of the occupied orbitals is usually denoted as Fermi energy $\varepsilon_F \geq \varepsilon_{n\mathbf{k}}$. The energy difference between the highest occupied state and the lowest unoccupied state is called *band gap* of the material. In the case of a vanishing band gap, the system is a metal for the considered mean field approach. Note that these properties strongly depend on the choice of the mean field Hamiltonian, e.g. a finite band gap does not necessarily predict that the material is not a metal in reality.

Born-von Karman boundary conditions

For all practical considerations, the first Brillouine zone can be discretized according to the *Born-von Karman* boundary conditions which read,

$$\varphi_{n\mathbf{k}}(\mathbf{r} + \mathcal{N}_i\mathbf{a}_i) = \varphi_{n\mathbf{k}}(\mathbf{r}) , \quad \mathcal{N}_i \text{ large} , \quad i = 1, 2, 3 . \quad (2.37)$$

This can be understood as decomposing an infinitely extended crystal into $\mathcal{N} = \mathcal{N}_1\mathcal{N}_2\mathcal{N}_3$ blocks with side lengths $\mathcal{N}_i\mathbf{a}_i$. The volume of the block is denoted as $\Omega = \mathcal{N}\Omega_0$, where Ω_0

is the volume of the unit cell. The larger N_i , the more harmless is this artificial requirement. Together with (2.35) this leads to the following discretization for the components of the \mathbf{k} -points, $\mathbf{k} = k_1 \mathbf{b}_1 + k_2 \mathbf{b}_2 + k_3 \mathbf{b}_3$,

$$k_i = \frac{2\pi l}{N_i}, \quad l \in \mathbb{Z}. \quad (2.38)$$

Hence, the Born-von Karman boundary conditions provide a useful scheme to discretize the continuous \mathbf{k} -space for computational algorithms. Furthermore, we introduce the following normalization convention for the Bloch orbitals.

$$\varphi_{n\mathbf{k}}(\mathbf{r}) = \frac{1}{\sqrt{\Omega}} e^{i\mathbf{k}\mathbf{r}} u_{n\mathbf{k}}(\mathbf{r}), \quad \langle \varphi_{m\mathbf{k}} | \varphi_{n\mathbf{q}} \rangle = \int_{\Omega} d^3r \varphi_{m\mathbf{k}}^*(\mathbf{r}) \varphi_{n\mathbf{q}}(\mathbf{r}) = \delta_{mn} \delta_{\mathbf{k}\mathbf{q}}, \quad (2.39)$$

which leads to

$$\int_{\Omega_0} d^3r u_{m\mathbf{k}}^*(\mathbf{r}) u_{n\mathbf{k}}(\mathbf{r}) = \Omega_0 \delta_{mn}. \quad (2.40)$$

2.5 What about the spin?

The electron spin has not yet been introduced. This is due to the fact that we restrict to a non-relativistic view of quantum mechanics. The spin, however, naturally emerges in a relativistic picture, based on the Dirac equation [6]. In the non-relativistic picture, it is a common practice to add the spin degree of freedom *ad-hoc*, even if the considered Hamiltonian acts only in the spatial Hilbert space. This is indispensable for many-particle calculations, since a missing spin degree of freedom leads to wrong consequences of the symmetrization postulate that will be introduced in Chap. 3. Introducing the spin in an *ad-hoc* manner also corresponds to the historical development of quantum theory. Pauli postulated the spin [7] as an additional quantum number in 1924. In combination with his exclusion principle (which will be introduced in Sec. 3.4), he was able to put the electron configuration of atoms on a sound theoretical footing. In order to describe this additional degree of freedom mathematically, we supplement the spatial electron orbitals by a spin state,

$$|\varphi\rangle \rightarrow |\chi\rangle = |\varphi\rangle \otimes |\sigma\rangle, \quad (2.41)$$

where we call $|\chi\rangle$ a *spin orbital*. For the spin state $|\sigma\rangle$ we usually use the eigenvectors of the z component of the spin operator as basis vectors, i.e. $|\uparrow\rangle$ and $|\downarrow\rangle$. We will also use the symbol $s = \uparrow, \downarrow$ to denote spin up or spin down states. To label spin orbitals we will use compound indices, which represent the Bloch wave vector, band index and spin, $|\chi_i\rangle = |\varphi_{n\mathbf{k}}\rangle \otimes |s\rangle$, i.e. $i \equiv (n, \mathbf{k}, s)$. In case of integrations, we will often make use of the notation $\mathbf{x} = (\mathbf{r}, s)$, such that

$$\int d\mathbf{x} \langle \mathbf{x} | \chi \rangle \dots = \int d\mathbf{x} \chi(\mathbf{x}) \dots = \sum_{s=\uparrow, \downarrow} \int d^3r \varphi(\mathbf{r}) \langle s | \sigma \rangle \dots \quad (2.42)$$

Having introduced the spin, it is possible to consider effective Hamiltonians which include spin-orbit coupling or magnetic fields in a non-relativistic fashion.

2.6 Pseudopotentials and the projector augmented wave method

Pseudopotentials

Albeit the many-electron Schrödinger equation can be tackled with mean field Hamiltonians, it is still a computationally ambitious task to solve those one-electron Schrödinger equations. This can be realized in the following way. All calculations have to be performed in a certain basis of the Hilbert space. In the plane wave basis, which is the underlying basis of all calculations in this thesis, the orbitals are stored by plane wave coefficients, $c_{nk}(\mathbf{G})$,

$$\varphi_{nk}(\mathbf{r}) = \sum_{\mathbf{G}}^{E_c} c_{nk}(\mathbf{G}) e^{i\mathbf{G}\mathbf{r}} . \quad (2.43)$$

This sum (which is essentially a Fourier transform) runs over all reciprocal lattice vectors \mathbf{G} truncated by the condition $\mathbf{G}^2/2 \leq E_c$, where E_c is a given cutoff parameter. To choose a sufficiently accurate grid is a crucial decision in plane-wave based methods. In particular, to cover the strong oscillations of the valence orbitals near the nuclei, requires very fine real space grids or, equivalently, very large Fourier cutoffs E_c . These oscillations originate from the Coulomb potential of the nuclei and are in principle equivalent to the oscillations which occur for bound states in the "particle in a box" toy model. The higher the orbital energy, the stronger its oscillations. Hence, near the nuclei the valence orbitals exhibit the strongest oscillations. However, since many important effects in materials physics (like bonding) can be explained by the behavior of the valence electrons only, one can argue that the sole contribution of the core orbitals is to shield the Coulomb potential of the nuclei. Therefore, it is a common approach to simplify the mean field approach by removing the core electrons from the calculations, i.e. we assume not only the nuclei to be frozen (Born-Oppenheimer approximation) but also the core electrons (*frozen core approximation*). Due to the opposite charge of the frozen nuclei and the frozen core electrons, the net potential for the valence electrons, which is often referred to as pseudopotential (PP), is softer and weaker. Formally, this means that we replace the effective potential, v_{eff} , of Eq. (2.26) by an effective pseudopotential, $v_{\text{eff}}^{\text{PP}}$, that mimics the valence electron-valence electron interaction, as well as the interaction of the valence electrons with the compound of the nuclei and the core electrons. The only degrees of freedom that are left and variable are those of the valence electrons. Thus, the mean field Schrödinger equation (2.28) is reduced to an eigenequation for the valence electrons only. The eigenstates of such a pseudopotential mean field approach are called *pseudo wavefunctions* or *pseudo reference states* and do not exhibit oscillations near the nuclei. Accordingly, the real space grid can be more coarse and the plane wave cutoff can be smaller in order to achieve a comparable accuracy. For instance, consider the silicon atom (14 electrons) with the configuration

$1s^2 2s^2 2p^6 3s^2 3p^2$. In many consideration only the electrons in the M shell are active and it is a good approximation to consider the electrons of the K and L shell as frozen core electrons. We are thus left with only 4 valence electrons.

Examples of well known implementations of pseudopotential techniques are the orthogonalized plane wave (OPW) [8] method or ultrasoft pseudopotentials [9].

The PAW method

All calculations in this thesis are based on the projector augmented wave (PAW) [10, 11] method, which is a generalized pseudopotential approach. The PAW allows to work with even smoother valence orbitals which are related to the real valence orbitals by a simple linear transformation. In the following the PAW is introduced.

In the PAW method, we aim to find a linear transformation,

$$|\psi_m\rangle = \mathcal{T}|\tilde{\psi}_m\rangle, \quad (2.44)$$

that relates the mean field eigenstates $|\psi_m\rangle$ to PAW orbitals $|\tilde{\psi}_m\rangle$ that are smooth functions inside augmentation spheres Ω_I around the nuclei $\{I\}$. The former are often called *all-electron (AE) orbitals* or *true orbitals*, whereas the latter are mostly denoted as *pseudo (PS) orbitals* or *PAW orbitals*. The index m is a compound index for the band, the crystal wave vector and the spin. Outside the augmentation spheres, both orbitals are equal, i.e. we can decompose the linear transformation into local linear transformations, \mathcal{T}_I , that act only inside the augmentation spheres Ω_I ,

$$\mathcal{T} = \mathbb{1} + \sum_I \mathcal{T}_I. \quad (2.45)$$

In order to distinguish between the inner and outer part of the augmentation spheres, we introduce the projector

$$P_I = \int_{\mathbf{r} \in \Omega_I} d^3r |\mathbf{r}\rangle\langle\mathbf{r}|, \quad (2.46)$$

which projects states into the augmentation sphere Ω_I . Furthermore, we use round brackets to denote states projected into the augmentation sphere, $|\dots\rangle = P_I|\dots\rangle$. The linear transformations \mathcal{T}_I are defined by

$$|\phi_{In}\rangle = [\mathbb{1} + \mathcal{T}_I]|\tilde{\phi}_{In}\rangle, \quad (2.47)$$

where $|\phi_{In}\rangle$ are usually atomic orbitals of the free atom I with atomic quantum numbers n , and $|\tilde{\phi}_{In}\rangle$ are smooth functions, which form a basis inside the augmentation spheres, i.e.

$$P_I \mathbb{1} P_I = \sum_n |\tilde{\phi}_{In}\rangle\langle\tilde{\phi}_{In}| \quad \forall I. \quad (2.48)$$

Thus, inside the spheres we can decompose the PAW orbitals as

$$|\tilde{\psi}_m\rangle = \sum_I \sum_n c_{In}^m |\tilde{\phi}_{In}\rangle, \quad (2.49)$$

where c_{In}^m are expansion coefficients. From (2.44), (2.45), and (2.47) we can conclude that, although the atomic orbitals $\{|\phi_{In}\rangle\}$ do not necessarily form a basis inside the augmentation spheres, the true orbitals can also be written as

$$|\psi_m\rangle = \mathcal{T}|\tilde{\psi}_m\rangle = \sum_I \sum_n c_{In}^m \mathcal{T}|\tilde{\phi}_{In}\rangle = \sum_I \sum_n c_{In}^m |\phi_{In}\rangle, \quad (2.50)$$

using the same coefficients c_{In}^m . Moreover, we introduce *projector states* $\langle\tilde{p}_{In}|$ which are dual to $\{|\tilde{\phi}_{In}\rangle\}$ inside the spheres

$$\langle\tilde{p}_{In}|\tilde{\phi}_{I'n'}\rangle = \delta_{II'}\delta_{nn'}, \quad (2.51)$$

and meet the completeness relation,

$$\sum_n |\tilde{\phi}_{In}\rangle\langle\tilde{p}_{In}| = P_I \mathbb{1} P_I. \quad (2.52)$$

Hence, we find

$$\langle\tilde{p}_{In}|\tilde{\psi}_m\rangle = c_{In}^m. \quad (2.53)$$

Note the following relations: The choice of the set $\{|\tilde{\phi}_{In}\rangle\}$ defines the linear transformation \mathcal{T} via (2.47) and (2.45), and also the coefficients c_{In}^m via (2.49). Hence the projector states $\langle\tilde{p}_{In}|$ are associated with \mathcal{T} due to the relation (2.51). According to Blöchl [10], given a set of linearly independent functions $\{f_{Im}\}$, the dual vectors $\langle\tilde{p}_{In}|$ can be calculated (Gram-Schmidt procedure) using the relation,

$$\langle\tilde{p}_{In}| = \sum_m M_{nm}^{-1}(I) \langle f_{Im}|. \quad (2.54)$$

where $M^{-1}(I)$ is the inverse of a matrix $M(I)$, defined by $M_{nm}(I) = \langle f_{In}|\tilde{\phi}_{Im}\rangle$ for each atom I . Having these ingredients, it is possible to construct a useful representation of the linear transformation \mathcal{T} . After subtracting (2.31) from (2.32) we obtain,

$$|\psi_m\rangle - |\tilde{\psi}_m\rangle = \sum_I \sum_n c_{In}^m [|\phi_{In}\rangle - |\tilde{\phi}_{In}\rangle] = \left(\sum_I \sum_n [|\phi_{In}\rangle - |\tilde{\phi}_{In}\rangle] \langle\tilde{p}_{In}| \right) |\tilde{\psi}_m\rangle. \quad (2.55)$$

However, since we assumed $|\psi_m\rangle = |\tilde{\psi}_m\rangle$ and $|\phi_{In}\rangle = |\tilde{\phi}_{In}\rangle$ outside the augmentation spheres, the left hand side and the right hand side are zero. Thus, Eq. (2.55) holds in the

entire space and we can replace $|\dots\rangle$ by $|\dots\rangle$,

$$|\psi_m\rangle = |\tilde{\psi}_m\rangle + \left(\sum_I \sum_n [|\phi_{In}\rangle - |\tilde{\phi}_{In}\rangle] \langle \tilde{p}_{In}| \right) |\tilde{\psi}_m\rangle = \mathcal{T} |\tilde{\psi}_m\rangle. \quad (2.56)$$

We can now identify the linear transformation by

$$\mathcal{T} = \mathbb{1} + \sum_I \sum_n [|\phi_{In}\rangle - |\tilde{\phi}_{In}\rangle] \langle \tilde{p}_{In}|. \quad (2.57)$$

Instead of solving the mean field Hamiltonian for the real orbitals, we can construct a PAW Hamiltonian by varying the underlying energy functional (as described in Chap. 2.4) with respect to $|\tilde{\psi}_m\rangle$ instead of $|\psi_m\rangle$, $\delta E[\mathcal{T}\tilde{\psi}]/\delta\tilde{\psi} = \varepsilon\mathcal{T}^\dagger\mathcal{T}\tilde{\psi}$, where E is the mean field energy functional for the real orbitals. The PAW orbitals can thus be calculated directly, whereas the real orbitals are available via \mathcal{T} . Moreover, the frozen core approximation can simply be incorporated by starting with a frozen core energy functional.

Also expectation values or matrix elements of operators can simply be calculated via the PAW orbitals only,

$$\langle\psi_m|A|\psi_n\rangle = \langle\tilde{\psi}_m|\tilde{A}|\tilde{\psi}_n\rangle, \quad \tilde{A} = \mathcal{T}^\dagger A \mathcal{T}, \quad (2.58)$$

where A is some operator. For later use, we derive the transformed version of $|\mathbf{r}\rangle\langle\mathbf{r}|$,

$$\begin{aligned} \mathcal{T}^\dagger |\mathbf{r}\rangle\langle\mathbf{r}| \mathcal{T} &= \left(\mathbb{1} + \sum_{Jm} |\tilde{p}_{Jm}\rangle [\langle\phi_{Jm}| - \langle\tilde{\phi}_{Jm}|] \right) |\mathbf{r}\rangle\langle\mathbf{r}| \left(\mathbb{1} + \sum_{In} [|\phi_{In}\rangle - |\tilde{\phi}_{In}\rangle] \langle\tilde{p}_{In}| \right) \\ &= |\mathbf{r}\rangle\langle\mathbf{r}| \\ &\quad + \sum_I \sum_n [|\mathbf{r}\rangle\langle\mathbf{r}|\phi_{In}\rangle - |\mathbf{r}\rangle\langle\mathbf{r}|\tilde{\phi}_{In}\rangle] \langle\tilde{p}_{In}| \\ &\quad + \sum_J \sum_n |\tilde{p}_{Jm}\rangle [\langle\phi_{Jm}|\mathbf{r}\rangle\langle\mathbf{r}| - \langle\tilde{\phi}_{Jm}|\mathbf{r}\rangle\langle\mathbf{r}|] \\ &\quad + \sum_{IJ} \sum_{nm} |\tilde{p}_{Jm}\rangle [\langle\phi_{Jm}| - \langle\tilde{\phi}_{Jm}|] [|\mathbf{r}\rangle\langle\mathbf{r}|\phi_{In}\rangle - |\mathbf{r}\rangle\langle\mathbf{r}|\tilde{\phi}_{In}\rangle] \langle\tilde{p}_{In}| \delta_{IJ}. \end{aligned} \quad (2.59)$$

For \mathbf{r} outside the augmentation spheres we find $\mathcal{T}^\dagger |\mathbf{r}\rangle\langle\mathbf{r}| \mathcal{T} = |\mathbf{r}\rangle\langle\mathbf{r}|$, which simply follows from the fact that \mathcal{T} is $\mathbb{1}$. For \mathbf{r} inside the augmentation spheres we can exploit Eq. (2.52) and find

$$\mathcal{T}^\dagger |\mathbf{r}\rangle\langle\mathbf{r}| \mathcal{T} = \sum_{IJ} \sum_{nm} |\tilde{p}_{Jm}\rangle \langle\phi_{Jm}|\mathbf{r}\rangle\langle\mathbf{r}|\phi_{In}\rangle \langle\tilde{p}_{In}| \delta_{IJ}, \quad \forall \mathbf{r} \in \bigcap_I \Omega_I. \quad (2.60)$$

Both cases are covered by

$$\mathcal{T}^\dagger |\mathbf{r}\rangle \langle \mathbf{r}| \mathcal{T} = |\mathbf{r}\rangle \langle \mathbf{r}| + \sum_I \sum_{nm} |\tilde{p}_{Im}\rangle [\langle \phi_{Im} | \mathbf{r}\rangle \langle \mathbf{r} | \phi_{In}\rangle - \langle \tilde{\phi}_{Im} | \mathbf{r}\rangle \langle \mathbf{r} | \tilde{\phi}_{In}\rangle] \langle \tilde{p}_{In} | . \quad (2.61)$$

To summarize, we can construct a linear transformation \mathcal{T} that relates smooth PAW orbitals to the true orbitals. \mathcal{T} is defined by choosing an appropriate set of smooth PAW basis functions $\{|\tilde{\phi}_{In}\rangle\}$ and projector states $\{|\tilde{p}_{In}\rangle\}$ that obey (2.51). This allows for even lower energy cutoffs and coarser real space grids than standard normconserving pseudopotential methods. All information of the solution of the real mean field Hamiltonian is encoded in the PAW orbitals and in the linear transformation. Note that all orbitals in this thesis have to be understood as PAW orbitals, however, we usually neglect the tilde to simplify the notation.

2.7 Lattice vibrations: relaxing the frozen nuclei

So far, we discussed the mean field treatment of the electronic Schrödinger equation (2.18). Although we aim almost exclusively to approximate the electronic part in this work, contributions due to the lattice vibrations (vibration of the nuclei) become important if temperature effects should be incorporated. Thus, we briefly present the important steps in order to calculate the free energy $F_n(T, V)$ of the lattice vibrations (see Eq. 2.24), i.e. approximately solve for the eigenvalues of (2.20).

As mentioned in Sec. 2.3 the lattice vibrations can often be calculated in the harmonic approximation. There, we assume, that all nuclei are connected by springs, such that the lattice vibrations can be considered as a superposition of harmonic oscillations of the nuclei around their equilibrium positions $\{\mathbf{R}_0\}$. It will turn out, that the Hamiltonian of the nuclei (2.19) can be written as an ensemble of *independent* harmonic oscillators,

$$H_n = T_n + E_{m=0}^{\{\mathbf{R}_I\}} \approx \sum_s \int d^3k \omega_{\mathbf{k}s}^{\{\mathbf{R}_I^0\}} \left(n_{\mathbf{k}s} + \frac{1}{2} \right) . \quad (2.62)$$

Here the summation and integration variables \mathbf{k} and s are similar to the crystal wave vector and band index of the electron mean field orbitals from Chap. 2.4 and will be explained below. The phonon number operator $n_{\mathbf{k}s}$ is equivalent to the standard bosonic operator for the quantum harmonic oscillator which is introduced in almost any quantum mechanics textbook. The crucial quantities are the frequencies, $\omega_{\mathbf{k}s}^{\{\mathbf{R}_I^0\}}$, that characterize the Hamiltonian and depend only on the equilibrium positions of nuclei $\{\mathbf{R}_I^0\}$. A brief derivation of the approximation (2.62) and the frequencies is in order.

Let us assume that the effective potential for the atoms can be written as a sum over all possible differences of the atom positions,

$$E_{m=0}^{\{\mathbf{R}_I\}} \approx \frac{1}{2} \sum_{IJ} \mathcal{V}(\mathbf{R}_I - \mathbf{R}_J) , \quad (2.63)$$

where \mathcal{V} will most likely have the form of a Lennard Jones-like potential for many materials. Furthermore, the following derivation only holds for Bravais lattices with only one atom in the basis. For materials with more than one atom in the basis the equations involve additional indices and clarity would be lost (see e.g. Ref. [12]). We now assume that each atom position can be decomposed into a fixed equilibrium position and an additional variable part, $\mathbf{R}_I = \mathbf{R}_I^0 + \mathbf{u}_I$. Since we assume the variable parts to be small, we expand the potential up to second order,

$$\begin{aligned} \frac{1}{2} \sum_{IJ} \mathcal{V}(\mathbf{R}_I - \mathbf{R}_J) &= \frac{1}{2} \sum_{IJ} \mathcal{V}(\mathbf{R}_I^0 - \mathbf{R}_J^0 + \mathbf{u}_I - \mathbf{u}_J) \\ &\approx \frac{1}{2} \sum_{IJ} \mathcal{V}(\mathbf{R}_I^0 - \mathbf{R}_J^0) + \frac{1}{2} \sum_{IJ} (\mathbf{u}_I - \mathbf{u}_J) \nabla \mathcal{V}(\mathbf{R}_I^0 - \mathbf{R}_J^0) \\ &\quad + \frac{1}{4} \sum_{IJ} [(\mathbf{u}_I - \mathbf{u}_J) \nabla]^2 \mathcal{V}(\mathbf{R}_I^0 - \mathbf{R}_J^0). \end{aligned} \quad (2.64)$$

The equilibrium positions, \mathbf{R}_I^0 , are intuitively defined as the minimum of the potential and thus the second term vanishes,

$$\sum_J \nabla \mathcal{V}(\mathbf{R}_I^0 - \mathbf{R}_J^0) = \sum_I \nabla \mathcal{V}(\mathbf{R}_I^0 - \mathbf{R}_J^0) = 0. \quad (2.65)$$

What remains is the term that contains a quadratic dependence of the deviations from the equilibrium, $(\mathbf{u}_I - \mathbf{u}_J)^2$. This corresponds to Hooke's law. For the second derivative, we introduce the following notation,

$$[(\mathbf{u}_I - \mathbf{u}_J) \nabla]^2 \mathcal{V}(\mathbf{R}_I^0 - \mathbf{R}_J^0) = (u_I^\mu - u_J^\mu) \partial_\mu \partial_\nu \mathcal{V}(\mathbf{R}_I^0 - \mathbf{R}_J^0) (u_I^\nu - u_J^\nu), \quad (2.66)$$

where $\mu, \nu = x, y, z$ are the components of the the vectors \mathbf{u} and ∂_μ are partial derivatives with respect to that coordinate. A summation over μ, ν is understood. Using the definition,

$$\mathcal{V}_{\mu\nu}(\mathbf{R}_I^0 - \mathbf{R}_J^0) := \delta_{IJ} \sum_K \partial_\mu \partial_\nu \mathcal{V}(\mathbf{R}_I^0 - \mathbf{R}_K^0) - \partial_\mu \partial_\nu \mathcal{V}(\mathbf{R}_I^0 - \mathbf{R}_J^0), \quad (2.67)$$

we can write

$$H_n \approx \sum_I \frac{p_I^2}{2M_I} + \frac{1}{2} \sum_{IJ} \mathcal{V}(\mathbf{R}_I^0 - \mathbf{R}_J^0) + \frac{1}{2} \sum_{IJ} u_I^\mu \mathcal{V}_{\mu\nu}(\mathbf{R}_I^0 - \mathbf{R}_J^0) u_J^\nu, \quad (2.68)$$

where p_I are the conjugate variables to \mathbf{u}_I , being the momentum operators of the nuclei, $p_I = -i\nabla_{\mathbf{u}_I}$, such that the canonical commutator relations,

$$[u_I^\mu, p_J^\nu] = i\delta_{\mu\nu} \delta_{IJ}, \quad (2.69)$$

hold. We can now define the *dynamical matrix* as

$$D_{\mu\nu}(\mathbf{k}) = \sum_I \mathcal{V}_{\mu\nu}(\mathbf{R}_I^0) e^{-i\mathbf{k}\mathbf{R}_I^0} . \quad (2.70)$$

For each \mathbf{k} this is a 3×3 matrix that will be denoted by $D(\mathbf{k})$. In order to arrive at an expression like (2.62) it is constructive to define the eigenvalues and eigenvectors of the dynamical matrix for every \mathbf{k} ,

$$D(\mathbf{k})\epsilon_{\mathbf{k}s} = \omega_{\mathbf{k}s}^2 \epsilon_{\mathbf{k}s} . \quad (2.71)$$

The choice of the symbols shows where we are heading. The eigenvalues of the dynamical matrix will turn out to be squared frequencies, $\omega_{\mathbf{k}s}$, of independent harmonic oscillators, whereas $\epsilon_{\mathbf{k}s}$ are the polarization vectors of these oscillations. The additional index $s = 1, 2, 3$ distinguishes the eigenvectors for each \mathbf{k} . For materials with more than one atom in the basis of the Bravais lattice one finds $s = 1, \dots, 3p$, where p is the number of atoms in the Bravais basis. Accordingly to the procedure to solve the quantum harmonic oscillator problem, we can define creation and annihilation operators by

$$a_{\mathbf{k}s} = \sum_I e^{-i\mathbf{k}\mathbf{R}_I^0} \epsilon_{\mathbf{k}s} \left[\sqrt{\frac{M_I \omega_{\mathbf{k}s}}{2}} \mathbf{u}_I + i \frac{1}{\sqrt{2M_I \omega_{\mathbf{k}s}}} \mathbf{p}_I \right] . \quad (2.72)$$

The creation operator $a_{\mathbf{k}s}^\dagger$ is simply the complex conjugate of $a_{\mathbf{k}s}$. These operators are bosonic creation and annihilation operator which obey the relations

$$[a_{\mathbf{k}s}, a_{\mathbf{k}'s'}^\dagger] = \delta_{\mathbf{k}\mathbf{k}'} \delta_{ss'} , \quad (2.73)$$

$$[a_{\mathbf{k}s}, a_{\mathbf{k}'s'}] = [a_{\mathbf{k}s}^\dagger, a_{\mathbf{k}'s'}^\dagger] = 0 . \quad (2.74)$$

Vice versa, we can express \mathbf{u}_I and \mathbf{p}_I by $a_{\mathbf{k}s}$ and $a_{\mathbf{k}s}^\dagger$,

$$\mathbf{u}_I = \sum_s \int d^3k e^{i\mathbf{k}\mathbf{R}_I^0} \sqrt{\frac{1}{2M_I \omega_{\mathbf{k}s}}} (a_{\mathbf{k}s} + a_{-\mathbf{k}s}^\dagger) \epsilon_{\mathbf{k}s} , \quad (2.75)$$

$$\mathbf{p}_I = -i \sum_s \int d^3k e^{i\mathbf{k}\mathbf{R}_I^0} \sqrt{\frac{M_I \omega_{\mathbf{k}s}}{2}} (a_{\mathbf{k}s} - a_{-\mathbf{k}s}^\dagger) \epsilon_{\mathbf{k}s} . \quad (2.76)$$

Plugging this into Eq. (2.68) we arrive at

$$H_n \approx \sum_s \int d^3k \omega_{\mathbf{k}s} \left(a_{\mathbf{k}s}^\dagger a_{\mathbf{k}s} + \frac{1}{2} \right) + \frac{1}{2} \sum_{IJ} \mathcal{V}(\mathbf{R}_I^0 - \mathbf{R}_J^0) , \quad (2.77)$$

where we could introduce $n_{\mathbf{k}s} = a_{\mathbf{k}s}^\dagger a_{\mathbf{k}s}$. The only difference between (2.62) and (2.77) is a constant. Hence, we approximated the Hamiltonian of the nuclei by infinitely many independent harmonic oscillators where the equilibrium positions $\{\mathbf{R}_I^0\}$ are the only

necessary parameters.

In this form, we can immediately read off the eigenvalues Ξ_l of H_n . For the zero point vibration energy we find

$$\Xi_0 = \frac{1}{2} \sum_s \int d^3k \omega_{ks} , \quad (2.78)$$

and the canonical partition function (only for the nuclei) results in

$$Z_n(T, V) = \sum_l e^{-\beta \Xi_l} = \prod_{ks} \frac{e^{-\omega_{ks}/(2k_B T)}}{1 - e^{-\omega_{ks}/(k_B T)}} . \quad (2.79)$$

Hence, we found the harmonic approximation of

the free energy of lattice vibrations

$$F_n(T, V) = \sum_s \int d^3k \left[\frac{\omega_{ks}}{2} + k_B T \ln \left(1 - e^{-\omega_{ks}/(k_B T)} \right) \right] , \quad (2.80)$$

where the the frequencies ω_{ks} implicitly depend on the volume V .

Summarized, the free energy of the lattice vibrations can be calculated by constructing the dynamical matrix (2.70), solving the eigenvalue equation (2.71) and computing the free energy via (2.80).

CHAPTER 3

The symmetry of the wave function for electrons

3.1 The symmetrization postulate for identical particles

Along with the postulate of the many-body Schrödinger equation (2.3), the symmetrization postulate is indispensable to correctly describe many-body systems. It states that any wave function that describes an observable system of *identical particles* is either *symmetric* or *antisymmetric*. To understand this postulate, we have to clarify the terms *identical particles*, *symmetric*, and *antisymmetric*.

Particles are *identical* if and only if they are *indistinguishable*. Particles are indistinguishable if there is no way, even in principle, to distinguish them from one another. As a consequence, the exchange of two identical particles (i.e. of their position) is a meaningless notion, since the exchange results in no change, and is therefore equivalent to no exchange. Consider, for example, the exchange of any two natural numbers in the expression $1 + 1 + 1$. This is clearly meaningless, since the natural number 1 is an abstract concept. In a comparable manner, electrons might be understood as an abstract concept to analyze matter.

To explain the terms *symmetric* and *antisymmetric*, we have to introduce the permutation operator. The permutation operator P_{ij} permutes two one-particle basis vectors, $|\alpha_i\rangle$ and $|\alpha_j\rangle$, in a N -particle basis vector, $|\alpha_1\rangle \otimes \dots \otimes |\alpha_N\rangle$,

$$\begin{aligned} P_{ij}|\alpha_1\rangle \otimes \dots \otimes |\alpha_i\rangle \otimes \dots \otimes |\alpha_j\rangle \otimes \dots \otimes |\alpha_N\rangle \\ = |\alpha_1\rangle \otimes \dots \otimes |\alpha_j\rangle \otimes \dots \otimes |\alpha_i\rangle \otimes \dots \otimes |\alpha_N\rangle . \end{aligned} \quad (3.1)$$

Since $P_{ij}^2 = \mathbb{1}$, the eigenvalues of P_{ij} are either $+1$ or -1 . An N -particle state is called symmetric, if it is an eigenstate of P_{ij} with eigenvalue $+1$,

$$P_{ij}|\psi_{\text{sym}}\rangle = +|\psi_{\text{sym}}\rangle \quad (3.2)$$

or antisymmetric if it is an eigenstate with eigenvalue -1 ,

$$P_{ij}|\psi_{\text{asym}}\rangle = -|\psi_{\text{asym}}\rangle , \quad (3.3)$$

for all i, j . We can then precisely formulate the

symmetrization postulate for identical particles:

- States that describe identical particles whose spin is an integer multiple of \hbar are symmetric. The particles are called *bosons*.
- States that describe identical particles whose spin is a half-odd integer multiple of \hbar are antisymmetric. The particles are called *fermions*.
- States that do not obey one of these two cases are absolutely forbidden.

Electrons are fermions with spin $\hbar/2$, therefore the electronic wave function (2.18) has to obey

$$P_{ij}|\Phi_e\rangle = -|\Phi_e\rangle, \quad \forall i, j. \quad (3.4)$$

From the symmetrization postulate, we can deduce, that any operator which represents a physical observable (including the Hamiltonian) has to be invariant under permutations of two quantum numbers. Let $|\psi\rangle$ be a quantum state that is either symmetric or antisymmetric, $P_{ij}|\psi\rangle = \pm|\psi\rangle$. For any observable A we find,

$$\langle\psi|A|\psi\rangle = (\pm)^2\langle\psi|P_{ij}^\dagger AP_{ij}|\psi\rangle, \quad (3.5)$$

and thus

$$A = P_{ij}^\dagger AP_{ij}. \quad (3.6)$$

or equivalently

$$[P_{ij}, A] = 0, \quad (3.7)$$

since $P_{ij}^\dagger = P_{ji} = P_{ij} = P_{ij}^{-1}$. This is nothing but the mathematical formulation of the assumption, that there is no physical observable which can distinguish identical particles.

3.2 Construction of N -electron states in mean field methods

As we introduced the mean field approach in Chap. 2.4, we deliberately omitted the construction of the full N -electron wave function using the one-electron eigenstates of the mean field Hamiltonian. This is due to the fact that the construction of N -electron states apparently requires the knowledge of the symmetrization postulate, which was not introduced at that stage.

The most simple construction of an N -electron mean field wave function $|\psi_{\text{asym}}^{\text{MF}}\rangle$ using one-electron spin orbitals $\{|\chi_i\rangle\}$ from a mean field calculation, is given by an antisymmetrization of an N -electron product state $|\chi_1\dots\chi_N\rangle$. The antisymmetrization is achieved

by the antisymmetrization operator \mathcal{A} that acts as follows,

$$|\psi_{\text{asym}}^{\text{MF}}\rangle = \mathcal{A}|\chi_1 \dots \chi_N\rangle = \frac{1}{\sqrt{N!}} \sum_{\sigma \in S_N} \text{sgn}(\sigma) |\chi_{\sigma_1} \dots \chi_{\sigma_N}\rangle, \quad (3.8)$$

where we sum over all permutations σ of the set $\{1, \dots, N\}$. In a certain basis (e.g. the real space basis), this corresponds to the definition of a determinant,

$$\langle \mathbf{r}_1 \dots \mathbf{r}_N | \mathcal{A} | \chi_1 \dots \chi_N \rangle = \frac{1}{\sqrt{N!}} \det \begin{pmatrix} \langle \mathbf{r}_1 | \chi_1 \rangle & \dots & \langle \mathbf{r}_1 | \chi_N \rangle \\ \vdots & \ddots & \vdots \\ \langle \mathbf{r}_N | \chi_1 \rangle & \dots & \langle \mathbf{r}_N | \chi_N \rangle \end{pmatrix}. \quad (3.9)$$

This formulation is also known as constructing a *Slater determinant* from one-electron spin orbitals. Exchanging any two spin orbitals obviously gives a minus sign, since it corresponds to a permutation of two columns in the matrix. For three spin orbitals the Slater determinant can be written out and reads

$$\begin{aligned} \mathcal{A}|\chi_1 \chi_2 \chi_3\rangle &= \frac{1}{\sqrt{6}} \sum_{\sigma \in S_3} \text{sgn}(\sigma) |\chi_{\sigma_1} \chi_{\sigma_2} \chi_{\sigma_3}\rangle \\ &= \frac{1}{\sqrt{6}} (|\chi_1 \chi_2 \chi_3\rangle + |\chi_3 \chi_1 \chi_2\rangle + |\chi_2 \chi_3 \chi_1\rangle - |\chi_3 \chi_2 \chi_1\rangle - |\chi_1 \chi_3 \chi_2\rangle - |\chi_2 \chi_1 \chi_3\rangle). \end{aligned} \quad (3.10)$$

The state operator of this system is simply given by $\rho = \mathcal{A}|\chi_1 \chi_2 \chi_3\rangle \langle \chi_1 \chi_2 \chi_3 | \mathcal{A}$. However, the one-electron reduced state operator is obtained by tracing out $3 - 1 = 2$ degrees of freedom and we obtain

$$\rho^{(1)} = \text{tr}_2 \text{tr}_3 \rho = \frac{1}{3} (|\chi_1\rangle \langle \chi_1| + |\chi_2\rangle \langle \chi_2| + |\chi_3\rangle \langle \chi_3|), \quad (3.11)$$

which is a maximally mixed state. Hence, associating an orbital with an electron is a misleading concept¹. In an antisymmetrized product state, each electron similarly occupies each spin orbital. Orbitals are rather mathematical ingredients to construct many-body states and every physical interpretation has to be treated with caution.

Clearly, the set of antisymmetrized product states, is only a small subset of all possible antisymmetric states. Consider, for example, the two-electron state

$$|\psi_{\text{triplet}}\rangle = \frac{1}{2} (|\varphi_1 \varphi_2\rangle - |\varphi_2 \varphi_1\rangle) \otimes (|\uparrow \downarrow\rangle + |\downarrow \uparrow\rangle). \quad (3.12)$$

The spin part forms a symmetric triplet state, whereas the spatial degree of freedom is antisymmetric, making the overall state antisymmetric. It is not possible to construct this state by antisymmetrizing two spin orbitals, $|\psi_{\text{triplet}}\rangle \neq \mathcal{A}|\chi_1 \chi_2\rangle$. At least two

¹This does not imply that mean-field approaches cannot lead to revealing results.

antisymmetrized product states (or equivalently, four spin orbitals) are necessary,

$$|\psi_{\text{triplet}}\rangle = \frac{1}{\sqrt{2}} \left(\mathcal{A}|\chi_1\chi_2\rangle + \mathcal{A}|\chi_3\chi_4\rangle \right), \quad (3.13)$$

with $|\chi_1\rangle = |\varphi_1\rangle \otimes |\uparrow\rangle$ and $|\chi_2\rangle = |\varphi_2\rangle \otimes |\downarrow\rangle$ as well as $|\chi_3\rangle = |\varphi_1\rangle \otimes |\downarrow\rangle$ and $|\chi_4\rangle = |\varphi_2\rangle \otimes |\uparrow\rangle$.

3.3 Slater-Condon rules

If two antisymmetrized product states differ only by one spin-orbital, we write that as

$$|\psi\rangle = \mathcal{A}|\chi_1 \dots \chi_i \dots \chi_N\rangle \rightarrow |\psi_i^a\rangle = \mathcal{A}|\chi_1 \dots \chi_a \dots \chi_N\rangle, \quad (3.14)$$

i.e. the spin orbital χ_i was replaced by χ_a . The same notation can be applied if more than one-spin orbital is replaced,

$$|\psi\rangle = \mathcal{A}|\chi_1 \dots \chi_i \dots \chi_j \dots \chi_N\rangle \rightarrow |\psi_{ij}^{ab}\rangle = \mathcal{A}|\chi_1 \dots \chi_a \dots \chi_b \dots \chi_N\rangle, \quad (3.15)$$

or

$$|\psi\rangle = \mathcal{A}|\chi_1 \dots \chi_i \dots \chi_j \dots \chi_k \dots \chi_N\rangle \rightarrow |\psi_{ijk}^{abc}\rangle = \mathcal{A}|\chi_1 \dots \chi_a \dots \chi_b \dots \chi_c \dots \chi_N\rangle, \quad (3.16)$$

and so on. If the spin-orbitals form an orthonormal basis in the one-electron Hilbert space, $\langle \chi_i | \chi_a \rangle = \delta_{ia}$, $\forall i, a$, then all possible antisymmetric Slater determinants form a orthonormal basis in the N -electron Hilbert space

$$\langle \psi | \psi_{ijk \dots}^{abc \dots} \rangle = 0, \quad (3.17)$$

$$\langle \psi_{ijk \dots}^{abc \dots} | \psi_{i'j'k' \dots}^{a'b'c' \dots} \rangle = \delta_{ii'} \delta_{jj'} \delta_{kk'} \dots \delta_{aa'} \delta_{bb'} \delta_{cc'} \dots \quad (3.18)$$

With this notation established, we formulate the *Slater-Condon rules* [13, 14], which drastically simplify the handling of one-electron and two-electron operators.

Slater-Condon rules I

If $f^{(m)}$ is a one-electron operator, acting in the m th one-electron Hilbert space, and

$$F = \sum_{m=1}^N f^{(m)}, \quad (3.19)$$

then

$$\langle \psi | F | \psi \rangle = \sum_{i=1}^N \langle \chi_i | f | \chi_i \rangle, \quad \langle \psi | F | \psi_i^a \rangle = \langle \chi_i | f | \chi_a \rangle, \quad \langle \psi | F | \psi_{ij}^{ab} \rangle = 0. \quad (3.20)$$

Slater-Condon rules II

If $g^{(mn)}$ is a two-electron operator, acting in the m th and n th one-electron Hilbert space, and

$$G = \sum_{m \neq n}^N g^{(mn)}, \quad (3.21)$$

then

$$\langle \psi | G | \psi \rangle = \sum_{i,j=1}^N \langle \chi_i \chi_j | g | \chi_i \chi_j \rangle - \langle \chi_i \chi_j | g | \chi_j \chi_i \rangle, \quad (3.22)$$

$$\langle \psi | G | \psi_i^a \rangle = \sum_{i=1}^N \langle \chi_i \chi_j | g | \chi_a \chi_j \rangle - \langle \chi_i \chi_j | g | \chi_j \chi_a \rangle, \quad (3.23)$$

$$\langle \psi | G | \psi_{ij}^{ab} \rangle = \langle \chi_i \chi_j | g | \chi_a \chi_b \rangle - \langle \chi_i \chi_j | g | \chi_b \chi_a \rangle. \quad (3.24)$$

All states with more than two replaced spin orbitals vanish for both F and G ,

$$\langle \psi | F | \psi_{ijk\dots}^{abc\dots} \rangle = \langle \psi | G | \psi_{ijk\dots}^{abc\dots} \rangle = 0. \quad (3.25)$$

To prove these rules, only careful bookkeeping of the indices is necessary, after applying the definition of the antisymmetrization operator (3.8).

3.4 Pauli exclusion

When constructing an antisymmetrized product state, the antisymmetrization postulate tells us, that any two spin-orbitals must never be equal. If two spin-orbitals $|\chi_i\rangle$ and $|\chi_j\rangle$ are equal, then the permutation operator P_{ij} would leave an antisymmetrized product state invariant. We would obtain

$$P_{ij} |\psi_{\text{asym}}^{\text{MF}}\rangle = |\psi_{\text{asym}}^{\text{MF}}\rangle \quad \text{and} \quad P_{ij} |\psi_{\text{asym}}^{\text{MF}}\rangle = -|\psi_{\text{asym}}^{\text{MF}}\rangle, \quad (3.26)$$

which is only possible if $|\psi_{\text{asym}}^{\text{MF}}\rangle = 0$. This is the famous Pauli exclusion principle [15], which states that it is not possible to construct an antisymmetrized product state where two or more spin-orbitals are equal. In other words, each set of one-electron quantum numbers, that characterizes a spin-orbital, can only occur once in an antisymmetrized product state.

Note, that common formulations of the Pauli exclusion principle, like "two electrons cannot be in the same state", are sloppy and misleading. In fact, if we consider two electrons, they are indeed described by one *single* state vector, namely the solution of the Schrödinger equation. It is therefore very important to distinguish between the exact quantum mechanical formalism, where all constituents are described by one single state vector, and the independent particle picture or mean field approach, where we construct approximations to the exact state vector using one-electron spin orbitals. Only for the

latter case, the Pauli exclusion principle can be formulated.

In general, the Pauli exclusion principle is not a fundamental principle but just a consequence of the more general antisymmetrization postulate for the special case of an antisymmetrized product state. If we pretend that the independent particle picture is sufficiently accurate (which is often a reasonable quantitative assumption for atoms), then we can understand why the Pauli exclusion principle was a cornerstone to explain the structure of the periodic table of the elements. For an atom, the mean field orbitals are described by the four well-known atomic quantum numbers (n, l, m, s) . According to the Pauli principle, we need exactly those N orbitals, which correspond to the N lowest eigenvalues, since no orbital can be used twice to construct the antisymmetric N electron wavefunction. Whenever an orbital of a new shell (increasing the principal quantum number n by 1) has to be added, the considered element starts a new period in the periodic table. According to this rule, we find the "magic numbers" 2, 8, 18, 36, 54, ..., which correspond to the lengths of the periods.

CHAPTER 4

The Hartree-Fock mean field approach

4.1 General idea

The Hartree-Fock (HF) method is a mean field approach to solve the electronic Schrödinger equation. In HF the ground state of the electronic Hamiltonian is approximated by restricting the Hilbert space to the class of antisymmetrized product states of spin orbitals. The method was introduced by Fock [16] in 1930. This restriction drastically reduces the complexity of the time-independent Schrödinger equation such that an exact numerical solution becomes accessible. Mathematically, the restriction of the N electron ground state $|\Phi\rangle$ to antisymmetrized product states can be formulated using the antisymmetrization operator \mathcal{A} , as introduced in Sec. 3.2.

$$|\Phi\rangle \rightarrow |\Phi_{\text{HF}}\rangle = \mathcal{A}|\chi_1 \dots \chi_N\rangle . \quad (4.1)$$

In a crystal, the quantum numbers i in $|\chi_i\rangle$ are understood as compound indices, including the band index, the crystal wave vector and the spin. In one sentence, the HF method aims to find an optimal set of one-electron spin orbitals $\{|\chi_i\rangle\}$ which minimizes the energy expectation value of the electronic Hamilton operator (2.15),

$$E_{\text{HF}} = \min_{\chi_1 \dots \chi_N} \langle \Phi_{\text{HF}} | H_e | \Phi_{\text{HF}} \rangle . \quad (4.2)$$

We dropped the superscript $\{\mathbf{R}_I\}$, since, from now on, we assume the positions of the nuclei as given parameters, see Sec. 2.3.

In a *spin-restricted* approach, only $N/2$ orbitals $|\varphi_i\rangle$ are necessary to construct N spin orbitals $|\chi_i\rangle$, since each $|\varphi_i\rangle$ can be dressed with $|\uparrow\rangle$ and $|\downarrow\rangle$. This is particularly useful for closed shell systems, with the same number of spin up and spin down electrons.

4.2 The Hartree-Fock equation

In this section, we will derive the Hartree-Fock equation for the general *spin-unrestricted* case. In order to perform the minimization in Eq. (4.2), we split the expectation value,

$$\langle \Phi_{\text{HF}} | H_{\text{el}} | \Phi_{\text{HF}} \rangle = \langle \Phi_{\text{HF}} | T_{\text{e}} | \Phi_{\text{HF}} \rangle + V_{\text{nn}} + \langle \Phi_{\text{HF}} | V_{\text{ne}} | \Phi_{\text{HF}} \rangle + \langle \Phi_{\text{HF}} | V_{\text{ee}} | \Phi_{\text{HF}} \rangle, \quad (4.3)$$

such that we can exploit the Slater-Condon rules (see Sec. 3.3),

$$\langle \Phi_{\text{HF}} | T_{\text{e}} | \Phi_{\text{HF}} \rangle = \frac{1}{2} \sum_i^N \langle \chi_i | \mathbf{P}^2 | \chi_i \rangle, \quad (4.4)$$

$$\langle \Phi_{\text{HF}} | V_{\text{ne}} | \Phi_{\text{HF}} \rangle = - \sum_I^M \sum_i^N \langle \chi_i | \frac{Z_I}{|\mathbf{R}_I - \mathbf{r}|} | \chi_i \rangle, \quad (4.5)$$

$$\langle \Phi_{\text{HF}} | V_{\text{ee}} | \Phi_{\text{HF}} \rangle = \frac{1}{2} \sum_{ij}^N \langle \chi_i \chi_j | r_{12}^{-1} | \chi_i \chi_j \rangle - \frac{1}{2} \sum_{ij}^N \langle \chi_i \chi_j | r_{12}^{-1} | \chi_j \chi_i \rangle, \quad (4.6)$$

where we have introduced the shorthand for the *electron repulsion integrals*,

$$\langle \chi_i \chi_j | r_{12}^{-1} | \chi_k \chi_l \rangle = \int d\mathbf{x} \int d\mathbf{x}' \frac{\chi_i^*(\mathbf{x}) \chi_j^*(\mathbf{x}') \chi_k(\mathbf{x}) \chi_l(\mathbf{x}')}{|\mathbf{r} - \mathbf{r}'|} \quad (4.7)$$

$$= \langle s_i | s_k \rangle \langle s_j | s_l \rangle \int d^3r \int d^3r' \frac{\varphi_i^*(\mathbf{r}) \varphi_j^*(\mathbf{r}') \varphi_k(\mathbf{r}) \varphi_l(\mathbf{r}')}{|\mathbf{r} - \mathbf{r}'|}. \quad (4.8)$$

Note that we also made use of the combined real space-spin integral notation, as introduced in Eq. (2.42), and the spin-orbitals $|\chi_i\rangle = |\varphi_i\rangle \otimes |s_i\rangle$. It is worthwhile mentioning that Eq. (4.6) includes not only the Coulomb repulsion between charge densities of the two orbitals $|\chi_i\rangle$ and $|\chi_j\rangle$ (often referred to as *direct term*), but also the *Pauli repulsion* where the indices i and j are exchanged due to the antisymmetrization (*exchange term*). Also note, that these exchange terms only contribute, when $|\chi_i\rangle$ and $|\chi_j\rangle$ have the same spin, since the electron repulsion integral is zero otherwise. We find the minimizing spin orbitals by a variation of the Lagrangian,

$$\mathcal{L}_{\text{HF}} = \langle \Phi_{\text{HF}} | H_{\text{el}} | \Phi_{\text{HF}} \rangle + \sum_{ij}^N \lambda_{ij} (\langle \chi_i | \chi_j \rangle - \delta_{ij}), \quad (4.9)$$

with respect to the spin orbitals, where the Lagrange multiplier λ_{ij} take care of the orthonormality of the orbitals. The variation,

$$\frac{\delta \mathcal{L}_{\text{HF}}}{\delta \langle \chi_i |} = 0, \quad (4.10)$$

yields

$$\left(\frac{\mathbf{P}^2}{2} - \sum_I^M \frac{Z_I}{|\mathbf{R}_I - \mathbf{r}|} + \mathcal{J} - \mathcal{K} \right) |\chi_i\rangle = \sum_j^N \lambda_{ij} |\chi_j\rangle, \quad (4.11)$$

where we introduced the *Coulomb operator* \mathcal{J} ,

$$\langle \mathbf{x} | \mathcal{J} | \chi_i \rangle = \sum_j^N \langle \mathbf{x} | \chi_j | r_{12}^{-1} | \chi_i \chi_j \rangle = \sum_j^N \int d\mathbf{x}' \frac{|\chi_j(\mathbf{x}')|^2}{|\mathbf{r} - \mathbf{r}'|} \chi_i(\mathbf{x}), \quad (4.12)$$

and the *exchange operator* \mathcal{K} ,

$$\langle \mathbf{x} | \mathcal{K} | \chi_i \rangle = \sum_j^N \langle \mathbf{x} | \chi_j | r_{12}^{-1} | \chi_j \chi_i \rangle = \sum_j^N \int d\mathbf{x}' \frac{\chi_j^*(\mathbf{x}') \chi_i(\mathbf{x}')}{|\mathbf{r} - \mathbf{r}'|} \chi_j(\mathbf{x}). \quad (4.13)$$

Note that both \mathcal{J} and \mathcal{K} depend on the spin orbitals such that (4.11) is a *self-consistent* equation. Spin orbitals that solve Eq. (4.11) would, indeed, minimize the energy expectation value (4.2). However, for practical consideration, it is beneficial to reformulate Eq. (4.11) into a self-consistent eigenvalue equation. This is possible by constructing a unitary matrix that diagonalizes the Lagrange multipliers,

$$\lambda_{ij} = \sum_k^N u_{ki}^* \varepsilon_k u_{kj}, \quad (4.14)$$

where ε_k represent the eigenvalues of λ_{ij} . Furthermore, we can define unitary transformed spin orbitals by

$$|\chi'_i\rangle = \sum_j^N u_{ij} |\chi_j\rangle. \quad (4.15)$$

If we multiply both sides of Eq. (4.11) by $\sum_i u_{ki}$, we obtain

$$\left(\frac{\mathbf{P}^2}{2} - \sum_I^M \frac{Z_I}{|\mathbf{R}_I - \mathbf{r}|} + \mathcal{J} - \mathcal{K} \right) |\chi'_k\rangle = \varepsilon_k |\chi'_k\rangle, \quad (4.16)$$

which is a self-consistent eigenvalue equation. Note that both \mathcal{J} and \mathcal{K} are invariant under this unitary transformation. Moreover, the construction of the antisymmetrized HF state (4.1) is also invariant under this unitary transformation,

$$|\Phi_{HF}\rangle = \mathcal{A} |\chi_1 \dots \chi_N\rangle = \mathcal{A} |\chi'_1 \dots \chi'_N\rangle, \quad (4.17)$$

which is a consequence of the fact that the determinant of a unitary matrix is always 1. Hence, the primed spin orbitals are perfectly valid to minimize the energy expectation value as well as to construct the antisymmetrized HF state and no back transformation is necessary. We can thus skip the prime and find the

canonical Hartree-Fock equation,

$$f|\chi_i\rangle = \varepsilon_i|\chi_i\rangle, \quad (4.18)$$

with the *Fock operator*

$$f = \left(\frac{\mathbf{P}^2}{2} - \sum_I^M \frac{Z_I}{|\mathbf{R}_I - \mathbf{r}|} + \mathcal{J} - \mathcal{K} \right). \quad (4.19)$$

Note again that (4.18) is a self-consistent eigenvalue equation, i.e. \mathcal{J} and \mathcal{K} and therefore the Fock operator f are constructed by the eigenvectors of f . The solution of self-consistent eigenvalue problems must be solved by iterative schemes.

The physical interpretation of the Coulomb operator \mathcal{J} is straightforward. If we introduce the electron density

$$n(\mathbf{r}) = \sum_i^N |\varphi_i(\mathbf{r})|^2, \quad (4.20)$$

where $\varphi_i(\mathbf{r})$ is just the spatial degree of freedom of $\langle \mathbf{x} | \chi_i \rangle = \langle \mathbf{r} s | \chi_i \rangle = \langle \mathbf{r} | \varphi_i \rangle \langle s | s_i \rangle$, then we can interpret \mathcal{J} as the interaction of the one-electron orbital $\varphi_i(\mathbf{r})$ with the charge density created by all one-electron spin-orbitals,

$$\langle \mathbf{r} s | \mathcal{J} | \chi_i \rangle = \langle s | s_i \rangle \int d^3 r' \frac{n(\mathbf{r}')}{|\mathbf{r} - \mathbf{r}'|} \varphi_i(\mathbf{r}). \quad (4.21)$$

Note that this includes *self-interaction* of orbitals, since the charge density created by $\varphi_i(\mathbf{r})$ is already included in $n(\mathbf{r})$. The form of the exchange operator \mathcal{K} , on the other hand, does not allow for such a simple physical interpretation. However, if we introduce the *exchange hole density*,

$$n_X^{(irs)}(\mathbf{r}') = \sum_j^N \langle s | s_j \rangle \langle s_j | s_i \rangle \frac{\varphi_j^*(\mathbf{r}') \varphi_i(\mathbf{r}') \varphi_i^*(\mathbf{r}) \varphi_j(\mathbf{r})}{|\varphi_i(\mathbf{r})|^2}, \quad (4.22)$$

we can also write the exchange operator as an interaction between the spin orbital $\chi_i(\mathbf{r})$ and a density,

$$\langle \mathbf{r} s | \mathcal{K} | \chi_i \rangle = \int d^3 r' \frac{n_X^{(irs)}(\mathbf{r}')}{|\mathbf{r} - \mathbf{r}'|} \varphi_i(\mathbf{r}). \quad (4.23)$$

In opposite to the Coulomb operator, the exchange hole density has to be constructed for each i , \mathbf{r} , s individually. This interpretation was introduced by Slater [17]. The exchange hole density $n_X^{(irs)}(\mathbf{r}')$ does not only correct the unphysical self-interaction of the orbitals, but also takes into account, that each spin orbital creates an "electron hole" in its surrounding, which cares for the fact that other spin orbitals with equal spin have to

pay a price, if they want to occupy this area (Pauli exclusion). The net charge that the spin orbital $\chi_i(\mathbf{r}, s)$ with spin s at position \mathbf{r} can feel, is thus given by the density

$$n(\mathbf{r}') - n_X^{(irs)}(\mathbf{r}'), \quad (4.24)$$

at all points \mathbf{r}' . Due to this subtraction, $n_X^{(irs)}$ is called exchange *hole* density.

Once the HF spin orbitals $|\chi_i\rangle$ and the HF spin orbital energies ε_i are found, the HF energy (4.2) can be calculated by

$$E_{\text{HF}} = \sum_i^N \varepsilon_i + V_{\text{nn}} - \frac{1}{2} \sum_{ij}^N \langle \chi_i \chi_j | r_{12}^{-1} | \chi_i \chi_j \rangle + \frac{1}{2} \sum_{ij}^N \langle \chi_i \chi_j | r_{12}^{-1} | \chi_j \chi_i \rangle, \quad (4.25)$$

which follows from

$$\begin{aligned} \varepsilon_i &= \langle \chi_i | f | \chi_i \rangle \\ &= \frac{1}{2} \langle \chi_i | \mathbf{P}^2 | \chi_i \rangle - \sum_I^M \langle \chi_i | \frac{Z_I}{|\mathbf{R}_I - \mathbf{r}|} | \chi_i \rangle + \sum_j^N \langle \chi_i \chi_j | r_{12}^{-1} | \chi_i \chi_j \rangle - \sum_j^N \langle \chi_i \chi_j | r_{12}^{-1} | \chi_j \chi_i \rangle. \end{aligned} \quad (4.26)$$

4.3 Excited determinants: singles, doubles, triples, ...

The number of spin orbitals $|\chi_i\rangle$ we used to construct the Hartree-Fock state (4.1) and to derive the Hartree-Fock equation (4.18) was assumed to be equal to the number of electrons, N . Therefore these spin orbitals are the *occupied spin orbitals*. However, it is also possible to calculate higher energy eigenstates of the Fock operator f , which are then called *virtual* or *unoccupied spin orbitals*. Since the Fock operator is a continuous operator, there are in principle infinitely many eigenstates above the highest occupied eigenstate. Throughout this work, unoccupied orbitals will be labeled by a, b, \dots in contrast to the indices for the occupied orbitals i, j, \dots . Note that also in this case the operators \mathcal{J} and \mathcal{K} are still constructed by the occupied spin orbitals only, since the mean field is generated by the N electrons. With unoccupied spin orbitals we can construct *excited determinants* by replacing an occupied orbital $|\chi_i\rangle$ with an unoccupied orbital $|\chi_a\rangle$, which leads to a *singles state* $|\Phi_i^a\rangle$,

$$|\Phi_{\text{HF}}\rangle = \mathcal{A}|\chi_1 \dots \chi_i \dots \chi_N\rangle \rightarrow |\Phi_i^a\rangle = \mathcal{A}|\chi_1 \dots \chi_a \dots \chi_N\rangle. \quad (4.27)$$

In the same manner, *doubles* and *triples states* can be constructed,

$$|\Phi_{\text{HF}}\rangle = \mathcal{A}|\chi_1 \dots \chi_i \dots \chi_j \dots \chi_N\rangle \rightarrow |\Phi_{ij}^{ab}\rangle = \mathcal{A}|\chi_1 \dots \chi_a \dots \chi_b \dots \chi_N\rangle, \quad (4.28)$$

$$|\Phi_{\text{HF}}\rangle = \mathcal{A}|\chi_1 \dots \chi_i \dots \chi_j \dots \chi_k \dots \chi_N\rangle \rightarrow |\Phi_{ijk}^{abc}\rangle = \mathcal{A}|\chi_1 \dots \chi_a \dots \chi_b \dots \chi_c \dots \chi_N\rangle. \quad (4.29)$$

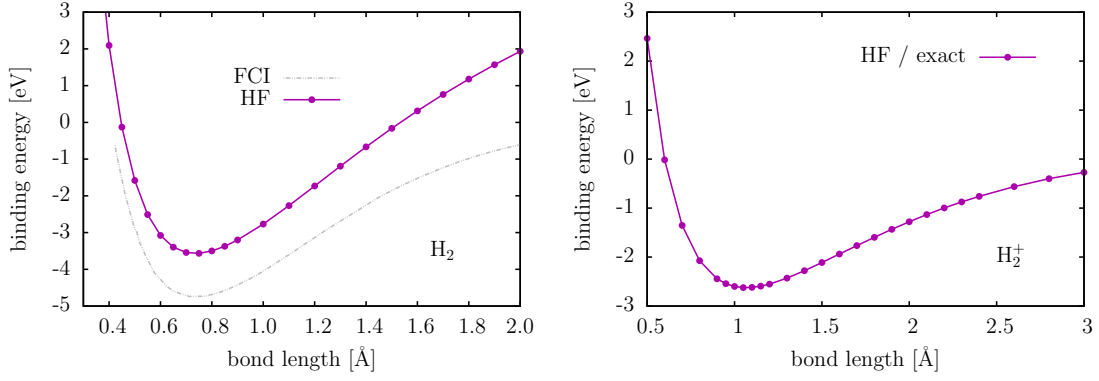


Figure 4.1: Dissociation of the diatomic molecules H_2 and H_2^+ into 2H and $\text{H}+\text{H}^+$ respectively. As an "exact" reference for the H_2 molecule, we chose full configuration interaction (FCI) calculations from [18]. We performed spin-polarized calculations for the molecules and the isolated atoms, except for H_2 , where spin-restriction was assumed. We used a cell size of $10 \times 8 \times 8 \text{ \AA}^3$ for H_2 and $15 \times 12 \times 12 \text{ \AA}^3$ for H_2^+ . The plane-wave cutoff was set to 300 eV and the PAW potential was chosen with an outmost cutoff radius of 1.1 Å. In the one-electron system H_2^+ , the HF approach is exact, apart from small errors due to the periodic images and the limited basis set size.

The singles, doubles, triples, ... form an orthonormal basis of the entire Hilbert space,

$$\langle \Phi_{\text{HF}} | \Phi_{ijk\dots}^{abc\dots} \rangle = 0, \quad (4.30)$$

$$\langle \Phi_{ijk\dots}^{abc\dots} | \Phi_{i'j'k'\dots}^{a'b'c'\dots} \rangle = \delta_{ii'} \delta_{jj'} \delta_{kk'} \dots \delta_{aa'} \delta_{bb'} \delta_{cc'} \dots. \quad (4.31)$$

The exact solution of the electronic Hamiltonian (2.18) can therefore be formally written as a superposition of all possible N electron determinants,

$$|\Phi_e\rangle = t_0 |\Phi_{\text{HF}}\rangle + \sum_i^N \sum_a^\infty t_i^a |\Phi_i^a\rangle + \frac{1}{2} \sum_{ij}^N \sum_{ab}^\infty t_{ij}^{ab} |\Phi_{ij}^{ab}\rangle + \frac{1}{6} \sum_{ijk}^N \sum_{abc}^\infty t_{ijk}^{abc} |\Phi_{ijk}^{abc}\rangle + \dots, \quad (4.32)$$

where the coefficients t_0 , t_i^a , t_{ij}^{ab} , t_{ijk}^{abc} , ... are inaccessible in an exact manner and can only be approximated by post-Hartree-Fock methods.

4.4 Illustrative HF calculations for molecules and solids

It is well known that the Hartree-Fock method provides good ground state energies for molecules, however, energy differences can suffer from significant errors. Consider, e.g., the dissociation of a diatomic molecules like H_2 , H_2^+ or Be_2 , Be_2^+ . In Fig. 4.1 and 4.2 a comparison of HF and exact ground state energies are shown.

For the H_2 molecule, the HF method provides a very accurate bond length but under-

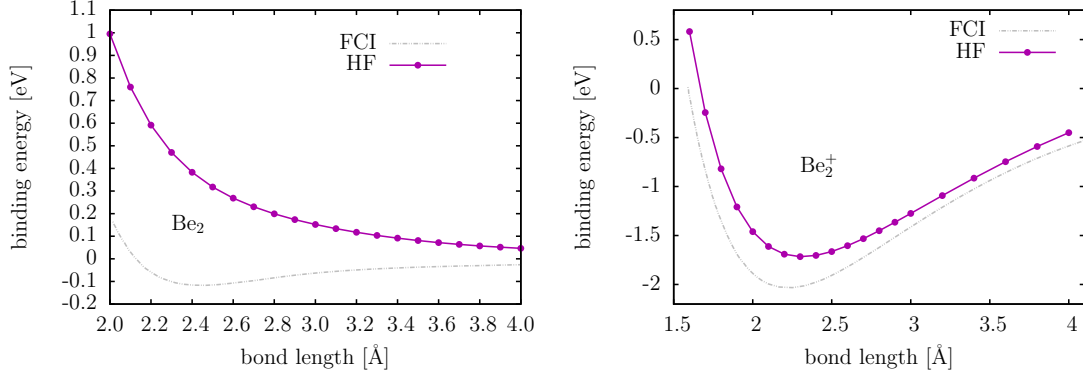


Figure 4.2: Dissociation of the diatomic molecules Be_2 and Be_2^+ into 2Be and $\text{Be}+\text{Be}^+$ respectively. As an "exact" reference for the H_2 molecule, we chose full configuration interaction (FCI) calculations from [18]. We performed spin-polarized calculations for the molecules and the isolated atoms, except for Be_2 , where spin-restriction was assumed. We used a cell size of $18 \times 14 \times 14 \text{ \AA}^3$ for Be_2 and $16 \times 12 \times 12 \text{ \AA}^3$ for Be_2^+ . The plane-wave cutoff was set to 300 eV and the PAW potential was chosen with an outmost cutoff radius of 1.9 \AA . Only the $2s^2$ orbitals of Be were treated as valence.

estimates the binding energy by about 25%. Also, for increasing core distances, the HF method overestimates the attractive force between the two hydrogen atoms, which should approach zero at a distance of 2 \AA . The HF ground state will always take the form of a singlet state, $|\Phi_{\text{HF}}\rangle = \mathcal{A}|\chi_1\chi_2\rangle$ with $|\chi_1\rangle = |\varphi_\sigma\rangle|\uparrow\rangle$ and $|\chi_2\rangle = |\varphi_\sigma\rangle|\downarrow\rangle$, such that

$$|\Phi_{\text{HF}}\rangle = \frac{1}{\sqrt{2}}|\varphi_\sigma\varphi_\sigma\rangle \otimes (|\uparrow\downarrow\rangle - |\downarrow\uparrow\rangle). \quad (4.33)$$

Here, $|\varphi_\sigma\rangle$ refers to the bonding σ molecular orbital. Since it is known, that the bound H_2 molecule is a spin singlet state, this is a reasonable approximation. Nevertheless, the single spatial orbital $|\varphi_\sigma\rangle$ has no other option but to create a nonvanishing probability of observing both electrons on one nucleus, thus predicting a covalent bonding for arbitrary distances. But for far-distant nuclei, this is unphysical, since the large separation leads to the following simple correlation between the electrons: if an electron is observed at one of the nuclei, then the probability of observing an electron at the other nucleus will be 1. This is simply the case of two non-interacting, separated hydrogen atoms and cannot be covered by the HF state (4.33). Instead, the superposition of two antisymmetrized product states (superposition of two Slater determinants), like

$$|\Phi\rangle = \frac{1}{\sqrt{2}}(\mathcal{A}|\chi_1\chi_2\rangle + \mathcal{A}|\chi_3\chi_4\rangle), \quad (4.34)$$

allow for an improved description of the H_2 molecule with a correct dissociation limit. An accurate realization of this approach is given by the Heitler-London wavefunction [19, 20].

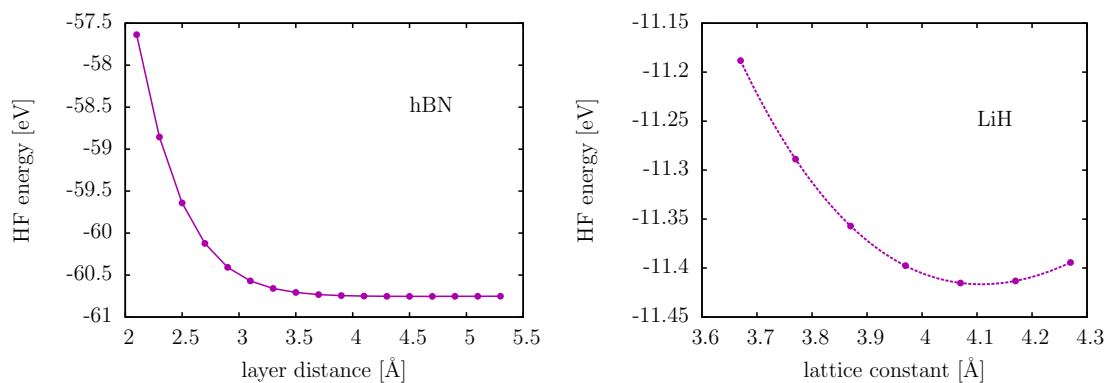


Figure 4.3: HF energy against the distance of the hexagonal layers of boron nitride (left) and the lattice constant of bulk LiH (right). For both systems spin-restricted calculations were performed and the plane-wave cutoff was set to 550 eV. The k-point mesh was set to $8 \times 8 \times 2$ for the hBN system and to $6 \times 6 \times 6$ for LiH. The HF energies of LiH were fitted with a Birch-Murnaghan equation of state (dotted line) and resulted in a equilibrium lattice constant of 4.11 Å.

Hence, the HF method provides a qualitatively reasonable description of the covalent bonding of H_2 but fails to predict the breaking of the bond. The dissociation of H_2^+ , in contrast, is exactly described by the HF method. Only one electron is involved and the mean field approach corresponds to the exact Schrödinger equation.

The Be_2 molecule is not bound in the HF approximation. Here, the prediction of HF corresponds to the prediction of molecular orbital theory, using the bond order of Be_2 . Since we have 4 bonding and 4 antibonding electrons, the bond order is 0. However, an exact solution of the Schrödinger equation yields a very weak binding energy of about 0.12 eV at 2.47 Å. Again, electron correlation causes the difference between the exact and the HF solution. The electron correlation leads to a mixed bonding type of covalent and van der Waals character, which HF fails to predict. On the other hand, the dimer ion Be_2^+ has a bond order of 1 and therefore also the HF method predicts a qualitatively reasonable binding energy and bond length.

Considering periodic systems, Fig. 4.3 shows results for hexagonal boron nitride (hBN) and lithium hydride (LiH). The hexagonal layers of boron nitride (see top of Fig. 2.1) are van der Waals bonded. Clearly, HF fails to predict the correct layer distance, which is about 3.33 Å, see Ref. [21]. In contrast, the covalent like bonding in bulk LiH is captured correctly by HF. The Birch-Murnaghan fit [22] yields a lattice constant of 4.11 Å, which is very close to the experimental value of 4.08 Å.

CHAPTER 5

Exchange and correlation

The terms *exchange* and *correlation* are widely used but rarely explained in the field of condensed matter physics. Compositions as *exchange correlation*, *exchange-correlation*, *exact exchange*, *dynamic correlation*, *static correlation* or *correlation energy* complete the confusion. This chapter is attempting to shed light on these terms in order to clarify their meaning.

In general, these terms refer to correlations in the N -electron spatial probability distribution, which is simply given by the magnitude square of the exact N -electron wave function. The correlations originate from the interaction between the electrons and the nuclei, the interactions between the electrons themselves, as well as from the symmetrization postulate, i.e. from the indistinguishability of the electrons. Since correlated probability distributions lead to different expectation values of observables than uncorrelated ones, the term correlation is analogously translated to those expectation values, like in the term *correlation energy*.

5.1 Exchange correlation of two non-interacting particles

Correlation of the position of two particles does not require interaction. Consider, for instance, two non-interacting fermions, whose Hamiltonian is simply given by

$$H = h \otimes \mathbb{1} + \mathbb{1} \otimes h, \quad h = \mathbf{P}^2/2. \quad (5.1)$$

In the non-interacting case the single particle picture is exact. The eigenstates of the one-particle Hamiltonian,

$$h|\mathbf{k}\rangle = \varepsilon_{\mathbf{k}}|\mathbf{k}\rangle, \quad (5.2)$$

are plane-waves $\langle \mathbf{r}|\mathbf{k}\rangle = \exp(i\mathbf{k}\mathbf{r})$ and $\varepsilon_{\mathbf{k}} = \mathbf{k}^2/2$. Any product state $|\mathbf{k}_1\rangle \otimes |\mathbf{k}_2\rangle$ is clearly an eigenstate of the full Hamiltonian H with energy $(\varepsilon_{\mathbf{k}_1} + \varepsilon_{\mathbf{k}_2})$. But the symmetrization postulate strictly prohibits such a simple product state, since it is neither symmetric nor antisymmetric. For fermions (e.g. electrons) the valid eigenstate with energy $(\varepsilon_{\mathbf{k}_1} + \varepsilon_{\mathbf{k}_2})$

is given by

$$|\Phi\rangle = \frac{1}{\sqrt{2}}(|\mathbf{k}_1\rangle \otimes |\mathbf{k}_2\rangle - |\mathbf{k}_2\rangle \otimes |\mathbf{k}_1\rangle) . \quad (5.3)$$

The spatial probability density of the two fermions,

$$\rho^{(2)}(\mathbf{r}_1, \mathbf{r}_2) = |\langle \mathbf{r}_1 \mathbf{r}_2 | \Phi \rangle|^2 = 1 - \cos [(\mathbf{k}_2 - \mathbf{k}_1)(\mathbf{r}_1 - \mathbf{r}_2)] , \quad (5.4)$$

can not be written as a product of one-particle probability densities, i.e. the positions of the two fermions are correlated. Because there is no interaction, the correlation is a consequence of the symmetrization postulate alone. This correlation is sometimes called *exchange correlation*, since it originates from the exchange of $|\mathbf{k}_1\rangle$ and $|\mathbf{k}_2\rangle$ which was necessary to antisymmetrize the state (5.3).

In general, the term *exchange* refers to all effects that originate from the antisymmetrization of one-electron product states, i.e. from the exchange of two one-electron states.

5.2 Correlation energy and the cusp conditions

The plain mathematical definition of the correlation energy E_c reads

$$E_c = E_e - E_{\text{HF}} , \quad (5.5)$$

where E_e is the exact solution of the electronic Schrödinger equation (2.18) and E_{HF} is the Hartree-Fock energy of the considered system. Indeed, the antisymmetrized product states of the Hartree-Fock method already ensure exchange correlation (as described in the last section), but cannot cover correlation due to the Coulomb interaction. Those additional correlations lead to ground state wave functions that have a lower energy than the Hartree-Fock energy, i.e. $E_c \leq 0$. This is a simple consequence of the variational principle, which states, that any trial wave function (in this case a single antisymmetrized product state) results in a higher ground state energy than the exact ground state. In short, the term correlation energy simply refers to all those contributions to the ground state energy, that cannot be covered by the Hartree-Fock approach. Note, that the correlation energy is sometimes alternatively defined as the difference between the exact energy and the energy obtained by a mean field set of orbitals (not necessarily Hartree Fock orbitals). Such a definition subsumes all those effects, which can not be covered by the independent particle picture. A very simple Coulomb correlation effect was described for the H_2 molecule in Chap. 4.4.

An illustration of a correlation effect is the electronic Coulomb cusp in the exact wave function. Consider, e.g., the Hamilton operator of the Helium atom

$$H = -\frac{1}{2}\nabla_1^2 - \frac{1}{2}\nabla_2^2 - \frac{Z}{|\mathbf{r}_1|} - \frac{Z}{|\mathbf{r}_2|} + \frac{1}{|\mathbf{r}_1 - \mathbf{r}_2|} , \quad Z = 2 . \quad (5.6)$$

If $\Phi(\mathbf{r}_1, s_1, \mathbf{r}_2, s_2)$ is an eigenstate of H with eigenvalue E , then

$$\frac{H\Phi(\mathbf{r}_1, s_1, \mathbf{r}_2, s_2)}{\Phi(\mathbf{r}_1, s_1, \mathbf{r}_2, s_2)} = E \quad (5.7)$$

is constant for all $\mathbf{r}_1, s_1, \mathbf{r}_2, s_2$. But for the case $\mathbf{r}_1 = \mathbf{r}_2$ the electron-electron interaction diverges, thus only the kinetic part can cure this divergence in order to restore the constant E . To see how this is achieved, we rewrite the Hamiltonian in the (r_1, r_2, r_{12}) form, where we introduce the difference vector $\mathbf{r}_{12} = \mathbf{r}_1 - \mathbf{r}_2$ and spherical coordinates [23],

$$H = -\frac{1}{2} \sum_{\mu=1,2} \left(\partial_{\mu}^2 + \frac{2}{r_{\mu}} \partial_{\mu} + \frac{2Z}{r_{\mu}} \right) - (\hat{\mathbf{r}}_1 \hat{\mathbf{r}}_{12} \partial_1 - \hat{\mathbf{r}}_2 \hat{\mathbf{r}}_{12} \partial_2) \partial_{12} - \left(\partial_{12}^2 + \frac{2}{r_{12}} \partial_{12} - \frac{1}{r_{12}} \right). \quad (5.8)$$

Here, we used the unit vectors $\hat{\mathbf{r}} = \mathbf{r}/r$ and introduced the shorthand $\partial_{\mu} = \partial/\partial r_{\mu}$. For $r_{12} = |\mathbf{r}_1 - \mathbf{r}_2| = 0$, the interesting part is the last term, where r_{12} appears in the denominator. Divergence can only be avoided, if

$$\left(\frac{2}{r_{12}} \partial_{12} - \frac{1}{r_{12}} \right) \Phi(\mathbf{r}_1, s_1, \mathbf{r}_2, s_2) \Big|_{r_{12}=0} = \text{const.}, \quad (5.9)$$

which is equivalent to

$$2 \frac{\partial \Phi}{\partial r_{12}}(\mathbf{r}_1, s_1, \mathbf{r}_1, s_2) = \Phi(\mathbf{r}_1, s_1, \mathbf{r}_1, s_2) \quad \text{or} \quad \left[\frac{1}{\Phi} \frac{\partial \Phi}{\partial r_{12}} \right]_{r_{12}=0}^{s_1 \neq s_2} = \frac{1}{2}. \quad (5.10)$$

Also, for $r_1 = 0$ or $r_2 = 0$ a divergence can only be cured if

$$\left(\frac{2}{r_{\mu}} \partial_{\mu} + \frac{2Z}{r_{\mu}} \right) \Phi(\mathbf{r}_1, s_1, \mathbf{r}_2, s_2) \Big|_{r_{\mu}=0} = \text{const.}, \quad (5.11)$$

leading to Kato's cusp condition [24]

$$\left[\frac{1}{\Phi} \frac{\partial \Phi}{\partial r_{\mu}} \right]_{r_{\mu}=0} = -Z. \quad (5.12)$$

Both conditions can be generalized to N -electron eigenstates and are called

cusp conditions for the exact eigenstates,

$$\left[\frac{1}{\Phi} \frac{\partial \Phi}{\partial r_{ij}} \right]_{r_{ij}=0}^{s_i \neq s_j} = \text{const.} , \quad (5.13)$$

and

$$\left[\frac{1}{\Phi} \frac{\partial \Phi}{\partial r_i} \right]_{r_i=R_I} \sim -Z_I , \quad (5.14)$$

where R_I is a position of a nucleus with charge Z_I .

Clearly, a Hartree-Fock wave function can never meet such conditions in this general form, since an antisymmetrized product state does not provide enough variational freedom. Therefore the cusp shows that there is more correlation than just the exchange correlation in the wave function, thus also the ground state energy will, in general, be lower than the Hartree-Fock energy, even for a seemingly simple system such as Helium.

5.3 Dynamic and static correlation

What if only one Slater determinant is simply not enough? In the Hartree-Fock method, the ground state is approximated by one Slater determinant, consisting of orbitals that minimize the expectation value (4.2). What if a large portion of the correlation energy can be covered if we, instead, consider a superposition of two or few Slater determinants? In such a case, the correlation is called *static correlation* since the mean field approach (i.e. each electron interacts with an average field of all other electrons) is not an obstacle to improve the energy, but simply more than one Slater determinant is necessary. An example for static correlation is the dissociation limit of the H_2 molecule (see Sec. 4.4).

On the other hand, if the mean field approach is conceptually and qualitatively reasonable, but the electron-electron interactions cannot be quantitatively covered by interactions of electrons with effective mean fields, then the correlation is called *dynamic correlation*. Examples are dispersion forces like van-der Waals interactions (see Sec. 4.4, 6.3, and 8.5).

It is not possible to strictly distinguish both types of correlation. Similar to chemical bonds, where there is no strict distinction between ionic and covalent bonds, there is no strict distinction between static and dynamic correlation. These notions are merely a product of the historical development of different approaches to approximate the correlation energy.

5.4 Exchange-correlation holes in the density

In principle, it is possible to express the exact energy of the electron-electron interaction, $\langle \Phi_e | V_{ee} | \Phi_e \rangle$, using the pair density $P(\mathbf{r}, \mathbf{r}')$,

$$\langle \Phi_e | V_{ee} | \Phi_e \rangle = \frac{1}{2} \int d^3\mathbf{r} \int d^3\mathbf{r}' \frac{P(\mathbf{r}, \mathbf{r}')}{|\mathbf{r} - \mathbf{r}'|}, \quad (5.15)$$

where the pair density is rigorously defined by the exact wavefunction via

$$P(\mathbf{r}, \mathbf{r}') = N(N-1) \sum_{s,s'=\uparrow,\downarrow} \int d\mathbf{x}_3 \dots \int d\mathbf{x}_N |\Phi_e(\mathbf{r}, s, \mathbf{r}', s', \mathbf{x}_3, \dots, \mathbf{x}_N)|^2. \quad (5.16)$$

Due to correlations, the pair density does not decay into a product of the electron density,

$$P(\mathbf{r}, \mathbf{r}') \neq n(\mathbf{r})n(\mathbf{r}'), \quad n(\mathbf{r}) = \sum_{s=\uparrow,\downarrow} \int d\mathbf{x}_2 \dots \int d\mathbf{x}_N |\Phi_e(\mathbf{r}, s, \mathbf{x}_2, \dots, \mathbf{x}_N)|^2. \quad (5.17)$$

The most simple way to prove this, is to realize that $P(\mathbf{r}, \mathbf{r}) = 0$, which follows from the antisymmetry of $\Phi_e(\mathbf{x}_1, \dots, \mathbf{x}_N)$. However, the form $P(\mathbf{r}, \mathbf{r}') = n(\mathbf{r})n(\mathbf{r}')$ can only obey this relation, if $n(\mathbf{r}) = 0 \forall \mathbf{r}$, which is unphysical. We can separate all the correlation effects into a so called *exchange-correlation hole density* $n_{XC}(\mathbf{r}, \mathbf{r}')$, which is implicitly defined by

$$P(\mathbf{r}, \mathbf{r}') = n(\mathbf{r})n(\mathbf{r}') + n(\mathbf{r})n_{XC}(\mathbf{r}, \mathbf{r}'). \quad (5.18)$$

Since it covers both, exchange *and* correlation, it is called exchange-correlation hole density, where the hyphen "-" is understood as "and" (not to be confused with "exchange correlation", where exchange is only the descriptor for a certain kind of correlation). With this definition, the electron-electron interaction energy decays into an interaction between the electron density with itself, and an interaction of the electron density with the exchange-correlation hole density,

$$\langle \Phi_e | V_{ee} | \Phi_e \rangle = \frac{1}{2} \int d^3\mathbf{r} \int d^3\mathbf{r}' \frac{n(\mathbf{r})n(\mathbf{r}')}{|\mathbf{r} - \mathbf{r}'|} + \frac{1}{2} \int d^3\mathbf{r} \int d^3\mathbf{r}' \frac{n(\mathbf{r})n_{XC}(\mathbf{r}, \mathbf{r}')}{|\mathbf{r} - \mathbf{r}'|}. \quad (5.19)$$

Moreover, if we integrate over Eq. (5.18), we find

$$\int d^3\mathbf{r}' n_{XC}(\mathbf{r}, \mathbf{r}') = -1, \quad (5.20)$$

which follows from

$$n(\mathbf{r}) = \frac{1}{N-1} \int d^3\mathbf{r}' P(\mathbf{r}, \mathbf{r}') \quad (5.21)$$

and the fact that $P(\mathbf{r}, \mathbf{r}') = P(\mathbf{r}', \mathbf{r})$, being a consequence of the symmetry of the wavefunction. Physically, Eq. (5.20) suggests, that the exchange-correlation hole density

n_{XC} corresponds to a deficit of one electron, i.e. to an electron hole. One can interpret this abstract hole as a spatial correlation effect, originating from the Coulomb interactions and the symmetrization of the wave function. A naive but descriptive interpretation is given by the picture, that each electron is unwilling to tolerate other electrons in its vicinity, in particular, if they have equal spin. Hence, each electron tries to establish an electron hole in its surroundings.

Note that the exchange hole density from the Hartree-Fock chapter 4 is based on the same idea as the exchange-correlation density from this chapter. At the Hartree-Fock level, the relation is given by

$$n_{\text{XC}}^{\text{HF}}(\mathbf{r}, \mathbf{r}') = -\frac{1}{n^{\text{HF}}(\mathbf{r})} \sum_i^N \sum_{s=\uparrow, \downarrow} \langle s_i | s \rangle |\varphi_i(\mathbf{r})|^2 n_{\text{X}}^{(irs)}(\mathbf{r}') , \quad (5.22)$$

such that

$$n^{\text{HF}}(\mathbf{r}) n_{\text{XC}}^{\text{HF}}(\mathbf{r}, \mathbf{r}') = \sum_{ij}^N \langle s_i | s_j \rangle \varphi_j^*(\mathbf{r}') \varphi_i(\mathbf{r}') \varphi_i^*(\mathbf{r}) \varphi_j(\mathbf{r}) . \quad (5.23)$$

This, however, only accounts for exchange correlation effects as defined in Sec. 5.1.

5.5 Exact exchange

In particular in the density functional theory community (we will discuss this theory in Chap. 6) the term *exact exchange* (EXX) is widely used. This technical term refers to a certain kind of energy functional $E_{\text{EXX}}[\{\chi\}]$ which takes exactly the form of the exchange energy in the Hartree-Fock method (compare to the second term in Eq. 4.6),

$$E_{\text{EXX}}[\{\chi\}] = -\frac{1}{2} \sum_{ij} \int d\mathbf{x} \int d\mathbf{x}' \frac{\chi_i^*(\mathbf{x}) \chi_j(\mathbf{x}) \chi_j^*(\mathbf{x}') \chi_i(\mathbf{x}')}{|\mathbf{r} - \mathbf{r}'|} . \quad (5.24)$$

From the derivation of Eq. (4.6), we know that such an expression arises from the expectation value of the Coulomb interaction energy for antisymmetrized product states. It is therefore the *exact* form of the exchange energy, if antisymmetrized product states are assumed. However, since antisymmetrized product states are no exact wave functions, the term exact should not be confused with an exact energy whatsoever.

CHAPTER 6

Density functional theory

Density functional theory (DFT) is often praised as the "working horse" for ground state calculations in *ab initio* computational materials physics and quantum chemistry. This is justified, because modern DFT implementations provide a very beneficial cost-performance ratio, where with cost we mean computational cost. Moreover, DFT is prominent, because it is exact in principle. Nevertheless, we will only briefly discuss DFT here, as the focus of this work is on post-DFT and post-HF methods.

The main idea of DFT is based on the fact that ground state properties like the ground state energy, are determined by a much simpler object than the N -electron ground state wavefunction, namely the electron density. It is therefore, in principle, not necessary, to solve the time-independent Schrödinger equation (2.18). The very heart of DFT are the Hohenberg-Kohn theorems [25]. They state that the ground state density can be found variationally by minimizing an energy functional. In the following sections, the Hohenberg-Kohn theorem and DFT will be introduced mathematically, leading us to a practical mean field like approach, the Kohn-Sham equations [26]. For brevity, we will ignore the spin.

6.1 The Hohenberg-Kohn theorems

Hohenberg and Kohn showed, that the electronic Schrödinger equation (2.18) is not the only route to calculate ground state properties of matter. Their seminal work [25] can be divided into two theorems.

The first Hohenberg-Kohn theorem states, that the potential created by the nuclei, which is the only characterizing quantity in the Hamiltonian, is uniquely determined by the electron density.

The proof is rather simple. Let us write the electronic Hamiltonian from Eq. (2.15) as $H = T + V_{\text{ext}} + V_{\text{ee}}$ where $V_{\text{ext}} = V_{\text{nn}} + V_{\text{ne}}$. Assume that the first theorem is wrong, i.e. there are two different external potentials $V_{\text{ext}}^{(1)}$ and $V_{\text{ext}}^{(2)}$ (which differ not only by a constant) that give rise to the same ground state electron density $n_0(\mathbf{r})$. If E_i is the ground

state energy to the nondegenerate ground state $|\Phi_i\rangle$ of the system $H_i = T + V_{\text{ext}}^{(i)} + V_{\text{ee}}$, we can conclude that $|\Phi_1\rangle \neq |\Phi_2\rangle$. This follows from the fact that $|\Phi_1\rangle = |\Phi_2\rangle$ leads to a contradiction, because

$$(E_1 - E_2)|\Phi_1\rangle = (H_1 - H_2)|\Phi_1\rangle = [V_{\text{ext}}^{(1)} - V_{\text{ext}}^{(2)}]|\Phi_1\rangle, \quad (6.1)$$

which is equivalent to

$$V_{\text{ext}}^{(1)}(\mathbf{r}) - V_{\text{ext}}^{(2)}(\mathbf{r}) = E_1 - E_2, \quad \forall \mathbf{r}, \quad (6.2)$$

since the external potentials are diagonal in real space. That both external potentials differ only by a constant was, however, excluded. We can thus safely write,

$$E_1 < \langle \Phi_2 | H_1 | \Phi_2 \rangle \quad \text{and} \quad E_2 < \langle \Phi_1 | H_2 | \Phi_1 \rangle. \quad (6.3)$$

Clearly also the addition of both inequalities must then be true,

$$E_1 + E_2 < \langle \Phi_2 | H_1 | \Phi_2 \rangle + \langle \Phi_1 | H_2 | \Phi_1 \rangle. \quad (6.4)$$

But if we rewrite the right hand side as

$$\begin{aligned} \langle \Phi_2 | H_1 | \Phi_2 \rangle + \langle \Phi_1 | H_2 | \Phi_1 \rangle &= \langle \Phi_2 | H_1 - H_2 | \Phi_2 \rangle + E_2 + \langle \Phi_1 | H_2 - H_1 | \Phi_1 \rangle + E_1 \\ &= \text{tr} \left[n_0 \left(V_{\text{ext}}^{(1)} - V_{\text{ext}}^{(2)} \right) \right] + E_2 + \text{tr} \left[n_0 \left(V_{\text{ext}}^{(2)} - V_{\text{ext}}^{(1)} \right) \right] + E_1 \\ &= E_2 + E_1, \end{aligned} \quad (6.5)$$

we arrive at a contradiction

$$E_1 + E_2 < E_1 + E_2. \quad (6.6)$$

Hence, the first Hohenberg-Kohn theorem is correct and we can write $V_{\text{ext}} = V_{\text{ext}}[n_0]$, i.e. the external potential is a unique functional of the ground state density.

According to *the second Hohenberg-Kohn theorem*, the ground state density is a function that minimizes a universal energy functional. This minimum can be calculated variationally.

Again, the proof is straightforward. From the first theorem we know that the ground state density $n_0(\mathbf{r})$ determines the external potential V_{ext} . Consequently, the Hamiltonian is also uniquely defined, which again, determines the ground state $|\Phi_0\rangle$ and the ground state energy E_0 . We can thus write the ground state energy as a functional of the density,

$$E_0 = \langle \Phi[n_0] | H[n_0] | \Phi[n_0] \rangle = F[n_0] + \text{tr} [n_0 V_{\text{ext}}[n_0]], \quad (6.7)$$

where $|\Phi_0\rangle = |\Phi[n_0]\rangle$ and the functional F covers only the kinetic and electron-electron interaction energy, $F[n] = \langle \Phi[n] | T | \Phi[n] \rangle + \langle \Phi[n] | V_{\text{ee}} | \Phi[n] \rangle$. The functional F is therefore equivalent for any material and does not depend on the positions of the nuclei. It is

universal. Analogously to the variation of the wave function, we now vary the density in order to find the ground state energy,

$$E_0 = \min_{\Phi} \langle \Phi | H | \Phi \rangle = \min_n E[n], \quad (6.8)$$

with

$$E[n] = F[n] + \text{tr}[nV_{\text{ext}}[n]]. \quad (6.9)$$

Similar to the condition $\langle \Phi | \Phi \rangle = 1$, we require $\text{tr}[n] = N$ for the minimization.

Both theorems are fundamental for DFT and promise to simplify ground state calculations in a remarkable way. The intractable $3N$ dimensional Schrödinger equation is replaced by the minimization of a functional of the 3 dimensional electron density only. But still, the solution of the N -electron problem remains very complicated, since neither the exact form nor a universal approximation of the universal functional $F[n]$ could be found.

A very early example for an energy functional, even before DFT was developed, is the Thomas-Fermi functional [27, 28],

$$E^{\text{TF}}[n] = F^{\text{TF}}[n] + \text{tr}[nV_{\text{ext}}[n]], \quad (6.10)$$

where

$$F^{\text{TF}}[n] = C_{\text{F}} \int d^3r n(\mathbf{r})^{5/3} + \frac{1}{2} \int d^3r \int d^3r' \frac{n(\mathbf{r})n(\mathbf{r}')}{|\mathbf{r} - \mathbf{r}'|}, \quad (6.11)$$

and $C_{\text{F}} \approx 2.871$. The special form of the kinetic energy, the first integral, is obtained from the homogeneous electron gas model. A variation yields the Thomas-Fermi equation, an integral equation, that determines the density, which minimizes the Thomas-Fermi energy functional,

$$n(\mathbf{r}) = \begin{cases} \left(\frac{5}{3}C_{\text{F}}\right)^{-\frac{3}{2}} [\mu - V(\mathbf{r})]^{\frac{3}{2}} & , \mu \geq V(\mathbf{r}) \\ 0 & , \mu < V(\mathbf{r}) \end{cases} \quad (6.12)$$

with the Lagrange multiplier μ being the chemical potential and

$$V(\mathbf{r}) = V_{\text{ext}}(\mathbf{r}) + \int d^3r' \frac{n(\mathbf{r}')}{|\mathbf{r} - \mathbf{r}'|}. \quad (6.13)$$

Although this energy functional was frequently used as a starting point for quantum mechanical investigations (see e.g. [29]), it is a rather crude approximation to an exact energy functional, since it only covers electrostatic interactions, neglecting electron correlations, and introduces significant errors in the kinetic energy term, which is only valid for the homogeneous electron gas.

6.2 The Kohn-Sham equations

For practical calculations, the energy functional (6.9) is not very useful, since $F[n]$ is unknown and the Thomas-Fermi approach is not accurate enough. In order to apply DFT in practice, the Kohn-Sham equations [26] provide an established route. In a first step, the functional (6.9) is splitted into

$$E[n] = G[n] + \frac{1}{2} \int d^3r \int d^3r' \frac{n(\mathbf{r})n(\mathbf{r}')}{|\mathbf{r} - \mathbf{r}'|} + \text{tr}[nV_{\text{ext}}[n]] , \quad (6.14)$$

such that $G[n]$ is also a universal functional excluding the electrostatic contributions. This universal functional,

$$G[n] = T_s[n] + E_{\text{xc}}[n] , \quad (6.15)$$

is then splitted into a part which contains the kinetic energy, $T_s[n]$, of a system of non-interacting electrons of density $n(\mathbf{r})$, and a so called exchange-correlation functional $E_{\text{xc}}[n]$, which covers all remaining energy contributions. The first approximative step enters, when an explicit form of $E_{\text{xc}}[n]$ is adopted. Kohn and Sham argued, that for a reasonably slow varying density, the exchange-correlation functional can be approximated, as

$$E_{\text{xc}}[n] \approx \int d^3r n(\mathbf{r}) \epsilon_{xc}^{\text{HEG}}(n(\mathbf{r})) , \quad (6.16)$$

where $\epsilon_{xc}^{\text{HEG}}$ is the exchange-correlation energy per electron of the homogeneous electron gas (HEG) model, which is a known function. But in contrast to the homogeneous electron gas, the density can vary with \mathbf{r} here. This is called the *local density approximation* (LDA). The minimum of $E[n]$ can then be calculated by solving the

Kohn-Sham equations

$$\left(-\frac{1}{2}\nabla^2 + V_{\text{ext}}(\mathbf{r}) + \int d^3r' \frac{n(\mathbf{r}')}{|\mathbf{r} - \mathbf{r}'|} + v_{\text{xc}}(\mathbf{r}) \right) \varphi_i(\mathbf{r}) = \varepsilon_i \varphi_i(\mathbf{r}) , \quad (6.17)$$

with the density

$$n(\mathbf{r}) = \sum_i^N |\varphi_i(\mathbf{r})|^2 , \quad (6.18)$$

and the *exchange-correlation potential*

$$v_{\text{xc}}(\mathbf{r}) = \frac{\delta E_{\text{xc}}}{\delta n(\mathbf{r})} . \quad (6.19)$$

These self-consistent equations follow from a variation $\delta E[n]/\delta n$ and yield the exact ground state energy, if the exact exchange-correlation functional E_{xc} is used. But since an exact form of E_{xc} is not known, the exact exchange-correlation potential v_{xc} is also not

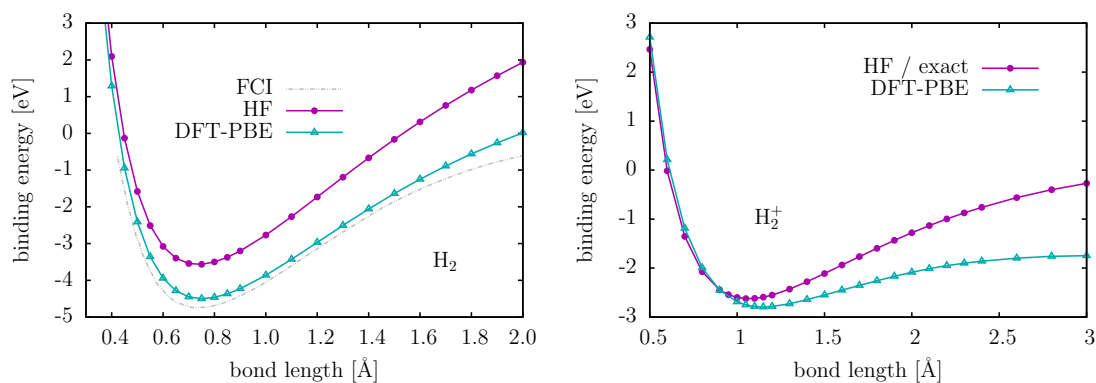


Figure 6.1: Dissociation of the diatomic molecules H₂ and H₂⁺ into 2H and H+H⁺ respectively. As an "exact" reference for the H₂ molecule, we chose full configuration interaction (FCI) calculations from [18]. The computational settings are identical as in described in Fig. 4.1. In the one-electron system H₂⁺, the HF approach is exact, apart from small errors due to the periodic images and the limited basis set size.

available. Besides the LDA, which leads to

$$\begin{aligned} v_{xc}(\mathbf{r}) &\rightarrow v_{xc}^{\text{LDA}}(\mathbf{r}) = \frac{\delta}{\delta n(\mathbf{r})} \int d^3r' n(\mathbf{r}') \epsilon_{xc}^{\text{HEG}}(n(\mathbf{r}')) \\ &= \epsilon_{xc}^{\text{HEG}}(n(\mathbf{r})) + n(\mathbf{r}) \frac{d\epsilon_{xc}^{\text{HEG}}}{dn}(\mathbf{r}), \end{aligned} \quad (6.20)$$

also the *generalized gradient approximation* (GGA) is a class of widely used exchange-correlation potentials of the form

$$v_{xc}(\mathbf{r}) \rightarrow v_{xc}^{\text{GGA}}(\mathbf{r}, n(\mathbf{r}), \nabla n(\mathbf{r})). \quad (6.21)$$

In the recent decades, a countless number of approximate exchange-correlation functionals have been developed [30]. However, a detailed discussion would go beyond the scope of this work.

The large variety of functionals introduces a severe issue. The results of DFT calculations strongly depend on the choice of the approximate exchange-correlation functional. Hence, DFT depends on reference methods or reference values to chose the right functional for the considered material.

6.3 Illustrative DFT calculations for molecules and solids

For the dissociation of the H₂ dimer, the DFT approach indeed improves the binding energy (compared to Hartree-Fock), but also fails to predict the correct dissociation limit. A calculation for larger distances can be found in Ref. [18]. Considering a one-electron

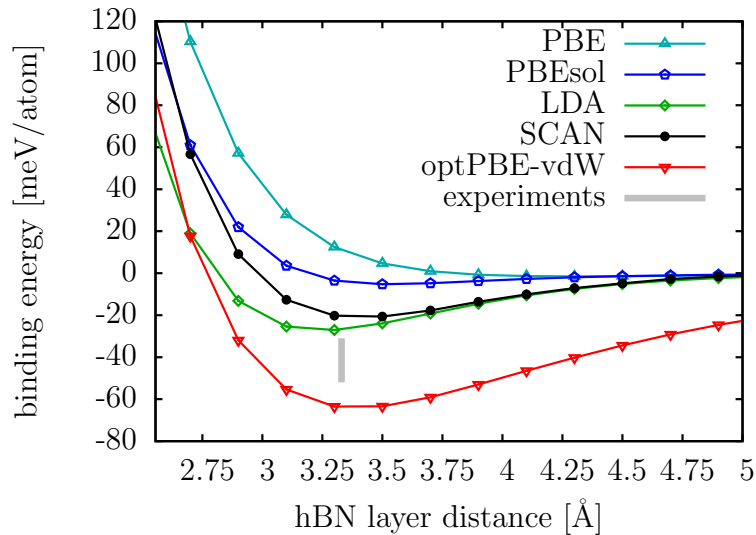


Figure 6.2: Calculation of the binding energy of the hexagonal layers of boron nitride using different DFT exchange-correlation functionals. The computational settings are given by a plane-wave cutoff of 550 eV and a k -point mesh of $8 \times 8 \times 4$ points to sample the Brillouine zone. The energy scale was shifted such that 0 meV/atom correspond to a single layer (or infinitely separated layers) of hBN. The experimental values can be found in [21] and references therein.

system like H_2^+ , the exchange-correlation potential falsely includes correlation contributions. This is known as the *self-correlation* problem and leads to a wrong dissociation curve. Both systems are illustrated in Fig. 6.1.

In the case of hexagonal boron nitride (hBN) the difficulty to choose the "right" approximative exchange-correlation functional becomes evident. Similar to the Hartree-Fock method, the standard DFT functional, PBE [31], fails to predict the bonding between the layers. Employing other well-known and often used functionals like PBEsol [32], LDA, SCAN [33], or even a van der Waals corrected functional like optPBE-vdW [34], leads to a variety of different results. As can be seen in Fig. 6.2, none of the curves meets the experimentally reported interval, even though some functional predict acceptable bond lengths.

CHAPTER 7

Excursion: Green's functions and the quantum field theoretical view

In this chapter, we leave the pedagogical path for an excursion to a quantum field theoretical formulation. The reader without basic knowledge in second-quantization and Feynman diagrams can skip this chapter since its main purpose is to introduce the Green's function and to provide a more modern view on the many-electron problem. Whenever we will use Green's functions after this chapter, we will also introduce them in an *ad-hoc* manner, mostly composed by Hartree-Fock orbitals, so that this chapter is not mandatory but advisable.

7.1 Green's function and self-energy

In the quantum field theoretical perspective, one-electron orbitals become dispensable.

Instead, *Green's functions* are the main quantity,

$$\langle \mathbf{x} | G(t - t') | \mathbf{x}' \rangle = G(\mathbf{x}, \mathbf{x}', t - t') = -i \langle \mathcal{T} \hat{\psi}(\mathbf{x}, t) \hat{\psi}^\dagger(\mathbf{x}', t') \rangle . \quad (7.1)$$

$$= \begin{cases} -i \langle \hat{\psi}(\mathbf{x}, t) \hat{\psi}^\dagger(\mathbf{x}', t') \rangle , & t > t' \\ i \langle \hat{\psi}^\dagger(\mathbf{x}', t') \hat{\psi}(\mathbf{x}, t) \rangle , & t < t' \end{cases} \quad (7.2)$$

Here, \mathcal{T} is the Wick time-ordering operator and $\langle \dots \rangle$ denotes an expectation value with respect to the exact ground state. The Heisenberg equation of motion,

$$i \frac{\partial}{\partial t} \hat{\psi}(\mathbf{x}, t) = [\hat{\psi}(\mathbf{x}, t), H_e] \quad (7.3)$$

\Leftrightarrow

$$\hat{\psi}(\mathbf{x}, t) = e^{iH_e t} \hat{\psi}(\mathbf{x}) e^{-iH_e t} , \quad (7.4)$$

determines the time evolution of the creation and annihilation operators, $\hat{\psi}^\dagger(\mathbf{x})$ and $\hat{\psi}(\mathbf{x})$, respectively, which create or annihilate an electron at \mathbf{x} . The full electronic Hamiltonian

H_e (see Eq. 2.15) has to be considered in the form of second-quantization, i.e. decomposed into electron creation and annihilation operators,

$$H_e = \int d\mathbf{x} \hat{\psi}^\dagger(\mathbf{x}) h(\mathbf{x}) \hat{\psi}(\mathbf{x}) + V_{\text{nn}} \quad (7.5)$$

$$+ \frac{1}{2} \int d\mathbf{x} \int d\mathbf{x}' \hat{\psi}^\dagger(\mathbf{x}) \hat{\psi}^\dagger(\mathbf{x}') \langle \mathbf{x}\mathbf{x}' | r_{12}^{-1} | \mathbf{x}\mathbf{x}' \rangle \hat{\psi}(\mathbf{x}') \hat{\psi}(\mathbf{x}), \quad (7.6)$$

where $h(\mathbf{x})$ covers only the kinetic energy and the nucleus-electron interaction, being both one-electron operators.

The Green's function can be interpreted as a correlation function. For $t > t'$ it represents the probability of finding an electron at (\mathbf{x}, t) , when an electron was added at (\mathbf{x}', t') . Note, that due to the indistinguishability of electrons, we cannot speak of adding and later finding the same electron. It is the entire system that propagates in time, not just one electron. All kinds of possible interactions and correlations of the considered quantum system are therefore covered. Furthermore, the Green's function intrinsically takes into account, that electrons are indistinguishable via the anti-commutator relations,

$$[\hat{\psi}(\mathbf{x}), \hat{\psi}^\dagger(\mathbf{x}')]_+ = \hat{\psi}(\mathbf{x}) \hat{\psi}^\dagger(\mathbf{x}') + \hat{\psi}^\dagger(\mathbf{x}') \hat{\psi}(\mathbf{x}) = \delta(\mathbf{x} - \mathbf{x}'), \quad (7.7)$$

$$[\hat{\psi}^\dagger(\mathbf{x}), \hat{\psi}^\dagger(\mathbf{x}')]_+ = [\hat{\psi}(\mathbf{x}), \hat{\psi}(\mathbf{x}')]_+ = 0. \quad (7.8)$$

By working out the commutator in Eq. (7.3), one can show, that the creation/annihilation operators obey the following equation,

$$i \frac{\partial}{\partial t} \hat{\psi}(\mathbf{x}, t) = h(\mathbf{x}) \hat{\psi}(\mathbf{x}, t) + \int d\mathbf{x}' \hat{\psi}^\dagger(\mathbf{x}', t) \langle \mathbf{x}\mathbf{x}' | r_{12}^{-1} | \mathbf{x}\mathbf{x}' \rangle \hat{\psi}(\mathbf{x}', t) \hat{\psi}(\mathbf{x}, t), \quad (7.9)$$

from which a differential equation for the Green's function can be deduced,

$$\left[i \frac{\partial}{\partial t} - \hat{h}(\mathbf{x}) \right] G(\mathbf{x}, \mathbf{x}', t - t') = \delta(\mathbf{x} - \mathbf{x}') \delta(t - t') - i \int d\mathbf{x}'' \langle \mathbf{x}\mathbf{x}'' | r_{12}^{-1} | \mathbf{x}\mathbf{x}'' \rangle \langle \mathcal{T} \hat{\psi}^\dagger(\mathbf{x}'', t) \hat{\psi}(\mathbf{x}'', t') \hat{\psi}(\mathbf{x}, t) \hat{\psi}^\dagger(\mathbf{x}', t') \rangle. \quad (7.10)$$

This equation explains the name "Green's function" from the mathematical perspective. For a vanishing electron-electron interaction (i.e. setting $\langle \mathbf{x}\mathbf{x}'' | r_{12}^{-1} | \mathbf{x}\mathbf{x}'' \rangle = 0$), Eq. (7.10) corresponds to the genuine mathematical definition of a Green's function. However, the complicated second term on the right hand side disturbs this picture. It is therefore common to define

the *self-energy* $\langle \mathbf{x} | \Sigma(\omega) | \mathbf{x}'' \rangle = \Sigma(\mathbf{x}, \mathbf{x}'', \omega)$ by

$$[\omega - h(\mathbf{x})] G(\mathbf{x}, \mathbf{x}', \omega) - \int d\mathbf{x}'' \Sigma(\mathbf{x}, \mathbf{x}'', \omega) G(\mathbf{x}'', \mathbf{x}', \omega) = \delta(\mathbf{x} - \mathbf{x}'), \quad (7.11)$$

where we also introduced the Fourier transformed Green's function in frequency space,

$$G(\mathbf{x}, \mathbf{x}', \omega) = \int dt G(\mathbf{x}, \mathbf{x}', t) e^{i\omega t} . \quad (7.12)$$

Note that the Green's function is already uniquely defined by (7.1), thus Eq. (7.11) readily defines the self-energy. It is beneficial to reformulate Eq. (7.11) as an operator equation, which holds in any basis,

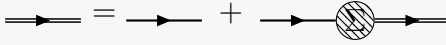
$$[\omega - h]G(\omega) - \Sigma(\omega)G(\omega) = \mathbf{1} . \quad (7.13)$$

If we, furthermore, define a *non-interacting Green's function*, $G_0(\omega)$, which obeys (7.13) for the case $\Sigma(\omega) = 0$,

$$[\omega - h]G_0(\omega) = \mathbf{1} , \quad (7.14)$$

we can formulate the

Dyson equation

$$G(\omega) = G_0(\omega) + G_0(\omega)\Sigma(\omega)G(\omega) \quad (7.15)$$


which relates the interacting and non-interacting Green's function, $G(\omega)$ and $G_0(\omega)$.

Once the Green's function and the self-energy are known, the total electronic energy of the quantum mechanical system can be calculated [35] by

$$E_e = V_{nn} + \lim_{\eta \rightarrow 0^+} \int \frac{d\omega}{2\pi i} e^{i\omega\eta} \left[\int d\mathbf{x} \int d\mathbf{x}' \delta(\mathbf{x} - \mathbf{x}') \times \left(h(\mathbf{x}') + \frac{1}{2}\Sigma(\mathbf{x}, \mathbf{x}', \omega) \right) G(\mathbf{x}', \mathbf{x}, \omega) \right] \quad (7.16)$$

$$= V_{nn} + \text{diagram 1} + \text{diagram 2} \quad (7.17)$$


It is possible to create a bridge between the Green's function formulation and the mean field orbital formulation of the many-body problem. This is known as the *Lehmann representation* [35],

$$G(\mathbf{x}, \mathbf{x}', \omega) = \sum_i^{\infty} \frac{f_i(\mathbf{x})f_i^*(\mathbf{x}')}{\omega - \epsilon_i} . \quad (7.18)$$

Here, the Green's function is decomposed into amplitude functions, defined by

$$f_i(\mathbf{x}) = \begin{cases} \langle \Phi_0^N | \hat{\psi}(\mathbf{x}) | \Phi_i^{N+1} \rangle, & \epsilon_i \geq \mu \\ \langle \Phi_i^{N-1} | \hat{\psi}(\mathbf{x}) | \Phi_0^N \rangle, & \epsilon_i < \mu, \end{cases} \quad (7.19)$$

where $|\Phi_0^N\rangle = |\Phi_e\rangle$ is the exact ground state of the N electron system, and $|\Phi_i^{N+1}\rangle$ is the exact i th excited state of the $N + 1$ electron system with energy E_i^{N+1} . The excitation energies are defined as

$$\epsilon_i = \begin{cases} E_i^{N+1} - E_0^N - i\eta, & \epsilon_i \geq \mu \\ E_0^N - E_i^{N-1} + i\eta, & \epsilon_i < \mu, \end{cases} \quad (7.20)$$

where η is an infinitesimal small but positive energy and μ is the chemical potential (or negative electron affinity),

$$\mu = E_0^{N+1} - E_0^N. \quad (7.21)$$

Starting from Eq. (7.11), we find an eigenvalue-like equation [36] for the functions $f_i(\mathbf{x})$,

$$h(\mathbf{x})f_i(\mathbf{x}) + \int d\mathbf{x}' \Sigma(\mathbf{x}, \mathbf{x}', \epsilon_i) f_i(\mathbf{x}') = \epsilon_i f_i(\mathbf{x}), \quad (7.22)$$

which takes the form of an effective one-electron Schrödinger equation. The solutions are sometimes called *Dyson orbitals*, leading to the exact Green's function and therefore to the exact ground state energy of the system. Like in the case of Hartree-Fock or density functional theory, the ground state density turns out to be the sum of the magnitude squares of those orbitals,

$$n(\mathbf{x}) = \langle \hat{\psi}^\dagger(\mathbf{x}) \hat{\psi}(\mathbf{x}) \rangle = -iG(\mathbf{x}, \mathbf{x}, t \rightarrow 0^-) = \sum_i^{\epsilon_i < \mu} |f_i(\mathbf{x})|^2, \quad (7.23)$$

where the last equality is not obvious and will be proven in Eq. (7.26). However, since the self-energy is unknown in general, also the exact $f_i(\mathbf{x})$ remain inaccessible.

7.2 Hartree-Fock from the QFT perspective

In Chap. 4 we introduced the Hartree-Fock approximation by minimizing the energy functional (4.2) while restricting to antisymmetrized product states of one-electron orbitals. Similarly, we can derive the Hartree-Fock approximation from the Green's function perspective, by postulating a certain form of the self-energy.

Green's function at the Hartree-Fock level as

$$G(\mathbf{x}, \mathbf{x}', \omega) = \sum_{i=1}^N \frac{\chi_i(\mathbf{x})\chi_i^*(\mathbf{x}')}{\omega - \varepsilon_i - i\eta} + \sum_{a=N+1}^{\infty} \frac{\chi_a(\mathbf{x})\chi_a^*(\mathbf{x}')}{\omega - \varepsilon_a + i\eta}. \quad (7.31)$$

Diagrammatic formulation of the Hartree-Fock energy

We can reproduce the Hartree-Fock energy (4.2) in a purely diagrammatic way. The reader unfamiliar with the Feynman diagrammatic technique is referred to [37]. We start with an expansion of the Dyson equation (7.15),

$$\Rightarrow = \longrightarrow + \longrightarrow \textcircled{\text{X}} \Rightarrow \quad (7.32)$$

$$= \longrightarrow + \longrightarrow \textcircled{\text{X}} \longrightarrow + \longrightarrow \textcircled{\text{X}} \longrightarrow \textcircled{\text{X}} \longrightarrow + \dots, \quad (7.33)$$

where \longrightarrow is simply the non-interacting Green's function, which can easily be calculated by solving (7.14). Again, the following approximation of the self-energy is postulated,

$$\textcircled{\text{X}} = \text{wavy circle} + \text{wavy arc} \quad (7.34)$$

Accordingly, the self-consistent solution of the Dyson equation, produces a set of infinitely many diagrams, of which only a few are shown here,

$$\begin{aligned} \Rightarrow = & \longrightarrow + \longrightarrow \text{wavy circle} \longrightarrow + \longrightarrow \text{wavy arc} \longrightarrow + \longrightarrow \text{wavy circle} \text{wavy arc} \longrightarrow + \longrightarrow \text{wavy circle} \text{wavy circle} \longrightarrow \quad (7.35) \\ & + \longrightarrow \text{wavy circle} \text{wavy arc} \longrightarrow + \longrightarrow \text{wavy arc} \text{wavy circle} \longrightarrow + \longrightarrow \text{wavy circle} \text{wavy arc} \text{wavy circle} \longrightarrow + \dots \end{aligned}$$

Therefore, the Hartree-Fock energy E_{HF} is made up of an infinite subclass of all possible closed Feynman diagrams, including

$$\text{Diagram 1} = \text{Diagram 2} + \text{Diagram 3} \quad (7.36)$$

$$= \text{Diagram 4} + \text{Diagram 5} + \text{Diagram 6} \quad (7.37)$$

$$+ \text{Diagram 7} + \text{Diagram 8} + \text{Diagram 9} + \dots \quad (7.38)$$

Indeed, the Hartree-Fock approach is a method, that includes the electron-electron interaction to infinity order. However, we already know, that Hartree-Fock does not cover electron correlation effects. This reveals, that infinite partial sums do not necessarily lead to a highly accurate method, as the calculations in Fig. 4.2 and 4.3 prove. This is due to the fact that the particular choice of the self-energy restricts the energy to a certain subclass of diagrams. The likewise infinitely large set of diagrams, which cover electron correlation, is neglected completely. For instance, a correlation energy diagram could look like

$$\text{Diagram 10} \quad (7.39)$$

which is included in

$$\text{Diagram 11} \quad (7.40)$$

The latter is called the direct MP2 diagram and will be introduced in Chap. 8.1. There we will supplement correlation effects by adding the MP2 correlation energy,

$$\text{Diagram 12} + \text{Diagram 13} + \text{Diagram 14} + \text{Diagram 15} \quad (7.41)$$

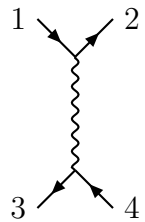
where the Green's function is still at the Hartree-Fock level.

7.3 Exchange from the QFT picture

The diagrammatic formulation of energy contributions allows for a simple an illustrative understanding of exchange. The symmetrization postulate, translated to diagrams, states that a diagram is only allowed to contribute to the energy if replacing any *vertex*


(7.42)

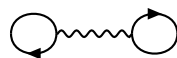
by


(7.43)

leads to another diagram that also contributes to the energy. If, instead, this replacement leads to a new diagram, which is not part of the energy method, then this method does not meet the symmetrization postulate. An example is given by forming


(7.44)

from


(7.45)

A method that violates the symmetrization postulate does not necessarily produce useless results. Such a method is given by the random phase approximation which will be introduced in Sec. 8.3. However, the missing diagrams can be seen as a possible starting point to construct systematic corrections. This will be shown in Sec. 8.4.

CHAPTER 8

Correlation energy methods

In this chapter we derive methods to systematically approximate the correlation energy for real materials. We start with an introduction to Møller-Plesset perturbation theory. We also present a derivation of the random phase approximation using the adiabatic-connection fluctuation-dissipation theorem. Illustrative calculations of dissociation energies of dimers and lattice parameters of solids are shown. We supplement this chapter with a short introduction to second-order screened exchange, being an exchange-like correction to the random phase approximation.

8.1 Second-order Møller-Plesset perturbation theory

Møller-Plesset perturbation theory [38] is a particular application of the well-known Rayleigh-Schrödinger perturbation theory [39, 40]. It relies on the idea, that all energy contributions, which are not covered by the Hartree-Fock method, can be treated as a perturbation. In other words, the effect of electron correlation is treated as a perturbation of uncorrelated electrons. It turns out, that the lowest order correction to the Hartree-Fock energy is quadratic in this perturbation. Dropping higher order corrections is denoted as *second-order Møller-Plesset perturbation theory* (MP2).

In this section we will derive the MP2 correlation energy and discuss some formal and physical features. This includes van der Waals interactions, the size consistency for periodic systems, as well as formal topics like different mathematical formulations of the MP2 correlation energy. The latter is especially useful for the development of new algorithms and will be taken up in Part II.

8.1.1 Canonical formulation

An expression for the MP2 correlation energy can easily be derived by recalling the lowest order correction terms of Rayleigh-Schrödinger perturbation theory,

$$E_0 = E_0^{(0)} + \lambda E_0^{(1)} + \lambda^2 E_0^{(2)} + O(\lambda^3), \quad (8.1)$$

with

$$E_0^{(0)} = \langle \Phi_0^{(0)} | H^{(0)} | \Phi_0^{(0)} \rangle, \quad E_0^{(1)} = \langle \Phi_0^{(0)} | \mathcal{V} | \Phi_0^{(0)} \rangle, \quad E_0^{(2)} = \sum_{n \neq 0}^{\infty} \frac{|\langle \Phi_0^{(0)} | \mathcal{V} | \Phi_n^{(0)} \rangle|^2}{E_0^{(0)} - E_n^{(0)}}. \quad (8.2)$$

Here, E_0 is the desired ground state energy of the fully perturbed Hamiltonian $H^{(0)} + \lambda \mathcal{V}$ and $E_0^{(i)}$ are its expansion terms of i th order. The unitless λ is commonly used to clarify the order of expansion in the perturbation \mathcal{V} and can safely be set to 1. For the unperturbed Hamiltonian, we assume the full spectrum as known, $H^{(0)} | \Phi_n^{(0)} \rangle = E_n^{(0)} | \Phi_n^{(0)} \rangle$.

In order to find the connection to the Hartree-Fock method, we need to construct an unperturbed Hamiltonian $H^{(0)}$ whose lowest eigenvalue is equal to the Hartree-Fock energy (4.25). This is achieved by the Hamiltonian,

$$H^{(0)} = \sum_i^N f^i + V_{\text{nn}} - \frac{1}{2} \sum_{ij}^N \langle \chi_i \chi_j | r_{12}^{-1} | \chi_i \chi_j \rangle + \frac{1}{2} \sum_{ij}^N \langle \chi_i \chi_j | r_{12}^{-1} | \chi_j \chi_i \rangle. \quad (8.3)$$

Note that f^i is the Fock operator (4.19), acting only in the i th one-orbital Hilbert space. Furthermore, we assume the Hartree-Fock problem to be solved, i.e. the orbitals $|\chi_i\rangle$ are known and the electron repulsion integrals $\langle \chi_i \chi_j | V | \chi_i \chi_j \rangle$ (see Eq. 4.8) as well as V_{nn} are simply numbers. We can then conclude, that the following equation must hold,

$$H^{(0)} | \Phi_{\text{HF}} \rangle = E_{\text{HF}} | \Phi_{\text{HF}} \rangle, \quad (8.4)$$

where $|\Phi_{\text{HF}}\rangle = \mathcal{A}|\chi_1 \dots \chi_N\rangle$ is the antisymmetrized Hartree-Fock state that can be identified with $|\Phi_0^{(0)}\rangle$, and E_{HF} is the Hartree-Fock energy. Accordingly, we find

$$E_0^{(0)} = \langle \Phi_0^{(0)} | H^{(0)} | \Phi_0^{(0)} \rangle = E_{\text{HF}} \quad (8.5)$$

for the unperturbed ground state energy, as desired. The perturbation \mathcal{V} is simply obtained by the difference between the full electronic Hamiltonian (2.15) and $H^{(0)}$,

$$\mathcal{V} = H_e - H^{(0)} = V_{\text{ee}} - \frac{1}{2} \sum_{ij}^N \langle \chi_i \chi_j | r_{12}^{-1} | \chi_i \chi_j \rangle + \frac{1}{2} \sum_{ij}^N \langle \chi_i \chi_j | r_{12}^{-1} | \chi_j \chi_i \rangle. \quad (8.6)$$

Again, the last two terms, the electron-repulsion integrals, are just numbers, such that the perturbation is simply given by a shifted electron-electron interaction operator V_{ee} , see Eq.

(2.6). This shift leads to a vanishing first order correction,

$$E_0^{(1)} = \langle \Phi_{\text{HF}} | \mathcal{V} | \Phi_{\text{HF}} \rangle \quad (8.7)$$

$$= \langle \Phi_{\text{HF}} | V_{\text{ee}} | \Phi_{\text{HF}} \rangle - \frac{1}{2} \sum_{ij}^N \langle \chi_i \chi_j | r_{12}^{-1} | \chi_i \chi_j \rangle + \frac{1}{2} \sum_{ij}^N \langle \chi_i \chi_j | r_{12}^{-1} | \chi_j \chi_i \rangle \quad (8.8)$$

$$= 0, \quad (8.9)$$

which directly follows from the Slater-Condon rules (Sec. 3.3) applied to $\langle \Phi_{\text{HF}} | V_{\text{ee}} | \Phi_{\text{HF}} \rangle$.

The first non-vanishing energy correction is the second-order term $E_0^{(2)}$. To calculate it, we need to clarify, that the excited determinants, introduced in Sec. 4.3 (singles, doubles, triples, etc.), are indeed eigenstates of $H^{(0)}$. First, applying $\sum_j^N f^j$ on a singles state $|\Phi_i^a\rangle$ (see Eq. 4.27), leads to

$$\begin{aligned} \sum_j^N f^j |\Phi_i^a\rangle &= \sum_j^N f^j \mathcal{A} | \chi_1 \dots \chi_{i-1} \chi_a \chi_{i+1} \dots \chi_N \rangle \\ &= \frac{1}{\sqrt{N!}} \sum_{\sigma \in \mathcal{S}_N} \text{sgn}(\sigma) \sum_j^N f^j | \chi_{\sigma_1} \dots \chi_{\sigma_N} \rangle \\ &= \frac{1}{\sqrt{N!}} \sum_{\sigma \in \mathcal{S}_N} \text{sgn}(\sigma) \sum_j^N \varepsilon_{\sigma_j} | \chi_{\sigma_1} \dots \chi_{\sigma_N} \rangle \\ &= (\varepsilon_1 + \dots + \varepsilon_{i-1} + \varepsilon_a + \varepsilon_{i+1} + \dots + \varepsilon_N) |\Phi_i^a\rangle. \end{aligned} \quad (8.10)$$

Combining Eq. (4.25), (8.3), and (8.10), then yields

$$H^{(0)} |\Phi_i^a\rangle = [E_{\text{HF}} - \varepsilon_i + \varepsilon_a] |\Phi_i^a\rangle, \quad (8.11)$$

hence, we found eigenstates and the corresponding eigenvalues. The same holds for doubles, triples, etc.,

$$H^{(0)} |\Phi_{ijk\dots}^{abc\dots}\rangle = [E_{\text{HF}} - \varepsilon_i - \varepsilon_j - \varepsilon_k - \dots + \varepsilon_a + \varepsilon_b + \varepsilon_c + \dots] |\Phi_{ijk\dots}^{abc\dots}\rangle, \quad (8.12)$$

The second order contribution can thus be written as

$$E_0^{(2)} = \sum_{n \neq 0}^{\infty} \frac{|\langle \Phi_0^{(0)} | \mathcal{V} | \Phi_n^{(0)} \rangle|^2}{E_0^{(0)} - E_n^{(0)}} \quad (8.13)$$

$$= \sum_{i=1}^N \sum_{a=N+1}^{\infty} \frac{|\langle \Phi_{\text{HF}} | \mathcal{V} | \Phi_i^a \rangle|^2}{\varepsilon_i - \varepsilon_a} + \frac{1}{2} \sum_{i,j=1}^N \sum_{a,b=N+1}^{\infty} \frac{|\langle \Phi_{\text{HF}} | \mathcal{V} | \Phi_{ij}^{ab} \rangle|^2}{\varepsilon_i + \varepsilon_j - \varepsilon_a - \varepsilon_b}. \quad (8.14)$$

Triples or higher excited states do not contribute due to the Slater-Condon rules, since \mathcal{V} is a two-electron operator. The factor $1/2$ in front of the doubles term avoids double counting for the cases $i \leftrightarrow j$ and $a \leftrightarrow b$. It is not necessary to explicitly exclude $i = j$ and

$a = b$, since the definition of excited Slater determinants $|\Phi_{ij}^{ab}\rangle$ automatically eliminated those cases via $|\Phi_{ii}^{ab}\rangle = |\Phi_{ij}^{aa}\rangle = 0$. Furthermore, one can show, that also the singles contributions vanish. This is known as

Brillouin's theorem

If H_e is the full electronic Hamiltonian and $|\Phi_{\text{HF}}\rangle$ and $|\Phi_i^a\rangle$ are the Hartree-Fock ground state and singles excited state, respectively, then

$$\langle \Phi_{\text{HF}} | H_e | \Phi_i^a \rangle = 0 . \quad (8.15)$$

This theorem can easily be proven by applying the Slater-Condon rules. We can immediately conclude

$$\langle \Phi_{\text{HF}} | \mathcal{V} | \Phi_i^a \rangle = \langle \Phi_{\text{HF}} | H_e - H^{(0)} | \Phi_i^a \rangle = \langle \Phi_{\text{HF}} | H^{(0)} | \Phi_i^a \rangle = \langle \chi_i | f | \chi_a \rangle = \varepsilon_a \delta_{ia} = 0 , \quad (8.16)$$

since $i \in \{1, \dots, N\}$ and $a \in \{N + 1, \dots, \infty\}$. Thus, only the doubles excited states contribute to the second-order correction.

$$E_0^{(2)} = \frac{1}{2} \sum_{i,j=1}^N \sum_{a,b=N+1}^{\infty} \frac{|\langle \Phi_{\text{HF}} | \mathcal{V} | \Phi_{ij}^{ab} \rangle|^2}{\varepsilon_i + \varepsilon_j - \varepsilon_a - \varepsilon_b} . \quad (8.17)$$

Employing the Slater-Condon rules once again, the numerator can be written as,

$$\langle \Phi_{\text{HF}} | \mathcal{V} | \Phi_{ij}^{ab} \rangle = \langle \chi_i \chi_j | r_{12}^{-1} | \chi_a \chi_b \rangle - \langle \chi_i \chi_j | r_{12}^{-1} | \chi_b \chi_a \rangle . \quad (8.18)$$

We eventually find the final canonical form of the

MP2 energy

$$E^{\text{MP2}} = E_0^{(2)} = \frac{1}{2} \sum_{i,j=1}^N \sum_{a,b=N+1}^{\infty} \frac{\langle \chi_i \chi_j | r_{12}^{-1} | \chi_a \chi_b \rangle \langle \chi_a \chi_b | r_{12}^{-1} | \chi_i \chi_j \rangle}{\varepsilon_i + \varepsilon_j - \varepsilon_a - \varepsilon_b} \quad (8.19)$$

$$- \frac{1}{2} \sum_{i,j=1}^N \sum_{a,b=N+1}^{\infty} \frac{\langle \chi_i \chi_j | r_{12}^{-1} | \chi_a \chi_b \rangle \langle \chi_a \chi_b | r_{12}^{-1} | \chi_j \chi_i \rangle}{\varepsilon_i + \varepsilon_j - \varepsilon_a - \varepsilon_b} . \quad (8.20)$$

The first term is commonly called *direct MP2* and the second term *exchange MP2*.

According to the definition of the correlation energy (5.5), the MP2 energy is the lowest order contribution to the correlation energy, since the unperturbed Hamiltonian already covers the full Hartree-Fock energy. In terms of charge densities, we can interpret the MP2 energy as an interaction of occupied-unoccupied overlap densities (also sometimes called *particle-hole pairs*),

$$\rho_{ia}(\mathbf{r}) = \langle s_i | s_a \rangle \varphi_i^*(\mathbf{r}) \varphi_a(\mathbf{r}) , \quad (8.21)$$

such that we can write (here only for the direct term),

$$\begin{aligned} & \frac{1}{2} \sum_{i,j=1}^N \sum_{a,b=N+1}^{\infty} \frac{\langle \chi_i \chi_j | r_{12}^{-1} | \chi_a \chi_b \rangle \langle \chi_a \chi_b | r_{12}^{-1} | \chi_i \chi_j \rangle}{\varepsilon_i + \varepsilon_j - \varepsilon_a - \varepsilon_b} \\ &= \frac{1}{2} \sum_{i,j=1}^N \sum_{a,b=N+1}^{\infty} \frac{1}{\varepsilon_i + \varepsilon_j - \varepsilon_a - \varepsilon_b} \int d^3 r_1 \dots \int d^3 r_4 \frac{\rho_{ia}(\mathbf{r}_1) \rho_{jb}(\mathbf{r}_2) \rho_{ia}^*(\mathbf{r}_3) \rho_{jb}^*(\mathbf{r}_4)}{|\mathbf{r}_1 - \mathbf{r}_2| |\mathbf{r}_3 - \mathbf{r}_4|}. \end{aligned} \quad (8.22)$$

Since

$$\int d^3 r \rho_{ia}(\mathbf{r}) = \langle \chi_i | \chi_a \rangle = \delta_{ia} = 0, \quad (8.23)$$

these charge densities contain no net charge but can be considered as neutral multipole charge densities.

8.1.2 MP2 for 3D periodic systems in the thermodynamic limit

The main goal is to implement algorithms for three dimensional periodic systems. Hence, we need to formulate all mathematical expressions in terms of Bloch orbitals and k -point integrals. This subsection largely follows the author's publication [41]. For a periodic system the MP2 energy per unit cell is simply given by Eq. (8.19) and (8.20) divided by the number of unit cells $\mathcal{N} = \Omega/\Omega_0$, where Ω is the total volume of the considered system, and Ω_0 the volume of one single unit cell (as introduced on p. 26). The indices i, j, a, b have to understood as compound indices including a band index, a crystal wave vector and a spin state: $i = (i, \mathbf{k}_1, s_1)$, $j = (j, \mathbf{k}_2, s_2)$, etc. The spin-unrestricted MP2 energy per unit cell of a three dimensional periodic system can thus be written as,

$$\begin{aligned} E^{\text{MP2}} &= \frac{1}{2} \frac{1}{\mathcal{N}} \sum_{\mathbf{k}_1 \dots \mathbf{k}_4}^{\text{BZ}} \sum_{ij}^{\text{occ.}} \sum_{ab}^{\text{virt.}} \sum_{ss'}^{\uparrow\downarrow} \frac{|\langle i\mathbf{k}_1 s, j\mathbf{k}_2 s' | a\mathbf{k}_3 s, b\mathbf{k}_4 s' \rangle|^2}{\varepsilon_{i\mathbf{k}_1 s} + \varepsilon_{j\mathbf{k}_2 s'} - \varepsilon_{a\mathbf{k}_3 s} - \varepsilon_{b\mathbf{k}_4 s'}}, \\ &- \frac{1}{2} \frac{1}{\mathcal{N}} \sum_{\mathbf{k}_1 \dots \mathbf{k}_4}^{\text{BZ}} \sum_{ij}^{\text{occ.}} \sum_{ab}^{\text{virt.}} \sum_s^{\uparrow\downarrow} \frac{\langle i\mathbf{k}_1 s, j\mathbf{k}_2 s | r_{12}^{-1} | a\mathbf{k}_3 s, b\mathbf{k}_4 s \rangle \langle a\mathbf{k}_3 s, b\mathbf{k}_4 s | r_{12}^{-1} | j\mathbf{k}_2 s, i\mathbf{k}_1 s \rangle}{\varepsilon_{i\mathbf{k}_1 s} + \varepsilon_{j\mathbf{k}_2 s} - \varepsilon_{a\mathbf{k}_3 s} - \varepsilon_{b\mathbf{k}_4 s}}, \end{aligned} \quad (8.24)$$

where BZ stands for the first Brillouin zone. For brevity, most of the following calculations are performed for the exchange part, termed E_x^{MP2} , only. Furthermore the spin-restricted case is assumed, i.e. $\sum_s^{\uparrow\downarrow} \rightarrow 2$, in order to attain a more compact notation,

$$E_x^{\text{MP2}} = -\frac{1}{\mathcal{N}} \sum_{\mathbf{k}_1 \dots \mathbf{k}_4}^{\text{BZ}} \sum_{ij}^{\text{occ.}} \sum_{ab}^{\text{virt.}} \frac{\langle i\mathbf{k}_1, j\mathbf{k}_2 | r_{12}^{-1} | a\mathbf{k}_3, b\mathbf{k}_4 \rangle \langle a\mathbf{k}_3, b\mathbf{k}_4 | r_{12}^{-1} | j\mathbf{k}_2, i\mathbf{k}_1 \rangle}{\varepsilon_{i\mathbf{k}_1} + \varepsilon_{j\mathbf{k}_2} - \varepsilon_{a\mathbf{k}_3} - \varepsilon_{b\mathbf{k}_4}}. \quad (8.25)$$

Note that the two-electron integrals $\langle i\mathbf{k}_1, j\mathbf{k}_2 | a\mathbf{k}_3, b\mathbf{k}_4 \rangle$ are non-vanishing only if $\mathbf{k}_1 + \mathbf{k}_2 = \mathbf{k}_3 + \mathbf{k}_4 + \mathbf{G}$, where \mathbf{G} is some arbitrary reciprocal lattice vector. This can be interpreted as crystal momentum conservation. Hence, the two-electron integrals depend

only on three \mathbf{k} -points. This can be seen by explicitly integrating out an electron repulsion integral $\langle i\mathbf{k}_1, j\mathbf{k}_2 | r_{12}^{-1} | a\mathbf{k}_3, b\mathbf{k}_4 \rangle$, using Bloch's theorem (2.4) and the Born-von Karman boundary conditions (2.39), leading to

$$\begin{aligned}
 \langle i\mathbf{k}_1, j\mathbf{k}_2 | r_{12}^{-1} | a\mathbf{k}_3, b\mathbf{k}_4 \rangle &= \int_{\Omega} d^3r \int_{\Omega} d^3r' \frac{\varphi_{i\mathbf{k}_1}^*(\mathbf{r})\varphi_{j\mathbf{k}_2}^*(\mathbf{r}')\varphi_{a\mathbf{k}_3}(\mathbf{r})\varphi_{b\mathbf{k}_4}(\mathbf{r}')}{|\mathbf{r} - \mathbf{r}'|} \\
 &= \frac{1}{\Omega} \sum_{\mathbf{R}, \mathbf{R}'} \int_{\Omega_0} d\mathbf{r} \int_{\Omega_0} d\mathbf{r}' \sum_{\mathbf{G}} \sum_{\mathbf{k}}^{\text{BZ}} \frac{4\pi}{(\mathbf{G} + \mathbf{k})^2} e^{i(\mathbf{G} + \mathbf{k})(\mathbf{r} + \mathbf{R} - \mathbf{r}' - \mathbf{R}')} \\
 &\quad \times e^{-i(\mathbf{k}_1 - \mathbf{k}_3)\mathbf{R}} e^{-i(\mathbf{k}_2 - \mathbf{k}_4)\mathbf{R}'} \varphi_{i\mathbf{k}_1}^*(\mathbf{r})\varphi_{j\mathbf{k}_2}^*(\mathbf{r}')\varphi_{a\mathbf{k}_3}(\mathbf{r})\varphi_{b\mathbf{k}_4}(\mathbf{r}') \\
 &= \frac{\mathcal{N}^2}{\Omega} \int_{\Omega_0} d\mathbf{r} \int_{\Omega_0} d\mathbf{r}' \sum_{\mathbf{G}} \sum_{\mathbf{k}}^{\text{BZ}} \frac{4\pi}{(\mathbf{G} + \mathbf{k})^2} e^{i(\mathbf{G} + \mathbf{k})(\mathbf{r} - \mathbf{r}')} \\
 &\quad \times \delta_{\mathbf{k}, T(\mathbf{k}_1 - \mathbf{k}_3)} \delta_{\mathbf{k}, T(\mathbf{k}_4 - \mathbf{k}_2)} \varphi_{i\mathbf{k}_1}^*(\mathbf{r})\varphi_{j\mathbf{k}_2}^*(\mathbf{r}')\varphi_{a\mathbf{k}_3}(\mathbf{r})\varphi_{b\mathbf{k}_4}(\mathbf{r}') \\
 &\quad \sim \delta_{T(\mathbf{k}_1 - \mathbf{k}_3), T(\mathbf{k}_4 - \mathbf{k}_2)} . \tag{8.26}
 \end{aligned}$$

An explanation is in order. First, we splitted the integration over the entire system Ω into integrals over one unit cell Ω_0 only, where the sum over the real space lattice vectors \mathbf{R}, \mathbf{R}' cares for all possible displacements of this unit cell. Additionally, we employed the Fourier transform of the Coulomb potential,

$$\frac{1}{|\mathbf{r} - \mathbf{r}'|} = \frac{1}{\Omega} \sum_{\mathbf{G}} \sum_{\mathbf{k}}^{\text{BZ}} \frac{4\pi}{(\mathbf{G} + \mathbf{k})^2} e^{i(\mathbf{G} + \mathbf{k})(\mathbf{r} - \mathbf{r}')} . \tag{8.27}$$

Note that this is only an approximation, since the sum over \mathbf{k} should actually be a continuous integral. However, in the thermodynamic limit it becomes exact. Second, we performed the sum over \mathbf{R} and \mathbf{R}' while exploiting the relation [42],

$$\sum_{\mathbf{R}} e^{\pm i(\mathbf{k} - \mathbf{k}')\mathbf{R}} = \mathcal{N} \delta_{T(\mathbf{k}), T(\mathbf{k}')} . \tag{8.28}$$

The function T simply maps a general reciprocal vector back to the first Brillouine zone,

$$T(\mathbf{k}) = \mathbf{k} + \mathbf{G} , \tag{8.29}$$

where \mathbf{G} is an appropriate reciprocal lattice vector such that $\mathbf{k} + \mathbf{G} \in \text{BZ}$.

If we define the overlap densities,

$$\langle i\mathbf{k}_1 | e^{-i\mathbf{G}\hat{r}} | a\mathbf{k}_3 \rangle_{\Omega_0} := \mathcal{N} \int_{\Omega_0} d^3r \varphi_{i\mathbf{k}_1}^*(\mathbf{r})\varphi_{a\mathbf{k}_3}(\mathbf{r}) e^{-i\mathbf{G}\mathbf{r}} . \tag{8.30}$$

we can finally write,

$$\begin{aligned}
 \langle ik_1, jk_2 | ak_3, bk_4 \rangle &= \frac{1}{\Omega} \delta_{T(\mathbf{k}_1 - \mathbf{k}_3), T(\mathbf{k}_4 - \mathbf{k}_2)} \sum_{\mathbf{G}} \frac{4\pi}{[\mathbf{G} + T(\mathbf{k}_1 - \mathbf{k}_3)]^2} \\
 &\times \langle ik_1 | e^{+i[\mathbf{G} + T(\mathbf{k}_1 - \mathbf{k}_3)]\hat{r}} | ak_3 \rangle_{\Omega_0} \\
 &\times \langle jk_2 | e^{-i[\mathbf{G} + T(\mathbf{k}_4 - \mathbf{k}_2)]\hat{r}} | bk_4 \rangle_{\Omega_0} .
 \end{aligned} \tag{8.31}$$

Note that the unitless quantity (8.30) does not explicitly depend on \mathcal{N} , since \mathcal{N} is balanced by the normalization factors of the orbitals (2.39), $\mathcal{N}/\Omega = 1/\Omega_0$. However, there is an implicit dependence since different \mathcal{N} lead to different Born-von Karman boundaries, hence a different mesh of crystal wave vectors (\mathbf{k} -point mesh). Inserting (8.31) into (8.25), one sum over the BZ, here $\mathbf{k}_4 \rightarrow T(\mathbf{k}_1 + \mathbf{k}_2 - \mathbf{k}_3)$, can be eliminated. Note that the Kronecker deltas for the \mathbf{k} -vectors which occur in $\langle ik_1, jk_2 | ak_3, bk_4 \rangle$ and $\langle ak_3, bk_4 | jk_2, ik_1 \rangle$ are equivalent. A substitution $\mathbf{q} = T(\mathbf{k}_2 - \mathbf{k}_3)$ then leads to

$$\begin{aligned}
 E_x^{\text{MP2}} &= -\frac{1}{\Omega_0^2} \frac{1}{\mathcal{N}^3} \sum_{\mathbf{k}_1 \mathbf{k}_2 \mathbf{q}}^{\text{BZ}} \sum_{ij}^{\text{occ.}} \sum_{ab}^{\text{virt.}} \sum_{\mathbf{G}} \frac{4\pi}{[\mathbf{G} + T(\mathbf{k}_1 - \mathbf{k}_2 + \mathbf{q})]^2} \sum_{\mathbf{G}'} \frac{4\pi}{(\mathbf{G}' - \mathbf{q})^2} \\
 &\times \langle ik_1 | e^{+i[\mathbf{G} + T(\mathbf{k}_1 - \mathbf{k}_2 + \mathbf{q})]\hat{r}} | aT(\mathbf{k}_2 - \mathbf{q}) \rangle_{\Omega_0} \langle aT(\mathbf{k}_2 - \mathbf{q}) | e^{+i(\mathbf{G}' - \mathbf{q})\hat{r}} | jk_2 \rangle_{\Omega_0} \\
 &\times \langle jk_2 | e^{-i[\mathbf{G} + T(\mathbf{k}_1 - \mathbf{k}_2 + \mathbf{q})]\hat{r}} | bT(\mathbf{k}_1 + \mathbf{q}) \rangle_{\Omega_0} \langle bT(\mathbf{k}_1 + \mathbf{q}) | e^{-i(\mathbf{G}' - \mathbf{q})\hat{r}} | ik_1 \rangle_{\Omega_0} \\
 &\times \frac{1}{\varepsilon_{ik_1} + \varepsilon_{jk_2} - \varepsilon_{aT(\mathbf{k}_2 - \mathbf{q})} - \varepsilon_{bT(\mathbf{k}_1 + \mathbf{q})}} .
 \end{aligned} \tag{8.32}$$

The MP2 energy per unit cell does not explicitly depend on \mathcal{N} , although $1/\mathcal{N}^3$ appears in the above formula. Again the \mathcal{N} dependence is only implicit since \mathcal{N} defines the density of the allowed \mathbf{k} -points. This becomes evident when we perform the thermodynamic limit, $\mathcal{N} \rightarrow \infty$, $\Omega/\mathcal{N} = \Omega_0 = \text{const.}$. The density of the crystal wave vectors \mathbf{k} becomes infinite and sums turn into integrals:

$$\frac{1}{\mathcal{N}} \sum_{\mathbf{k}}^{\text{BZ}} \dots \longrightarrow \Omega_0 \int_{\text{BZ}} \frac{d^3k}{(2\pi)^3} \dots , \tag{8.33}$$

which implies:

$$\frac{1}{\Omega_0^2} \frac{1}{\mathcal{N}^3} \sum_{\mathbf{k}_1 \mathbf{k}_2 \mathbf{q}}^{\text{BZ}} \dots \longrightarrow \Omega_0 \int_{(\text{BZ})^3} \frac{d^3k_1}{(2\pi)^3} \frac{d^3k_2}{(2\pi)^3} \frac{d^3q}{(2\pi)^3} \dots . \tag{8.34}$$

Since $\Omega \rightarrow \infty$ the normalization factor has to be dropped in (2.39) and we write $\varphi_{ik}(\mathbf{r}) \rightarrow e^{i\mathbf{k}\mathbf{r}} u_{ik}(\mathbf{r})$ such that the overlap densities (8.30) now read:

$$\langle ik_1 | e^{-i\mathbf{G}\hat{r}} | ak_3 \rangle_{\Omega_0} \longrightarrow \frac{1}{\Omega_0} \int_{\Omega_0} d^3r \varphi_{ik_1}^*(\mathbf{r}) \varphi_{ak_3}(\mathbf{r}) e^{-i\mathbf{G}\mathbf{r}} . \tag{8.35}$$

We eventually arrive at the

MP2 correlation energy per unit cell (here only the exchange term) for three dimensional periodic systems in the thermodynamic limit,

$$\begin{aligned}
E_x^{\text{MP2}} = & -\Omega_0 \int_{(\text{BZ})^3} \frac{d^3 k_1}{(2\pi)^3} \frac{d^3 k_2}{(2\pi)^3} \frac{d^3 q}{(2\pi)^3} \sum_{ij}^{\text{occ.}} \sum_{ab}^{\text{virt.}} \sum_{\mathbf{G}\mathbf{G}'} \frac{4\pi}{[\mathbf{G} + T(\mathbf{k}_1 - \mathbf{k}_2 + \mathbf{q})]^2} \frac{4\pi}{(\mathbf{G}' - \mathbf{q})^2} \\
& \times \langle i\mathbf{k}_1 | e^{+i[\mathbf{G}+T(\mathbf{k}_1-\mathbf{k}_2+\mathbf{q})]\hat{r}} | aT(\mathbf{k}_2 - \mathbf{q}) \rangle_{\Omega_0} \langle aT(\mathbf{k}_2 - \mathbf{q}) | e^{+i(\mathbf{G}'-\mathbf{q})\hat{r}} | j\mathbf{k}_2 \rangle_{\Omega_0} \\
& \times \langle j\mathbf{k}_2 | e^{-i[\mathbf{G}+T(\mathbf{k}_1-\mathbf{k}_2+\mathbf{q})]\hat{r}} | bT(\mathbf{k}_1 + \mathbf{q}) \rangle_{\Omega_0} \langle bT(\mathbf{k}_1 + \mathbf{q}) | e^{-i(\mathbf{G}'-\mathbf{q})\hat{r}} | i\mathbf{k}_1 \rangle_{\Omega_0} \\
& \times \frac{1}{\varepsilon_{i\mathbf{k}_1} + \varepsilon_{j\mathbf{k}_2} - \varepsilon_{aT(\mathbf{k}_2-\mathbf{q})} - \varepsilon_{bT(\mathbf{k}_1+\mathbf{q})}} . \tag{8.36}
\end{aligned}$$

The calculation of the thermodynamic limit also proves the size consistency of the MP2 energy. The main reason for the size consistency is the collapse of one of the four k -point summations, such that the remaining $1/\mathcal{N}^3$ term in Eq. (8.32) exactly fuses to three k -point integrals.

8.1.3 Periodic MP2 in the PAW and the long-wavelength limit

In this section, we discuss the application of the PAW method and the long-wavelength limit for MP2, which both become crucial when the MP2 formulas shall be translated into a computer code.

PAW charge densities

When using the PAW method for an implementation of a periodic MP2 algorithm (similar derivations hold for non-periodic approaches), the electron-repulsion integrals, Eq. (8.26), need some special treatment. As already mentioned, the electron-repulsion integrals, can be considered as interactions of neutral charge densities (for brevity, we neglect the spin here),

$$\begin{aligned}
& \langle aT(\mathbf{k}_2 - \mathbf{q}), bT(\mathbf{k}_1 + \mathbf{q}) | r_{12}^{-1} | j\mathbf{k}_2, i\mathbf{k}_1 \rangle \\
& = \int_{\Omega} d^3 r \int_{\Omega} d^3 r' \frac{\varphi_{aT(\mathbf{k}_2-\mathbf{q})}^*(\mathbf{r}) \varphi_{bT(\mathbf{k}_1+\mathbf{q})}^*(\mathbf{r}') \varphi_{j\mathbf{k}_2}(\mathbf{r}) \varphi_{i\mathbf{k}_1}(\mathbf{r}')}{|\mathbf{r} - \mathbf{r}'|} \\
& = \int_{\Omega} d^3 r \int_{\Omega} d^3 r' \frac{\rho_{aj}^{k_2\mathbf{q}}(\mathbf{r}) \rho_{bi}^{k_1\mathbf{q}}(\mathbf{r}')}{|\mathbf{r} - \mathbf{r}'|} , \tag{8.37}
\end{aligned}$$

with the overlap densities,

$$\rho_{aj}^{k_2\mathbf{q}}(\mathbf{r}) = \langle aT(\mathbf{k}_2 - \mathbf{q}) | \mathbf{r} \rangle \langle \mathbf{r} | j\mathbf{k}_2 \rangle . \tag{8.38}$$

However, if the Hartree-Fock orbitals are calculated using the PAW method, we only have the pseudo orbitals available, hence we need to calculate

$$\rho_{aj}^{k_2q}(\mathbf{r}) = \langle aT(\mathbf{k}_2 - \mathbf{q}) | \mathcal{T}^\dagger | \mathbf{r} \rangle \langle \mathbf{r} | \mathcal{T} | j\mathbf{k}_2 \rangle, \quad (8.39)$$

which follows from Eq. (2.58). Fortunately, we already evaluated $\mathcal{T}^\dagger | \mathbf{r} \rangle \langle \mathbf{r} | \mathcal{T}$ in Eq. (2.61) and find,

$$\rho_{aj}^{k_2q}(\mathbf{r}) = \tilde{\rho}_{aj}^{k_2q}(\mathbf{r}) + {}^1\rho_{aj}^{k_2q}(\mathbf{r}) - {}^1\tilde{\rho}_{aj}^{k_2q}(\mathbf{r}), \quad (8.40)$$

with

$$\tilde{\rho}_{aj}^{k_2q}(\mathbf{r}) = \langle aT(\mathbf{k}_2 - \mathbf{q}) | \mathbf{r} \rangle \langle \mathbf{r} | j\mathbf{k}_2 \rangle, \quad (8.41)$$

$${}^1\rho_{aj}^{k_2q}(\mathbf{r}) = \sum_I \sum_{nm} \langle \phi_{Im} | \mathbf{r} \rangle \langle \mathbf{r} | \phi_{In} \rangle \langle aT(\mathbf{k}_2 - \mathbf{q}) | \tilde{p}_{Im} \rangle \langle \tilde{p}_{In} | j\mathbf{k}_2 \rangle, \quad (8.42)$$

$${}^1\tilde{\rho}_{aj}^{k_2q}(\mathbf{r}) = \sum_I \sum_{nm} \langle \tilde{\phi}_{Im} | \mathbf{r} \rangle \langle \mathbf{r} | \tilde{\phi}_{In} \rangle \langle aT(\mathbf{k}_2 - \mathbf{q}) | \tilde{p}_{Im} \rangle \langle \tilde{p}_{In} | j\mathbf{k}_2 \rangle. \quad (8.43)$$

Note that ${}^1\rho_{aj}^{k_2q}(\mathbf{r}) - {}^1\tilde{\rho}_{aj}^{k_2q}(\mathbf{r})$ vanishes outside the augmentation spheres, hence, for this charge contributions, the electron-repulsion integrals reduce to interactions between the augmentation spheres, and are evaluated in the partial wave bases $\{|\phi_{In}\rangle\}$ and $\{|\tilde{\phi}_{In}\rangle\}$. Additionally, *compensation charges* are added to $\tilde{\rho}_{aj}^{k_2q}(\mathbf{r})$ and ${}^1\tilde{\rho}_{aj}^{k_2q}(\mathbf{r})$, such that the two-electron integrals can simply be splitted into three parts

$$\begin{aligned} \langle aT(\mathbf{k}_2 - \mathbf{q}), bT(\mathbf{k}_1 + \mathbf{q}) | r_{12}^{-1} | j\mathbf{k}_2, i\mathbf{k}_1 \rangle &= \int_{\Omega} d^3r \int_{\Omega} d^3r' \frac{\tilde{\rho}_{aj}^{k_2q}(\mathbf{r}) \tilde{\rho}_{bi}^{k_1q}(\mathbf{r}')}{|\mathbf{r} - \mathbf{r}'|} \\ &+ \int_{\Omega} d^3r \int_{\Omega} d^3r' \frac{{}^1\rho_{aj}^{k_2q}(\mathbf{r}) {}^1\rho_{bi}^{k_1q}(\mathbf{r}')}{|\mathbf{r} - \mathbf{r}'|} \\ &- \int_{\Omega} d^3r \int_{\Omega} d^3r' \frac{{}^1\tilde{\rho}_{aj}^{k_2q}(\mathbf{r}) {}^1\tilde{\rho}_{bi}^{k_1q}(\mathbf{r}')}{|\mathbf{r} - \mathbf{r}'|} \end{aligned} \quad (8.44)$$

For brevity, we pass a deeper investigation of the compensations charges, that allow for such a decomposition, and refer to [43, 44].

It is only the first part, involving $\tilde{\rho}_{aj}^{k_2q}(\mathbf{r}) \tilde{\rho}_{bi}^{k_1q}(\mathbf{r}')$, for which the derivations from the previous section 8.1.2 were performed. Hence, all Hartree-Fock orbitals were understood there as PAW pseudo orbitals.

The long-wavelength limit

The long-wavelength limit refers to the case, when $(\mathbf{G}' - \mathbf{q})$ and/or $[\mathbf{G} + T(\mathbf{k}_1 - \mathbf{k}_2 + \mathbf{q})]$ approaches zero in Eq. (8.36), leading to a divergence of the Fourier transformed Coulomb kernel. Conventionally, this is called *head* if both limits are considered at once, or *wing* if only one of the limits is considered. This divergence is compensated by the overlap densities, that also decay to zero, such that a finite limit is approached. This limit is here

calculated for the case of $(\mathbf{G}' - \mathbf{q}) \rightarrow 0$, being equivalent to $\mathbf{G}' = 0$ and $\mathbf{q} \rightarrow 0$,

$$F_{ijab}^{k_1 k_2} = \lim_{\mathbf{q} \rightarrow 0} \frac{4\pi}{q^2} \langle aT(\mathbf{k}_2 - \mathbf{q}) | e^{-i\mathbf{q}\hat{r}} | j\mathbf{k}_2 \rangle_{\Omega_0} \langle bT(\mathbf{k}_1 + \mathbf{q}) | e^{i\mathbf{q}\hat{r}} | i\mathbf{k}_1 \rangle_{\Omega_0}. \quad (8.45)$$

The orbitals are here understood as PAW pseudo orbitals, but we suppress the tilde for notational clarity. In a first step, we expand the overlap densities in powers of \mathbf{q} ,

$$\begin{aligned} \langle aT(\mathbf{k}_2 - \mathbf{q}) | e^{-i\mathbf{q}\hat{r}} | j\mathbf{k}_2 \rangle_{\Omega_0} = \\ \langle a\mathbf{k}_2 | j\mathbf{k}_2 \rangle_{\Omega_0} + \left[\nabla_{\mathbf{q}} \langle aT(\mathbf{k}_2 - \mathbf{q}) | e^{-i\mathbf{q}\hat{r}} | j\mathbf{k}_2 \rangle_{\Omega_0} \right]_{\mathbf{q}=0} \cdot \mathbf{q} + \mathcal{O}(q^2). \end{aligned} \quad (8.46)$$

The first contribution vanishes due to the orthogonality of the orbitals, see Eq. (2.40). The derivative can be simplified to

$$\begin{aligned} \left[\nabla_{\mathbf{q}} \langle aT(\mathbf{k}_2 - \mathbf{q}) | e^{-i\mathbf{q}\hat{r}} | j\mathbf{k}_2 \rangle_{\Omega_0} \right]_{\mathbf{q}=0} = -\langle \nabla_{\mathbf{k}_2} (a\mathbf{k}_2) | j\mathbf{k}_2 \rangle_{\Omega_0} - i \langle a\mathbf{k}_2 | \hat{r} | j\mathbf{k}_2 \rangle_{\Omega_0} \\ = - \int_{\Omega_0} d^3r (\nabla_{\mathbf{k}_2} u_{a\mathbf{k}_2}^*)(\mathbf{r}) u_{j\mathbf{k}_2}(\mathbf{r}), \end{aligned} \quad (8.47)$$

such that we find for overlap densities,

$$\langle aT(\mathbf{k}_2 - \mathbf{q}) | e^{-i\mathbf{q}\hat{r}} | j\mathbf{k}_2 \rangle_{\Omega_0} = -|\mathbf{q}| \int_{\Omega_0} d^3r (\hat{\mathbf{q}} \nabla_{\mathbf{k}_2} u_{a\mathbf{k}_2}^*)(\mathbf{r}) u_{j\mathbf{k}_2}(\mathbf{r}) + \mathcal{O}(q^2), \quad (8.48)$$

where $\hat{\mathbf{q}} = \mathbf{q}/|\mathbf{q}|$ stands for the unit vector and u refers to the cell periodic part of the orbitals. This reveals, that the limit $\mathbf{q} \rightarrow 0$ depends on the direction of \mathbf{q} . We find

$$F_{ijab}^{k_1 k_2} = -4\pi \left[\int_{\Omega_0} d^3r (\hat{\mathbf{q}} \nabla_{\mathbf{k}_2} u_{a\mathbf{k}_2}^*)(\mathbf{r}) u_{j\mathbf{k}_2}(\mathbf{r}) \right] \left[\int_{\Omega_0} d^3r (\hat{\mathbf{q}} \nabla_{\mathbf{k}_1} u_{b\mathbf{k}_1}^*)(\mathbf{r}) u_{i\mathbf{k}_1}(\mathbf{r}) \right]. \quad (8.49)$$

For discretized implementations of Eq. (8.36) in a computer code, the cases $(\mathbf{G}' - \mathbf{q})$ and $[\mathbf{G} + T(\mathbf{k}_1 - \mathbf{k}_2 + \mathbf{q})]$ have to be excluded from the summation and be replaced by the long-wavelength limit $F_{ijab}^{k_1 k_2}$.

8.1.4 Van der Waals interactions in HF and MP2

In this section, we will turn back to the canonical MP2 formulation, ignoring explicit k -point sampling. Figure 4.3 suggests, that the weak van der Waals interactions can not be covered by the Hartree-Fock method. That is no surprise, since van der Waals interactions are based on correlations in the electron polarization of the considered subsystems. Since Hartree-Fock, by definition, does not cover electron correlation, also the van der Waals interactions are invisible. This is corrected by the MP2 energy.

From the mathematical point of view, this can be rationalized in the following way. Imagine two separated neutral regions (A and B) of a quantum system, e.g. two separated molecules (Fig. 8.1) or the far separated layers of boron nitride (Fig. 2.1). The center of both regions be separated by the distance R along the z axes. If R is large enough, one

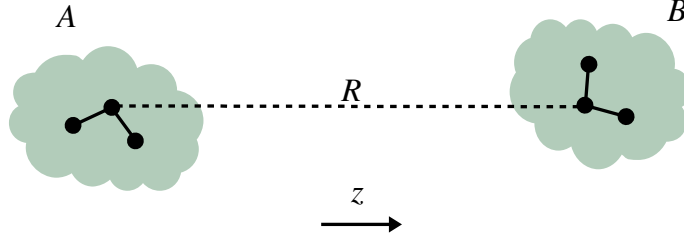


Figure 8.1: Schematic illustration of two separated molecules with a non overlapping electron density (green area).

can show, that the Hartree-Fock exchange contribution (second term in Eq. 4.6) vanishes. For this, remember that the spin-orbitals can be unitarily transformed, without changing the Hartree-Fock energy, as discussed in Chap. 4. We can transform the orbitals in such a way, that they are localized either in region A or B . If they are localized, then the overlap density

$$\rho_{ij}(\mathbf{r}) = \langle s_i | s_j \rangle \varphi_i^*(\mathbf{r}) \varphi_j(\mathbf{r}) \approx 0, \quad (8.50)$$

vanishes, if i and j are from different regions. Hence the Hartree-Fock exchange contribution,

$$-\frac{1}{2} \sum_{ij}^N \langle \chi_i \chi_j | r_{12}^{-1} | \chi_j \chi_i \rangle = -\frac{1}{2} \sum_{ij}^N \int d^3r \int d^3r' \frac{\rho_{ij}(\mathbf{r}) \rho_{ij}^*(\mathbf{r}')}{|\mathbf{r} - \mathbf{r}'|} \approx 0, \quad (8.51)$$

will also vanish and the interaction between both regions reduces to the classical electrostatic interactions between the nuclei and the electron charge densities. The attraction between the nuclei in A and the electron density of B can easily be compensated by the repulsion between the nuclei in A and the nuclei in B . The remaining repulsion between the electron density A and B can quickly dominate the interaction in the Hartree-Fock picture.

The MP2 correction, providing an attractive force, can be derived as follows. Note that we now use the canonical Hartree-Fock orbitals again, instead of unitarily transformed ones. We expand the Coulomb potential in powers of $1/R$,

$$\frac{1}{|\mathbf{r}_1 - \mathbf{r}_2|} = \frac{1}{R} + \frac{z_1 - z_2}{R^2} + \frac{2z_1^2 - x_1^2 - y_1^2 + 2z_2^2 - x_2^2 - y_2^2}{2R^3} \quad (8.52)$$

$$+ \frac{2x_1x_2 + 2y_1y_2 - z_1z_2}{2R^3} + O(R^{-4}). \quad (8.53)$$

The electron-repulsion integrals then reduce to

$$\begin{aligned} \langle \chi_i \chi_j | r_{12}^{-1} | \chi_a \chi_b \rangle &= \\ &= \frac{2\langle \chi_i | x | \chi_a \rangle \langle \chi_j | x | \chi_b \rangle + 2\langle \chi_i | y | \chi_a \rangle \langle \chi_j | y | \chi_b \rangle - \langle \chi_i | z | \chi_a \rangle \langle \chi_j | z | \chi_b \rangle}{2R^3} + \mathcal{O}(R^{-4}), \end{aligned} \quad (8.54)$$

where only the R^{-3} term survives, due to the orthogonality of the occupied $\{|\chi_i\rangle\}$ and unoccupied orbitals $\{|\chi_a\rangle\}$, which implies

$$\langle \chi_i \chi_j | \frac{z_1 - z_2}{R^2} | \chi_a \chi_b \rangle = \frac{1}{R} \langle \chi_i | z | \chi_a \rangle \langle \chi_j | \chi_b \rangle - \frac{1}{R} \langle \chi_i | \chi_a \rangle \langle \chi_j | z | \chi_b \rangle = 0. \quad (8.55)$$

The vanishing spatial overlap between separated occupied orbitals, $\rho_{ij}(\mathbf{r}) \approx 0$, is irrelevant, since only the occupied-unoccupied overlap densities, $\rho_{ia}(\mathbf{r})$ from Eq. (8.21), contribute in the electron-repulsion integrals of the MP2 energy. The sum over all unoccupied orbitals a, b assures, that the numerator of the right hand side of (8.54) can indeed provide a significant contribution. For the direct MP2 energy (8.19), this results in a van der Waals-like potential,

$$\langle \chi_i \chi_j | r_{12}^{-1} | \chi_a \chi_b \rangle \langle \chi_a \chi_b | r_{12}^{-1} | \chi_i \chi_j \rangle \sim -\frac{1}{R^6} + \mathcal{O}(R^{-7}). \quad (8.56)$$

This $1/R^6$ potential is attractive, since the direct MP2 term is strictly negative, as follows from the positive definite numerator and negative denominator of Eq. (8.19). For the MP2 exchange term (8.20), a similar derivation holds, however, its contribution will be smaller. The exchange of i and j in the second electron-repulsion integral requires that all overlap densities ρ_{ia} and ρ_{jb} as well as ρ_{ja} and ρ_{ib} must be sizable at the same time. The likelihood of such a combination is decreasing with increasing R . Since the exchange MP2 energy is strictly positive, it slightly weakens the attractive interaction of the direct MP2 term.

8.1.5 Laplace transformed formulation

It is possible to bring the MP2 energy (8.19)+(8.20) in a form, that is invariant under unitary transformations of *time-dependent Hartree-Fock spin-orbitals*. This formulation is both very simple and very useful for the development of efficient implementations in a computer code. It is based on a work by Almlöf [45] and uses a simple Laplace transform,

$$\frac{1}{\varepsilon_i + \varepsilon_j - \varepsilon_a - \varepsilon_b} = - \int_0^\infty d\tau e^{(\varepsilon_i + \varepsilon_j - \varepsilon_a - \varepsilon_b)\tau}. \quad (8.57)$$

Note, that $\varepsilon_i + \varepsilon_j - \varepsilon_a - \varepsilon_b$ is always negative, since i and j denote occupied orbitals and a and b unoccupied ones, i.e. the former are always smaller than the latter, $\varepsilon_i + \varepsilon_j < \varepsilon_a + \varepsilon_b$.

We introduce time-dependent Hartree-Fock spin-orbitals by,

$$|\chi_i^\tau\rangle = e^{\varepsilon_i\tau/2}|\chi_i\rangle, \quad |\chi_a^\tau\rangle = e^{-\varepsilon_a\tau/2}|\chi_a\rangle, \quad (8.58)$$

The term "time-dependent" refers to the fact that τ can be interpreted as an imaginary time parameter. We will clarify the notion of imaginary time in Sec. 8.1.6. Using the time-dependent spin-orbitals, we can immediately formulate the

Laplace transformed MP2 expression (LTMP2)

$$E^{\text{MP2}} = -\frac{1}{2} \int_0^\infty d\tau \sum_{i,j=1}^N \sum_{a,b=N+1}^\infty \langle \chi_i^\tau \chi_j^\tau | r_{12}^{-1} | \chi_a^\tau \chi_b^\tau \rangle \langle \chi_a^\tau \chi_b^\tau | r_{12}^{-1} | \chi_i^\tau \chi_j^\tau \rangle \quad (8.59)$$

$$+ \frac{1}{2} \int_0^\infty d\tau \sum_{i,j=1}^N \sum_{a,b=N+1}^\infty \langle \chi_i^\tau \chi_j^\tau | r_{12}^{-1} | \chi_a^\tau \chi_b^\tau \rangle \langle \chi_a^\tau \chi_b^\tau | r_{12}^{-1} | \chi_j^\tau \chi_i^\tau \rangle. \quad (8.60)$$

Any unitary transformations

$$|\chi_i^\tau\rangle \rightarrow |\tilde{\chi}_i^\tau\rangle = \sum_{j=1}^N u_{ij} |\chi_j^\tau\rangle, \quad (8.61)$$

$$|\chi_a^\tau\rangle \rightarrow |\tilde{\chi}_a^\tau\rangle = \sum_{b=N+1}^\infty v_{ab} |\chi_b^\tau\rangle, \quad (8.62)$$

where u_{ij} and v_{ab} are unitary matrices, leave the LTMP2 expression invariant. The proof is straight forward and can be found in Sec. 11.2.1 or in the publication [46] of the author of this thesis.

8.1.6 Green's function formulation

Yet another useful formulation of the MP2 energy can be found by using a Green's function approach. We start with an *ad-hoc* introduction of the Green's function in imaginary time,

$$G(\mathbf{x}, \mathbf{x}', \tau) = \theta(-\tau)G^<(\mathbf{x}, \mathbf{x}', \tau) + \theta(\tau)G^>(\mathbf{x}, \mathbf{x}', \tau), \quad (8.63)$$

split into a retarded part,

$$G^<(\mathbf{x}, \mathbf{x}', \tau) = \sum_{i=1}^N \chi_i(\mathbf{x}) \chi_i^*(\mathbf{x}') e^{-\varepsilon_i\tau} = \sum_{i=1}^N \chi_i^{-\tau}(\mathbf{x}) \chi_i^{-\tau}(\mathbf{x}')^*, \quad (8.64)$$

and into an advanced part,

$$G^>(\mathbf{x}, \mathbf{x}', \tau) = - \sum_{a=N+1}^{\infty} \chi_a(\mathbf{x}) \chi_a^*(\mathbf{x}') e^{-\varepsilon_a \tau} = - \sum_{a=N+1}^{\infty} \chi_a^\tau(\mathbf{x}) \chi_a^\tau(\mathbf{x}')^*, \quad (8.65)$$

We also made use of the imaginary time evolved Hartree-Fock spin orbitals from Eq. (8.58). Careful bookkeeping of all indices and coordinates leads directly to the

Green's function formulation of the MP2 energy

$$E^{\text{MP2}} = - \frac{1}{2} \int_0^\infty d\tau \int d\mathbf{x}_1 \dots \int d\mathbf{x}_4 \frac{\delta_{s_1 s_3} \delta_{s_2 s_4}}{|\mathbf{r}_1 - \mathbf{r}_2| |\mathbf{r}_3 - \mathbf{r}_4|} \quad (8.66)$$

$$\begin{aligned} & \times G^>(\mathbf{x}_1, \mathbf{x}_3, \tau) G^<(\mathbf{x}_3, \mathbf{x}_1, -\tau) G^>(\mathbf{x}_2, \mathbf{x}_4, \tau) G^<(\mathbf{x}_4, \mathbf{x}_2, -\tau) \\ & + \frac{1}{2} \int_0^\infty d\tau \int d\mathbf{x}_1 \dots \int d\mathbf{x}_4 \frac{\delta_{s_1 s_2} \delta_{s_2 s_3} \delta_{s_3 s_4}}{|\mathbf{r}_1 - \mathbf{r}_2| |\mathbf{r}_3 - \mathbf{r}_4|} \quad (8.67) \\ & \times G^>(\mathbf{x}_1, \mathbf{x}_3, \tau) G^<(\mathbf{x}_4, \mathbf{x}_1, -\tau) G^>(\mathbf{x}_2, \mathbf{x}_4, \tau) G^<(\mathbf{x}_3, \mathbf{x}_2, -\tau) . \end{aligned}$$

This simple transition to the Green's function notation, which usually requires the background of second-quantization, is possible due to the introduction of the Laplace transformed formulation of MP2 from Sec. 8.1.5. The Laplace transform serves as a bridge between the *sum over states* representation and the Green's function representation. Translating the Green's functions into Feynman diagrams (as used in Chap. 7), the MP2 correlation energy can be written as

$$E^{\text{MP2}} = \text{Diagram 1} + \text{Diagram 2} \quad (8.68)$$

The Wick rotation and the connection to the QFT picture

For the sake of completeness, we briefly justify that (8.63) is indeed a Green's function. In Sec. 7.2 we derived a Green's function expression (see Eq. 7.31) at the Hartree-Fock level in frequency space, reading

$$G(\mathbf{x}, \mathbf{x}', \omega) = \sum_{i=1}^N \frac{\chi_i(\mathbf{x}) \chi_i^*(\mathbf{x}')}{\omega - \varepsilon_i - i\eta} + \sum_{a=N+1}^{\infty} \frac{\chi_a(\mathbf{x}) \chi_a^*(\mathbf{x}')}{\omega - \varepsilon_a + i\eta} . \quad (8.69)$$

One can show that this corresponds to the Green's function (8.63) after transforming from the real frequency to the imaginary time space. In Chap. 7.2 we introduced the pair (t, ω) by Eq. (7.12). For instance, the Fourier transform of the first part of the Green's function, involving the occupied Hartree-Fock energies ε_i , can be calculated by a contour integral

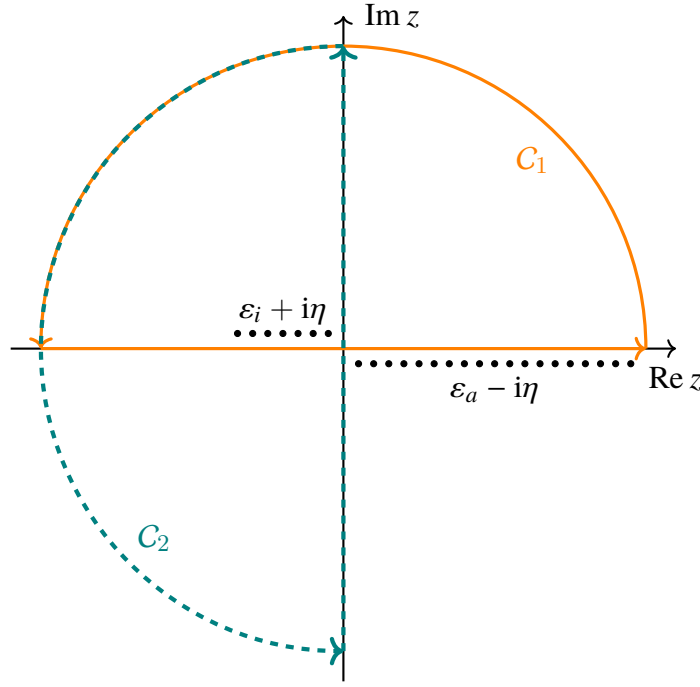


Figure 8.2: Two contours in the complex plane, which enclose the occupied orbitals ε_i . The contour C_2 is obtained by a rotation of C_1 .

along the path C_1 (Fig. 8.2),

$$\begin{aligned} \int_{-\infty}^{\infty} \frac{d\omega}{2\pi} \frac{1}{\omega - \varepsilon_i - i\eta} e^{-i\omega t} &= \theta(-t) \oint_{C_1} \frac{dz}{2\pi} \frac{1}{z - \varepsilon_i - i\eta} e^{-izt} \\ &= i \theta(-t) e^{-i\varepsilon_i t} . \end{aligned} \quad (8.70)$$

Here, $\theta(-t)$ arises from the fact that the integral vanishes if the contour is closed in the lower half-plane. In addition, we find that the path C_2 also encloses all occupied energies ε_i , hence, a transformation using C_2 would cover exactly the same information as C_1 . Note that C_2 is simply a rotation of C_1 , called Wick rotation. Both paths, C_1 and C_2 require the analytic continuation of the integrand $(\omega - \varepsilon_i - i\eta)^{-1} \rightarrow (z - \varepsilon_i - i\eta)^{-1}$. However, the C_2 contour exists only if e^{-izt} is finite along C_2 , i.e. if t has a positive imaginary part ($-it > 0$). Hence, the analytic continuation has to be performed also for t , i.e. we have to consider t as a complex number. Since nothing prevents us from doing so, we can calculate,

$$\theta(-it) \oint_{C_2} \frac{dz}{2\pi} \frac{1}{z - \varepsilon_i - i\eta} e^{-izt} = i \theta(-it) e^{-i\varepsilon_i t} . \quad (8.71)$$

Moreover, the integrand is nonvanishing only along $z \in (-i\infty, +i\infty)$, hence we can also write

$$\begin{aligned} i\theta(-it)e^{-i\varepsilon_i t} &= \theta(-it) \int_{-i\infty}^{i\infty} \frac{d\omega}{2\pi} \frac{1}{\omega - \varepsilon_i - i\eta} e^{-i\omega t} \\ &= \theta(-it) \int_{-\infty}^{\infty} \frac{d\nu}{2\pi} \frac{i}{i\nu - \varepsilon_i - i\eta} e^{\nu t}, \end{aligned} \quad (8.72)$$

where we substituted $\nu = -i\omega$ in the last step. If we, furthermore, introduce the substitution $\tau = it$, we arrive at

$$\theta(-\tau)e^{-\varepsilon_i \tau} = \theta(-\tau) \int_{-\infty}^{\infty} \frac{d\nu}{2\pi} \frac{1}{i\nu - \varepsilon_i - i\eta} e^{-i\nu\tau}. \quad (8.73)$$

Note, that the assumption of an imaginary time t leads to purely real valued τ and ν . This procedure is called Wick rotation and we can complement the Fourier pair

$$(t, \omega): \quad \frac{1}{\omega - \varepsilon_i - i\eta} \leftrightarrow i\theta(-t)e^{-i\varepsilon_i t} \quad (8.74)$$

with

$$(\tau, \nu): \quad \frac{1}{i\nu - \varepsilon_i - i\eta} \leftrightarrow \theta(-\tau)e^{-\varepsilon_i \tau} \quad (8.75)$$

A similar derivation holds for the terms with the unoccupied energies ε_a , leading to the pairs

$$(t, \omega): \quad \frac{1}{\omega - \varepsilon_a + i\eta} \leftrightarrow -i\theta(t)e^{-i\varepsilon_a t} \quad (8.76)$$

and

$$(\tau, \nu): \quad \frac{1}{i\nu - \varepsilon_a + i\eta} \leftrightarrow -\theta(\tau)e^{-\varepsilon_a \tau} \quad (8.77)$$

Altogether, the Green's function in imaginary time results in

$$\begin{aligned} G(\mathbf{x}, \mathbf{x}', \tau) &= \int_{-\infty}^{\infty} \frac{d\nu}{2\pi} G(\mathbf{x}, \mathbf{x}', i\nu) e^{-i\nu\tau} \\ &= \theta(-\tau) \sum_i \chi_i(\mathbf{x}) \chi_i^*(\mathbf{x}') e^{-\varepsilon_i \tau} - \theta(\tau) \sum_a \chi_a(\mathbf{x}) \chi_a^*(\mathbf{x}') e^{-\varepsilon_a \tau}, \end{aligned} \quad (8.78)$$

which is equivalent to (8.63).

In summary, the Laplace transform (8.57) provides a simple and convenient bridge between the orbital based formulation and the Green's function based formulation of the MP2 energy. More general, it provides a bridge between Feynman diagrams and Goldstone diagrams.

8.2 Adiabatic connection and fluctuation-dissipation

In this section we provide an alternative approach to approximate the correlation energy. First, we derive an exact expression of the correlation energy in terms of the so called response function, employing the adiabatic-connection fluctuation-dissipation theorem (ACFDT). Second, we present schemes to approximate the response function, leading to the random phase approximation. We will use the random phase approximation to calculate the pressure-temperature phase diagram of lead selenide in Chap. 13.

The adiabatic connection

The adiabatic connection links a mean field Hamiltonian with the exact many-electron Hamiltonian. This is achieved by a set of Hamiltonians $\{H_\lambda | \lambda \in [0, 1]\}$ such that $H_{\lambda=1} = H_e$ is the full electronic Hamiltonian from Eq. (2.15),

$$H_{\lambda=1} = T_e + V_{\text{ext}} + V_{\text{ee}} , \quad (8.79)$$

where $V_{\text{ext}} = V_{\text{nn}} + V_{\text{ne}}$, and $H_{\lambda=0}$ represents a mean field Hamiltonian, i.e. the one-electron DFT Hamiltonian of Eq. (6.17), summed over all electrons,

$$\begin{aligned} H_{\lambda=0} &= \sum_{i=1}^N \left(-\frac{1}{2} \nabla_i^2 + V_{\text{ext}}(\mathbf{r}_i) + \int d^3r' \frac{n(\mathbf{r}')}{|\mathbf{r}_i - \mathbf{r}'|} + v_{\text{xc}}(\mathbf{r}_i) \right) \\ &= T_e + V_{\text{ext}} + V_{\text{KS}} , \end{aligned} \quad (8.80)$$

where KS stands for Kohn-Sham. It is convenient to connect the Hamiltonians in the following way,

$$H_\lambda = T_e + V_{\text{ext}} + \lambda V_{\text{ee}} + V_\lambda , \quad (8.81)$$

where V_λ is a purely local potential, such that $V_{\lambda=0} = V_{\text{KS}}$ and $V_{\lambda=1} = 0$. For each λ we formally define the ground state $|\Phi_\lambda\rangle$ and the ground state energy E_λ by

$$H_\lambda |\Phi_\lambda\rangle = E_\lambda |\Phi_\lambda\rangle . \quad (8.82)$$

Since the Kohn-Sham equations (6.17) are solvable, we can construct the ground state $|\Phi_{\lambda=0}\rangle$ as the Slater-determinant of the Kohn-Sham orbitals φ_i ,

$$|\Phi_0\rangle = \mathcal{A} |\varphi_1 \dots \varphi_N\rangle , \quad (8.83)$$

where \mathcal{A} is the antisymmetrization operator, as defined in Eq. (3.8). In analogy to Eq. (5.5) we now define the desired quantity, the correlation energy by

$$E_c = \langle \Phi_1 | H_1 | \Phi_1 \rangle - \langle \Phi_0 | H_1 | \Phi_0 \rangle = E_1 - \langle \Phi_0 | H_1 | \Phi_0 \rangle , \quad (8.84)$$

i.e. as the difference between the exact many-electron ground state energy E_1 and the expectation value of the exact many-electron Hamiltonian in the DFT ground state, $\langle \Phi_0 | H_1 | \Phi_0 \rangle$.

Note, that the latter is accessible and is sometimes incorrectly called Hartree-Fock energy, due to its formal equivalence to the Hartree-Fock energy of Eq. (4.3),

$$\langle \Phi_0 | H_1 | \Phi_0 \rangle = \sum_{i=1}^N \left(-\frac{1}{2} \langle \varphi_i | \nabla_i^2 | \varphi_i \rangle + \langle \varphi_i | V_{\text{ext}} | \varphi_i \rangle \right) \quad (8.85)$$

$$+ \frac{1}{2} \sum_{i,j=1}^N \left(\langle \varphi_i \varphi_j | r_{12}^{-1} | \varphi_i \varphi_j \rangle - \langle \varphi_i \varphi_j | r_{12}^{-1} | \varphi_j \varphi_i \rangle \right), \quad (8.86)$$

however, here, the orbitals are solutions of the Kohn-Sham equations. We can derive a useful equation for the correlation energy E_c , by employing the Hellmann-Feynman theorem [47],

$$\frac{dE_\lambda}{d\lambda} = \left\langle \Phi_\lambda \left| \frac{dH_\lambda}{d\lambda} \right| \Phi_\lambda \right\rangle, \quad (8.87)$$

allowing for the following formulation,

$$\begin{aligned} E_c &= E_1 - \langle \Phi_0 | H_1 | \Phi_0 \rangle = E_1 - \langle \Phi_0 | H_0 | \Phi_0 \rangle - \langle \Phi_0 | H_1 - H_0 | \Phi_0 \rangle \\ &= E_1 - E_0 - \langle \Phi_0 | V_{\text{ee}} - V_{\text{KS}} | \Phi_0 \rangle = \int_0^1 d\lambda \frac{dE_\lambda}{d\lambda} - \langle \Phi_0 | V_{\text{ee}} - V_{\text{KS}} | \Phi_0 \rangle \\ &= \int_0^1 d\lambda \left\langle \Phi_\lambda \left| \frac{dH_\lambda}{d\lambda} \right| \Phi_\lambda \right\rangle - \langle \Phi_0 | V_{\text{ee}} - V_{\text{KS}} | \Phi_0 \rangle \\ &= \int_0^1 d\lambda \left\langle \Phi_\lambda \left| V_{\text{ee}} + \frac{dV_\lambda}{d\lambda} \right| \Phi_\lambda \right\rangle - \langle \Phi_0 | V_{\text{ee}} - V_{\text{KS}} | \Phi_0 \rangle. \end{aligned} \quad (8.88)$$

In accordance with the original work [48], we require, that the one-electron density is constant along the connection $\lambda \in [0, 1]$. For $\lambda = 0$, this strong assumption is met by the exact DFT Hamiltonian using the exact exchange-correlation potential v_{xc} . In practice, however, exact agreement is never fully reached. A constant density implies

$$\begin{aligned} \int_0^1 d\lambda \left\langle \Phi_\lambda \left| \frac{dV_\lambda}{d\lambda} \right| \Phi_\lambda \right\rangle &= \int_0^1 d\lambda \int d^3r n(\mathbf{r}) \frac{dV_\lambda(\mathbf{r})}{d\lambda} \\ &= \int d^3r n(\mathbf{r}) [V_1(\mathbf{r}) - V_0(\mathbf{r})] \\ &= -\langle \Phi_0 | V_{\text{KS}} | \Phi_0 \rangle, \end{aligned} \quad (8.89)$$

since $V_1 = 0$. Finally, we find for the correlation energy

$$\begin{aligned} E_c &= \int_0^1 d\lambda \langle \Phi_\lambda | V_{\text{ee}} | \Phi_\lambda \rangle - \langle \Phi_0 | V_{\text{ee}} | \Phi_0 \rangle \\ &= \frac{1}{2} \int_0^1 d\lambda \int d^3r \int d^3r' \frac{P_\lambda(\mathbf{r}, \mathbf{r}') - P_0(\mathbf{r}, \mathbf{r}')}{|\mathbf{r} - \mathbf{r}'|}, \end{aligned} \quad (8.90)$$

where we have used the pair density

$$P_\lambda(\mathbf{r}, \mathbf{r}') = N(N-1) \int d^3r_3 \dots \int d^3r_N |\Phi_\lambda(\mathbf{r}, \mathbf{r}', \mathbf{r}_3, \dots, \mathbf{r}_N)|^2, \quad (8.91)$$

which is clearly unknown for the fully interacting Hamiltonian, $\lambda = 1$. Although Eq. (8.90) may seem to have no advantage, it is a convenient starting point for the fluctuation-dissipation theorem.

The fluctuation-dissipation theorem

The fluctuation-dissipation theorem provides a link between the pair density and the response function, which will be introduced. The theorem states, that internal density fluctuations have the same effect as small external perturbations [49]. Small perturbations, however, are treated with the response function, for which approximations schemes are available.

First, we introduce the density fluctuation operator,

$$\delta\hat{n}(\mathbf{r}) = \hat{n}(\mathbf{r}) - n(\mathbf{r}), \quad (8.92)$$

which is the difference between the density operator,

$$\hat{n}(\mathbf{r}) = \sum_{i=1}^N \delta(\mathbf{r} - \hat{\mathbf{r}}_i), \quad (8.93)$$

and the electron density, $n(\mathbf{r})$, being the expectation value of $\hat{n}(\mathbf{r})$,

$$n(\mathbf{r}) = \langle \Phi_\lambda | \hat{n}(\mathbf{r}) | \Phi_\lambda \rangle = N \int d^3r_2 \dots \int d^3r_N |\Phi_\lambda(\mathbf{r}, \mathbf{r}_2, \dots, \mathbf{r}_N)| \quad \forall \lambda. \quad (8.94)$$

Note, that the electron density is kept constant along the connection λ . Using these definitions, we can rewrite the pair density as

$$P_\lambda(\mathbf{r}, \mathbf{r}') = \langle \Phi_\lambda | \hat{n}(\mathbf{r}) \hat{n}(\mathbf{r}') | \Phi_\lambda \rangle - \delta(\mathbf{r} - \mathbf{r}') n(\mathbf{r}), \quad (8.95)$$

or, equivalently, as

$$P_\lambda(\mathbf{r}, \mathbf{r}') = \langle \Phi_\lambda | \delta\hat{n}(\mathbf{r}) \delta\hat{n}(\mathbf{r}') | \Phi_\lambda \rangle + n(\mathbf{r}) n(\mathbf{r}') - \delta(\mathbf{r} - \mathbf{r}') n(\mathbf{r}). \quad (8.96)$$

Plugging Eq. (8.96) into (8.90) leads to a formulation of the correlation energy in terms of density fluctuations (note again that the density is assumed to be constant along λ),

$$E_c = \frac{1}{2} \int_0^1 d\lambda \int d^3r \int d^3r' \frac{\langle \Phi_\lambda | \delta\hat{n}(\mathbf{r}) \delta\hat{n}(\mathbf{r}') | \Phi_\lambda \rangle - \langle \Phi_0 | \delta\hat{n}(\mathbf{r}) \delta\hat{n}(\mathbf{r}') | \Phi_0 \rangle}{|\mathbf{r} - \mathbf{r}'|}. \quad (8.97)$$

At this point, we can link the fluctuations (the term $\langle \Phi_\lambda | \delta\hat{n}(\mathbf{r}) \delta\hat{n}(\mathbf{r}') | \Phi_\lambda \rangle$) with the so

called *response function* (describing the response of the system to an external potential, i.e. dissipation). Even if the connection between response and correlation energy is not clear at first, we will soon arrive at an expression for the correlation energy using the response function. The response function is commonly defined as the variation of the density with respect to the external potential, which we now generalize to a time-dependent potential, $v_{\text{ext}}(\mathbf{r}, t)$, allowing for time-dependent perturbations like varying electric or magnetic fields,

$$\chi_{\lambda}(\mathbf{r}, \mathbf{r}', t - t') := \frac{\delta n_{\lambda}(\mathbf{r}, t)}{\delta v_{\text{ext}}(\mathbf{r}', t')} . \quad (8.98)$$

Clearly, the density inherits the time-dependency from the external potential. An explicit form of $\chi_{\lambda}(\mathbf{r}, \mathbf{r}', t - t')$ is known from linear response theory (see e.g. the Fourier transform of Eq. (2.24) and its derivation in Ref. [50]),

$$\chi_{\lambda}(\mathbf{r}, \mathbf{r}', t) = -i \langle \Phi_{\lambda} | \mathcal{T} \delta \hat{n}_{\lambda}(\mathbf{r}, t) \delta \hat{n}_{\lambda}(\mathbf{r}', 0) | \Phi_{\lambda} \rangle . \quad (8.99)$$

Here \mathcal{T} is the time ordering operator (later times right) and the time dependent density operator is simply given by the density operator in the Heisenberg picture,

$$\hat{n}_{\lambda}(\mathbf{r}, t) = e^{iH_{\lambda}t} \hat{n}(\mathbf{r}) e^{-iH_{\lambda}t} . \quad (8.100)$$

By comparing (8.99) with (8.97) we find,

$$E_{\text{c}} = -\frac{1}{2} \int_0^1 d\lambda \int d^3r \int d^3r' \frac{i\chi_{\lambda}(\mathbf{r}, \mathbf{r}', 0^-) - i\chi_0(\mathbf{r}, \mathbf{r}', 0^-)}{|\mathbf{r} - \mathbf{r}'|} . \quad (8.101)$$

Conventionally, the correlation energy is expressed in terms of the response function in imaginary frequency, $\chi_{\lambda}(\mathbf{r}, \mathbf{r}', \nu)$, which can be obtained using the Wick rotation, as introduced previously. We find the

correlation energy in the ACFDT framework,

$$E_{\text{c}} = -\frac{1}{2} \int_0^1 d\lambda \int_{-\infty}^{\infty} \frac{d\nu}{2\pi} \int d^3r \int d^3r' \frac{\chi_{\lambda}(\mathbf{r}, \mathbf{r}', \nu) - \chi_0(\mathbf{r}, \mathbf{r}', \nu)}{|\mathbf{r} - \mathbf{r}'|} . \quad (8.102)$$

In the next chapter, we will derive a practical approximation for the response function χ_{λ} , in order to calculate the correlation energy in the ACFDT formulation.

8.3 The random phase approximation

What is still missing to calculate the correlation energy, is a practical scheme to treat the λ dependent response function χ_{λ} . Such a scheme is given by the time-dependent density functional theory (TDDFT). An introduction to TDDFT is far beyond the scope of this thesis, hence, we restrict to one of the main results. The mean field response function χ_0

and the full interacting one, χ_λ , are connected by a Dyson like equation [51],

$$\chi_\lambda(\mathbf{r}_1, \mathbf{r}_2, \nu) = \chi_0(\mathbf{r}_1, \mathbf{r}_2, \nu) + \int d^3r_3 \int d^3r_4 \chi_0(\mathbf{r}_1, \mathbf{r}_3, \nu) \left[\frac{\lambda}{|\mathbf{r}_3 - \mathbf{r}_4|} + f_\lambda^{\text{xc}}(\mathbf{r}_3, \mathbf{r}_4, \nu) \right] \chi_\lambda(\mathbf{r}_4, \mathbf{r}_2, \nu), \quad (8.103)$$

where the so called *exchange-correlation kernel* f_λ^{xc} accounts for the exact connection. In terms of operators, we can rewrite this equation as

$$\chi(\nu) = \chi_0(\nu) + \chi_0(\nu) [\lambda \hat{r}_{12}^{-1} + f_\lambda^{\text{xc}}(\nu)] \chi_\lambda(\nu). \quad (8.104)$$

In passing, we mention that for $\lambda = 0$ (here, the DFT case) the exchange correlation kernel is given by the change of the exchange correlation potential with respect to the density,

$$f_0^{\text{xc}}(\mathbf{r}, \mathbf{r}', \tau - \tau') = \frac{\delta v_{\text{xc}}(\mathbf{r}, \tau)}{\delta n(\mathbf{r}', \tau')}. \quad (8.105)$$

Since TDDFT considers time-dependent Hamiltonians, also the exchange-correlation potential inherits the time-dependency (i.e. frequency dependency in Fourier space). The random phase approximation (RPA) is obtained by simply neglecting the exchange-correlation kernel,

$$\chi_\lambda(\nu) \approx \chi_0(\nu) + \chi_0(\nu) \lambda \hat{r}_{12}^{-1} \chi_\lambda(\nu), \quad (8.106)$$

which, after infinite iterations, leads to

$$[\chi_\lambda(\nu) - \chi_0(\nu)] \hat{r}_{12}^{-1} \approx \sum_{k=2}^{\infty} \lambda^{k-1} [\chi_0(\nu) \hat{r}_{12}^{-1}]^k. \quad (8.107)$$

We can, thus, rewrite Eq. (8.102) as

$$E_c \approx E_c^{\text{RPA}} = -\frac{1}{2} \int_0^1 d\lambda \int_{-\infty}^{\infty} \frac{d\nu}{2\pi} \text{tr} \left[\sum_{k=2}^{\infty} \lambda^{k-1} [\chi_0(\nu) \hat{r}_{12}^{-1}]^k \right], \quad (8.108)$$

where tr stands for the trace. The λ integration can now be performed explicitly and results in

$$E_c^{\text{RPA}} = -\frac{1}{2} \int_{-\infty}^{\infty} \frac{d\nu}{2\pi} \text{tr} \left[\sum_{k=2}^{\infty} \frac{1}{k} [\chi_0(\nu) \hat{r}_{12}^{-1}]^k \right]. \quad (8.109)$$

Furthermore, the sum can be rewritten in terms of the natural logarithm,

$$\sum_{k=2}^{\infty} \frac{1}{k} [\chi_0(\nu) \hat{r}_{12}^{-1}]^k = \sum_{k=1}^{\infty} \frac{1}{k} [\chi_0(\nu) \hat{r}_{12}^{-1}]^k - \chi_0(\nu) \hat{r}_{12}^{-1} = -\ln \left(1 - \chi_0(\nu) \hat{r}_{12}^{-1} \right) - \chi_0(\nu) \hat{r}_{12}^{-1}, \quad (8.110)$$

leading to the formula of the

correlation energy in the random phase approximation

$$E_c^{\text{RPA}} = \frac{1}{2} \int_{-\infty}^{\infty} \frac{d\nu}{2\pi} \text{tr} \left[\ln \left(1 - \chi_0(\nu) \hat{r}_{12}^{-1} \right) + \chi_0(\nu) \hat{r}_{12}^{-1} \right] . \quad (8.111)$$

The explicit form of χ_0 in the real space basis can be calculated straightforward using (8.99) and reads

$$\chi_0(\mathbf{r}, \mathbf{r}', \nu) = \sum_i^{\text{occ.}} \sum_a^{\text{unocc.}} \left[\frac{\varphi_i^*(\mathbf{r}) \varphi_i(\mathbf{r}') \varphi_a^*(\mathbf{r}') \varphi_a(\mathbf{r})}{\varepsilon_a - \varepsilon_i - i\nu} + \text{c.c.} \right] \quad (8.112)$$

where the φ 's and ε 's are the DFT orbitals and orbital energies, respectively. A detailed derivation can be found in Ref. [50].

Another convenient formulation of the RPA correlation energy makes use of the screened interaction $W(\nu)$. At the RPA level we can define $W(\nu)$ by

$$\begin{aligned} W(\nu) &= \hat{r}_{12}^{-1} \sum_{k=2}^{\infty} \frac{1}{k} \left[\chi_0(\nu) \hat{r}_{12}^{-1} \right]^{k-2} \\ &= \frac{1}{2} \hat{r}_{12}^{-1} + \frac{1}{3} \hat{r}_{12}^{-1} \chi_0(\nu) \hat{r}_{12}^{-1} + \frac{1}{4} \hat{r}_{12}^{-1} \chi_0(\nu) \hat{r}_{12}^{-1} \chi_0(\nu) \hat{r}_{12}^{-1} + \dots \\ &= -\hat{r}_{12}^{-1} \left(\chi_0(\nu) \hat{r}_{12}^{-1} \right)^{-2} \left[\chi_0(\nu) \hat{r}_{12}^{-1} + \ln \left(1 - \chi_0(\nu) \hat{r}_{12}^{-1} \right) \right] . \end{aligned} \quad (8.113)$$

Mathematically, the screened interaction $W(\nu)$ can easily be found in Eq. (8.109), allowing for the formulation

$$E_c^{\text{RPA}} = -\frac{1}{2} \int_{-\infty}^{\infty} \frac{d\nu}{2\pi} \text{tr} \left[\chi_0(\nu) \hat{r}_{12}^{-1} \chi_0(\nu) W(\nu) \right] . \quad (8.114)$$

Indeed, the RPA approach covers electron screening effects in materials. The series in Eq. (8.113) can be interpreted as an effective interaction, which takes internal correlations of the electrons into account. Interactions of far distant regions are, thus, not described by the bare Coulomb interaction, but by the effective screened interaction, including the intermediate reordering of the electrons (described by the response function).

8.4 RPA with exchange: second-order screened exchange

Using formulation (8.114) of the RPA correlation energy, an analogy with the direct MP2 correlation energy can be established, which can then be extended to an exchange-like expression. For brevity, this section only provides a schematic view. First, we realize that the response function (8.112) can also be written as a product of two Green's functions

(8.63) at the mean field level,

$$\chi_0(\mathbf{r}, \mathbf{r}', \tau) = G(\mathbf{r}, \mathbf{r}', \tau)G(\mathbf{r}', \mathbf{r}, -\tau). \quad (8.115)$$

A proof can be found in Ref. [35]. In terms of diagrams, one could sketch the RPA correlation energy (8.114) as

$$E_c^{\text{RPA}} = \text{Diagram}, \quad (8.116)$$

where the thick wiggly line represents the screened interaction $W(\nu)$. According to Eq. (8.113), the screened interactions can be written as

$$\text{wiggly} = \frac{1}{2} \text{wavy} + \frac{1}{3} \text{wavy} \text{---} \text{loop} \text{---} \text{wavy} + \frac{1}{4} \text{wavy} \text{---} \text{loop} \text{---} \text{loop} \text{---} \text{wavy} + \dots \quad (8.117)$$

If we apply the simple rule of Sec. 7.3, to check whether the random phase approximation meets the symmetrization postulate, we find that all exchange diagrams are missing. Replacing any vertex by its exchange counterpart leads to a new diagram which is not part of the RPA. In analogy to the MP2 diagrams, some of the missing exchange could be introduced by considering a diagram like

$$\text{Diagram}, \quad (8.118)$$

This leads to the so called *second-order screened exchange* (SOSEX) correction of the RPA as introduced by Grüneis et al. [52]. We will skip a detailed derivation and refer to Ref. [18, 52, 53, 54]. The final result has a similar form as the exchange part of the MP2 energy (see Eq. 8.20) and reads,

$$E^{\text{SOSEX}} = \frac{1}{2} \int_{-\infty}^{\infty} \frac{d\nu}{2\pi} \sum_{ij}^{\text{occ.}} \sum_{ab}^{\text{unocc.}} \frac{2(\varepsilon_a - \varepsilon_i)}{(\varepsilon_a - \varepsilon_i)^2 + \nu^2} \frac{2(\varepsilon_b - \varepsilon_j)}{(\varepsilon_b - \varepsilon_j)^2 + \nu^2} \times \langle \varphi_j \varphi_i | r_{12}^{-1} | \varphi_a \varphi_b \rangle \langle \varphi_a \varphi_b | W(\nu) | \varphi_i \varphi_j \rangle. \quad (8.119)$$

This expression becomes the exchange MP2 energy (8.20), when replacing $W(\nu)$ by its lowest order term, $\frac{1}{2}r_{12}^{-1}$, and integrating over ν , since

$$\int_{-\infty}^{\infty} \frac{d\nu}{2\pi} \frac{2(\varepsilon_a - \varepsilon_i)}{(\varepsilon_a - \varepsilon_i)^2 + \nu^2} \frac{2(\varepsilon_b - \varepsilon_j)}{(\varepsilon_b - \varepsilon_j)^2 + \nu^2} = -\frac{2}{\varepsilon_i + \varepsilon_j - \varepsilon_a - \varepsilon_b}. \quad (8.120)$$

In this thesis, the SOSEX correction to the RPA is not used in practice. However, SOSEX is introduced to demonstrate the development of low-complexity algorithms. This can be found in Sec. 10.2.

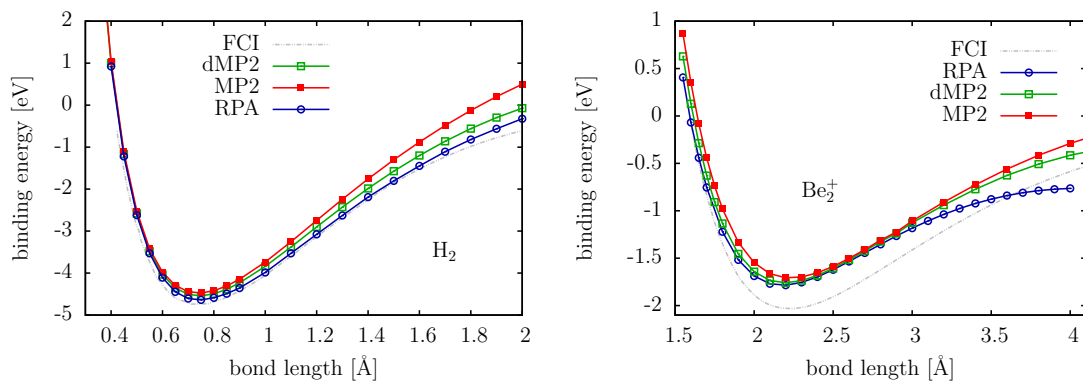


Figure 8.3: Dissociation of the diatomic molecules H_2 and Be_2^+ into 2H and $\text{Be}+\text{Be}^+$, respectively. As an "exact" reference we chose full configuration interaction (FCI) calculations from [18, 55]. We performed spin-polarized calculations for the molecules and the isolated atoms, except for H_2 , where spin-restriction was assumed. We used a cell size of $10 \times 8 \times 8 \text{ \AA}^3$ and a cutoff of 350 eV for H_2 and $16 \times 12 \times 12 \text{ \AA}^3$, and 300 eV for Be_2^+ . The PAW potentials were chosen with an outmost cutoff radius of 1.1 Å (H) and 1.9 Å (Be).

8.5 Illustrative MP2 and RPA calculations for molecules and solids

Even for the correlation energy methods like MP2 and RPA, the calculation of dissociation curves of simple dimers remains a great difficulty. In particular the dissociation limit requires to cover static correlations. Again, as HF and DFT, both MP2 and RPA fail to predict the correct dissociation of the H_2 molecule (left graph in Fig. 8.3). Both energy curves first push through the zero binding energy line at intermediate distances (at about 2 Å) and then turn around again (this can be seen in Ref. [18]). Interestingly, the RPA method predicts the correct dissociation limit, i.e. approaches zero again¹. For the dissociation of Be_2^+ both MP2 and RPA improve upon the bond length compared to the HF method (right graph in Fig. 8.3). Here, MP2 is almost identical to the reference method (FCI) except for an almost constant energy shift. This can be seen in in Fig. 8.4. Interestingly, the RPA fails badly in the dissociation limit, predicting a binding energy which is off by about 50%. A similar but weaker behavior can be read from the direct MP2 energy (dMP2). One tends to conclude that this error is originated by the missing exchange, since the MP2 curve (including the second order exchange contribution) perfectly resembles the slope of the reference curve. This, however, would imply that exchange is not only important for very local, i.e. short-range effects. A similar deviation between MP2 and dMP2 can be recognized for the H_2 dimer at intermediate distances. For a deeper investigation, a molecular code is preferable since dissociation

¹But only if spin-unrestricted calculations are performed, corresponding to an unphysical Slater determinant with an up orbital on one site and a down orbital on the other site.

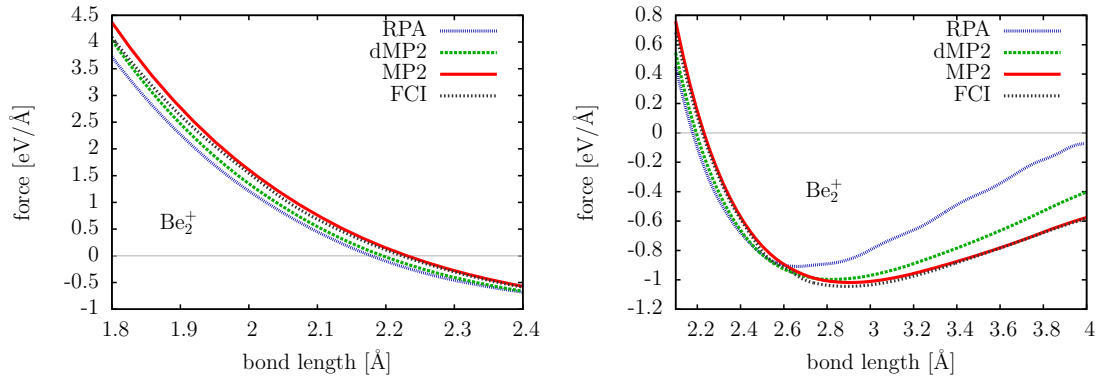


Figure 8.4: Negative derivative of the Be_2^+ energy dissociation curves from Fig. 8.3. The MP2 curve perfectly matches the reference curve from 2 to 4 Å. Both RPA and dMP2 possess a less consistency with the reference curve and deviate significantly from a distance of 2.6 Å onward, indicating a wrong prediction of the dissociation limit.

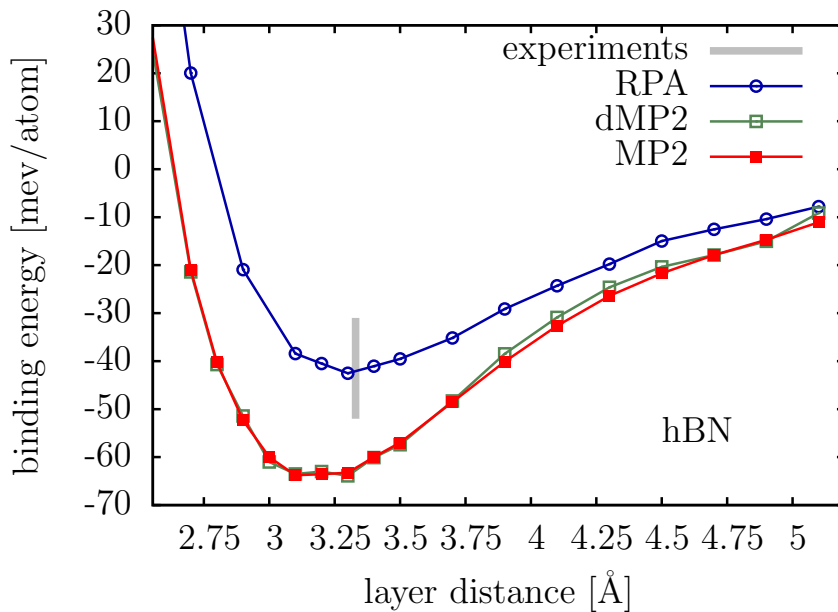


Figure 8.5: Calculation of the binding energy of the hexagonal layers of boron nitride using RPA and MP2 (dMP2 refers to the direct MP2 contribution, neglecting the exchange part). The computational settings are given by a plane-wave cutoff of 500 eV and a k -point mesh of $6 \times 6 \times 2$ points to sample the Brillouine zone. The energy scale was shifted such that 0 meV/atom corresponds to a single layer (or infinitely separated layers) of hBN. The experimental values can be found in [21] and references therein.

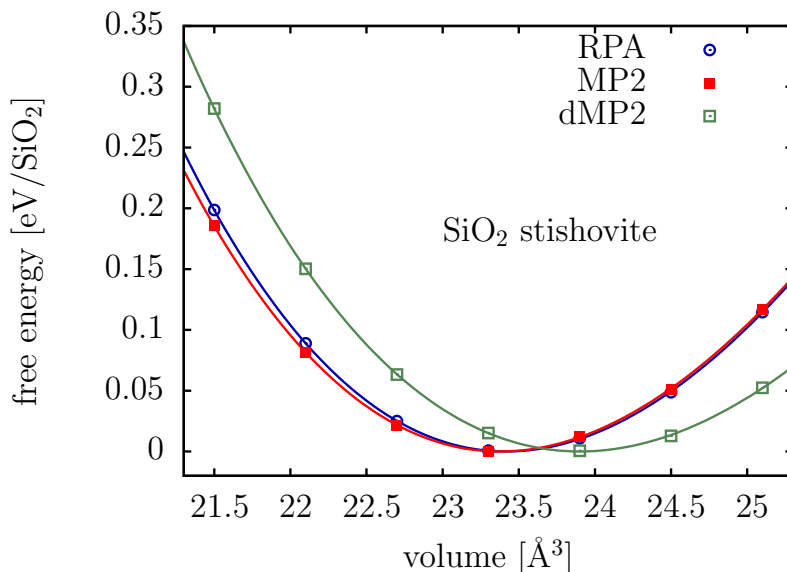


Figure 8.6: Free energy of the SiO_2 stishovite structure. The free energies are shifted such that the minima of all methods coincide. We performed spin-unpolarized calculations with a $3 \times 3 \times 5$ k -points mesh and a cutoff of 500 eV. The c/a ratio was fixed to the experimental value [56] of 0.638. The solid lines are Birch-Murnaghan fits [22].

calculations with VASP require large supercells to avoid interactions with the periodic images of the atoms, making the calculations fairly expensive.

A reverse picture is obtained for the binding energy of the layers of hexagonal boron nitride (Fig. 8.5). Here the RPA perfectly matches the experimental values. But also MP2 can be considered as a reliable method, that predicts a reasonable layer distance, although the binding energy is clearly overestimated.

Another example to show the difference between MP2 and direct MP2 is depicted in Fig 8.6. Here, the RPA and MP2 almost perfectly coincide (except for a constant shift which is not visible in Fig. 8.6). However, going from dMP2 to MP2 (i.e. adding the exchange term) changes the equilibrium volume from 23.90 to 23.38 Å, where the experimental value [56] is given by 23.26 Å. This also holds for the atomization energy of stishovite SiO_2 , given by a experimental value of 18.71 eV/ SiO_2 . In the calculations we find 17.89, 20.44, 21.08 eV/ SiO_2 with RPA, MP2, dMP2, respectively. The Hartree-Fock method results in an equilibrium volume of 22.70 Å³ and a atomization energy of 12.82 eV/ SiO_2 , indicating significant correlation effects.

Note that all presented MP2 and RPA results ignore the head and wing contribution as described in Sec. 8.1.3. This is due to the fact that this contribution was not yet implemented in the low-scaling LTMP2 code from Chap. 10.1. However, simple cross-checking with the RPA (where those contributions were available) revealed that they can safely be neglected. Regarding the molecules, this can be understood by the large supercells, leading to fine reciprocal grids, which sampled head and wing sufficiently

accurate. For the periodic systems, neglecting head and wing required finer k -point grids and lead to the somewhat unsmooth but acceptable energy curves.

Part II

Low-complexity algorithms for the correlation energy

CHAPTER 9

Overview of the developed algorithms

In this part of the thesis, the core of the research work is presented. We will introduce six newly developed algorithms which reduce the computational complexity of correlation energy calculations, with a special attention to the exchange contributions. Three of them are *deterministic* (Chap. 10) and are distinguished from another three algorithms which are based on *stochastic* techniques (Chap. 11). As benchmark methods, we employed MP2 and SOSEX. For a better overview, we will briefly describe the techniques below.

Quartic scaling MP2 for periodic systems

Sec. 10.1 on page 103

This implementation is the first proof, that MP2 calculations can be performed with a quartic scaling, without introducing approximations. The complexity is reduced by pure analytic reformulations based on the Laplace transformed version of the MP2 correlation energy, Eq. (8.59) and (8.60). The corresponding publication [41] was awarded the *Editors' Choice Collection 2017* of the *Journal of Chemical Physics*.

Quartic scaling SOSEX for periodic systems

Sec. 10.2 on page 118

In this section we formally demonstrate that also the SOSEX correction to the RPA can be evaluated with a quartic scaling computer code. Similar steps as for the quartic scaling MP2 algorithm are applied. The presented scheme was not yet implemented and serves as a technical instruction for future implementations.

Cubic scaling MP2

Sec. 10.3 on page 122

The possibility of a cubic scaling MP2 algorithm is demonstrated. This section can be considered as an illustration that very careful analytical considerations can lead to surprising improvements of the scaling behavior of algorithms. The presented MP2 scheme possesses the same scaling as DFT calculations. We also stress the limitations of the presented approach.

Real space Monte Carlo sampling of Feynman diagrams

Sec. 11.1 on page 126

Translating Feynman diagrams of the correlation energy into the real space basis, allows for Monte Carlo integrations. For the MP2 correlation energy, this was derived in Eq. (8.66) and (8.67). In this work we present new and fundamentally enhanced importance sampling functions, which reduce the sampling variance, such that fast and accurate MP2 calculations of large systems become possible.

Periodic MP2 with stochastic orbitals

Sec. 11.2 on page 139

One bottleneck of MP2 energy calculations is the tremendous amount of possible occupied-unoccupied pairs. In this implementation, we stochastically average the occupied and unoccupied manifold, leading to a code that can sample the MP2 energy with significantly fewer stochastic occupied-unoccupied pairs. The highly parallelized algorithm is especially useful for large systems, where only the relative statistical error per electron is of interest.

Electron-repulsion integrals in a random basis

Sec. 11.3 on page 156

Correlation energy methods like MP2 or RPA often suffer from a slow convergence with respect to the basis set size. In particular, this is true for the plane-wave basis. However, it is known, that this problem can be eased by choosing a proper basis, like natural orbitals. In this code we present the effect of a random basis, which replaces the plane-wave basis for the evaluation of electron-repulsion integrals.

CHAPTER 10

Deterministic algorithms

10.1 Quartic scaling MP2 for periodic systems

We present a low-complexity algorithm to calculate the correlation energy of periodic systems in second-order Møller-Plesset perturbation theory (MP2). In contrast to previous approximation-free MP2 codes, our implementation possesses a quartic scaling, $\mathcal{O}(N^4)$, with respect to the system size N and offers an almost ideal parallelization efficiency. The general issue that the correlation energy converges slowly with the number of basis functions is eased by an internal basis set extrapolation. The key concept to reduce the scaling is to eliminate all summations over virtual orbitals which can be elegantly achieved in the Laplace transformed MP2 (LTMP2) formulation using plane wave basis sets and Fast Fourier transforms. The method is implemented in the Vienna ab-initio simulation package (VASP) [57, 11]. This section largely follows the author's peer reviewed publication [41].

10.1.1 Reducing the computational cost

The strategy

The summation over the unoccupied states is a major obstacle in MP2 calculations. As can be seen from Eq. (8.60), the MP2 energy involves the following summation,

$$\sum_{ab}^{\text{unocc.}} \langle \chi_i^\tau \chi_j^\tau | r_{12}^{-1} | \chi_a^\tau \chi_b^\tau \rangle \langle \chi_a^\tau \chi_b^\tau | r_{12}^{-1} | \chi_j^\tau \chi_i^\tau \rangle. \quad (10.1)$$

If we formally define a bipartite state

$$|\Psi_{ji}^\tau\rangle = \sum_{ab}^{\text{unocc.}} \langle \chi_a^\tau \chi_b^\tau | r_{12}^{-1} | \chi_j^\tau \chi_i^\tau \rangle | \chi_a^\tau \chi_b^\tau \rangle, \quad (10.2)$$

we can hide the expensive summation and write

$$\sum_{ab}^{\text{unocc.}} \langle \chi_i^\tau \chi_j^\tau | r_{12}^{-1} | \chi_a^\tau \chi_b^\tau \rangle \langle \chi_a^\tau \chi_b^\tau | r_{12}^{-1} | \chi_j^\tau \chi_i^\tau \rangle = \langle \chi_i^\tau \chi_j^\tau | r_{12}^{-1} | \Psi_{ji}^\tau \rangle . \quad (10.3)$$

The main idea is now to find a *Schmidt decomposition* of the bipartite state $|\Psi_{ji}^\tau\rangle$ such that the expensive summation over all combinations of a and b is avoided. In the plane-wave basis this turns out to be surprisingly simple. One can easily construct auxiliary states $|w_i^{\mathbf{G}\tau}\rangle$ such that

$$|\Psi_{ji}^\tau\rangle = \sum_{\mathbf{G}} |w_j^{\mathbf{G}\tau} w_i^{\mathbf{G}\tau}\rangle , \quad (10.4)$$

where \mathbf{G} is a reciprocal lattice vector (plane-wave). We thus reduced the expensive summation by one order of magnitude,

$$\sum_{ab}^{\text{unocc.}} \langle \chi_i^\tau \chi_j^\tau | r_{12}^{-1} | \chi_a^\tau \chi_b^\tau \rangle \langle \chi_a^\tau \chi_b^\tau | r_{12}^{-1} | \chi_j^\tau \chi_i^\tau \rangle = \sum_{\mathbf{G}} \langle \chi_i^\tau \chi_j^\tau | r_{12}^{-1} | w_j^{\mathbf{G}\tau} w_i^{\mathbf{G}\tau} \rangle \quad (10.5)$$

The key concept, the Schmidt decomposition, will be elaborated in the following. Note, that no approximation will be used and all derivations are purely analytical.

Application to 3D periodic materials

We now turn to the case of periodic systems and restrict ourselves to the computationally most expensive part, the exchange term of the MP2 energy, given by

$$\begin{aligned} E_x^{\text{MP2}} = & \Omega_0 \int_0^\infty d\tau \int_{(\text{BZ})^3} \frac{d^3 k_1}{(2\pi)^3} \frac{d^3 k_2}{(2\pi)^3} \frac{d^3 q}{(2\pi)^3} \sum_{ij}^{\text{occ.}} \sum_{ab}^{\text{virt.}} \sum_{\mathbf{G}\mathbf{G}'} \frac{4\pi}{[\mathbf{G} + T(\mathbf{k}_1 - \mathbf{k}_2 + \mathbf{q})]^2} \frac{4\pi}{(\mathbf{G}' - \mathbf{q})^2} \\ & \times \langle i\mathbf{k}_1 | e^{+i[\mathbf{G} + T(\mathbf{k}_1 - \mathbf{k}_2 + \mathbf{q})]\hat{r}} | aT(\mathbf{k}_2 - \mathbf{q}) \rangle_{\Omega_0} \langle aT(\mathbf{k}_2 - \mathbf{q}) | e^{+i(\mathbf{G}' - \mathbf{q})\hat{r}} | j\mathbf{k}_2 \rangle_{\Omega_0} \\ & \times \langle j\mathbf{k}_2 | e^{-i[\mathbf{G} + T(\mathbf{k}_1 - \mathbf{k}_2 + \mathbf{q})]\hat{r}} | bT(\mathbf{k}_1 + \mathbf{q}) \rangle_{\Omega_0} \langle bT(\mathbf{k}_1 + \mathbf{q}) | e^{-i(\mathbf{G}' - \mathbf{q})\hat{r}} | i\mathbf{k}_1 \rangle_{\Omega_0} \\ & \times e^{(\varepsilon_{i\mathbf{k}_1} + \varepsilon_{j\mathbf{k}_2} - \varepsilon_{aT(\mathbf{k}_2 - \mathbf{q})} - \varepsilon_{bT(\mathbf{k}_1 + \mathbf{q})})\tau} . \end{aligned} \quad (10.6)$$

where Eq. (10.6) is LTMP2 formulation of Eq. (8.36) in the thermodynamic limit. The orbitals,

$$|i\mathbf{k}\rangle = \sum_{\mathbf{G}} \tilde{\varphi}_{i\mathbf{k}}(\mathbf{G}) |\mathbf{G} + \mathbf{k}\rangle , \quad (10.7)$$

are represented in terms of the plane wave coefficients $\tilde{\varphi}_{i\mathbf{k}}(\mathbf{G})$, where $\langle \mathbf{r} | \mathbf{G} + \mathbf{k} \rangle = e^{i(\mathbf{G} + \mathbf{k})\mathbf{r}}$ is a plane wave. In practice, the basis for the orbitals is truncated at a plane wave cutoff E_{cut} (ENCUT in vasp) and only plane waves observing

$$\frac{\mathbf{G}^2}{2} \leq E_{\text{cut}} \quad (10.8)$$

are taken into account. Switching between the real space basis and the plane-waves basis is achieved by a Fourier transform,

$$\varphi_{i\mathbf{k}}(\mathbf{r}) = \langle \mathbf{r} | i\mathbf{k} \rangle = \sum_{\mathbf{G}} \tilde{\varphi}_{i\mathbf{k}}(\mathbf{G}) e^{i(\mathbf{G}+\mathbf{k})\mathbf{r}}, \quad (10.9)$$

which is replaced by a Fast Fourier transform (FFT) in a computer code. For the overlap densities,

$$\langle aT(\mathbf{k}_2 - \mathbf{q}) | e^{+i(\mathbf{G}'-\mathbf{q})\hat{r}} | j\mathbf{k}_2 \rangle_{\Omega_0} = \frac{1}{\Omega_0} \int_{\Omega_0} d^3r \varphi_{aT(\mathbf{k}_2-\mathbf{q})}^*(\mathbf{r}) \varphi_{j\mathbf{k}_2}(\mathbf{r}) e^{+i(\mathbf{G}'-\mathbf{q})\mathbf{r}}, \quad (10.10)$$

a different cutoff $E_{\text{cut}}^{\text{aux}}$ (ENCUTGW in VASP) is used in the Fourier transform, which is commonly chosen as $2/3E_{\text{cut}}$. This second basis set is analogous to the auxiliary basis sets used in Gaussian type orbital codes. As will be discussed later, the internal basis set extrapolation is performed with respect to the auxiliary basis set size. This approach has been successfully used in the random phase approximation (RPA) in the past [58].

Our strategy to reduce the computational cost, consists of the idea to exploit the decoupling of the indices i, j, a, b in the expression (10.6). Note that this is only possible in a Laplace transformed formulation of the MP2 energy. We can then perform the summations over a and b in advance, for given \mathbf{G}' , \mathbf{q} , and τ , and define auxiliary states,

$$\left| w_{i\mathbf{k}}^{(\mathbf{G}'\mathbf{q}\tau)} \right\rangle = \sum_b^{\text{virt.}} C_{ib,\mathbf{k}}^{(\mathbf{G}'\mathbf{q}\tau)} | b\mathbf{k} \rangle. \quad (10.11)$$

where the coefficients are defined as,

$$C_{ib,\mathbf{k}}^{(\mathbf{G}'\mathbf{q}\tau)} = e^{(\varepsilon_{iT(\mathbf{k}-\mathbf{q})} - \varepsilon_{b\mathbf{k}})\tau} \langle b\mathbf{k} | e^{-i(\mathbf{G}'-\mathbf{q})\hat{r}} | iT(\mathbf{k}-\mathbf{q}) \rangle_{\Omega_0}. \quad (10.12)$$

The MP2 energy per unit cell can be written in a form which involves summations only over the occupied indices i, j ,

$$\begin{aligned} E_x^{\text{MP2}} = & \Omega_0 \int_0^\infty d\tau \int_{(\text{BZ})^3} \frac{d^3q}{(2\pi)^3} \frac{d^3k_1}{(2\pi)^3} \frac{d^3k_2}{(2\pi)^3} \sum_{\mathbf{G}\mathbf{G}'} \frac{4\pi}{[\mathbf{G} + T(\mathbf{k}_1 - \mathbf{k}_2 + \mathbf{q})]^2} \frac{4\pi}{(\mathbf{G}' - \mathbf{q})^2} \\ & \times \sum_{ij}^{\text{occ.}} \left\langle i\mathbf{k}_1 \left| e^{+i[\mathbf{G}+T(\mathbf{k}_1-\mathbf{k}_2+\mathbf{q})]\hat{r}} \right| w_{jT(\mathbf{k}_2-\mathbf{q})}^{(-\mathbf{G}',-\mathbf{q},\tau)} \right\rangle_{\Omega_0} \\ & \times \left\langle j\mathbf{k}_2 \left| e^{-i[\mathbf{G}+T(\mathbf{k}_1-\mathbf{k}_2+\mathbf{q})]\hat{r}} \right| w_{iT(\mathbf{k}_1+\mathbf{q})}^{(+\mathbf{G}',+\mathbf{q},\tau)} \right\rangle_{\Omega_0}. \end{aligned} \quad (10.13)$$

The expressions,

$$\left\langle i\mathbf{k}_1 \left| e^{+i[\mathbf{G}+T(\mathbf{k}_1-\mathbf{k}_2+\mathbf{q})]\hat{r}} \right| w_{jT(\mathbf{k}_2-\mathbf{q})}^{(-\mathbf{G}',-\mathbf{q},\tau)} \right\rangle_{\Omega_0} \quad (10.14)$$

can be evaluated for all \mathbf{G} in linear scaling, using a Fast Fourier transform, if i, j , as well as \mathbf{G}' , \mathbf{k}_1 , \mathbf{k}_2 , \mathbf{q} and τ are given. The system size scaling is thus reduced to $N_i^2 N_G^2 \times N_k^3$.

Here, N_i and N_G are the number of unoccupied states and plane-waves respectively, and N_k is the number of k -points. This is to be compared with the previous scaling, $N_i^2 N_a^2 N_G \times N_k^3$, where N_a is the number of unoccupied orbitals. The number of τ -points is largely independent of the system size and will be discussed in a more comprehensive analysis of the system size scaling.

10.1.2 Exploiting the time reversal symmetry

For a more convenient implementation in a computer code, it is advantageous to exploit the time reversal symmetry. With its aid we can turn both overlap densities in Eq. (10.13) into the same form, i.e. to avoid mixtures of $+G$ and $-G$ as well as mixtures of $+G'$ and $-G'$. This can be done in the following way. If no external magnetic field is applied and spin-orbit coupling is ignored the orbitals obey time reversal symmetry: $\varphi_{ik}^* = \varphi_{i-k}$ and $\varepsilon_{ik} = \varepsilon_{i-k}$. If we apply this time reversal symmetry to the coefficients (10.12) we obtain:

$$\left(C_{ib,+k}^{(+G',+q,\tau)} \right)^* = C_{ib,-k}^{(-G',-q,\tau)}. \quad (10.15)$$

Hence for (10.11) we find:

$$\left| \left(w_{i,+k}^{(+G',+q,\tau)} \right)^* \right\rangle = \left| w_{i,-k}^{(-G',-q,\tau)} \right\rangle. \quad (10.16)$$

This relation can be applied to the overlap densities in (10.13). Consider, e.g.,

$$\begin{aligned} & \left\langle i\mathbf{k}_1 \left| e^{+i[\mathbf{G}+T(\mathbf{k}_1-\mathbf{k}_2+\mathbf{q})]\hat{r}} \right| w_{jT(\mathbf{k}_2-\mathbf{q})}^{(-G',-q,\tau)} \right\rangle_{\Omega_0} \\ &= \left\langle w_{jT(\mathbf{k}_2-\mathbf{q})}^{(-G',-q,\tau)} \left| e^{-i[\mathbf{G}+T(\mathbf{k}_1-\mathbf{k}_2+\mathbf{q})]\hat{r}} \right| i\mathbf{k}_1 \right\rangle_{\Omega_0}^* \\ &= \left\langle (i\mathbf{k}_1)^* \left| e^{-i[\mathbf{G}+T(\mathbf{k}_1-\mathbf{k}_2+\mathbf{q})]\hat{r}} \right| w_{jT(-\mathbf{k}_2+\mathbf{q})}^{(G'q\tau)} \right\rangle_{\Omega_0}^* \end{aligned} \quad (10.17)$$

In a last step we substituted $\mathbf{k}_2 \rightarrow -\mathbf{k}_2$ in (10.13), such that we find a convenient and more "symmetric" formula for the

MP2 exchange energy per unit cell:

$$\begin{aligned} E_x^{\text{MP2}} &= \Omega_0 \int_0^\infty d\tau \int_{(\text{BZ})^3} \frac{d^3q}{(2\pi)^3} \frac{d^3k_1}{(2\pi)^3} \frac{d^3k_2}{(2\pi)^3} \sum_{GG'} \frac{4\pi}{[\mathbf{G} + T(\mathbf{k}_1 + \mathbf{k}_2 + \mathbf{q})]^2} \frac{4\pi}{(\mathbf{G}' - \mathbf{q})^2} \\ &\quad \times \sum_{ij}^{\text{occ.}} \left\langle (i\mathbf{k}_1)^* \left| e^{-i[\mathbf{G}+T(\mathbf{k}_1+\mathbf{k}_2+\mathbf{q})]\hat{r}} \right| w_{jT(\mathbf{k}_2+\mathbf{q})}^{(G'q,\tau)} \right\rangle_{\Omega_0}^* \\ &\quad \times \left\langle (j\mathbf{k}_2)^* \left| e^{-i[\mathbf{G}+T(\mathbf{k}_1+\mathbf{k}_2+\mathbf{q})]\hat{r}} \right| w_{iT(\mathbf{k}_1+\mathbf{q})}^{(G'q\tau)} \right\rangle_{\Omega_0}. \end{aligned} \quad (10.18)$$

As for the exchange term the same procedure can be applied to

the direct MP2 term,

$$E_d^{\text{MP2}} = -2\Omega_0 \int_0^\infty d\tau \int_{\text{BZ}} \frac{d^3q}{(2\pi)^3} \sum_{\mathbf{G}\mathbf{G}'} \frac{4\pi}{(\mathbf{G} + \mathbf{q})^2} \frac{4\pi}{(\mathbf{G}' - \mathbf{q})^2} \times \left| \int_{\text{BZ}} \frac{d^3k}{(2\pi)^3} \sum_i^{\text{occ.}} \langle i\mathbf{k} | e^{-i(\mathbf{G}+\mathbf{q})\hat{r}} | w_{iT(\mathbf{k}+\mathbf{q})}^{(\mathbf{G}'\mathbf{q}\tau)} \rangle_{\Omega_0} \right|^2. \quad (10.19)$$

10.1.3 Implementation

The presented LTMP2 method is implemented in `VASP` [57, 11] based on the projector augmented wave (PAW) [10] method (see Sec. 8.1.3).

General strategy

The four major steps of the algorithm can be summarized as follows:

- (i) Compute and store all overlap densities (10.10).
- (ii) Loop over all τ -points, \mathbf{q} -points, and reciprocal vectors \mathbf{G}' as outer loops in Eq. (10.18) and (10.19).
- (iii) Calculate the transformation matrix (10.12) for this τ , \mathbf{q} , and \mathbf{G}' using the stored overlap densities of step (i) and construct the transformed states (10.11).
- (iv) Perform the inner loops and evaluate the overlap densities between the Hartree-Fock states and the transformed state (10.11) and contract them over all \mathbf{G} .
 - (a) for the direct term (10.19) the inner loops involve only i and \mathbf{k} .
 - (b) for the exchange term (10.18) the inner loops run over i, j and $\mathbf{k}_1, \mathbf{k}_2$.

The loops over plane waves \mathbf{G}, \mathbf{G}' are limited by an adjustable plane wave cutoff $E_{\text{cut}}^{\text{aux}}$. The outer loop over the τ -points is performed by a quadrature [59]. The Figures 10.1 and 10.2 show pseudocode for the serial and parallel Γ -only implementation of the algorithm.

Parallelization

The outer \mathbf{G}' -loop provides a powerful approach to parallelize the algorithm. The entire set of reciprocal lattice vectors \mathcal{G} can be divided into $N_{\mathcal{G}}$ independent subsets. This leads to a very high parallelization efficiency as long as the total number of reciprocal lattice vectors $N_{\mathcal{G}}$ is larger than $N_{\mathcal{G}}$. Furthermore, on a second level, a parallelization is implemented for the evaluation of the sum over occupied bands: the set of occupied bands

```

# overlap densities (i)
for all  $i, a$  do
     $\rho_{ai}(\mathbf{r}) \leftarrow \varphi_a^*(\mathbf{r})\varphi_i(\mathbf{r})$ 
     $\tilde{\rho}_{ai} \leftarrow \text{FFT}[\rho_{ai}]$ 
    store  $\tilde{\rho}_{ai}$ 
end for
for all  $\tau$  do
    for all  $G$  do
        # transformed states (iii)
        for all  $i$  do
            for all  $a$  do
                 $C_{ia} \leftarrow e^{(\varepsilon_i - \varepsilon_a)\tau} \tilde{\rho}_{ai}(\mathbf{G})$ 
            end for
             $\tilde{w}_i \leftarrow \sum_a C_{ia} \tilde{\varphi}_a$ 
            store  $\tilde{w}_i$ 
        end for
        # direct term (iv.a)
         $w_i \leftarrow \text{FFT}^{-1}[\tilde{w}_i]$  for all  $i$ 
         $\varrho(\mathbf{r}) \leftarrow \sum_i \varphi_i^*(\mathbf{r})w_i(\mathbf{r})$ 
         $\tilde{\varrho} \leftarrow \text{FFT}[\varrho]$ 
         $e_d^{(2)} \leftarrow e_d^{(2)} + \sum_{\mathbf{G}'} \frac{4\pi}{\mathbf{G}'^2} |\tilde{\rho}(\mathbf{G}')|^2$ 
        # exchange term (iv.b)
         $w_i \leftarrow \text{FFT}^{-1}[\tilde{w}_i]$  for all  $i$ 
        for all  $i, j$  ( $i \leq j$ ) do
             $\varrho_1(\mathbf{r}) \leftarrow \varphi_i^*(\mathbf{r})w_j(\mathbf{r})$ 
             $\varrho_2(\mathbf{r}) \leftarrow \varphi_j^*(\mathbf{r})w_i(\mathbf{r})$ 
             $\tilde{\varrho}_1 \leftarrow \text{FFT}[\varrho_1]$ 
             $\tilde{\varrho}_2 \leftarrow \text{FFT}[\varrho_2]$ 
             $e_x^{(2)} \leftarrow e_x^{(2)} + \sum_{\mathbf{G}'} \frac{4\pi}{\mathbf{G}'^2} \tilde{\rho}_1^*(\mathbf{G}')\tilde{\rho}_2(\mathbf{G}')$ 
        end for
         $E_d^{(2)} \leftarrow E_d^{(2)} + \frac{4\pi}{\mathbf{G}^2} e_d^{(2)}$ 
         $E_x^{(2)} \leftarrow E_x^{(2)} + \frac{4\pi}{\mathbf{G}^2} e_x^{(2)}$ 
    end for
end for

```

Figure 10.1: Pseudocode of the serial Γ -only implementation. Hartree-Fock orbitals φ_i, φ_a and energies $\varepsilon_i, \varepsilon_a$ for all occupied and virtual states are assumed.

step	system size	k-points
(i)	$N_i N_a N_{\text{FFT}} \ln N_{\text{FFT}}$	N_k^2
(iii)	$N_i N_a N_G^2$	N_k^2
(iv.a)	$N_i N_G N_{\text{FFT}} \ln N_{\text{FFT}}$	N_k^2
(iv.b)	$N_i^2 N_G N_{\text{FFT}} \ln N_{\text{FFT}}$	N_k^3

Table 10.1: Formal scaling of the computation time for the different steps of the algorithm. The steps are described in Sec. 10.1.3. N_i and N_a are the number of occupied and virtual orbitals respectively. N_G is the number of reciprocal lattice vectors, N_{FFT} the number of FFT grid points, and N_k is the number of \mathbf{k} -points.

\mathcal{I} is divided into \mathcal{N}_B subsets such that one band summation (say over j) can be calculated in parallel. Pseudocode for this strategy can be found in Fig. 10.2.

We also provide pseudocode of the parallel Γ -only implementation in Fig. 10.2. The number \mathcal{N} of CPUs is divided into \mathcal{N}_B groups parallelizing over bands and \mathcal{N}_G groups parallelizing over plane waves such that $\mathcal{N} = \mathcal{N}_B \mathcal{N}_G$. The set \mathcal{G} of all plane waves is evenly divided into \mathcal{N}_G disjoint subsets: $\mathcal{G} = \bigcup_n \mathcal{G}_n$, $n \in [1, \mathcal{N}_G]$. Likewise the set of all occupied indices \mathcal{I} and virtual indices \mathcal{A} is evenly divided into \mathcal{N}_B disjoint subsets: $\mathcal{I} = \bigcup_n \mathcal{I}_n$, $\mathcal{A} = \bigcup_n \mathcal{A}_n$, $n \in [1, \mathcal{N}_B]$. Moreover, each subset of virtual band indices \mathcal{A}_n is further divided into \mathcal{N}_G disjoint subsets: $\mathcal{A}_n = \bigcup_m \mathcal{A}_n^{(m)}$, $m \in [1, \mathcal{N}_G]$, since for the calculation of the overlap densities the plane wave parallelization is inapplicable. See Fig. 10.3 for an illustration.

Formal system size scaling: computation time and memory

Calculating the exchange term (which has the steepest scaling) results in a computation time that scales with the fourth power of the system size. This stems from the fact that for every combination of \mathbf{G}, i, j , fast Fourier transforms (FFT) have to be performed. In a spin-unrestricted calculation, the computation time will be twice as large as for a spin-restricted case. The number of τ -points for the quadrature, to numerically evaluate the τ -integration, is largely independent of the system size. Table 10.1 shows the formal scaling for each step.

Regarding the memory consumption only the orbitals and the overlap densities (10.10) are of relevance. The latter has the steepest scaling: $N_i N_a N_G$. The memory requirement of the orbitals scales only quadratically. Regarding \mathbf{k} -point sampling of the Brillouin zone, a linear dependence of N_k has to be multiplied in both cases. For a spin-unrestricted calculation the memory requirement doubles.

Internal cutoff extrapolation

Similar to other MP2 implementations or RPA codes the LTMP2 algorithm converges slowly with respect to the number of basis functions (plane wave cutoff). However, within the presented algorithm an internal extrapolation of the auxiliary plane wave cutoff, $E_{\text{cut}}^{\text{aux}}$,

```

Distribute occ. orbitals over  $\mathcal{I}$  among  $\mathcal{N}_B$  groups
Distribute virt. orbitals over  $\mathcal{A}$  among  $\mathcal{N}_B$  groups
# overlap densities (i)
for all  $i \in \mathcal{I}$  do
  fetch  $\varphi_i$  from other band groups
  for all  $a \in \mathcal{A}_{\text{this}}^{(\text{this})}$  do
     $\rho_{ai}(\mathbf{r}) \leftarrow \varphi_a^*(\mathbf{r})\varphi_i(\mathbf{r})$ 
     $\tilde{\rho}_{ai} \leftarrow \text{FFT}[\rho_{ai}]$ 
    gather  $\tilde{\rho}_{ai}$  of this band group
    store  $\tilde{\rho}_{ai}(\mathbf{G})$  for  $\mathbf{G} \in \mathcal{G}_{\text{this}}$ 
  end for
end for
Distribute virt. orbitals over  $\mathcal{G}$  among  $\mathcal{N}_G$  groups
for all  $\tau$  do
  for all  $\mathbf{G} \in \mathcal{G}_{\text{this}}$  do
    # transformed states (iii)
    for all  $i \in \mathcal{I}$  do
      fetch  $\varphi_i$  from other band groups
      for all  $a \in \mathcal{A}_{\text{this}}$  do
         $C_{ia} \leftarrow e^{(e_i - e_a)\tau} \tilde{\rho}_{ai}(\mathbf{G})$ 
      end for
      gather  $C_{ia}$  of this plane-wave group
       $\tilde{w}_i(\mathbf{G}') \leftarrow \sum_a C_{ia} \tilde{\varphi}_a(\mathbf{G}')$  for  $\mathbf{G}' \in \mathcal{G}_{\text{this}}$ 
      redistribute  $\tilde{w}_i$  over  $\mathcal{I}$  among  $\mathcal{N}_B$  groups
      store  $\tilde{w}_i$ 
    end for
    # direct term (iv.a)
     $w_i \leftarrow \text{FFT}^{-1}[\tilde{w}_i]$  for  $i \in \mathcal{I}_{\text{this}}$ 
     $\varrho(\mathbf{r}) \leftarrow \sum_{i \in \mathcal{I}_{\text{this}}} \varphi_i^*(\mathbf{r})w_i(\mathbf{r})$ 
     $\tilde{\varrho} \leftarrow \text{FFT}[\varrho]$ 
    add  $\tilde{\varrho}$  of this plane-wave group together
     $e_d^{(2)} \leftarrow e_d^{(2)} + \sum_{\mathbf{G}' \in \mathcal{G}} \frac{4\pi}{\mathbf{G}'^2} |\tilde{\varrho}(\mathbf{G}')|^2$ 
    # exchange term (iv.b)
     $w_i \leftarrow \text{FFT}^{-1}[\tilde{w}_i]$  for  $i \in \mathcal{I}$ 
    for all  $i \in \mathcal{I}$  do
      fetch  $\varphi_i$  from other band groups
      for all  $j \in \mathcal{I}_{\text{this}}, j \leq i$  do
         $\varrho_1(\mathbf{r}) \leftarrow \varphi_i^*(\mathbf{r})w_j(\mathbf{r})$ 
         $\varrho_2(\mathbf{r}) \leftarrow \varphi_j^*(\mathbf{r})w_i(\mathbf{r})$ 
         $\tilde{\varrho}_1 \leftarrow \text{FFT}[\varrho_1]$ 
         $\tilde{\varrho}_2 \leftarrow \text{FFT}[\varrho_2]$ 
        add  $\tilde{\varrho}_1, \tilde{\varrho}_2$  of this plane-wave group together
         $e_x^{(2)} \leftarrow e_x^{(2)} + \sum_{\mathbf{G}'} \frac{4\pi}{\mathbf{G}'^2} \tilde{\varrho}_1^*(\mathbf{G}')\tilde{\varrho}_2(\mathbf{G}')$ 
      end for
    end for
     $E_d^{(2)} \leftarrow E_d^{(2)} + \frac{4\pi}{\mathbf{G}^2} e_d^{(2)}$ 
     $E_x^{(2)} \leftarrow E_x^{(2)} + \frac{4\pi}{\mathbf{G}^2} e_x^{(2)}$ 
  end for
  add  $E_d^{(2)}$  of this band group together
  add  $E_x^{(2)}$  of this band group together
end for

```

Figure 10.2: Pseudocode of the parallel Γ -only implementation. Hartree-Fock energies and orbitals for all occupied and virtual states are assumed.

		bands							
		group 1				group 2			
plane-waves	group 1	\mathcal{G}_1	\mathcal{I}_1	\mathcal{A}_1	$\mathcal{A}_1^{(1)}$	\mathcal{G}_1	\mathcal{I}_2	\mathcal{A}_2	$\mathcal{A}_2^{(1)}$
	group 2	\mathcal{G}_2	\mathcal{I}_1	\mathcal{A}_1	$\mathcal{A}_1^{(2)}$	\mathcal{G}_2	\mathcal{I}_2	\mathcal{A}_2	$\mathcal{A}_2^{(2)}$
	group 3	\mathcal{G}_3	\mathcal{I}_1	\mathcal{A}_1	$\mathcal{A}_1^{(3)}$	\mathcal{G}_3	\mathcal{I}_2	\mathcal{A}_2	$\mathcal{A}_2^{(3)}$
	group 4	\mathcal{G}_4	\mathcal{I}_1	\mathcal{A}_1	$\mathcal{A}_1^{(4)}$	\mathcal{G}_4	\mathcal{I}_2	\mathcal{A}_2	$\mathcal{A}_2^{(4)}$

Figure 10.3: Illustration of the parallelization for the case of $\mathcal{N} = 8$ CPUs with $\mathcal{N}_B = 2$ band groups and $\mathcal{N}_G = 4$ plane wave groups.

can be implemented comfortably with negligible influence on the computation time. The cutoff extrapolation makes use of the known asymptotic behavior of the MP2 energy E^{MP2} for large cutoffs $E_{\text{cut}}^{\text{aux}}$ [58, 60]:

$$E^{\text{MP2}}(E_{\text{cut}}^{\text{aux}}) - E^{\text{MP2}}(E_{\text{cut}}^{\text{aux}} = \infty) \sim E_{\text{cut}}^{\text{aux}-3/2}. \quad (10.20)$$

The idea is to calculate the MP2 energy for a sufficient number of different cutoffs $E_{\text{cut}}^{\text{aux}}$ in order to extrapolate these energies according to Eq. (11.66). Since the plane wave cutoff, $E_{\text{cut}}^{\text{aux}}$, truncates only the \mathbf{G} -loops, the MP2 energy can be calculated for different cutoffs on the fly. This is achieved in the following way. First an array of different cutoffs is defined by

$$E_{\text{cut}}^{\text{aux}}[\mathbf{n}] = \frac{E_{\text{cut}}^{\text{aux}}}{\alpha^{n-1}}, \quad (10.21)$$

where $E_{\text{cut}}^{\text{aux}}$ is the user-given cutoff, $\alpha > 1$, $n = 1, \dots, n_c$, and n_c is the number of cutoffs for the extrapolation. In this work we chose $\alpha = 1.05$ and $n_c = 8$. Each cutoff, $E_{\text{cut}}^{\text{aux}}[\mathbf{n}]$, defines the maximum length of the plane wave vectors,

$$G_{\text{max}}[\mathbf{n}] = \sqrt{2E_{\text{cut}}^{\text{aux}}[\mathbf{n}]}. \quad (10.22)$$

Also for the MP2 energy an array, $E^{\text{MP2}}[\mathbf{n}]$, is created. Whenever a loop over plane waves in the auxiliary basis, $\sum_{\mathbf{G}} \dots$, is performed, only $|\mathbf{G}| \leq G_{\text{max}}[\mathbf{n}]$ contributes to $E^{\text{MP2}}[\mathbf{n}]$. This is implemented by simple `if...then...else...` statements in plane wave loops in the auxiliary basis. The different MP2 energies, $E^{\text{MP2}}[\mathbf{n}]$, can then be extrapolated to $E_{\text{cut}}^{\text{aux}} \rightarrow \infty$ by solving the linear regression $y = a + bx$ with the samples $y = E^{\text{MP2}}[\mathbf{n}]$ and $x = E_{\text{cut}}^{\text{aux}}[\mathbf{n}]^{-3/2}$, according to Eq. (11.66). The solution for a is the extrapolated energy $E^{\text{MP2}}(E_{\text{cut}}^{\text{aux}} = \infty)$. The reliability of this extrapolation depends on the user-given $E_{\text{cut}}^{\text{aux}}$ since the asymptotic behavior (11.66) is strictly true only for $E_{\text{cut}}^{\text{aux}} \rightarrow \infty$.

10.1.4 Benchmark calculations

In order to show the potential of the new LTMP2 method, we performed several benchmark calculations. Computations on supercells of solid lithium hydride (LiH) served as a

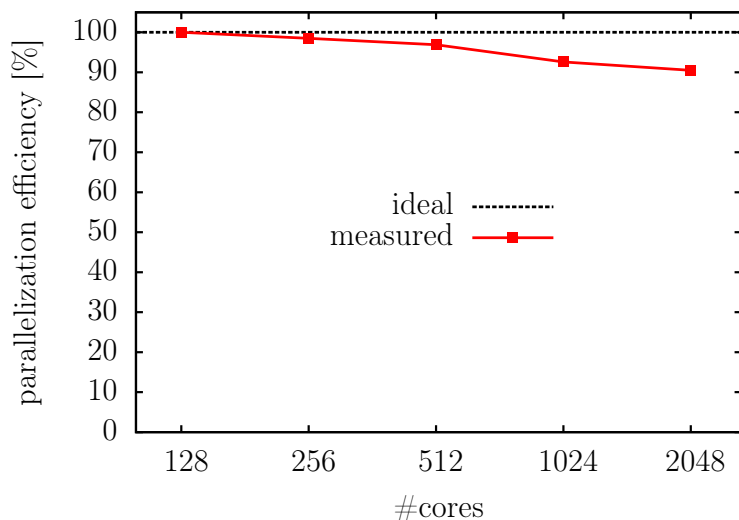


Figure 10.4: Parallelization efficiency of the LTMP2 calculation of a $4 \times 4 \times 4$ supercell of solid LiH. The efficiency was calculated with reference to the computation time t_{128} of a run using 128 cores: $t_{128}/t_{\#cores}/(\#cores/128)$. Note that the abscissa has a logarithmic scale.

benchmark to demonstrate the parallelization efficiency and system size scaling. The advantage of an internal auxiliary plane wave cutoff extrapolation is shown by means of binding energy calculations of methane (CH_4) in a chabazite crystal ($\text{AlHO}_2\text{Si}_{11}$). The calculations were performed with `vasp` in which the new LTMP2 code was implemented. For each benchmark calculation shown in this chapter we used a Γ -only and spin-restricted setting. Furthermore, we used the previous MP2 implementation as a reference for the LTMP2 implementation of this work whenever possible. For the τ -integration, 6 τ -points turned out to be accurate enough ($\ll 1\text{meV}$ agreement between MP2 and LTMP2) for all considered systems in this section.

Measured parallelization efficiency

To demonstrate the parallelization efficiency we computed the MP2 energy of solid LiH using a supercell containing $4 \times 4 \times 4$ primitive cells and 128 atoms. The computation time was measured against the number of cores. An auxiliary plane wave cutoff of 289 eV lead to 5600 reciprocal lattice vectors for the outer \mathbf{G} -loop. The total number of orbitals was set to 20480 whereas the number of occupied orbitals amounted to 128. In each run the number of plane wave groups was set to $\mathcal{N}_{\mathbf{G}} = \#cores/4$ which implies $\mathcal{N}_{\mathbf{B}} = 4$ for the band parallelization. Figures 10.4 and 10.5 show the parallelization efficiency and the strong scaling. The strong scaling shows that with increasing number of cores the computation time approaches zero as long as the number of reciprocal lattice vectors, $\mathcal{N}_{\mathbf{G}}$, is divisible by the number of plane wave groups, $\mathcal{N}_{\mathbf{G}}$.

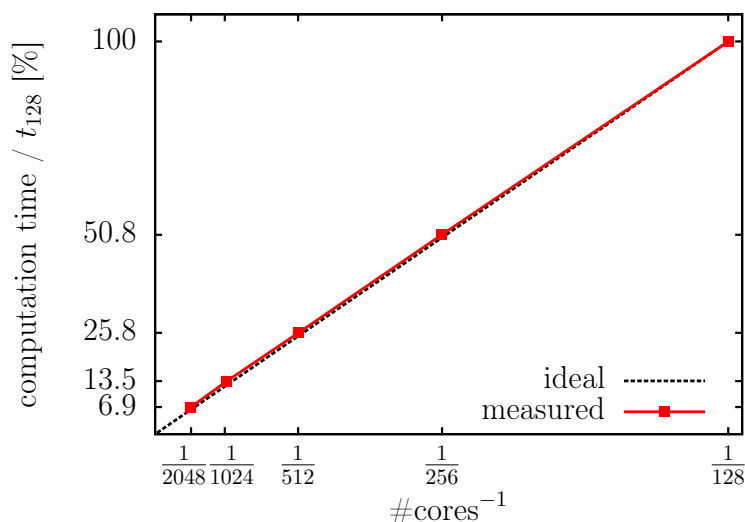


Figure 10.5: Strong scaling of the LTMP2 calculation of a 4x4x4 supercell of solid LiH. Here t_{128} is the computation time of a calculation with 128 cores. In the case of 2048 cores the computation time is reduced to 6.9% of t_{128} which is close to the ideal case of $128/2048 = 6.25\%$.

Measured system size scaling: computation time and memory

To evaluate the time and memory scaling of the LTMP2 algorithm with respect to the system size, the computation time and the memory consumption was measured against the number of atoms for various supercells of solid LiH. The smallest system containing 8 atoms corresponds to the conventional unit cell of LiH. This cell was replicated in numerous ways to form supercells containing up to 128 atoms. The plane wave cutoff was set to 289 eV leading to about 44 plane waves of the auxiliary basis set per LiH formula. The calculations were performed on 64 Intel Xeon E5-2650 v2 2.8 GHz processors with 8 GB memory per core, although 6 GB per core would suffice for up to 128 atoms. For the parallelization we used $\mathcal{N}_G = 32$ and $\mathcal{N}_B = 2$. Figure 10.6 and 10.7 show the measured scaling of the computation time and memory for this (LTMP2) and the previous (MP2) implementation. The measured scaling exponents match the predicted values.

Internal cutoff extrapolation

The internal cutoff extrapolation described in Sec. 10.1.3 is illustrated by an adsorption energy calculation of CH_4 in a chabazite crystal (Chab):

$$E_{\text{ad}}^{\text{MP2}} = E_{\text{CH}_4}^{\text{MP2}} + E_{\text{Chab}}^{\text{MP2}} - E_{\text{CH}_4+\text{Chab}}^{\text{MP2}} \quad (10.23)$$

The MP2 correlation contribution, $E_{\text{ad}}^{\text{MP2}}$, of the adsorption energy was computed against the auxiliary plane wave cutoff $E_{\text{cut}}^{\text{aux}}$. Figure 10.9 shows the result of the previous code (MP2) and this work (LTMP2). The lattice parameters and the orientation of the CH_4

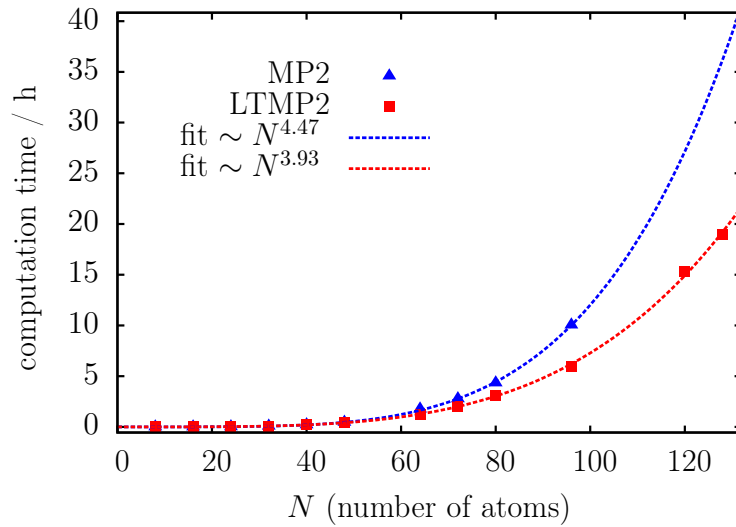


Figure 10.6: System size scaling of the computation time for various supercells of solid LiH on a system with 64 cores and 8 GB memory per core. MP2 refers to the previous implementation, whereas LTMP2 is the algorithm of this work. With the previous implementation it was not possible to exceed 96 atoms due to larger memory requirements.

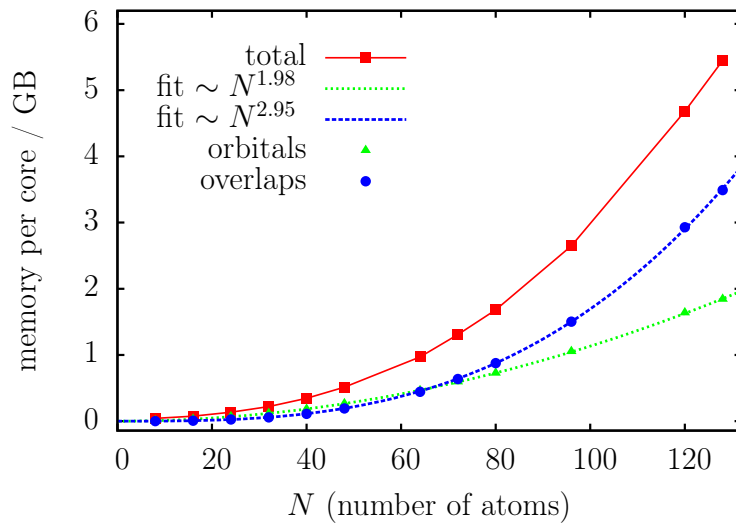


Figure 10.7: Scaling of the used memory per core with respect to the system size. The two most relevant quantities are the orbitals and the overlap densities (10.10). The calculations were performed on a system with 64 cores and 8 GB memory per core.

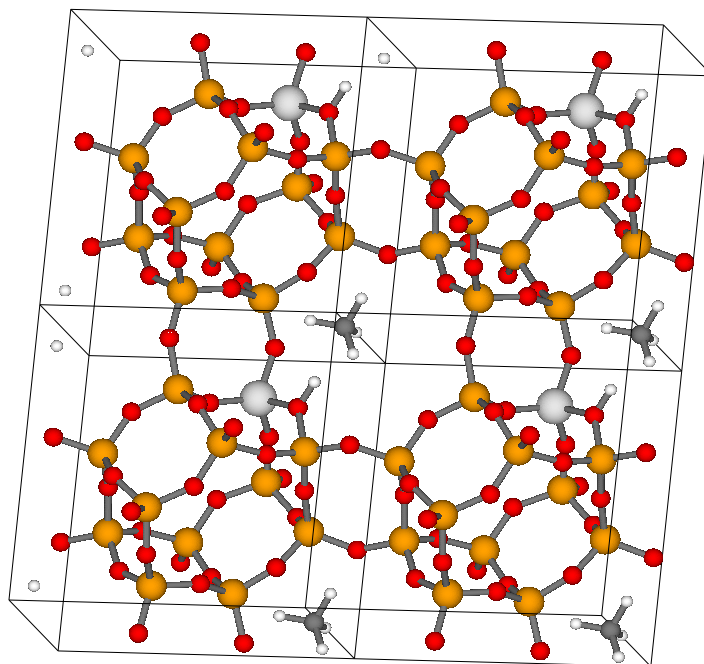


Figure 10.8: Four unit cells of the chabazite crystal with adsorbed methane molecules. The color code reads: Al (light gray), C (dark gray), H (white), O (red), Si (yellow).

molecule in the chabazite cage were taken from [61] and then reoptimized using the optB88-vdW functional [34]. The largest system (CH_4+Chab) consists of 42 atoms (100 valence electrons) in a unit cell of about 810 \AA^3 . A visualization can be found in Fig. 10.8. In the Hartree-Fock steps to calculate the orbitals, plane wave cutoffs (E_{cut} or ENCUT flag in `VASP`) of 450, 550, 650, 750, and 850 eV were used. In the subsequent MP2 calculation auxiliary plane wave cutoffs ($E_{\text{cut}}^{\text{aux}}$ or ENCUTGW flag in `VASP`) of 300, 366, 433, 500, and 566 eV were used for the two-electron integrals. In the case of $E_{\text{cut}}^{\text{aux}} = 566$ eV the computation of $E_{\text{CH}_4+\text{Chab}}^{\text{MP2}}$ included about 46 000 bands (100 occupied bands) and about $N_G = 12\,500$ plane wave vectors. The previous MP2 code clearly shows the mentioned $E_{\text{cut}}^{\text{aux}-3/2}$ behavior (11.66) as can be seen in Fig. 10.9. With the previous MP2 code, the procedure was to perform the extrapolation manually leading to $E_{\text{ad}}^{\text{MP2}} = 295.51 \pm 0.07$ meV, where the error stems from the fitting. This is at the cost of about 65 000 cpu hours, as can be seen in Fig. 10.10 (adding up the timings of all five MP2 calculations, which are necessary for a manual extrapolation). Without an extrapolation this adsorption energy could not be achieved below a cutoff of $E_{\text{cut}}^{\text{aux}} = 1100$ eV, if a tolerance of 1 meV is assumed. However, with the new implementation this accuracy is achieved already at $E_{\text{cut}}^{\text{aux}} = 500$ eV leading to $E_{\text{ad}}^{\text{MP2}} = 294.8 \pm 0.2$ meV. This is at the cost of about 3 770 cpu hours which is only a small fraction of about 6% compared to the cost of the previous code.

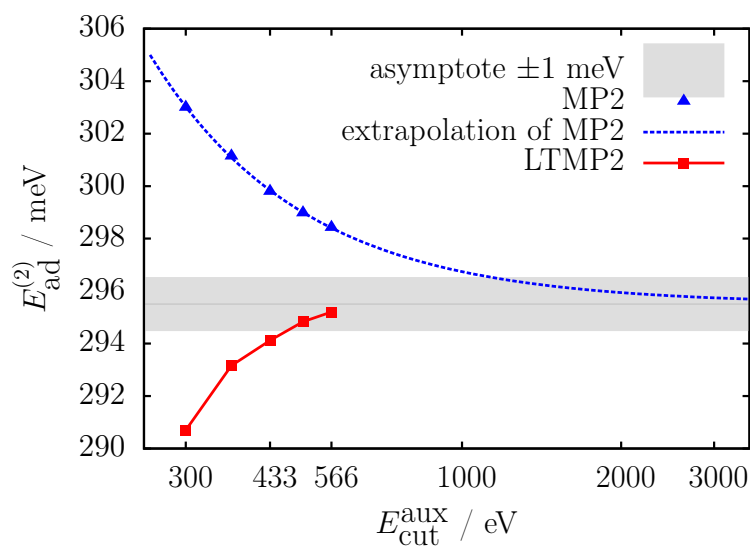


Figure 10.9: Adsorption energy of methane in a chabazite cage as a function of the auxiliary plane wave cutoff $E_{\text{cut}}^{\text{aux}}$. MP2 refers to the previous implementation without basis set extrapolation, whereas LTMP2 is the algorithm of this work. The manual extrapolation (dashed blue line) was calculated using (11.66). Note the logarithmic scaling of the abscissa.

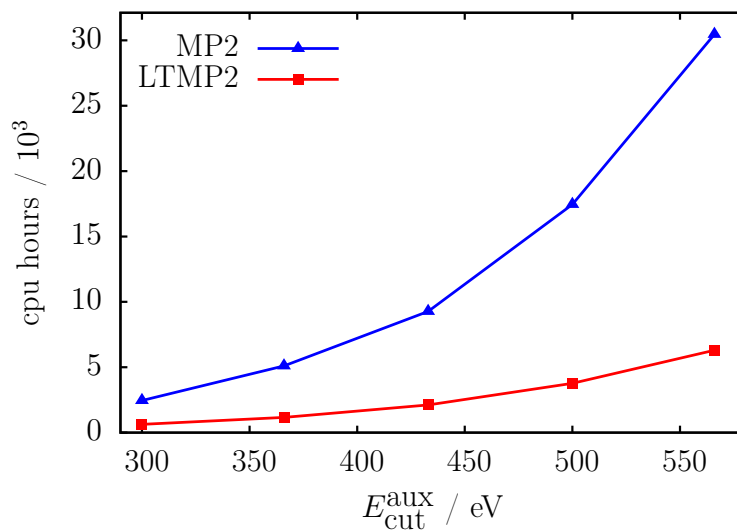


Figure 10.10: CPU hours spend to calculate the adsorption energy of methane in a chabazite cage against the auxiliary plane wave cutoff $E_{\text{cut}}^{\text{aux}}$. The calculations were performed on 256 (lowest cutoff) to 1280 (highest cutoff) Intel Xeon E5-2650 v2 2.8 GHz processors with 4 GB memory per core.

10.1.5 Conclusion and Outlook

We have presented an algorithm to calculate the exact MP2 energy for periodic systems, scaling only with the fourth power of the system size, $O(N^4)$. The lower scaling is a consequence of a Laplace transformed energy denominator of the traditional MP2 formulation and of the use of Fast Fourier transforms. In doing so the summations over the virtual bands can be carried out first, leading to transformed states in dependence of a plane wave index and a τ -point. The loop over these plane waves is an outer loop that can be distributed over the CPUs without communication, leading to a very high parallelization efficiency. We showed that the parallelization is extremely close to ideal as long as the number of plane waves, N_G , of the auxiliary basis set can be divided by the number, N_G , of parallelized plane wave groups.

The slow convergence of the MP2 energy with respect to the number of basis functions is dealt with an extrapolation to an infinite basis set using the exact asymptotic cutoff behavior. In a comparison with the previous MP2 code in `VASP`, we demonstrated that this internal extrapolation leads to faster converging MP2 energies, reducing the computational effort significantly.

In future the presented approach could be adapted to more involved electronic correlation energy methods, like second-order screened exchange (SOSEX) [62, 52] or particle-hole ladder diagrams, in order to obtain a similar low complexity. Hence, the presented method can be considered as a step towards systematically improved correlation energies.

Also, calculating interatomic forces should be possible using the presented low-complexity concept, as the self-energy at MP2 level can be obtained along the same lines presented here for the MP2 energy. With the respective self-energy at hand, the recently published Green's function approach allows to efficiently calculate interatomic forces for perturbative methods, in this case MP2 [63].

10.2 Quartic scaling SOSEX for periodic systems

In this section we provide a scheme to evaluate the periodic SOSEX correction (8.119) to the RPA with a quartic scaling instead of a quintic scaling as in Ref. [52]. Again, as for the quartic scaling MP2 code, the presented algorithm purely relies on analytic rearrangements of the SOSEX expression. Hence, this low-scaling approach yields equivalent results as the original work in [52]. Note that this scheme was not yet implemented but serves as a technical instruction for future implementations.

For brevity we restrict to a spin-restricted and Γ -only description. We start with the expression (8.119), derived in Sec. 8.4,

$$E^{\text{SOSEX}} = \frac{1}{2} \int_{-\infty}^{\infty} \frac{d\nu}{2\pi} \sum_{ij}^{\text{occ.}} \sum_{ab}^{\text{unocc.}} c_{ia}(\nu) c_{jb}(\nu) \langle \varphi_j \varphi_i | r_{12}^{-1} | \varphi_a \varphi_b \rangle \langle \varphi_a \varphi_b | W(\nu) | \varphi_i \varphi_j \rangle, \quad (10.24)$$

where the following shorthand was used,

$$c_{ia}(\nu) = \frac{2(\varepsilon_a - \varepsilon_i)}{(\varepsilon_a - \varepsilon_i)^2 + \nu^2}. \quad (10.25)$$

For convenience, the screened interaction $W(\nu)$ (see Eq. 8.113) is assumed to be available in the reciprocal space (plane-wave basis), where the relation to the real space reads,

$$\begin{aligned} \langle \varphi_a \varphi_b | W(\nu) | \varphi_i \varphi_j \rangle &= \int d^3r \int d^3r' W(\mathbf{r}, \mathbf{r}', \nu) \varphi_a^*(\mathbf{r}) \varphi_i(\mathbf{r}) \varphi_b^*(\mathbf{r}') \varphi_j(\mathbf{r}') \\ &= \sum_{\mathbf{G}\mathbf{G}'} W(\mathbf{G}, \mathbf{G}', \nu) \langle \varphi_a | e^{i\mathbf{G}\hat{\mathbf{r}}} | \varphi_i \rangle_{\Omega_0} \langle \varphi_b | e^{i\mathbf{G}'\hat{\mathbf{r}}} | \varphi_j \rangle_{\Omega_0}. \end{aligned} \quad (10.26)$$

Note, that $\langle \varphi_a | e^{i\mathbf{G}\hat{\mathbf{r}}} | \varphi_i \rangle_{\Omega_0}$ was already defined in Eq. (8.30). Since here and in the following k -point sampling is restricted to the Γ -point, we can also assume real valued spatial orbitals and exploit the relations,

$$\langle \varphi_a | e^{i\mathbf{G}\hat{\mathbf{r}}} | \varphi_i \rangle_{\Omega_0} = \langle \varphi_i | e^{i\mathbf{G}\hat{\mathbf{r}}} | \varphi_a \rangle_{\Omega_0} = \langle \varphi_a | e^{-i\mathbf{G}\hat{\mathbf{r}}} | \varphi_i \rangle_{\Omega_0}^*. \quad (10.27)$$

Our strategy consists of the idea to write the SOSEX correction as a trace over an effective polarizability $P(\nu)$ and the screened interaction $W(\nu)$,

$$E^{\text{SOSEX}} = \frac{1}{2} \int_{-\infty}^{\infty} \frac{d\nu}{2\pi} \sum_{\mathbf{G}\mathbf{G}'} P(\mathbf{G}, \mathbf{G}', \nu) W(\mathbf{G}, \mathbf{G}', \nu). \quad (10.28)$$

Starting with (10.24), it is not difficult to identify $P(\nu)$ by

$$\begin{aligned}
 P(\mathbf{G}, \mathbf{G}', \nu) &= \sum_{ij}^{\text{occ.}} \sum_{ab}^{\text{unocc.}} c_{ia}(\nu) c_{jb}(\nu) \langle \varphi_a | e^{-i\mathbf{G}\hat{\mathbf{r}}} | \varphi_i \rangle_{\Omega_0}^* \langle \varphi_b | e^{-i\mathbf{G}'\hat{\mathbf{r}}} | \varphi_j \rangle_{\Omega_0}^* \langle \varphi_j \varphi_i | r_{12}^{-1} | \varphi_a \varphi_b \rangle \\
 &= \sum_{ij}^{\text{occ.}} \sum_{ab}^{\text{unocc.}} c_{ia}(\nu) c_{jb}(\nu) \langle \varphi_a | e^{-i\mathbf{G}\hat{\mathbf{r}}} | \varphi_i \rangle_{\Omega_0}^* \langle \varphi_b | e^{-i\mathbf{G}'\hat{\mathbf{r}}} | \varphi_j \rangle_{\Omega_0}^* \\
 &\quad \times \sum_{\mathbf{G}''} \frac{4\pi}{\mathbf{G}''^2} \langle \varphi_j | e^{-i\mathbf{G}''\hat{\mathbf{r}}} | \varphi_a \rangle_{\Omega_0} \langle \varphi_i | e^{i\mathbf{G}''\hat{\mathbf{r}}} | \varphi_b \rangle_{\Omega_0}
 \end{aligned} \tag{10.29}$$

As will be shown in the following, this quantity can be evaluated in an only quartic scaling algorithm. To achieve this, we first introduce auxiliary states, similar to the definition (10.11),

$$|\psi_i^{\mathbf{G}\nu}\rangle = \sum_a^{\text{unocc.}} c_{ia}(\nu) \langle \varphi_a | e^{-i\mathbf{G}\hat{\mathbf{r}}} | \varphi_i \rangle_{\Omega_0}^* | \varphi_a \rangle. \tag{10.30}$$

The summation over the unoccupied states a can be performed with BLAS level 3 routines, such that the auxiliary state $|\psi_i^{\mathbf{G}\nu}\rangle$ can be calculated with quartic scaling: $N_i N_a N_{\mathbf{G}}^2 \times N_\nu$. Similar to the τ -points of the LTMP2 algorithm, the number of frequency points N_ν is assumed to be largely independent of the system size. Thus, we can write,

$$\begin{aligned}
 P(\mathbf{G}, \mathbf{G}', \nu) &= \sum_{ij}^{\text{occ.}} \sum_b^{\text{unocc.}} c_{jb}(\nu) \langle \varphi_b | e^{-i\mathbf{G}'\hat{\mathbf{r}}} | \varphi_j \rangle_{\Omega_0}^* \\
 &\quad \times \sum_{\mathbf{G}''} \frac{4\pi}{\mathbf{G}''^2} \langle \varphi_j | e^{-i\mathbf{G}''\hat{\mathbf{r}}} | \psi_i^{\mathbf{G}\nu} \rangle_{\Omega_0} \langle \varphi_i | e^{i\mathbf{G}''\hat{\mathbf{r}}} | \varphi_b \rangle_{\Omega_0}.
 \end{aligned} \tag{10.31}$$

In this expression, we find the quantity

$$A_j^{\mathbf{G}\nu}(\mathbf{r}) := \sum_i^{\text{occ.}} \varphi_i^*(\mathbf{r}) \cdot \sum_{\mathbf{G}''} \frac{4\pi}{\mathbf{G}''^2} \langle \varphi_j | e^{-i\mathbf{G}''\hat{\mathbf{r}}} | \psi_i^{\mathbf{G}\nu} \rangle_{\Omega_0} e^{i\mathbf{G}''\mathbf{r}}, \tag{10.32}$$

being essentially a Fourier transform, which is similar to the evaluation of the action of the Fock operator (4.19) on the orbital $|\psi_i^{\mathbf{G}\nu}\rangle$. Here, $A_j^{\mathbf{G}\nu}(\mathbf{r})$ can easily be calculated with a quartic scaling, since a Fast Fourier transform only scales with $N_{\mathbf{G}} \ln N_{\mathbf{G}}$, which is essentially a linear scaling. Hence, we finally obtain,

$$P(\mathbf{G}, \mathbf{G}', \nu) = \sum_j^{\text{occ.}} \sum_b^{\text{unocc.}} c_{jb}(\nu) \langle \varphi_b | e^{-i\mathbf{G}'\hat{\mathbf{r}}} | \varphi_j \rangle_{\Omega_0}^* \int_{\Omega_0} d^3r A_j^{\mathbf{G}\nu}(\mathbf{r}) \varphi_b(\mathbf{r}), \tag{10.33}$$

and after defining

$$B_{jb}^{\mathbf{G}\nu} := c_{jb}(\nu) \int_{\Omega_0} d^3r A_j^{\mathbf{G}\nu}(\mathbf{r}) \varphi_b(\mathbf{r}), \tag{10.34}$$

```

for all  $i, a$  do
   $\rho_{ai}(\mathbf{r}) \leftarrow \varphi_a^*(\mathbf{r})\varphi_i(\mathbf{r})$ 
   $\tilde{\rho}_{ai}(\mathbf{G}) \leftarrow \text{FFT}_{\mathbf{G}}[\rho_{ai}]$ 
  store  $\tilde{\rho}_{ai}(\mathbf{G})$ 
end for
for all  $\nu$  do
  for all  $\mathbf{G}_1$  do
     $c_{ai} \leftarrow (\varepsilon_a - \varepsilon_i)/[(\varepsilon_a - \varepsilon_i)^2 + \nu^2] \quad \forall i, a$ 
     $|w_i\rangle \leftarrow \sum_a c_{ai} \tilde{\rho}_{ai}^*(\mathbf{G}_1)|\varphi_a\rangle \quad \forall i \quad \# \text{ BLAS}$ 
    for all  $j$  do
      for all  $i$  do
         $\varrho(\mathbf{r}) \leftarrow \varphi_j^*(\mathbf{r})w_i(\mathbf{r})$ 
         $\tilde{\varrho}(\mathbf{G}) \leftarrow \text{FFT}_{\mathbf{G}}[\varrho]$ 
         $\tilde{\varrho}(\mathbf{G}) \leftarrow \frac{4\pi}{\mathbf{G}^2}\tilde{\varrho}(\mathbf{G})$ 
         $\varrho(\mathbf{r}) \leftarrow \text{FFT}_{\mathbf{r}}^{-1}[\tilde{\varrho}]$ 
         $A_j(\mathbf{r}) \leftarrow A_j(\mathbf{r}) + \varphi_i^*(\mathbf{r})\varrho(\mathbf{r})$ 
      end for
      for all  $b$  do
         $B_{jb} \leftarrow c_{bj} \int_{\Omega_0} d^3r A_j(\mathbf{r}) \varphi_b(\mathbf{r})$ 
      end for
      store  $B_{jb}$ 
    end for
    for all  $\mathbf{G}_2$  do
       $P(\mathbf{G}_1, \mathbf{G}_2, \nu) \leftarrow \sum_{jb} \tilde{\rho}_{bj}(\mathbf{G}_2)B_{jb} \quad \# \text{ BLAS}$ 
    end for
  end for
end for

```

Figure 10.11: Pseudocode for the calculation of the quantity $P(\mathbf{G}, \mathbf{G}', \nu)$ for the SOSEX algorithm. DFT orbitals φ and orbital energies ε are assumed.

we arrive at

$$P(\mathbf{G}, \mathbf{G}', \nu) = \sum_j^{\text{occ.}} \sum_b^{\text{unocc.}} \langle \varphi_b | e^{-i\mathbf{G}'\hat{\mathbf{r}}} | \varphi_j \rangle_{\Omega_0}^* B_{jb}^{\mathbf{G}\nu}. \quad (10.35)$$

The remaining summation over j and b can, again, be evaluated with BLAS level 3 routines, if the overlap densities are considered as matrices with components b and \mathbf{G}' (for each j). This completes the calculation of the effective polarizability $P(\nu)$, which can be used to evaluate the SOSEX correction via Eq. (10.28). Since all intermediate quantities like $|\psi_i^{\mathbf{G}\nu}\rangle$, $A_j^{\mathbf{G}\nu}(\mathbf{r})$, and $B_{jb}^{\mathbf{G}\nu}$ can be evaluated with a quartic scaling complexity, the entire algorithm will follow a largely quartic scaling. Pseudocode for this algorithm can be found in Fig. 10.11.

The presented scheme was not yet implemented. Due to similarities to the quartic scaling MP2 algorithm, some routines can be recycled (e.g. the calculation of the auxiliary states). The measurement of the prefactor and the break point compared to the quintic scaling code are open questions for future work. Nevertheless, we formally showed that also the SOSEX correction to the RPA can be evaluated with an improved scaling without introducing any additional approximation.

Furthermore, the quantity $P(\mathbf{G}, \mathbf{G}', \nu)$ can serve as an important building block for other many-body diagrams (which are present in the BSE equation),

$$P(\mathbf{G}, \mathbf{G}', \nu) = \text{Diagram 1} = \text{Diagram 2} \quad (10.36)$$

The equation shows two diagrams representing the quantity $P(\mathbf{G}, \mathbf{G}', \nu)$. The first diagram on the left is a folded loop structure with two vertices labeled $G\nu$ and $G'\nu$. The second diagram on the right is a circular loop structure with two vertices labeled $G\nu$ and $G'\nu$. The two diagrams are shown to be equivalent with an equals sign between them.

We note that except for MP2, a formulation in the frequency domain is preferable. In the imaginary time, foldings over two times would occur.

10.3 Cubic scaling MP2: prospects and limitations

It is possible to rearrange the terms of the MP2 correlation energy, such that an evaluation would scale only with the third power of the system size. We present this technique here, however, we stress right away that a large prefactor most likely prohibits its use except for very large systems. Nevertheless, this section illustrates once again that scaling improvements are possible without sacrificing the accuracy.

In Sec. 8.1.6 we presented an expression of the MP2 correlation energy based on Green's functions (8.63). As a reminder, we repeat the exchange part (8.67) for the spin-restricted case here,

$$E_x^{\text{MP2}} = \int_0^\infty d\tau \int d^3r_1 \dots \int d^3r_4 \frac{1}{|\mathbf{r}_1 - \mathbf{r}_2| |\mathbf{r}_3 - \mathbf{r}_4|} \quad (10.37)$$

$$\times G^>(\mathbf{r}_1, \mathbf{r}_3, \tau) G^<(\mathbf{r}_4, \mathbf{r}_1, -\tau) G^>(\mathbf{r}_2, \mathbf{r}_4, \tau) G^<(\mathbf{r}_3, \mathbf{r}_2, -\tau).$$

Note that this expression is not suitable for periodic systems (since the integrals range over the entire space instead of only over one unit cell) and we refer to Sec. 11.1 for a correct periodic formulation which restricts the integrals to the unit cells. Here, the focus is on the concept to achieve a cubic scaling.

The Green's function formulation of the MP2 correlation energy naturally provides a quartic scaling method (only four real space integrals), however, it requires fine real space grids, and therefore, leads to a very large prefactor. For details to the prefactor and real space grids, see Sec. 11.1. The main idea of the cubic scaling approach is to rewrite one of the Coulomb kernels in reciprocal space and then to shift the Fourier transform to the product of two Green's functions. In a first step, we write

$$E_x^{\text{MP2}} = \frac{1}{\Omega} \int_0^\infty d\tau \int d^3r_1 \dots \int d^3r_4 \frac{1}{|\mathbf{r}_1 - \mathbf{r}_2|} \sum_{\mathbf{G}} \frac{4\pi}{\mathbf{G}^2} e^{i\mathbf{G}(\mathbf{r}_3 - \mathbf{r}_4)} \quad (10.38)$$

$$\times G^>(\mathbf{r}_1, \mathbf{r}_3, \tau) G^<(\mathbf{r}_4, \mathbf{r}_1, -\tau) G^>(\mathbf{r}_2, \mathbf{r}_4, \tau) G^<(\mathbf{r}_3, \mathbf{r}_2, -\tau).$$

Secondly, we now consider the real space integrals over \mathbf{r}_3 and \mathbf{r}_4 as Fourier transforms from real space to reciprocal space, and define

$$A_{\mathbf{G}}(\mathbf{r}_1, \mathbf{r}_2, \tau) = \int d^3r_4 G^<(\mathbf{r}_4, \mathbf{r}_1, -\tau) G^>(\mathbf{r}_2, \mathbf{r}_4, \tau) e^{-i\mathbf{G}\mathbf{r}_4}. \quad (10.39)$$

This quantity can be evaluated in a cubic scaling computation time, since a fast Fourier transform scales essentially linear for each pair $\mathbf{r}_1, \mathbf{r}_2$. This allows us to write,

$$E_x^{\text{MP2}} = \frac{1}{\Omega} \int_0^\infty d\tau \int d^3r_1 \int d^3r_2 \frac{1}{|\mathbf{r}_1 - \mathbf{r}_2|} \sum_{\mathbf{G}} \frac{4\pi}{\mathbf{G}^2} A_{\mathbf{G}}(\mathbf{r}_1, \mathbf{r}_2, \tau) A_{-\mathbf{G}}(\mathbf{r}_2, \mathbf{r}_1, \tau), \quad (10.40)$$

which already completes the algorithm. This simple procedure proves that a correlation

method, commonly denoted as quintic scaling, can quickly be converted into a cubic scaling procedure.

The bottleneck, however, is clearly the calculation of the innocent looking quantity $A_G(\mathbf{r}_1, \mathbf{r}_2, \tau)$. Although formally cubic scaling, the calculations require N_r^2 calls of fast Fourier transformation routines, where N_r is the number of real space grid points. This can lead to a tremendous prefactor, shifting the break point of the entire algorithm to huge systems.

We performed quick test calculations with supercells of LiH, containing 8 and 16 atoms using standard cutoff parameters. The presented cubic scaling code took 17.2 minutes and 4 hours for the small and large system, respectively. The quintic scaling code [43], on the other hand, yield the same numerical results after 16.7 seconds and 6.5 minutes, respectively. The break point is estimated to be at about 100 atoms, including about 250 correlated electrons. Compared to the quartic scaling code of Sec. 10.1, the break point will clearly shift to even larger systems.

Nevertheless, in not too distant future, the presented algorithm could become useful, in particular, if the computer power continuous to improve. Clearly, the strategy can also be adapted to the SOSEX method, if the screened interaction is available in real space. The author of this thesis notes, that the presented scheme was developed independently of Ref. [64, 65], where also cubic scaling methods for the correlation energy are presented, however, without numerical performance comparisons to other algorithms.

CHAPTER 11

Stochastic algorithms

Stochastic algorithms are considered as a promising avenue to overcome the high computational effort in wave function based methods in order to calculate the correlation energy of molecules or solids. The computation time can be reduced by allowing for a statistical error. The balance between computation time and statistical error is determined by the sample variance. Hence, the sample variance is the crucial quantity to probe whether a stochastic algorithm can outperform deterministic approaches. Four algorithms, based on stochastic techniques, will be introduced in the following sections. Each section can be considered and read independently.

11.1 Real space Monte Carlo sampling of Feynman diagrams

The canonical formulation of the MP2 energy (8.19) and (8.20) is also called *sum-over-state* representation or *Slater determinant* formulation since it is written as a sum over Hartree-Fock states, which build the Hartree-Fock or also excited Slater determinants. A fundamentally different representation of the MP2 energy is given by the Green's function formulation (8.66) and (8.67),

$$E^{\text{MP2}} = -2 \int_0^\infty d\tau \int d^3r_1 \dots \int d^3r_4 \frac{1}{|\mathbf{r}_1 - \mathbf{r}_2| |\mathbf{r}_3 - \mathbf{r}_4|} \times G^>(\mathbf{r}_1, \mathbf{r}_3, \tau) G^<(\mathbf{r}_3, \mathbf{r}_1, -\tau) G^>(\mathbf{r}_2, \mathbf{r}_4, \tau) G^<(\mathbf{r}_4, \mathbf{r}_2, -\tau) \quad (11.1)$$

$$+ \int_0^\infty d\tau \int d^3r_1 \dots \int d^3r_4 \frac{1}{|\mathbf{r}_1 - \mathbf{r}_2| |\mathbf{r}_3 - \mathbf{r}_4|} \times G^>(\mathbf{r}_1, \mathbf{r}_3, \tau) G^<(\mathbf{r}_4, \mathbf{r}_1, -\tau) G^>(\mathbf{r}_2, \mathbf{r}_4, \tau) G^<(\mathbf{r}_3, \mathbf{r}_2, -\tau) . \quad (11.2)$$

Here, the MP2 energy is the result of a 12 dimensional real space integration (four 3D integrals) over a product of Green's functions and Coulomb potentials (which corresponds to the real space translations of the MP2 Feynman diagrams). Once the Green's function (8.63) is available, the implementation of the real space integration is an embarrassingly simple task, in particular for grid based codes like VASP. Moreover, its system size scaling is inherently quartic (due to the four real space integrals over the entire unit cell), compared to the quintic scaling of the canonical sum-over-states MP2 formulation. Though, fine grids are required to obtain accurate results, leading to extremely large prefactors, which prohibit a direct evaluation of the real space integrals. Note that already a relatively coarse grid of the primitive cell of diamond consists of 10^3 grid points. Hence, in this case, the full integration would cover a volume containing $(10^3)^4 = 10^{12}$ points. Therefore, it is an attractive route to probe whether a stochastic Monte Carlo sampling of the 12 dimensional real space yields fast and accurate MP2 energies. This idea was first suggested by Willow, Kim, and Hirata for molecules [66] and periodic systems [67]. As they write, the "core intellectual contribution" [68] is to find a proper importance sampling function in order to reduce the sample variance. Here, we present new importance sampling techniques, which reduce the variance significantly and provide a possible route for fast and accurate MP2 calculations of large systems.

11.1.1 Monte Carlo integration and importance sampling

In grid based codes like VASP, real space integrations are evaluated using discretized real space grids, i.e. real space integrals are evaluated as a sum over all grid points. A general

real space integral can thus be written as

$$I = \int_{\Omega} d^3r_1 \dots \int_{\Omega} d^3r_d f(\mathbf{r}_1, \dots, \mathbf{r}_d) \rightarrow \left(\frac{\Omega}{N_r} \right)^d \sum_{\mathbf{r}_1 \dots \mathbf{r}_d}^{\text{grid}} f(\mathbf{r}_1, \dots, \mathbf{r}_d), \quad (11.3)$$

where Ω is the volume of integration. In the sum, each \mathbf{r}_i runs over all points of the discretized real space grid. If the grid consists of N_r points, the evaluation of the above sum involves N_r^d summands. We can consider the value I/Ω^d as the population mean of the population $\{ f(\mathbf{r}_1, \dots, \mathbf{r}_d) \mid \mathbf{r}_1, \dots, \mathbf{r}_d \in \text{grid} \}$.

Uniform sampling

The Monte Carlo integration technique estimates this population mean by a random sample mean. We write a sample as $\{ X_i = f(\mathbf{r}_1^{[i]}, \dots, \mathbf{r}_d^{[i]}) \mid i = 1, \dots, N_{\text{MC}} \}$, where $(\mathbf{r}_1^{[i]}, \dots, \mathbf{r}_d^{[i]})$ are N_{MC} tuples of uniformly distributed random grid points. We can now introduce the sample mean,

$$\bar{f} = \frac{1}{N_{\text{MC}}} \sum_{j=1}^{N_{\text{MC}}} X_j, \quad (11.4)$$

and the expectation value of the sample mean,

$$E[\bar{f}] = I/\Omega^d, \quad (11.5)$$

being a consequence of the law of large numbers. Note, that a sample mean \bar{f} is itself a random number, since the sample is a random subset of the full population. We can use \bar{f} to approximate the desired integral I by

$$I_{\text{MC}} = \Omega^d \bar{f} \approx I. \quad (11.6)$$

In order to estimate the reliability of \bar{f} , we use Bienaymés formula to estimate the variance of \bar{f} ,

$$\text{Var}[\bar{f}] = \frac{\text{Var}[X_i]}{N_{\text{MC}}}, \quad (11.7)$$

where the sample variance $\text{Var}[X_i]$ is estimated by the corrected sample variance,

$$\text{Var}[X_i] \approx \frac{1}{N_{\text{MC}} - 1} \sum_{i=1}^{N_{\text{MC}}} (X_i - \bar{f})^2. \quad (11.8)$$

Commonly, the standard deviation is used to estimate the error of an estimated mean (here, the sample mean), hence, we write the error of the sample mean as

$$\sigma[\bar{f}] = \sqrt{\text{Var}[\bar{f}]} = \sqrt{\frac{\text{Var}[X_i]}{N_{\text{MC}}}}, \quad (11.9)$$

which directly yields the error of the approximation of the integral $\sigma[I_{\text{MC}}] = \Omega^d \sigma[\bar{f}]$. Thus, we can improve the approximation simply by increasing N_{MC} , i.e. by increasing the sample size. However, if the sample variance $\text{Var}[X_i]$ is large, the Monte Carlo integration can become unpractical or rather very expensive. Hence, the sample variance $\text{Var}[X_i]$ is the key quantity which determines whether a Monte Carlo approach is competitive to a full evaluation of the integral. If, for instance, 10^{-2} eV is an acceptable error, the Monte Carlo approach is competitive only if

$$\sqrt{\frac{\text{Var}[X_i]}{N_r^d}} \ll 10^{-2} \text{ eV} \quad \Leftrightarrow \quad \text{Var}[X_i] \ll N_r^d \cdot 10^{-4} \text{ eV}^2. \quad (11.10)$$

Employing the mentioned example of the diamond primitive cell, consisting of $N_r = 10^3$ grid points, the Monte Carlo integration of a MP2 calculation ($d = 4$) is competitive if $\text{Var}[X_i] \ll 10^8 \text{ eV}^2$. Surprisingly, we find a sample variance of roughly 10^8 eV^2 for a uniformly sampled Monte Carlo evaluation. Hence, uniform sampling is far from efficient.

Importance sampling

The importance sampling technique allows to focus the sampling points to those areas of the integral volume where the contributions are large. It is defined by a probability function $p(\mathbf{r}_1, \dots, \mathbf{r}_d) > 0$ which can be easily integrated and normalized to

$$\sum_{\mathbf{r}_1 \dots \mathbf{r}_d} p(\mathbf{r}_1, \dots, \mathbf{r}_d) = 1. \quad (11.11)$$

The random samples are then defined by

$$\left\{ Y_i = \frac{f(\mathbf{r}_1^{[i]}, \dots, \mathbf{r}_d^{[i]})}{p(\mathbf{r}_1^{[i]}, \dots, \mathbf{r}_d^{[i]})} \mid i = 1, \dots, N_{\text{MC}} \right\}, \quad (11.12)$$

where the tuples $\{ (\mathbf{r}_1^{[i]}, \dots, \mathbf{r}_d^{[i]}) \mid i = 1, \dots, N_{\text{MC}} \}$ are not drawn uniformly but obey the probability distribution (sampling function) $p(\mathbf{r}_1, \dots, \mathbf{r}_d)$. The sample mean similarly reads

$$\bar{f} = \frac{1}{N_{\text{MC}}} \sum_{j=1}^{N_{\text{MC}}} Y_j, \quad (11.13)$$

and the error of the integral approximation is given by

$$\sigma[I_{\text{MC}}] = \Omega^d \sqrt{\frac{\text{Var}[Y_i]}{N_{\text{MC}}}}. \quad (11.14)$$

The main challenge is therefore to find a suitable sampling function $p(\mathbf{r}_1, \dots, \mathbf{r}_d)$ which reduces the variance significantly $\text{Var}[Y_i] \ll \text{Var}[X_i]$, allowing for a faster convergence of the integral estimator I_{MC} . In general, a good sampling function resembles the integrand

up to a constant, $p(\mathbf{r}_1, \dots, \mathbf{r}_d) \approx Cf(\mathbf{r}_1, \dots, \mathbf{r}_d)$. In practice, however, the requirement to quickly normalize the sampling function, restricts us to product functions of the form

$$p(\mathbf{r}_1, \dots, \mathbf{r}_d) = p_{12}(\mathbf{r}_1, \mathbf{r}_2)p_{34}(\mathbf{r}_3, \mathbf{r}_4)\dots, \quad (11.15)$$

such that the calculation of the necessary normalization factors also reduces to products

$$\sum_{\mathbf{r}_1 \dots \mathbf{r}_d} p(\mathbf{r}_1, \dots, \mathbf{r}_d) = \left(\sum_{\mathbf{r}_1 \mathbf{r}_2} p_{12}(\mathbf{r}_1, \mathbf{r}_2) \right) \left(\sum_{\mathbf{r}_3 \mathbf{r}_4} p_{34}(\mathbf{r}_3, \mathbf{r}_4) \right) \dots \quad (11.16)$$

Here, we picked products of probability functions which depend only on two coordinates, $(\mathbf{r}_1, \mathbf{r}_2)$, $(\mathbf{r}_3, \mathbf{r}_4)$, etc., but also different choices like three or only one coordinate are possible.

11.1.2 Monte Carlo integration of the MP2 energy for periodic systems

With Eq. (8.67) we derived an expression for the MP2 energy (here only the exchange part). For spin-restricted systems, this equation reads,

$$E_x^{\text{MP2}} = \int_0^\infty d\tau \int_\Omega d^3r_1 \dots \int_\Omega d^3r_4 \frac{1}{|\mathbf{r}_1 - \mathbf{r}_2| |\mathbf{r}_3 - \mathbf{r}_4|} \\ \times G^>(\mathbf{r}_1, \mathbf{r}_3, \tau) G^<(\mathbf{r}_4, \mathbf{r}_1, -\tau) G^>(\mathbf{r}_2, \mathbf{r}_4, \tau) G^<(\mathbf{r}_3, \mathbf{r}_2, -\tau).$$

Here, Ω is the volume of the entire system (not just one unit cell), and $G^<$, $G^>$ are the retarded and advanced Green's functions, see Eq. (8.64) and (8.65). However, for periodic systems, we can restrict the integration volume to the unit cell by a simple reformulation of the Green's function and the Coulomb potential. If we start with the periodic MP2 expression of Eq. (8.36), we find that the Green's functions possess a k -point dependency,

$$G_k^>(\mathbf{r}, \mathbf{r}', \tau) = i \sum_a^{\text{virt.}} \langle \mathbf{r} | a\mathbf{k} \rangle \langle a\mathbf{k} | \mathbf{r}' \rangle e^{-\varepsilon_{a\mathbf{k}} \tau}. \quad (11.17)$$

The same holds for the retarded counterpart. Furthermore, the Coulomb potential has to be rewritten as a periodic function,

$$v_{\mathbf{k}}(\mathbf{r}, \mathbf{r}') = v_{\mathbf{k}}(\mathbf{r} - \mathbf{r}') = \sum_{\mathbf{G}} \frac{4\pi}{(\mathbf{G} + \mathbf{k})^2} e^{i(\mathbf{G} + \mathbf{k})(\mathbf{r} - \mathbf{r}')}, \quad (11.18)$$

in order to restrict the integrals to the unit cell. Note, that the sum over all reciprocal lattice vectors \mathbf{G} ensures that $v_{\mathbf{k}}(\mathbf{r} + \mathbf{R}) = e^{i\mathbf{k}\mathbf{R}} v_{\mathbf{k}}(\mathbf{r})$. An equivalent formulation, which

recalls the original Coulomb potential, reads

$$v_{\mathbf{k}}(\mathbf{r}, \mathbf{r}') = \Omega_0 \sum_{\mathbf{R}} \frac{1}{|\mathbf{r} - \mathbf{r}' - \mathbf{R}|} e^{i\mathbf{k}\mathbf{R}}. \quad (11.19)$$

The original Coulomb potential would be restored, if we also integrate \mathbf{k} over the Brillouine zone,

$$\int_{\text{BZ}} \frac{d^3k}{(2\pi)^3} v_{\mathbf{k}}(\mathbf{r}, \mathbf{r}') = \frac{1}{|\mathbf{r} - \mathbf{r}'|}. \quad (11.20)$$

Using this definitions, we can write for a periodic system with unit cell volume Ω_0

$$\begin{aligned} E_x^{\text{MP2}} = & \frac{1}{\Omega_0^3} \int_0^\infty d\tau \int_{\text{BZ}} \frac{d^3k_1}{(2\pi)^3} \int_{\text{BZ}} \frac{d^3k_2}{(2\pi)^3} \int_{\text{BZ}} \frac{d^3q}{(2\pi)^3} \int_{\Omega_0} d^3r_1 \dots \int_{\Omega_0} d^3r_4 \\ & \times G_{T(\mathbf{k}_2 - \mathbf{q})}^>(\mathbf{r}_1, \mathbf{r}_3, \tau) G_{\mathbf{k}_1}^<(\mathbf{r}_4, \mathbf{r}_1, -\tau) G_{T(\mathbf{k}_1 + \mathbf{q})}^>(\mathbf{r}_2, \mathbf{r}_4, \tau) G_{\mathbf{k}_1}^<(\mathbf{r}_3, \mathbf{r}_2, -\tau) \\ & \times v_{T(\mathbf{k}_1 - \mathbf{k}_2 + \mathbf{q})}(\mathbf{r}_1, \mathbf{r}_2) v_{-\mathbf{q}}(\mathbf{r}_3, \mathbf{r}_4). \quad (11.21) \end{aligned}$$

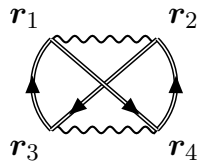
11.1.3 Implementation of efficient importance sampling techniques

For simplicity, our implementation is constrained to the Γ -only sampling of the Brillouine zone. Hence, discretizing Eq. (11.21) results in,

$$\begin{aligned} E_x^{\text{MP2}} = & \frac{1}{\Omega_0^2} \frac{1}{N_r^4} \sum_{\tau} w_{\tau} \sum_{\mathbf{r}_1 \dots \mathbf{r}_4}^{\Omega_0} v(\mathbf{r}_1, \mathbf{r}_2) v(\mathbf{r}_3, \mathbf{r}_4) \\ & \times G^>(\mathbf{r}_1, \mathbf{r}_3, \tau) G^<(\mathbf{r}_4, \mathbf{r}_1, -\tau) G^>(\mathbf{r}_2, \mathbf{r}_4, \tau) G^<(\mathbf{r}_3, \mathbf{r}_2, -\tau), \quad (11.22) \end{aligned}$$

where we suppress the subscript for the k -points. Here, w_{τ} and N_r denote the weights of the quadrature of the τ integration [59] and the number of real space grid points, respectively. Note, that we also restrict our implementation to norm conserving pseudopotentials (neglecting the PAW method) during this chapter. We do this for a simpler evaluation of the real space Green's functions.

We can write the exchange MP2 energy as a Feynman diagram¹,



$$(11.23)$$

which we will also use to illustrate the importance sampling techniques. The symbol

¹Feynman diagrams were not introduced in this thesis. The interested reader is referred to Ref. [37].

method	variance [keV ²]	time [min]	E_x^{MP2} [eV]	break cond. [eV]
0	40500	(~ 1 year)	-	0.01
1	232	(38 · 60)	-	0.01
2	54	(9 · 60)	-	0.01
3	5.0	49.0	16.899	0.01
4	1.9	18.2	16.900	0.01
5	6.5	63.8	16.880	0.01
6	1.2	11.9	16.920	0.01
7	0.8	7.6	16.921	0.01
8	0.7	6.3	16.901	0.01
exact	-	2.3	16.907	-

Table 11.1: Comparison of the variance of the different importance sampling methods for the described benchmark system. The calculations were performed on 8 Intel Xeon E5-2620 v4 @ 2.10GHz processors. We also provide the exact result of the exchange MP2 energy, calculated with the quintic scaling MP2 algorithm [43]. The Monte Carlo sampling is stopped when the statistical error (11.14) is less or equal to the break condition. The choice of 0.01 eV corresponds to 0.31 meV per valence electron. Values in brackets are only estimates.

⇒ corresponds to the Green's functions at the Hartree-Fock level.

We implemented eight different importance sampling procedures. We distinguish these eight methods by the index $i = 0, 1, \dots, 8$ in the sampling probability distribution $p^{(i)}$, where 0 stands for a uniform sampling. A comparison of the sample variance can be found in Tab. 11.1. The benchmark system is a diamond supercell containing 8 C atoms. Since we use a norm conserving pseudopotential (no PAW) the plane-wave cutoffs were set to quite large values, $E_{\text{cut}} = 800$ eV and $E_{\text{cut}}^{\text{aux}} = 533$ eV. Each C atom provides 4 valence electrons, hence one supercell includes 32 electrons. This results in a total of 2328 Hartree-Fock orbitals and a three dimensional real space grid with $18^3 = 5832$ points. The τ -integration is evaluated on 8 quadrature points.

Importance sampling probability distributions

The first and most simple approach samples the real space grid points according to the periodic electron-electron potential, i.e. we draw the random grid points according to

$$p^{(1)}(\mathbf{r}_1, \mathbf{r}_2) = v(\mathbf{r}_1, \mathbf{r}_2) = \underbrace{\mathbf{r}_1 \text{ --- } \mathbf{r}_2}_{\text{wavy line}}, \quad (11.24)$$

where the full distribution reads,

$$p^{(1)}(\mathbf{r}_1, \mathbf{r}_2, \mathbf{r}_3, \mathbf{r}_4) = \gamma^{(1)} p^{(1)}(\mathbf{r}_1, \mathbf{r}_2) p^{(1)}(\mathbf{r}_3, \mathbf{r}_4), \quad (11.25)$$

with the normalization factor

$$\gamma^{(1)} = \left(\sum_{\mathbf{r}_1 \mathbf{r}_2} p^{(1)}(\mathbf{r}_1, \mathbf{r}_2) \right)^{-2}. \quad (11.26)$$

This approach seems promising, since the the electron-electron potential is singular for $\mathbf{r}_1 = \mathbf{r}_2$, suggesting large contributions. However, numerically, the periodic potential $v(\mathbf{r}_1, \mathbf{r}_2)$ is not singular at $\mathbf{r}_1 = \mathbf{r}_2$ since the sum,

$$v(\mathbf{r}, \mathbf{r}) = \sum_{\mathbf{G}} \frac{4\pi}{G^2} e^{i(\mathbf{G}+\mathbf{k})(\mathbf{r}-\mathbf{r})} = \sum_{\mathbf{G}} \frac{4\pi}{G^2} < \infty \quad (11.27)$$

is limited by the auxiliary cutoff $E_{\text{cut}}^{\text{aux}}$. Still, the energy contribution for $\mathbf{r}_1 = \mathbf{r}_2$ will be large. As evident from Tab. 11.1, the variance is reduced by 2 orders of magnitude compared to a uniform sampling (method 0).

Alternatively, we can include a density-like quantity into the importance sampling by

$$\begin{aligned} p^{(2)}(\mathbf{r}_1, \mathbf{r}_2) &= |v(\mathbf{r}_1, \mathbf{r}_2) G^<(\mathbf{r}_1, \mathbf{r}_1, -\tau_{\min}) G^<(\mathbf{r}_2, \mathbf{r}_2, -\tau_{\min})| \\ &= \text{ABS} \left[\text{Diagram} \right]. \end{aligned} \quad (11.28)$$

Here, ABS stands for the absolute value. A similar approach was suggested in Ref. [68]. Note that for small/vanishing τ the diagonal of the real space Green's function is similar/equal to the electron density. In our implementation, we picked the smallest τ value of the quadrature [59], denoted as τ_{\min} . We observe a clear improvement compared to method 1.

Instead of the electron-electron interaction, method 3 tries to mimic the advanced and retarded Green's function in the exchange MP2 diagram. But since one advanced and one retarded Green's function cover three real space points in the exchange MP2 diagram, we have to trace out one of them, in order to arrive at a reduced probability distribution, that only depends on two points,

$$p^{(3)}(\mathbf{r}_1, \mathbf{r}_3, \tau) = \sum_{\mathbf{r}_4}^{\Omega_0} |G^>(\mathbf{r}_1, \mathbf{r}_3, \tau) G^<(\mathbf{r}_4, \mathbf{r}_1, -\tau)| = \sum_{\mathbf{r}_4}^{\Omega_0} \text{ABS} \left[\text{Diagram} \right]. \quad (11.29)$$

Here, we decided to keep the full advanced Green's function and to trace over the retarded Green's function. This is because the ratio of the diagonal to the off-diagonal elements is much larger for the advanced than for the retarded Green's function. Hence, the case

$\mathbf{r}_1 = \mathbf{r}_3$ is more important than $\mathbf{r}_1 = \mathbf{r}_4$. The variance is reduced by 4 orders of magnitude compared to uniform sampling and by 1 order of magnitude compared to method 2. We conclude that $\mathbf{r}_1 = \mathbf{r}_3$ seems to be more important than $\mathbf{r}_1 = \mathbf{r}_2$. Method 3 has to be calculated for each τ point individually and the full probability distribution reads,

$$p^{(3)}(\mathbf{r}_1, \mathbf{r}_2, \mathbf{r}_3, \mathbf{r}_4, \tau) = \gamma^{(3)} p^{(3)}(\mathbf{r}_1, \mathbf{r}_3, \tau) p^{(3)}(\mathbf{r}_2, \mathbf{r}_4, \tau), \quad (11.30)$$

with the normalization factor

$$\gamma^{(3)} = \left(\sum_{\mathbf{r}_1 \mathbf{r}_3} p^{(3)}(\mathbf{r}_1, \mathbf{r}_3) \right)^{-2}. \quad (11.31)$$

Method 4 is a variation of method 3, including also the electron-electron interaction,

$$p^{(4)}(\mathbf{r}_1, \mathbf{r}_3, \tau) = \sum_{\mathbf{r}_2}^{\Omega_0} | G^>(\mathbf{r}_1, \mathbf{r}_3, \tau) G^<(\mathbf{r}_3, \mathbf{r}_2, -\tau) v(\mathbf{r}_1, \mathbf{r}_2) |$$

$$= \sum_{\mathbf{r}_2}^{\Omega_0} \text{ABS} \left[\begin{array}{c} \mathbf{r}_1 \qquad \mathbf{r}_2 \\ \curvearrowright \\ \mathbf{r}_3 \end{array} \right]. \quad (11.32)$$

There is, however, a major differences to method 3. The calculation of $p^{(4)}$ involves a cubic scaling matrix-matrix multiplication. Nevertheless, in our benchmark calculations, method 4 shows a smaller variance than to method 3.

A more symmetric approach is given by method 5, where we start with both advanced Green's functions and both electron-electron interactions, however, tracing out the points \mathbf{r}_2 and \mathbf{r}_4 ,

$$p^{(5)}(\mathbf{r}_1, \mathbf{r}_3, \tau) = \sum_{\mathbf{r}_2 \mathbf{r}_4}^{\Omega_0} | v(\mathbf{r}_1, \mathbf{r}_2) v(\mathbf{r}_3, \mathbf{r}_4) G^>(\mathbf{r}_1, \mathbf{r}_3, \tau) G^>(\mathbf{r}_2, \mathbf{r}_4, \tau) |$$

$$= \sum_{\mathbf{r}_2, \mathbf{r}_4}^{\Omega_0} \text{ABS} \left[\begin{array}{c} \mathbf{r}_1 \qquad \mathbf{r}_2 \\ \curvearrowright \\ \mathbf{r}_3 \qquad \mathbf{r}_4 \end{array} \right]. \quad (11.33)$$

The performance of the variance is of the same order as method 3. We can improve method 5 by including one retarded Green's function, which leads to method 6,

$$\begin{aligned}
 p^{(6)}(\mathbf{r}_1, \mathbf{r}_3, \tau) &= \sum_{\mathbf{r}_2, \mathbf{r}_4}^{\Omega_0} |v(\mathbf{r}_1, \mathbf{r}_2) v(\mathbf{r}_3, \mathbf{r}_4) G^>(\mathbf{r}_1, \mathbf{r}_3, \tau) G^>(\mathbf{r}_2, \mathbf{r}_4, \tau) G^<(\mathbf{r}_4, \mathbf{r}_1, -\tau)| \\
 &= \sum_{\mathbf{r}_2, \mathbf{r}_4}^{\Omega_0} \text{ABS} \left[\begin{array}{c} \mathbf{r}_1 \qquad \mathbf{r}_2 \\ \text{---} \text{---} \text{---} \text{---} \\ \text{---} \text{---} \text{---} \text{---} \\ \mathbf{r}_3 \qquad \mathbf{r}_4 \end{array} \right]. \quad (11.34)
 \end{aligned}$$

Including also the second retarded Green's function, which would complete the exchange MP2 diagram, is not possible, since we want to limit the computational complexity of the calculation of the importance sampling to cubic scaling.

Surprisingly, the smallest variance was achieved by weighting functions, that are not building blocks of the exchange diagram at all. The absolute value of the polarizability $\chi(\mathbf{r}_1, \mathbf{r}_3, \tau)$, being part of the direct MP2 diagram, turns out to be a cheap and efficient probability for importance sampling of the exchange diagram,

$$p^{(7)}(\mathbf{r}_1, \mathbf{r}_3, \tau) = \underbrace{|G^>(\mathbf{r}_1, \mathbf{r}_3, \tau) G^<(\mathbf{r}_3, \mathbf{r}_1, -\tau)|}_{\chi(\mathbf{r}_1, \mathbf{r}_3, \tau)} = \text{ABS} \left[\begin{array}{c} \mathbf{r}_1 \\ \text{---} \text{---} \text{---} \\ \mathbf{r}_3 \end{array} \right], \quad (11.35)$$

and is denoted as method 7. We also generalized this to the absolute value of the full direct MP2 diagram, reduced by the points \mathbf{r}_2 and \mathbf{r}_4 . The corresponding weight function is termed as method 8 and reads,

$$\begin{aligned}
 p^{(8)}(\mathbf{r}_1, \mathbf{r}_3, \tau) &= \\
 &\sum_{\mathbf{r}_2, \mathbf{r}_4}^{\Omega_0} |v(\mathbf{r}_1, \mathbf{r}_2) v(\mathbf{r}_3, \mathbf{r}_4) G^>(\mathbf{r}_1, \mathbf{r}_3, \tau) G^>(\mathbf{r}_2, \mathbf{r}_4, \tau) G^<(\mathbf{r}_3, \mathbf{r}_1, -\tau) G^<(\mathbf{r}_4, \mathbf{r}_2, -\tau)| \\
 &= \sum_{\mathbf{r}_2, \mathbf{r}_4}^{\Omega_0} \text{ABS} \left[\begin{array}{c} \mathbf{r}_1 \qquad \mathbf{r}_2 \\ \text{---} \text{---} \text{---} \text{---} \\ \text{---} \text{---} \text{---} \text{---} \\ \mathbf{r}_3 \qquad \mathbf{r}_4 \end{array} \right]. \quad (11.36)
 \end{aligned}$$

As evident from Tab. 11.1, method 8 shows the best performance for our benchmark system. The variance is reduced by a factor of 6000 compared to a uniform sampling and by roughly two orders of magnitude compared to method 2. Until now, method 2 was the state of the art, introduced by Hirata and co workers in Ref. [68, 66, 67]. We thus

improved the efficiency of the Monte Carlo MP2 approach significantly. With method 8, the algorithm becomes competitive with existing and efficient periodic MP2 codes. Due to the low system size scaling (see Sec. 11.1.4) the Monte Carlo MP2 method can be considered as a promising candidate to outperform exact MP2 algorithms.

Details of implementation, illustrated for method 8

For our implementation we resort on existing routines which provide the Green's functions in reciprocal space (see Ref. [69]). A simple Fourier transform yields the real space Green's functions $G^<(\mathbf{r}, \mathbf{r}', \tau)$ and $G^>(\mathbf{r}, \mathbf{r}', \tau)$. This requires a cubic scaling step, however, negligible for our benchmark calculations. Storing the Green's functions leads to a favorable quadratic scaling of the memory requirement with respect to the system size.

The code is parallelized via the τ points. Each core calculates the Green's function and the MP2 energy for one τ point. This strategy is sufficient for the considered benchmark system. For larger systems, however, it is not applicable, and would have to be recoded, since it restricts the number of cores to the number of τ points (usually not larger than 8) and can not exploit the fact, that the variance of the Monte Carlo sampling is different for each τ point.

To calculate the probability distribution $p^{(8)}(\mathbf{r}_1, \mathbf{r}_3, \tau)$, we introduce and store the matrix $\tilde{\chi}$ for each τ point, corresponding to the absolute value of the polarizability,

$$\tilde{\chi}(\mathbf{r}_1, \mathbf{r}_3, \tau) = |G^>(\mathbf{r}_1, \mathbf{r}_3, \tau) G^<(\mathbf{r}_3, \mathbf{r}_1, -\tau)|. \quad (11.37)$$

The probability distribution $p^{(8)}(\mathbf{r}_1, \mathbf{r}_3, \tau)$ can then be written as

$$\begin{aligned} p^{(8)}(\mathbf{r}_1, \mathbf{r}_3, \tau) &= \sum_{\mathbf{r}_2 \mathbf{r}_4}^{\Omega_0} v(\mathbf{r}_1, \mathbf{r}_2) v(\mathbf{r}_3, \mathbf{r}_4) \tilde{\chi}(\mathbf{r}_1, \mathbf{r}_3, \tau) \tilde{\chi}(\mathbf{r}_2, \mathbf{r}_4, \tau) \\ &= \tilde{\chi}(\mathbf{r}_1, \mathbf{r}_3, \tau) \cdot (v \tilde{\chi} v)(\mathbf{r}_1, \mathbf{r}_3, \tau) \end{aligned} \quad (11.38)$$

where $v \tilde{\chi} v$ is understood as matrix-matrix multiplications. The distribution $p^{(8)}(\mathbf{r}_1, \mathbf{r}_3, \tau)$ can simply be interpreted as the importance of the tuple $(\mathbf{r}_1, \mathbf{r}_3)$ to the direct MP2 energy for this τ point. The full probability distribution for all points $(\mathbf{r}_1, \mathbf{r}_2, \mathbf{r}_3, \mathbf{r}_4)$ reads

$$p^{(8)}(\mathbf{r}_1, \mathbf{r}_2, \mathbf{r}_3, \mathbf{r}_4, \tau) = \gamma^{(8)} p^{(8)}(\mathbf{r}_1, \mathbf{r}_3, \tau) p^{(8)}(\mathbf{r}_2, \mathbf{r}_4, \tau), \quad (11.39)$$

with the normalization factor

$$\gamma^{(8)} = \left(\sum_{\mathbf{r}_1 \mathbf{r}_3} \tilde{\chi}(\mathbf{r}_1, \mathbf{r}_3, \tau) \cdot (v \tilde{\chi} v)(\mathbf{r}_1, \mathbf{r}_3, \tau) \right)^{-2}. \quad (11.40)$$

The tuples $(\mathbf{r}_1, \mathbf{r}_3)$ and $(\mathbf{r}_2, \mathbf{r}_4)$ are drawn independently using the inversion sampling method based on the cumulative distribution of $p^{(8)}$. Furthermore, we use the redundant pairs technique as described in Ref. [68] to accelerate the generation of random real space

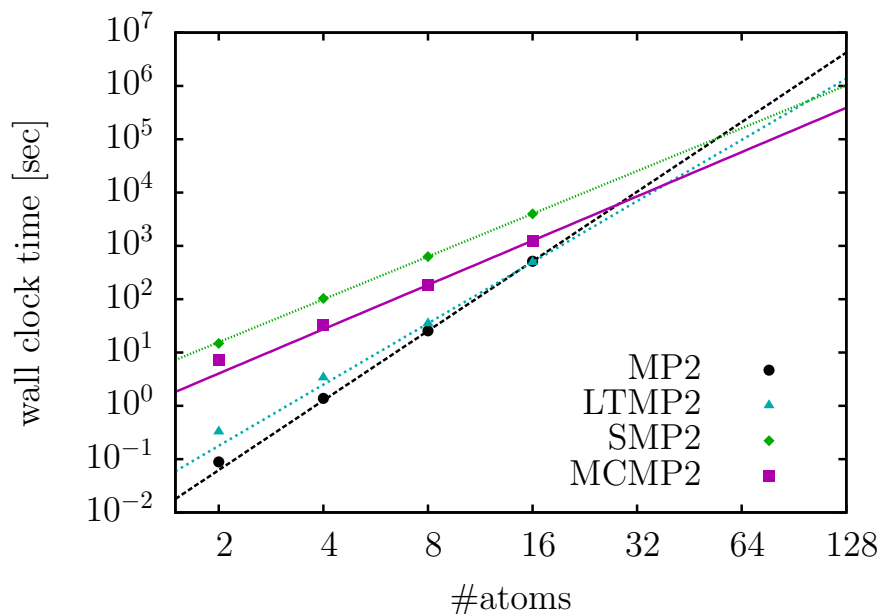


Figure 11.1: Comparison of the system size scaling of the Monte Carlo MP2 code based on method 8 with different MP2 implementations. The curves were fitted and extrapolated to 128 C atoms. The exponents of the MP2 / LTMP2 / SMP2 / MCMP2 fits read 4.3 / 3.8 / 2.7 / 2.8.

pairs (r_1, r_3) and (r_2, r_4) .

11.1.4 Measured system size scaling

In this section, we present the system size scaling of the variance and the computation time. We considered supercells of cubic diamond containing 2, 4, 8 and 16 carbon atoms. We set the plane-wave cutoff to $E_{\text{cut}} = 500$ eV and $E_{\text{cut}}^{\text{aux}} = 333$ eV. The number of real space grid points amounts to 1000, 2000, 4000, and 8000 for the cells containing 2, 4, 8, and 16 C atoms, respectively.

The calculations are performed on 8 Intel Xeon E5-2620 v4 @ 2.10GHz processors and include the Monte Carlo MP2 algorithm (MCMP2) based on method 8, the stochastic MP2 algorithm (SMP2) from Sec. 11.2 (see also Ref. [46]), the quartic scaling LTMP2 algorithm from Sec. 10.1 (see also Ref. [41]), and the quintic scaling MP2 code (MP2) from Ref. [43]. Since method 8 makes use of cubic scaling BLAS level 3 routines, we included the exact calculation of the direct MP2 term in the MCMP2 code without noticeably increasing the computation time. Thus all algorithms in the comparison evaluate the full MP2 correlation energy. The break condition for the stochastic codes was set to an absolute error of 0.016 eV. The result for the computation times in dependence of the cell size can be seen in Fig. 11.1. According to the extrapolation of the curves, the break point for the MCMP2 code can be expected around 32 C atoms (128 correlated electrons). Although the calculation of the importance sampling probability $p^{(8)}$ scales cubically with

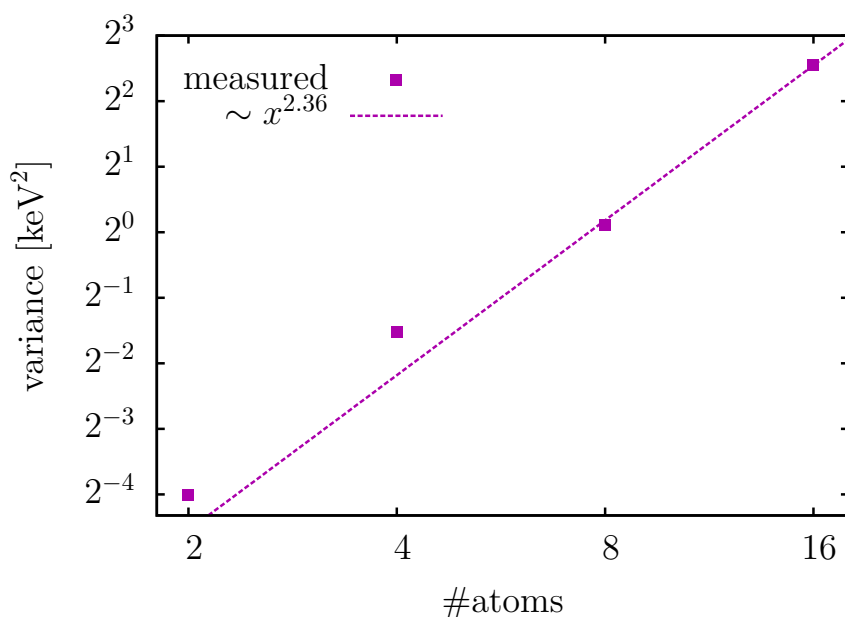


Figure 11.2: Scaling of the sample variance with respect to the system size. Supercells of diamond containing 2 to 16 C atoms were used. The fit yields a scaling exponent of 2.36.

the system size, the Monte Carlo sampling by itself possesses only a roughly quadratic scaling, as evident from Fig. 11.2. Note, that the computation time is directly proportional to the variance, if a fixed absolute statistical error is assumed. Thus, if necessary, a quadratic scaling of the MCMP2 code can be achieved, if both, the direct and the exchange contribution, are calculated stochastically using method 7 instead of 8.

We also measured the scaling of the sample variance with respect to the basis set size, using the 8 C supercell of diamond. The plane-wave cutoff, that controls the number of plane-waves, was varied from 50 to 1100 eV, being the basis to store to Hartree-Fock orbitals. For large bases the sample variance is surprisingly insensitive to the basis set size and possesses a sublinear scaling, as can be seen in Fig. 11.3. We explain this by the fact, that the importance sampling probability itself depends on the basis set size and therefore compensates a possible increasing roughness of the integrand. This is favorable, since the MP2 energy converges slowly with respect to the basis set size.

11.1.5 Conclusion

We presented importance sampling techniques for the real space Monte Carlo MP2 algorithm, which allow for competitive MP2 calculations of large systems. Compared to the current state of the art, given by the sampling based on the electron-electron interaction and the density (method 2), we reduced the variance by roughly two orders of magnitude (method 8). We also showed, that the Monte Carlo sampling outperforms the stochastic MP2 algorithm based on random orbitals from Sec. 11.2. We believe that further

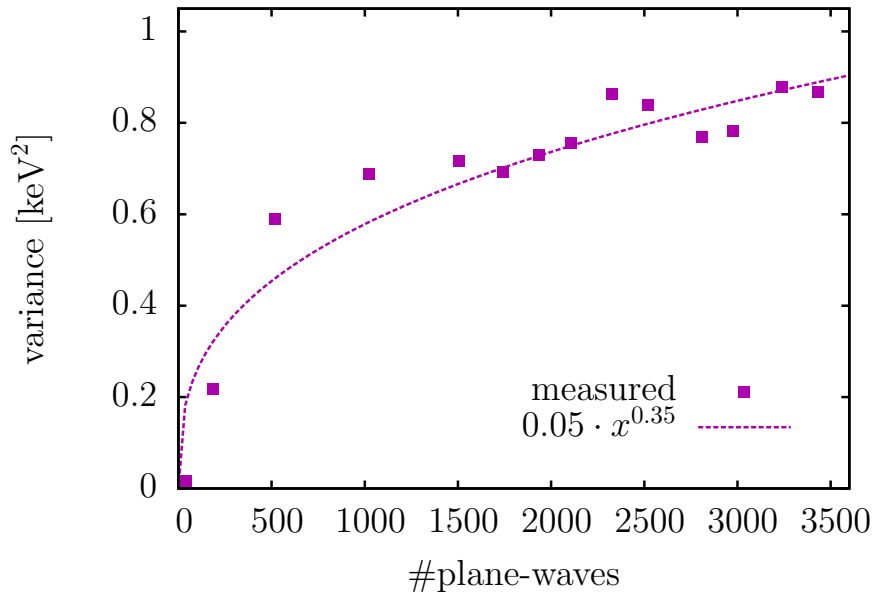


Figure 11.3: Sublinear scaling of the sample variance with respect to the basis set size. The strong scattering of the points is caused by the slow convergence of the sample variance with respect to the sample size.

investigations of the Monte Carlo samples will lead to even better importance sampling techniques. Statistical outliers could be sampled systematically by rejection based techniques, allowing for sampling distributions which depend on more than just two real space points. Highly efficient parallelization schemes are accessible, since the generation and evaluation of random real space points can be distributed among the the cores without difficulty. Exploiting the fact that the correlation energy converges faster for large τ , could lead to a significant speed up, that was missed in our simple implementation. Moreover, the presented importance sampling techniques can easily be adopted to any Feynman diagram in the real space basis like the second-order screened exchange (SOSEX) diagram. The only drawback for routine calculations is that we can presently only use norm conserving pseudo potentials. An implementation for the PAW technique would require a substantial coding effort.

Summarized, the new developed importance sampling techniques make the real space Monte Carlo sampling of Feynman diagrams a promising route for fast and accurate correlation energy calculations for periodic systems with large unit cells.

11.2 Periodic MP2 with stochastic orbitals

In this section we present a stochastic MP2 approach, based on the unitary invariant Laplace transformed MP2 formulation (LTMP2). The time-dependent HF orbitals are rotated stochastically in the Hilbert space. The LTMP2 expression is then evaluated with these stochastic orbitals in the plane wave basis, giving a stochastic energy whose expectation value is the MP2 energy. The algorithm is inspired by the work of Neuhauser et. al. [70]. As an extension we implemented correlated sampling which drastically speeds up the calculation. The algorithm is highly parallelized with MPI and OpenMP. One of our main objectives is to study the scaling of the variance with the system size and whether this method is competitive on systems with about 100 valence orbitals when absolute accuracies below 1 meV per valence orbital are required, like for adsorption energies, binding energies, or surface energies. If a fixed absolute statistical error, independent of the system size, is desired, the algorithm scales cubically with system size, whereas linear scaling can be observed in the case of a fixed relative statistical error (per valence orbital). The algorithm is implemented in the Vienna ab initio simulation package (VASP) [57, 11]. This section largely follows the author's peer reviewed publication [46].

11.2.1 Stochastic orbitals in the plane wave basis

Since the LTMP2 formulation was already derived in Sec. 8.1.5, we directly start with the spin-restricted version of Eq. (8.60),

$$E_x^{\text{MP2}} = \int_0^\infty d\tau \sum_{ij}^{\text{occ.}} \sum_{ab}^{\text{virt.}} \langle \varphi_i^\tau \varphi_j^\tau | r_{12}^{-1} | \varphi_a^\tau \varphi_b^\tau \rangle \langle \varphi_a^\tau \varphi_b^\tau | r_{12}^{-1} | \varphi_j^\tau \varphi_i^\tau \rangle. \quad (11.41)$$

For brevity all derivations are performed for the exchange part only and also k -point sampling is omitted. As in Eq. (8.58), the imaginary time-dependent Hartree-Fock orbitals are defined by

$$|\varphi_i^\tau\rangle = e^{\varepsilon_i \tau/2} |\varphi_i\rangle, \quad |\varphi_a^\tau\rangle = e^{-\varepsilon_a \tau/2} |\varphi_a\rangle. \quad (11.42)$$

The LTMP2 formulation is invariant under unitary transformations of the time-dependent Hartree-Fock orbitals. This invariance can be recognized by defining a new set of unitary transformed time-dependent orbitals via

$$|\psi_i^\tau\rangle = \sum_k^{\text{occ.}} u_{ik} |\varphi_k^\tau\rangle, \quad |\psi_a^\tau\rangle = \sum_c^{\text{virt.}} v_{ac} |\varphi_c^\tau\rangle, \quad (11.43)$$

where u and v are two arbitrary unitary matrices in the occupied and unoccupied manifold, respectively. After replacing all φ 's by ψ 's, the unitary matrices lead to Kronecker deltas

that take care of the invariance,

$$\begin{aligned}
 & \sum_{ij}^{\text{occ. virt.}} \sum_{ab} \langle \psi_i^\tau \psi_j^\tau | \psi_a^\tau \psi_b^\tau \rangle \langle \psi_a^\tau \psi_b^\tau | \psi_j^\tau \psi_i^\tau \rangle \\
 &= \sum_{\substack{ij \\ k_1 \dots k_4}}^{\text{occ.}} \sum_{\substack{ab \\ c_1 \dots c_4}}^{\text{virt.}} \langle \varphi_{k_1}^\tau \varphi_{k_2}^\tau | \varphi_{c_1}^\tau \varphi_{c_2}^\tau \rangle \langle \varphi_{c_3}^\tau \varphi_{c_4}^\tau | \varphi_{k_3}^\tau \varphi_{k_4}^\tau \rangle \underbrace{u_{ik_1}^* u_{ik_4}^*}_{\delta_{k_1 k_4}} \underbrace{u_{jk_2}^* u_{jk_3}^*}_{\delta_{k_2 k_3}} \underbrace{v_{ac_1}^* v_{ac_3}^*}_{\delta_{c_1 c_3}} \underbrace{v_{bc_2}^* v_{bc_4}^*}_{\delta_{c_2 c_4}} \\
 &= \sum_{ij}^{\text{occ. virt.}} \sum_{ab} \langle \varphi_i^\tau \varphi_j^\tau | \varphi_a^\tau \varphi_b^\tau \rangle \langle \varphi_a^\tau \varphi_b^\tau | \varphi_j^\tau \varphi_i^\tau \rangle \quad (11.44)
 \end{aligned}$$

When random coefficients and expectation values are used, the Kronecker deltas in Eq. (11.44) can be generated by yet another transformation, which, for MP2, was first published by Neuhauser et al. [70]. Consider a set of independent complex random coefficients $\{p_i\}$ where both the real and imaginary parts are uniformly distributed over the range $[-\sqrt{3/2}, +\sqrt{3/2}]$, such that we find for the expectation values $E[p_i] = 0$ and $E[p_i^* p_i] = 1$. We can then write the Kronecker delta as an expectation value: $\delta_{ij} = E[p_i^* p_j]$. Note that the upright letter $E[\dots]$ stands for an expectation value, whereas energies are written by the italic letter E . If we plug this definition of Kronecker deltas into the third line of Eq. (11.44), we find that the MP2 energy can be written as an expectation value of stochastic energies X^τ ,

$$E_x^{\text{MP2}} = \frac{1}{2} \int_0^\infty E[X^\tau] d\tau, \quad (11.45)$$

where

$$X^\tau = \langle \kappa^\tau \lambda^\tau | r_{12}^{-1} | \alpha^\tau \beta^\tau \rangle \langle \alpha^\tau \beta^\tau | r_{12}^{-1} | \lambda^\tau \kappa^\tau \rangle, \quad (11.46)$$

with the stochastic orbitals

$$\begin{aligned}
 |\kappa^\tau\rangle &= \sum_i^{\text{occ.}} p_i |\varphi_i^\tau\rangle, & |\lambda^\tau\rangle &= \sum_i^{\text{occ.}} q_i |\varphi_i^\tau\rangle, \\
 |\alpha^\tau\rangle &= \sum_a^{\text{virt.}} r_a |\varphi_a^\tau\rangle, & |\beta^\tau\rangle &= \sum_a^{\text{virt.}} s_a |\varphi_a^\tau\rangle.
 \end{aligned} \quad (11.47)$$

Here $\{p_i\}$, $\{q_i\}$, $\{r_a\}$, and $\{s_a\}$ are independent sets of uniformly distributed complex random coefficients as described above. The main idea is to generate a sufficiently large sample of the stochastic energies X^τ in order to obtain a reliable estimation for the expectation value $E[X^\tau]$ and therefore an estimation for the MP2 energy.

In this work, we assume that the occupied and virtual HF orbitals and energies are available through a preceding HF calculation. The HF orbitals are stored in the plane wave basis, $\{\langle \mathbf{G} | i \rangle, \langle \mathbf{G} | a \rangle\}$, where \mathbf{G} is a reciprocal lattice vector. In VASP the number of lattice vectors \mathbf{G} is truncated by a cutoff, E_{cut} (ENCUT flag in VASP), such that $\mathbf{G}^2/2 < E_{\text{cut}}$. Also the number of orbitals (sum of occupied plus unoccupied) is limited to the same

number as the number of reciprocal lattice vectors.

In order to calculate a single stochastic energy X^τ , Eq. (11.46), the stochastic orbitals are set up in the plane wave basis using (11.47), e.g.

$$\langle \mathbf{G} | \kappa^\tau \rangle = \sum_i^{\text{occ.}} p_i e^{\varepsilon_i \tau / 2} \langle \mathbf{G} | i \rangle. \quad (11.48)$$

The electron-repulsion integrals in (11.46) are evaluated in reciprocal space as

$$\langle \kappa^\tau \lambda^\tau | r_{12}^{-1} | \alpha^\tau \beta^\tau \rangle = \frac{1}{\Omega} \sum_{\mathbf{G}} \frac{E_{\text{cut}}^{\text{aux}}}{G^2} \langle \kappa^\tau | e^{-i\mathbf{G}\hat{r}} | \alpha^\tau \rangle \langle \lambda^\tau | e^{+i\mathbf{G}\hat{r}} | \beta^\tau \rangle. \quad (11.49)$$

Note that here the reciprocal lattice vectors are limited by an auxiliary cutoff, $E_{\text{cut}}^{\text{aux}}$ (ENCUTGW flag in VASP), which is usually equal to $\frac{2}{3}E_{\text{cut}}$. Also, Ω is the volume of the system and $\langle \kappa^\tau | e^{-i\mathbf{G}\hat{r}} | \alpha^\tau \rangle$ are the overlap densities, defined by

$$\begin{aligned} \langle \kappa^\tau | e^{-i\mathbf{G}\hat{r}} | \alpha^\tau \rangle &= \int_{\Omega} d^3r \langle \kappa^\tau | \mathbf{r} \rangle \langle \mathbf{r} | \alpha^\tau \rangle e^{-i\mathbf{G}\mathbf{r}} \\ &= \mathcal{F}_{\mathbf{G}}[\{\langle \kappa^\tau | \mathbf{r} \rangle \langle \mathbf{r} | \alpha^\tau \rangle\}], \end{aligned} \quad (11.50)$$

where the stochastic orbitals in real space can easily be obtained by a Fourier transform,

$$\{\langle \mathbf{r} | \kappa^\tau \rangle\} = \mathcal{F}_{\mathbf{r}}^{-1}[\{\langle \mathbf{G} | \kappa^\tau \rangle\}]. \quad (11.51)$$

In this way, a stochastic energy X^τ can be calculated for a given τ -point.

Variance and error

To estimate the expectation value of the sample for a given τ -point, $E[X^\tau]$, the mean, μ_n^τ , is calculated by

$$\mu_n^\tau = \frac{1}{n} \sum_{l=1}^n X_l^\tau, \quad (11.52)$$

where n is the number of all generated stochastic energies of this sample, since $\mu_n^\tau \rightarrow E[X^\tau]$ as $n \rightarrow \infty$. To measure the reliability of this estimation for finite n , the error of the mean is estimated via

$$\delta\mu_n^\tau = \frac{\sigma_n^\tau}{\sqrt{n}}. \quad (11.53)$$

Here σ_n^τ is an estimate for the standard deviation of the samples, obeying $\sigma_n^\tau \rightarrow \sqrt{\text{Var}[X^\tau]}$ as $n \rightarrow \infty$, and $\text{Var}[X^\tau] = E[(X^\tau - E[X^\tau])^2]$. In practice the standard deviation, σ_n^τ , is calculated using Welford's algorithm [71]. Since the MP2 energy is the sum over the

independent expectation values of all τ -points,

$$E_x^{\text{MP2}} = \frac{1}{2} \int_0^\infty E[X^\tau] d\tau \approx \frac{1}{2} \sum_\tau w_\tau E[X^\tau], \quad (11.54)$$

the statistical error of the MP2 energy is simply estimated by the formula for the propagation of error,

$$\delta E_x^{\text{MP2}} = \frac{1}{2} \sqrt{\sum_\tau (w_\tau \delta \mu_n^\tau)^2}. \quad (11.55)$$

In general, the system size scaling of the sample variance, $(\sigma_n^\tau)^2$, plays an important role for the prefactor and the system size scaling of the computation time. If the variance obeys a polynomial system size scaling with the power c_{var} , we can conclude that the number, n , of necessary stochastic energies follows exactly the same scaling behavior if the statistical error should be kept constant (see Eq. 11.53). Moreover, let the calculation time of a single stochastic energy, X^τ , have a polynomial system size scaling to the power of c_{rnd} . The total scaling of the computation time is then polynomial with the power $c_{\text{var}} + c_{\text{rnd}}$. Thus, due to Eq. (11.53), the sample variance has a strong impact on both the scaling and the prefactor of the algorithm, making the variance the key quantity that determines whether the stochastic approach is competitive.

Correlated sampling

For correlated sampling we calculate a set of stochastic orbitals $|\kappa_\theta^\tau\rangle, |\lambda_\theta^\tau\rangle, |\alpha_\theta^\tau\rangle, |\beta_\theta^\tau\rangle$, as indicated by the new index $\theta = 1, \dots, N_\theta$. Clearly, the vectors of random coefficients, p_i, q_i, r_a, s_a , in Eq. (11.47) have to be replaced by matrices of random coefficients $p_{i\theta}, q_{i\theta}, r_{a\theta}, s_{a\theta}$. To calculate a sample we can now write

$$X^\tau = \langle \kappa_\theta^\tau \lambda_{\theta'}^\tau | r_{12}^{-1} | \alpha_\theta^\tau \beta_{\theta'}^\tau \rangle \langle \alpha_{\theta'}^\tau \beta_\theta^\tau | r_{12}^{-1} | \lambda_{\theta'}^\tau \kappa_\theta^\tau \rangle, \quad (11.56)$$

which is equal to uncorrelated sampling of Eq. (11.46) as long as $\theta = \theta'$, but activates correlated sampling when combinations of $\theta \neq \theta'$ are allowed. Hence, a larger sample can be calculated with the same amount of stochastic orbitals. Comparable sampling techniques for MP2 were applied in the real space Monte Carlo algorithm in Sec. 11.1 as well as in Ref. [68, 72]. Since the generation of stochastic orbitals has a steeper system size scaling than the evaluation of the two-electron integrals, correlated sampling leads to a significant speed up. This will be discussed in detail in the next section.

11.2.2 Implementation

The algorithm presented in this paper is implemented in the Vienna ab initio simulation package (VASP). Since VASP is designed for periodic systems, it naturally rests upon the plane wave basis. The basis set size can thus easily be controlled by the plane wave cutoff E_{cut} . Hence, we can focus on the statistical fluctuations and no additional error has to be considered, as it appears in local correlation methods. On the other hand, we forgo

the benefits of localized basis sets, which reportedly allow to sample energy differences accurately even using a small number of stochastic orbitals [73]. Furthermore, as every method in VASP, the implementation is based on the projector augmented wave (PAW) method. However, for brevity, the PAW is ignored in all formulas of this work.

Algorithm and scaling

The algorithm can be divided into three simple parts: for each τ -point (i) calculate the stochastic orbitals (11.48) from the HF orbitals, (ii) calculate the overlap densities (11.50), (iii) calculate the two-electron integrals (11.49) using the overlap densities, and the stochastic energy (11.46) and update the statistics. Repeat this procedure until the error of the mean for this τ -point is below the desired threshold. In the following, correlated sampling is considered, i.e. the additional index θ comes into play, as introduced in Sec. 11.2.1. Pseudocode of the algorithm can be found in Fig. 11.4.

In step (i), N_θ stochastic orbitals are calculated using BLAS level 3 routines and stored in memory, where N_θ is user given. The scaling with computation time and memory reads

$$|\kappa_\theta^\tau\rangle, |\lambda_\theta^\tau\rangle \sim \begin{cases} \mathcal{O}(N_\theta N_G N_i) & \text{in time} \\ \mathcal{O}(N_\theta N_r) & \text{in memory,} \end{cases} \quad (11.57)$$

$$|\alpha_\theta^\tau\rangle, |\beta_\theta^\tau\rangle \sim \begin{cases} \mathcal{O}(N_\theta N_G N_a) & \text{in time} \\ \mathcal{O}(N_\theta N_r) & \text{in memory.} \end{cases} \quad (11.58)$$

Here, N_G is the number of reciprocal lattice vectors limited by the cutoff E_{cut} , and N_i and N_a are the number of occupied and virtual HF orbitals, respectively. The number of real space grid points, N_r , determines the memory scaling when the stochastic orbitals are Fourier transformed to real space to calculate the overlap densities. Since the number of τ -points is largely independent of the system size, we ignore this factor in the analysis.

For step (ii), the following overlap densities have to be calculated for the stochastic energies (11.56):

$$\begin{aligned} \langle \kappa_\theta^\tau | e^{-i\mathbf{G}\hat{r}} | \alpha_\theta^\tau \rangle \\ \langle \beta_\theta^\tau | e^{-i\mathbf{G}\hat{r}} | \lambda_\theta^\tau \rangle \end{aligned} \sim \mathcal{O}(N_\theta N_G^{\text{aux}} \ln N_G^{\text{aux}}) \quad \text{in time,} \quad (11.59)$$

$$\begin{aligned} \langle \alpha_{\theta'}^\tau | e^{-i\mathbf{G}\hat{r}} | \lambda_\theta^\tau \rangle \\ \langle \kappa_\theta^\tau | e^{-i\mathbf{G}\hat{r}} | \beta_{\theta'}^\tau \rangle \end{aligned} \sim \mathcal{O}(N_\theta^2 N_G^{\text{aux}} \ln N_G^{\text{aux}}) \quad \text{in time,} \quad (11.60)$$

where N_G^{aux} is the number of reciprocal lattice vectors limited by the auxiliary cutoff $E_{\text{cut}}^{\text{aux}}$. Note that the first two overlap densities involve only one θ index, whereas the last two overlap densities have to be calculated for combinations of θ and θ' . It is also worth mentioning, that for the direct MP2 energy, only the first two overlap densities (11.59) are necessary. Thus, in each loop cycle the algorithm checks, whether the accuracy of the exchange energy was already reached, in order to decide whether the computation of the more expensive overlap densities (11.60) is necessary. Since the variance of the direct

```

for all  $\tau$  do
  while  $\delta\mu > \text{stop\_criterion}$  do
    # (i) stochastic orbitals
     $p_{i\theta}, q_{i\theta}, r_{a\theta}, s_{a\theta} = \text{random} \quad \forall i, a, \theta$ 
     $p_{i\theta} = p_{i\theta} \cdot e^{+\varepsilon_i\tau/2} \quad \forall i, \theta$ 
     $q_{i\theta} = q_{i\theta} \cdot e^{+\varepsilon_i\tau/2} \quad \forall i, \theta$ 
     $r_{a\theta} = r_{a\theta} \cdot e^{-\varepsilon_a\tau/2} \quad \forall a, \theta$ 
     $s_{a\theta} = s_{a\theta} \cdot e^{-\varepsilon_a\tau/2} \quad \forall a, \theta$ 
     $\langle \mathbf{G} | \kappa_\theta \rangle = \sum_i^{\text{occ}} \langle \mathbf{G} | i \rangle p_{i\theta}$ 
     $\langle \mathbf{G} | \lambda_\theta \rangle = \sum_i^{\text{occ}} \langle \mathbf{G} | i \rangle q_{i\theta}$ 
     $\langle \mathbf{G} | \alpha_\theta \rangle = \sum_a^{\text{virt}} \langle \mathbf{G} | a \rangle r_{a\theta}$ 
     $\langle \mathbf{G} | \beta_\theta \rangle = \sum_a^{\text{virt}} \langle \mathbf{G} | a \rangle s_{a\theta}$ 
     $\{ \langle \mathbf{r} | \kappa_\theta \rangle \} = \text{FFT}_{\mathbf{r}}^{-1}[\{ \langle \mathbf{G} | \kappa_\theta \rangle \}]$ 
     $\{ \langle \mathbf{r} | \lambda_\theta \rangle \} = \text{FFT}_{\mathbf{r}}^{-1}[\{ \langle \mathbf{G} | \lambda_\theta \rangle \}]$ 
     $\{ \langle \mathbf{r} | \alpha_\theta \rangle \} = \text{FFT}_{\mathbf{r}}^{-1}[\{ \langle \mathbf{G} | \alpha_\theta \rangle \}]$ 
     $\{ \langle \mathbf{r} | \beta_\theta \rangle \} = \text{FFT}_{\mathbf{r}}^{-1}[\{ \langle \mathbf{G} | \beta_\theta \rangle \}]$ 
    for all  $\theta$  do
      # (ii) overlap densities
       $\rho_\theta^{(1)}(\mathbf{G}) = \text{FFT}_{\mathbf{G}}[\langle \kappa_\theta | \mathbf{r} \rangle \langle \mathbf{r} | \alpha_\theta \rangle]$ 
       $\rho_\theta^{(2)}(\mathbf{G}) = \text{FFT}_{\mathbf{G}}[\langle \beta_\theta | \mathbf{r} \rangle \langle \mathbf{r} | \lambda_\theta \rangle]$ 
      for all  $\theta'$  do
         $\rho_{\theta\theta'}^{(3)}(\mathbf{G}) = \text{FFT}_{\mathbf{G}}[\langle \alpha_\theta | \mathbf{r} \rangle \langle \mathbf{r} | \lambda_{\theta'} \rangle]$ 
         $\rho_{\theta\theta'}^{(4)}(\mathbf{G}) = \text{FFT}_{\mathbf{G}}[\langle \kappa_\theta | \mathbf{r} \rangle \langle \mathbf{r} | \beta_{\theta'} \rangle]$ 
        # (iii) stochastic energies
         $d = \sum_{\mathbf{G}}^{E_{\text{cut}}^{\text{aux}}} \frac{4\pi}{\mathbf{G}^2} \rho_\theta^{(1)}(\mathbf{G}) \rho_{\theta'}^{(2)}(\mathbf{G})^*$ 
         $x = \sum_{\mathbf{G}}^{E_{\text{cut}}^{\text{aux}}} \frac{4\pi}{\mathbf{G}^2} \rho_{\theta\theta'}^{(3)}(\mathbf{G}) \rho_{\theta\theta'}^{(4)}(\mathbf{G})^*$ 
         $X = x \cdot d$ 
         $D = -2|d|^2$ 
      end for
    end for
    Update mean  $\mu$ 
    Update error  $\delta\mu$ 
  end while
   $E_{\text{d}}^{(2)} = E_{\text{d}}^{(2)} + w_\tau \mu(D)$ 
   $E_{\text{x}}^{(2)} = E_{\text{x}}^{(2)} + w_\tau \mu(X)$ 
end for

```

Figure 11.4: Pseudocode of the MP2 algorithm with stochastic orbitals. Note that the HF orbitals, $|i\rangle$, $|a\rangle$, and energies, ε_i , ε_a , stem from a preceding HF calculation.

MP2 energy turns out to be larger than the variance of the exchange energy, this approach leads to a significant speed up of the algorithm.

Having the overlap densities we can calculate the stochastic energies (iii) that scale as

$$\langle \kappa_{\theta}^{\tau} \lambda_{\theta'}^{\tau} | r_{12}^{-1} | \alpha_{\theta}^{\tau} \beta_{\theta'}^{\tau} \rangle \langle \alpha_{\theta}^{\tau} \beta_{\theta'}^{\tau} | r_{12}^{-1} | \lambda_{\theta'}^{\tau} \kappa_{\theta}^{\tau} \rangle \sim \mathcal{O}(N_{\theta}^2 N_{\mathbf{G}}^{\text{aux}}) \quad (11.61)$$

in time. The prefactor of this step (iii) is small compared to that of (ii), since step (ii) involves FFTs, whereas here only summations over reciprocal lattice vectors are performed.

With this at hand one can calculate the actual scaling of the algorithm with the system size (independent of N_{θ}) and demonstrate the benefit of the correlated sampling. For a given system and fixed absolute statistical error, the sample size reads $n = n_{\text{L}} N_{\theta}^2$, where n_{L} is the number of loop cycles of the steps (i)-(iii), since the variance is independent of N_{θ} (as will be shown in Sec. 11.2.3). With (11.57)-(11.61) we can then write the computation time as a function of N_{θ} :

$$\begin{aligned} T(N_{\theta}) &= 2\gamma_{\text{BLAS}} \frac{n}{N_{\theta}} N_{\mathbf{G}} (N_a + N_i) & (i) \\ &+ 2\gamma_{\text{FFT}} n \left(1 + \frac{1}{N_{\theta}}\right) N_{\mathbf{G}}^{\text{aux}} \ln N_{\mathbf{G}}^{\text{aux}} & (ii) \\ &+ \gamma n N_{\mathbf{G}}^{\text{aux}} & (iii) . \end{aligned} \quad (11.62)$$

Here γ_{BLAS} , γ_{FFT} , and γ are the prefactors of the BLAS routines, fast Fourier transforms, and simple multiplications, respectively. Equation (11.62) shows clearly that correlated sampling (increasing N_{θ}) asymptotically reduces the computation time. In this approach the largest possible N_{θ} is given by $n_{\text{L}} = 1 \Rightarrow n = N_{\theta}^2$ such that the entire sample is generated in one single loop cycle and only N_{θ} stochastic orbitals have to be generated for the MP2 calculation. In this optimal case the computation time reduces to

$$\begin{aligned} T(N_{\theta} = \sqrt{n}) &\approx 2\gamma_{\text{BLAS}} \sqrt{n} N_{\mathbf{G}} N_a & (i) \\ &+ 2\gamma_{\text{FFT}} n N_{\mathbf{G}}^{\text{aux}} \ln N_{\mathbf{G}}^{\text{aux}} & (ii) \\ &+ \gamma n N_{\mathbf{G}}^{\text{aux}} & (iii) , \end{aligned} \quad (11.63)$$

where we have assumed $N_i/N_a \ll 1$ and $1/\sqrt{n} \ll 1$. Later, in Sec. 11.2.3, we will show that the sample variance and therefore also the sample size, n , scales quadratically with the system size, if a fixed absolute statistical error is required. Thus, Eq. (11.63) shows, that each step of the algorithm possesses a cubic scaling with the system size.

If only a fixed relative error is required, then the sample size can be chosen independently of the system size and the scaling reduces to a largely quadratic scaling of step (i). In practice, however, the computation time is dominated by the linear scaling of step (ii), as long as

$$\frac{\gamma_{\text{FFT}}}{\gamma_{\text{BLAS}}} > 1.84 \cdot \frac{N_a}{\sqrt{n}} \quad (11.64)$$

where $N_{\mathbf{G}}/N_{\mathbf{G}}^{\text{aux}} \approx 1.84$ was assumed, following from the mentioned ratio $E_{\text{cut}}^{\text{aux}} = 2E_{\text{cut}}/3$. It is only this scenario of a fixed relative error in combination with a moderate system size

where approximate "linear scaling" can be expected.

Furthermore, we want to stress how the correlated sampling is responsible for the reduction to a cubical scaling in the case of a fixed absolute statistical error. For this, we look at the speed up which can be obtained by the correlated sampling,

$$\frac{T(N_\theta = 1)}{T(N_\theta = \sqrt{n})} \sim N_a . \quad (11.65)$$

We conclude, that the possible speed up due to correlated sampling increases linearly with the system size. This, and the fact that the variance and, therefore, the sample size scale quadratically, is the reason why a cubic scaling of the stochastic MP2 algorithm can be achieved. Without correlated sampling the generation of stochastic orbitals (i) would be the dominant step, yielding for the entire algorithm a quartic scaling behavior.

Also, the key differences between this approach and the method by Neuhauser [70] can now be summarized as follows. We use the exact HF orbitals in the plane wave basis as the starting point, instead of generating completely random orbitals that are purified to the occupied or unoccupied space. Our HF orbitals stem from a full HF calculation where the Fock-matrix is not to be assumed as sparse. The stochastic orbitals are propagated in imaginary time instead of real time by a simple multiplication and no application of the Fock matrix is necessary. Additionally, we introduced correlated sampling, which reduces the seemingly most expensive step of generating stochastic orbitals from HF orbitals to a less relevant contribution to the computation time (see Eq. (11.62) or Fig. (11.6)).

Complex vs. real random coefficients

The stochastic orbitals were introduced as linear combinations of time-dependent Hartree-Fock orbitals with uniformly distributed random complex numbers as coefficients. Instead of complex random coefficients, also real random coefficients can be used. In the case of Γ -only sampling of the Brillouine zone, the spatial HF orbitals are real, hence, the stochastic orbitals would inherit this property, if only real random coefficients are used. For calculations in the plane wave basis, real spatial orbitals are beneficial, since the overlap densities have to be calculated only for half of the number of plane wave vectors. This is a consequence of the identity $\langle \psi | e^{-i\mathbf{G}\hat{r}} | \varphi \rangle = \langle \psi | e^{+i\mathbf{G}\hat{r}} | \varphi \rangle^*$, for real spatial orbitals ψ, φ . Also, the orbitals are stored only for half of the plane wave coefficients, since $\langle \mathbf{G} | \varphi \rangle = \langle -\mathbf{G} | \varphi \rangle^*$ for any real spatial orbital φ . Hence, the computational effort to calculate a stochastic energy, X^τ , is halved in time and memory for all three steps, (i)-(iii), of the algorithm.

However, this comes at the price of a larger variance. This can be estimated by calculating the variance of the stochastic approximation of the Kronecker deltas, where the random coefficients were introduced initially. As described in Sec. 11.2.1, the Kronecker deltas are approximated as expectation values $\delta_{ii} = 1 = \mathbb{E}[z^*z]$, where $z = a + ib$ is a random complex number whose real and imaginary part are uniformly distributed over the range $[-\sqrt{3}/2, +\sqrt{3}/2]$. The variance can be calculated as $\text{Var}[z^*z] = \mathbb{E}[(z^*z - 1)^2] = 0.4$. If instead only real random coefficients are used, the Kronecker deltas are approximated

as $\delta_{ii} = 1 = E[r^2]$, where r is a uniformly distributed real random number over the range $[-\sqrt{3}, +\sqrt{3}]$. But in this case the variance is twice as large as in the case of complex numbers, $\text{Var}[r^2] = E[(r^2 - 1)^2] = 0.8$.

Analytically, it is not possible to conclude whether the variance of the stochastic MP2 algorithm also doubles, when real instead of complex random coefficients are employed. However, in Sec. 11.2.3 we present a comparison of stochastic MP2 runs using real and complex random coefficients, confirming that the variance roughly doubles for real random coefficients.

Internal cutoff extrapolation

It is known, that the correlation energy for wave-function based methods like MP2 or RPA (random phase approximation) converges slowly with respect to the basis set size (plane wave cutoff). However, the exact asymptotic behavior for large plane wave cutoffs is also known and can be exploited for an internal cutoff extrapolation. In this work, the cutoff that controls the basis set size of the calculations of the two-electron integrals (11.49) is $E_{\text{cut}}^{\text{aux}}$ and according to Ref. [58, 60] the asymptotic behavior reads,

$$E^{\text{MP2}}(E_{\text{cut}}^{\text{aux}}) - E^{\text{MP2}}(E_{\text{cut}}^{\text{aux}} = \infty) \sim (E_{\text{cut}}^{\text{aux}})^{-3/2}. \quad (11.66)$$

The internal cutoff extrapolation calculates the two-electron integrals for the user given cutoff $E_{\text{cut}}^{\text{aux}}$ and also for a certain number (8 in this work) of smaller cutoffs on the fly. This set of MP2 energies can be extrapolated to infinity according to Eq. (11.66). A detailed description of this extrapolation scheme can be found in Sec. III.D in Ref. [41], where it was implemented for our deterministic quartic scaling MP2 algorithm.

Parallelization

For the parallelization, we use a combination of MPI and OpenMP. Since stochastic orbitals and overlap densities can be generated independently on all MPI ranks, the parallelization of the algorithm is rather simple and efficient. However, the access to the shared memory of the CPU sockets via OpenMP is favorable. Having the entire set of HF orbitals (occupied+unoccupied) available at each MPI rank, allows to calculate the stochastic orbitals (11.48) without MPI communication. For large cells and large basis sets this requirement can quickly exceed the memory per single CPU, making shared memory the obvious solution. Hence, each MPI rank runs through the algorithm depicted in Fig. 11.4 and calculates correlated stochastic energies independently, whereas the OpenMP parallelization works differently in each of the steps (i)-(iii): In step (i) the BLAS routines are parallelized over the OpenMP threads (OpenMP aware BLAS). In step (ii) the FFTs are parallelized over the OpenMP threads (OpenMP aware FFT). And in step (iii) the sums over plane waves \mathbf{G} are parallelized over the OpenMP threads.

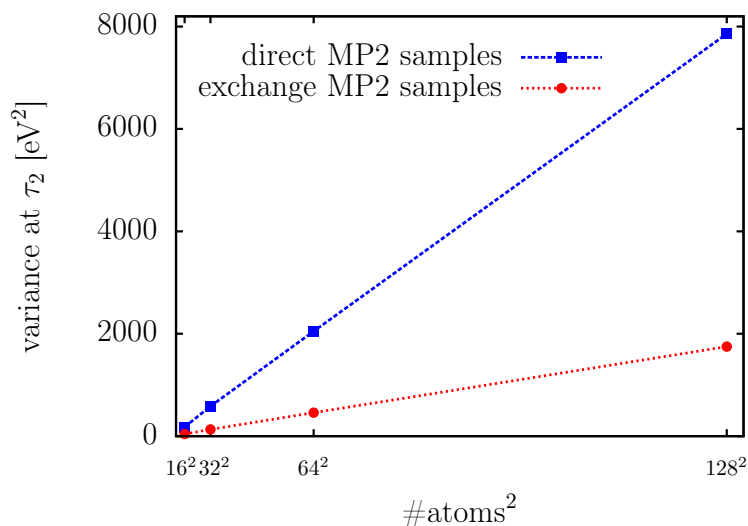


Figure 11.5: Sample variance of the direct MP2 term at the second τ -point for various supercells of LiH as a function of the number of atoms squared. This graph shows that the variance scales quadratically with the system size.

11.2.3 Benchmark calculations

To compare the results with those of our recent publication of an exact quartic scaling MP2 algorithm [41] we, again, chose lithium hydride (LiH) and methane in a chabazite crystal as benchmark systems to test the parallelization efficiency, the system size scaling, the scaling of the variance, and the competitiveness of the stochastic approach. All computations were performed on Intel Xeon E5-2650 v2 2.8 GHz processors. The timings are measured in CPU hours which is the CPU time in hours multiplied by the number of employed CPUs. We use VASP for all calculations, where we restrict on Γ -only sampling of the Brillouine zone, a spin-restricted setting, and 6 τ -points for the quadrature of the Laplace transform. If not explicitly stated, real random coefficients are used for the stochastic orbitals.

Measured scaling of the sample variance

The variance is estimated by the sample variance, $(\sigma_n^\tau)^2$, as described on p. 141. In Fig. 11.5 the sample variance at the second τ -point of the τ quadrature (which gives the largest contribution to the MP2 energy) is plotted against the number of atoms squared. Since this results in a straight line, we can conclude that the variance possesses a quadratic scaling with the system size for each τ point. If the stopping criterion for the algorithm is given by a fixed absolute error, the sample size n also needs to scale quadratically with the system size for each τ point, since the error behaves as $\sqrt{(\sigma_n^\tau)^2/n}$.

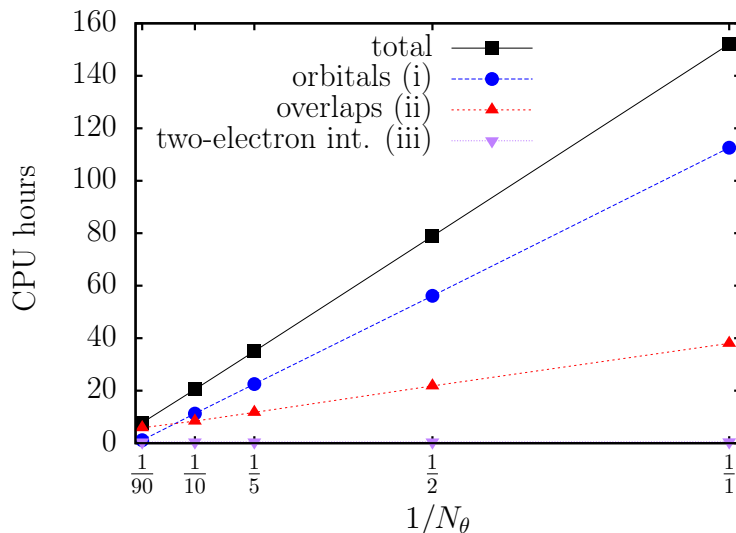


Figure 11.6: Reducing the computation time using correlated sampling. The MP2 energy of a LiH supercell containing 32 atoms was calculated for different N_θ , controlling the correlated sampling. The measured timings are in agreement with the prediction in Eq. (11.62).

Correlated sampling

In a previous section we derived that correlated sampling reduces the computation time to a plateau, see Eq. (11.62). We put this equation to test with a supercell of solid LiH containing 32 atoms. The computation time of each step of the algorithm, (i)-(iii) (see Sec. 11.2.2), was measured against N_θ , which controls the correlated sampling such that N_θ^2 stochastic energies are calculated in each loop cycle. In Fig. 11.6 the computation time is plotted against $1/N_\theta$, providing an apparent verification of the $1/N_\theta$ law of Eq. (11.62).

Furthermore, *a priori* it is not clear if the correlated sampling affects the variance. To probe this, we plot the sample variance of the second τ -point for both the direct and exchange MP2 energy against N_θ , using the same benchmark system. The result can be seen in Fig. 11.7. Apparently, there is no visible effect of the correlated sampling, aside from stochastic fluctuations which are smaller than 0.7%. Thus, we assume the variance to be independent of N_θ .

Measured system size scaling and memory consumption

In order to measure the scaling of the stochastic MP2 algorithm with the system size, calculations on various supercells of LiH were performed. Figure 11.8 shows the result. As predicted in section 11.2.2, the stochastic MP2 approach possesses a roughly cubic scaling, if a fixed absolute error is imposed. For a fixed relative error (per valence orbital) the scaling is roughly linear in the measured range of atoms. Detailed computational settings are provided in Tab. 11.2. We also checked the sensitivity of the variance if the

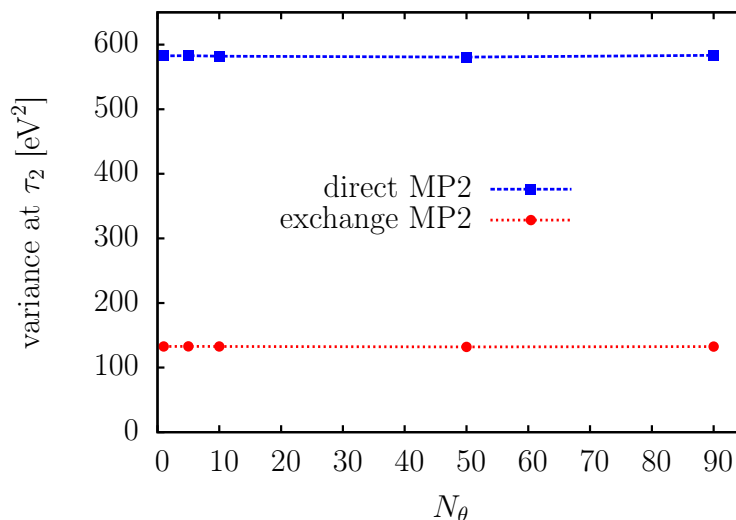


Figure 11.7: Sample variance at the second τ -point for different N_θ . For both, the direct and exchange part, the variance is independent of N_θ .

symmetry of a cell is broken. Therefore, we performed the calculation with 32 LiH atoms also with a supercell containing slightly displaced atoms, corresponding to a snapshot of a supercell at 1000 K. For each τ point we found no measurable effect on the variance, besides fluctuations around 1%.

If the statistical error should be decreased by a factor c , then the computation time increases by a factor of c^2 , since the statistical error decreases as $1/\sqrt{n}$, as was mentioned in the last section. Thus the break point of the stochastic approach compared to the deterministic codes depends mostly on the desired accuracy. Increasing, e.g., the accuracy of the stochastic calculations in Fig. 11.8 by a factor of 10 would shift the stochastic lines upwards by a factor of 100 in the computation time.

Regarding memory consumption the major contribution stems from the HF orbitals and the stochastic orbitals. In Tab. 11.2 the computational settings and the memory consumption is presented for three systems, including methane in a chabazite crystal and two different supercells of LiH. Of course, the memory requirements could be lowered considerably if the HF orbitals are distributed over all MPI ranks instead of only over the OpenMP threads, however, then the calculation of the stochastic orbitals (i) would require MPI communication, which would lower the parallelization efficiency.

Measured parallelization efficiency

We measured the strong scaling of the stochastic MP2 algorithm for both MPI and OpenMP separately. As benchmark systems we used supercells of solid LiH with 128 atoms for the MPI scaling and with 32 atoms for the OpenMP scaling. Figure 11.9 shows the result. As expected, the parallelization with MPI is almost ideal, since communication is necessary only when the statistics are updated and all stochastic energies have to be gathered from

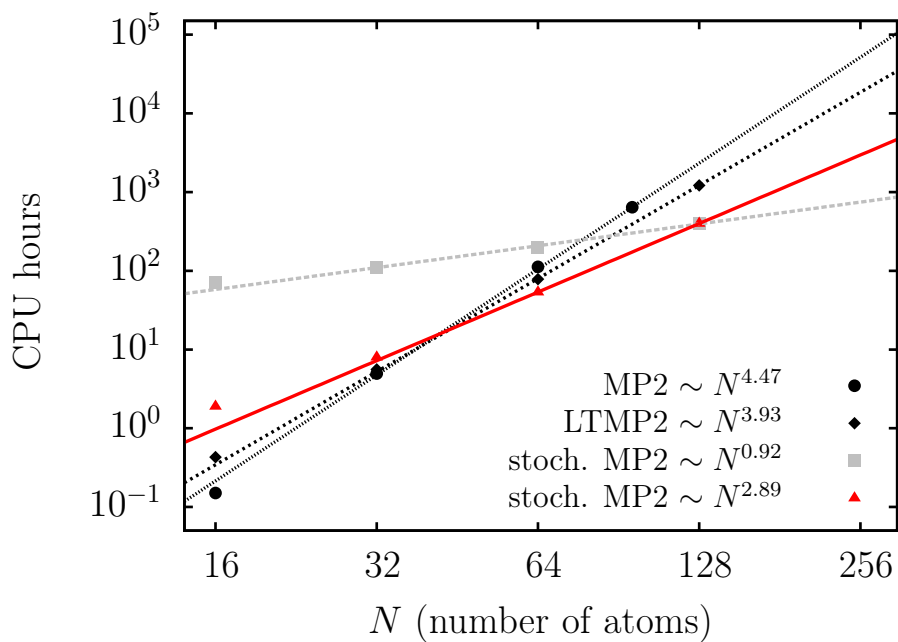


Figure 11.8: System size scaling of different MP2 algorithms in VASP for various supercells of solid LiH. The red triangles are stochastic MP2 calculations with a fixed absolute error of 17.3 meV. The gray squares are stochastic MP2 calculations with a fixed relative error of 0.135 meV per valence band. The black squares are calculations using the deterministic quintic scaling algorithm [43, 74] and the black diamond symbols refer to the recently published deterministic quartic scaling MP2 algorithm (LTMP2) [41].

	CH ₄ in Chab.	LiH	LiH
#atoms	42	32	128
E_{cut}	750 eV	434 eV	434 eV
$E_{\text{cut}}^{\text{aux}}$	500 eV	289 eV	289 eV
$N_{\mathbf{G}}$	18 873	2 563	10 263
$N_{\mathbf{G}}^{\text{aux}}$	10 231	1 418	5 559
$N_{\mathbf{r}}$	74 088	10 976	43 904
N_i	100	32	128
N_a	37 660	5 104	20 400
N_{θ}	150	120	240
n for $E_d^{(2)}$	$5.3 \cdot 10^9$	$5.9 \cdot 10^7$	$7.4 \cdot 10^8$
n for $E_x^{(2)}$	$0.9 \cdot 10^9$	$1.5 \cdot 10^7$	$1.7 \cdot 10^8$
standard deviation	9.2 meV	13.8 meV	15.0 meV
CPU hours	7 121	8	398
HF orbitals	11.5 GB	238.2 MB	3.8 GB
stoch. orbitals	1.1 GB	130.3 MB	1.1 GB
total memory	13.4 GB	692.0 MB	6.1 GB

Table 11.2: Computational settings and costs for different benchmark systems. The memory consumption is listed per MPI rank. The difference between the total memory and the orbital memory consumption is also due to the module for the statistics that temporarily stores the stochastic energies until the next MPI communication. The standard deviation refers to the statistical standard deviation of the MP2 energy, hence, all calculations are converged well below 1 meV per valence orbital, where N_i is the number of occupied/valence orbitals. The sample size is denoted by n .

System	Variance at τ_2 [eV ²]		ratio
	real	complex	
CH ₄ in Chab.	3664.36	1736.57	2.1
CH ₄	9.38	3.03	3.1
LiH (32 atoms)	133.01	56.21	2.4
LiH (128 atoms)	1748.56	829.18	2.1

Table 11.3: Ratio of the sample variance at the second τ point of the exchange MP2 part for calculations with real and complex coefficients for the stochastic orbitals.

all MPI ranks. The OpenMP parallelization, which is useful only if shared memory is required, shows also a tolerable strong scaling. The lower efficiency is a consequence of the simultaneous memory access of the OpenMP threads as well as the OpenMP overhead in e.g. OpenMP aware BLAS and FFT routines.

Measured variance with real and complex random coefficients

How real numbers instead of complex random coefficients affect the variance, as discussed in Sec. 11.2.2, was measured for four different systems. Since the presented algorithm calculates the variance for each τ -point individually, we compare the variance of the exchange MP2 energy again at the second τ -point, τ_2 . Table 11.3 shows that, for large systems, the variance roughly doubles, as supposed, when changing from complex to real random coefficients. However, for smaller systems, as for the methane molecule, the variance increases by a factor of 3.1 for real coefficients, making the calculation slower by a factor of $\sqrt{3.1/2} = 1.24$ at this τ -point. It seems, that complex coefficients are beneficial for small systems, where the larger memory consumption is unproblematic and the speed up can be exploited. For larger systems, real random coefficients outperform the approach with complex random coefficients, since the effect on the computation time is negligible but the memory consumption is halved.

Adsorption energy of methane in a chabazite crystal cage

In our previous publication [41], where we presented a deterministic and quartic scaling MP2 algorithm for solids (LTMP2), we calculated the MP2 correlation part of the adsorption energy of a methane molecule (CH₄) in a chabazite crystal (AlHO₂₄Si₁₁) cage. The geometry of the chabazite crystal and the position of the methane molecule are taken from [61] and then reoptimized using the optB88-vdW functional [34]. We repeated the calculation with the presented stochastic MP2 approach, using the exact same computational settings (see Tab. 11.2 for CH₄ in Chab.). The calculation consists of three steps, calculating the MP2 correlation energy of the bare methane molecule, the bare chabazite cage, and the methane molecule inside the chabazite cage. Table 11.4 shows the result for the adsorption energy and the computation time for the stochastic MP2 approach, and the two other MP2 algorithms [43, 41] in VASP. Those can be used as a reference. If an error below 5% is required, the stochastic MP2 approach outperforms the deterministic quintic

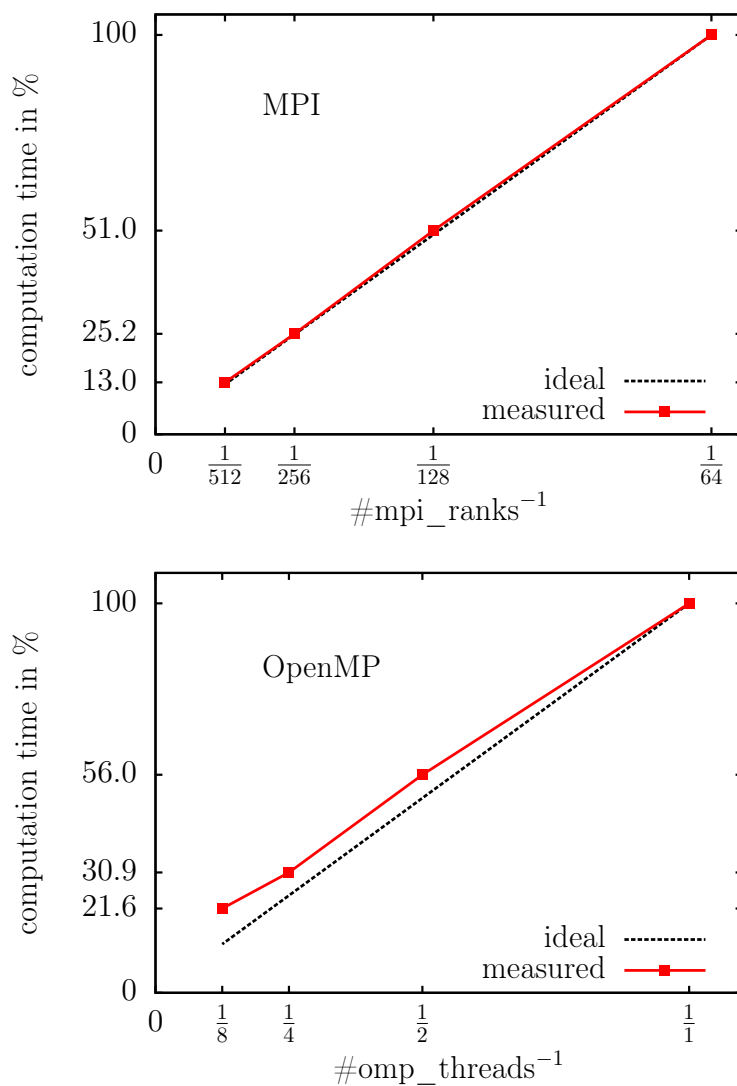


Figure 11.9: Strong scaling of the MPI (upper graph) and the OpenMP parallelization (lower graph) for a stochastic MP2 calculation of a supercell of solid LiH containing 128 (upper) and 32 (lower) atoms. In all calculations a fixed number of stochastic energies was generated for each τ -point. In the upper graph the number of OpenMP threads was fixed to 1 whereas in the lower graph the number of MPI ranks was fixed to 16.

algo.	$E_{\text{ad}}^{(2)}$	$E_{\text{ad}}^{(2)} _{E_{\text{cut}}^{\text{aux}} \rightarrow \infty}$	CPU hours
MP2 [43]	298.98	-	17 448
LTMP2 [41]	299.02	294.83	3 769
stoch. MP2	254 ± 50	261 ± 50	788
stoch. MP2	318 ± 23	316 ± 23	3 518
stoch. MP2	287 ± 15	281 ± 15	10 988

Table 11.4: Correlation part of the adsorption energy in meV of a methane molecule in a chabazite crystal cage using three different MP2 algorithms in VASP. Here, $E_{\text{ad}}^{(2)}|_{E_{\text{cut}}^{\text{aux}} \rightarrow \infty}$ stands for the result of the internal cutoff extrapolation.

scaling algorithm [43] but is not competitive compared to the deterministic quartic scaling MP2 code [41]. The stochastic algorithm is favorable only if an error of about 20% is accepted.

11.2.4 Conclusion

We implemented a stochastic algorithm to calculate the MP2 correlation energy of three dimensional periodic systems in VASP. The parallelization is highly efficient such that thousands of CPUs can be used. In principal, the exact MP2 energy can be reached employing sufficiently large samples for each τ -point and the internal basis set extrapolation. We found a cubic scaling with the system size, if a fixed absolute statistical error is required. Linear scaling could be reached for a fixed relative error per valence orbital. This is a consequence of the quadratic scaling of the variance with the system size. We also demonstrated the limitations of the stochastic approach by calculating the adsorption energy of a methane molecule in a chabazite crystal cage. If errors of about 20% are acceptable for this calculation, the stochastic approach is preferable, however, an error of about 5% already leads to a higher computational effort than for the deterministic quartic scaling algorithm.

We believe that stochastic approaches are indeed a promising way to handle the high computational effort of MP2 calculations, however, we emphasize, that the advantage of the lower complexity can quickly be compensated by larger prefactors when high accuracies are required. It is indispensable to develop techniques that considerably reduce the sample variance, if statistical errors below 1 meV per valence band are required.

11.3 Electron repulsion integrals in a random basis

Correlation energy methods like MP2 or RPA often suffer from a slow convergence with respect to the basis set size. This applies both to the number of unoccupied Hartree-Fock orbitals as well as to the number of plane-waves. While the former could be eased by the presummation over all unoccupied Hartree-Fock orbitals in the quartic scaling LTMP2 algorithm (see Sec. 10.1 or Ref. [41]), the latter remains an open problem that has only been dealt by extrapolation techniques so far. However, it is also known, that converged correlation energies can be obtained by significantly smaller basis set sizes, if, for instance, the natural orbital basis instead of the Hartree-Fock orbital basis is employed [75]. In this section, we present the idea, that the plane-wave basis can be replaced by a *random basis*. Usually, stochastic approaches suffer from the loss of error cancellation effects for energy differences. In contrast, the random basis technique, which will be presented here, can still exploit error cancellation for energy differences, if the random basis transformation is reused. We implemented this approach into the quartic scaling LTMP2 code by replacing the outer plane-wave loop by an outer loop over the the random basis. We then probed, if it is possible to use significantly smaller basis set sizes within the random basis.

11.3.1 The random basis

In the plane-wave basis, we evaluate the electron repulsion integrals by (see Eq. 8.27),

$$\langle \varphi_i \varphi_j | r_{12}^{-1} | \varphi_a \varphi_b \rangle = \frac{1}{\Omega} \sum_{\mathbf{G}} \frac{4\pi}{G^2} \langle \varphi_i | e^{i\mathbf{G}\hat{r}} | \varphi_a \rangle \langle \varphi_j | e^{-i\mathbf{G}\hat{r}} | \varphi_b \rangle \quad (11.67)$$

where Ω is the volume of the system and \mathbf{G} are reciprocal lattice vectors (plane-waves). For brevity, we neglect k -point sampling and spin here. We introduce the *Coulomb vertex*,

$$\Gamma_{ia}^{\mathbf{G}} = \sqrt{\frac{4\pi}{G^2}} \langle \varphi_i | e^{i\mathbf{G}\hat{r}} | \varphi_a \rangle \quad (11.68)$$

and inflate our expression to

$$\langle \varphi_i \varphi_j | r_{12}^{-1} | \varphi_a \varphi_b \rangle = \frac{1}{\Omega} \sum_{\mathbf{G}\mathbf{G}'} \Gamma_{ia}^{\mathbf{G}} (\Gamma_{bj}^{\mathbf{G}'})^* \delta_{\mathbf{G}\mathbf{G}'}. \quad (11.69)$$

We can now use the Kronecker delta to perform basis transformations. Consider the unitary matrix $u_{\theta\mathbf{G}}$ which transforms from the plane-wave basis to the θ basis. Since it is unitary, we can write

$$\delta_{\mathbf{G}\mathbf{G}'} = \sum_{\theta} u_{\theta\mathbf{G}} u_{\theta\mathbf{G}'}^*, \quad (11.70)$$

and thus

$$\langle \varphi_i \varphi_j | r_{12}^{-1} | \varphi_a \varphi_b \rangle = \frac{1}{\Omega} \sum_{\theta} \Gamma_{ia}^{\theta} (\Gamma_{bj}^{\theta})^*, \quad (11.71)$$

with the transformed Coulomb vertices

$$\Gamma_{ia}^\theta = \sum_{\mathbf{G}} u_{\theta\mathbf{G}} \Gamma_{ia}^{\mathbf{G}}. \quad (11.72)$$

If $N_{\mathbf{G}}$ and N_θ denote the number of basis vectors in the plane-wave and θ basis respectively, we aim to find a θ basis such that

$$\frac{1}{\Omega} \sum_{\theta}^{N_\theta} \Gamma_{ia}^\theta (\Gamma_{bj}^\theta)^* \approx \frac{1}{\Omega} \sum_{\mathbf{G}}^{N_{\mathbf{G}}} \Gamma_{ia}^{\mathbf{G}} (\Gamma_{bj}^{\mathbf{G}})^*, \quad (11.73)$$

where $N_\theta \ll N_{\mathbf{G}}$.

In general, any unitary matrix $u_{\theta\mathbf{G}}$ represents a valid basis transformation. Thus, nothing prevents us from testing random unitary matrices, corresponding to random bases.

Application to MP2 calculations

We apply this technique to the quartic scaling LTMP2 algorithm presented in Sec. 10.1. We neglect k -point sampling, hence Eq. (10.18) reduces to

$$E_x^{\text{MP2}} = \frac{1}{\Omega^2} \int_0^\infty d\tau \sum_{\mathbf{G}\mathbf{G}'} \frac{4\pi}{\mathbf{G}^2} \sum_{ij}^{\text{occ.}} \langle \varphi_i | e^{-i\mathbf{G}\hat{r}} | w_j^{\mathbf{G}\tau} \rangle^* \langle \varphi_j | e^{-i\mathbf{G}\hat{r}} | w_i^{\mathbf{G}\tau} \rangle, \quad (11.74)$$

with

$$|w_j^{\mathbf{G}\tau}\rangle = \sum_a^{\text{unocc.}} e^{(\varepsilon_a - \varepsilon_i)\tau} \Gamma_{aj}^{\mathbf{G}} |\varphi_a\rangle. \quad (11.75)$$

Applying the unitary basis transformation to the θ basis, we achieve

$$E_x^{\text{MP2}} = \frac{1}{\Omega^2} \int_0^\infty d\tau \sum_{\theta} \sum_{\mathbf{G}} \frac{4\pi}{\mathbf{G}^2} \sum_{ij}^{\text{occ.}} \langle \varphi_i | e^{-i\mathbf{G}\hat{r}} | w_j^{\theta\tau} \rangle^* \langle \varphi_j | e^{-i\mathbf{G}\hat{r}} | w_i^{\theta\tau} \rangle, \quad (11.76)$$

with

$$|w_j^{\theta\tau}\rangle = \sum_a^{\text{unocc.}} e^{(\varepsilon_a - \varepsilon_i)\tau} \Gamma_{aj}^\theta |\varphi_a\rangle. \quad (11.77)$$

The plane-wave sum over \mathbf{G} remains, since we want to keep the quartic scaling of the LTMP2 approach. In the canonical, quintic scaling, MP2 formulation both plane-wave summations over \mathbf{G} and \mathbf{G}' could be evaluated in the θ basis, however, at the price of a higher algorithmic complexity.

11.3.2 Implementation

Since Eq. (11.76) has exactly the same form as the Gamma-only version of (10.18), we only need to slightly adapt the algorithm presented in Sec. 10.1 or in [41]. This small

change consists in providing the Coulomb vertex Γ_{aj}^θ in the θ basis instead in the plane-wave basis, in order to calculate the auxiliary states $|w_j^{\theta\tau}\rangle$. This is simply achieved by Eq. (11.72), thus the only thing worth clarifying is the construction of the random unitary matrix $u_{\theta G}$.

Constructing the random basis

In order to construct random unitary transformation matrices, we pursue the following two approaches. First, one can construct a random matrix, which exactly obeys the condition to be unitary, and second, one can construct a matrix, which is unitary only on average.

The first approach can be performed by calculating a QR decomposition of a random matrix. The entries of the random matrix are sampled by complex numbers with a uniformly distributed real part and a uniformly distributed imaginary part from the interval $[-0.5, +0.5]$.

The second approach is even simpler in practice. There, we sample both the real part, $x_{\theta G}$, and the imaginary part, $y_{\theta G}$, of each matrix element $u_{\theta G}$ with uniformly distributed random numbers from the interval $[-\sqrt{\frac{3}{2N_\theta}}, +\sqrt{\frac{3}{2N_\theta}}]$. As a consequence, we find a similar result for the expectation value $E[\dots]$ as for the stochastic orbitals from in Sec. 11.2,

$$E \left[\sum_{\theta}^{N_\theta} u_{\theta G} u_{\theta G}^* \right] = E \left[\sum_{\theta}^{N_\theta} (x_{\theta G} + iy_{\theta G})(x_{\theta G} - iy_{\theta G}) \right] \quad (11.78)$$

$$= E \left[\sum_{\theta}^{N_\theta} (x_{\theta G}^2 + y_{\theta G}^2) \right] \quad (11.79)$$

$$= 2N_\theta E[r^2], \quad (11.80)$$

where r is a random number, sampled in the same interval as the real and imaginary parts of the transformation matrix. We find

$$E[r^2] = \frac{1}{2 \cdot \sqrt{\frac{3}{2N_\theta}}} \int_{-\sqrt{\frac{3}{2N_\theta}}}^{+\sqrt{\frac{3}{2N_\theta}}} r^2 dr = \frac{1}{2N_\theta}. \quad (11.81)$$

Thus, our constructed matrix is unitary on average,

$$E \left[\sum_{\theta}^{N_\theta} u_{\theta G} u_{\theta G}^* \right] = 1. \quad (11.82)$$

The same can be applied for the case of orthogonal transformation matrices, where the matrix elements are purely real valued. But if not explicitly stated, the presented results rely on complex unitary matrices.

The first approach (QR decomposition) has the advantage, that it is exact, if we sample

the random basis with $N_\theta = N_G$. For decreasing N_θ we expect a growing statistical error, i.e. a growing variance. The second approach even has a statistical error for the case $N_\theta = N_G$, but the variance might grow slower for decreasing N_θ , such that it could perform similar as (or even outperform) the first approach for small ratios N_θ/N_G .

Recycling the random basis for error cancellations

In many cases we are interested in energy differences. Usually, energy differences converge faster with respect to the basis set size than absolute energies, especially if systems with similar spatial structure are compared. In contrast to many other stochastic techniques, the random basis approach still allows to exploit this kind of error cancellation. We can store the unitary matrix $u_{\theta G}$ and "recycle" it for another MP2 calculation. This is especially simple, if the number of plane-waves is equal for all considered systems. Illustrations can be found in Sec. 11.3.3

11.3.3 Results

So far, the algorithm is only available in a serial and Gamma-only version, thus testing is limited to small systems. For proof of principle calculations, we chose a simple system, the dissociation of a C_2 dimer. We only calculate the energy difference between the atom distance 1.2 Å (system 2) and 1.5 Å (system 1). The calculations are performed in a supercell of size $5 \times 3 \times 3 \text{ \AA}^3$, and we use the first axes for the atom separation². Due to the frozen core approximation, we use 4 valence electrons for each C atom, resulting in a total of 8 occupied bands. The plane-wave cutoff E_{cut} was set to 650 eV where we used 433 eV for the auxiliary plane-wave cutoff $E_{\text{cut}}^{\text{aux}}$, that controls the evaluation of the electron repulsion integrals. This results in $N_G = 449$, where N_G is limited by $E_{\text{cut}}^{\text{aux}}$. The number of unoccupied Hartree-Fock bands was set to 1687. As a reference, we calculated the energy difference of system 1 and 2 with a deterministic MP2 code,

$$\Delta E = E_1^{\text{xMP2}} - E_2^{\text{xMP2}} = 4338.749 \text{ meV} - 3929.988 \text{ meV} = 408.76 \text{ meV} , \quad (11.83)$$

where we only look at the most expensive part, the exchange MP2 contribution (xMP2). We then calculated a sample of 100 energy differences, using the random basis approach, again, restricting to the exchange contribution (rbxMP2),

$$\Delta \tilde{E} = E_1^{\text{rbxMP2}} - E_2^{\text{rbxMP2}} . \quad (11.84)$$

We are interested in the error, defined by

$$\delta E = \Delta \tilde{E} - \Delta E , \quad (11.85)$$

²This cell is indeed too small to produce meaningful results, since the periodic images of the atoms are too close. However, the MP2 energy difference for this setup is 0.977 eV, which is not too far from to the FCI result of 1.159 eV from [76]. Hence, the benchmark system does not seem to be completely without physical significance.

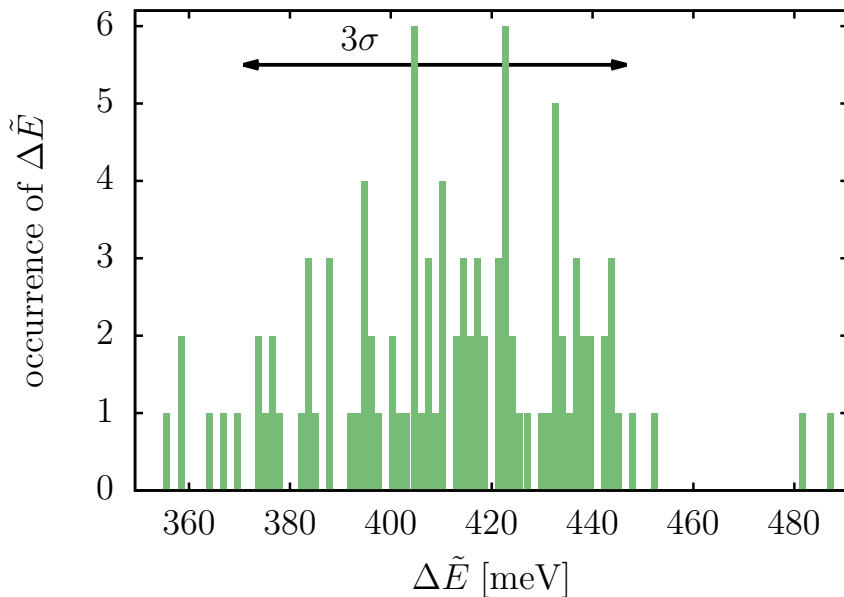


Figure 11.10: Histogram of $n = 100$ calculations of $\Delta\tilde{E}$ using recycled unitary basis transformations and $N_\theta/N_G = 0.8$. This results in $3\sigma = 76$ meV. The reference value is $\Delta E = 408.76$ meV.

which allows to define the mean absolute error (MAE)

$$\text{MAE} = \frac{1}{n} \sum_{i=1}^n |\delta E^{(i)}|, \quad (11.86)$$

with $n = 100$. Furthermore, we introduce the variance that measures the spread of the $\delta E^{(i)}$'s,

$$\sigma^2 = \frac{1}{n-1} \sum_{i=1}^n |\delta E^{(i)}|^2, \quad (11.87)$$

such that we can use σ as the standard deviation. Note that the MP2 exchange energy difference, that we want to reproduce with the random basis is very small. Thus our system can be considered as a very challenging benchmark.

In Fig. 11.10 we show the histogram of results for the ratio $N_\theta/N_G = 0.8$. We can deduce that this N_θ/N_G ratio introduces an error of about 76 meV in the MP2 exchange energy, if we chose 3σ as the measure. This corresponds to an error of about 9.5 meV/electron, or to a relative error of about 19%.

Error cancellation and comparison of the methods to construct the unitary matrix

Recycling the unitary matrix clearly reduces the mean average error as well as the standard deviation, as Fig. 11.11 shows. For this particular benchmark system, the basis recycling roughly halved the mean average error and standard deviation.

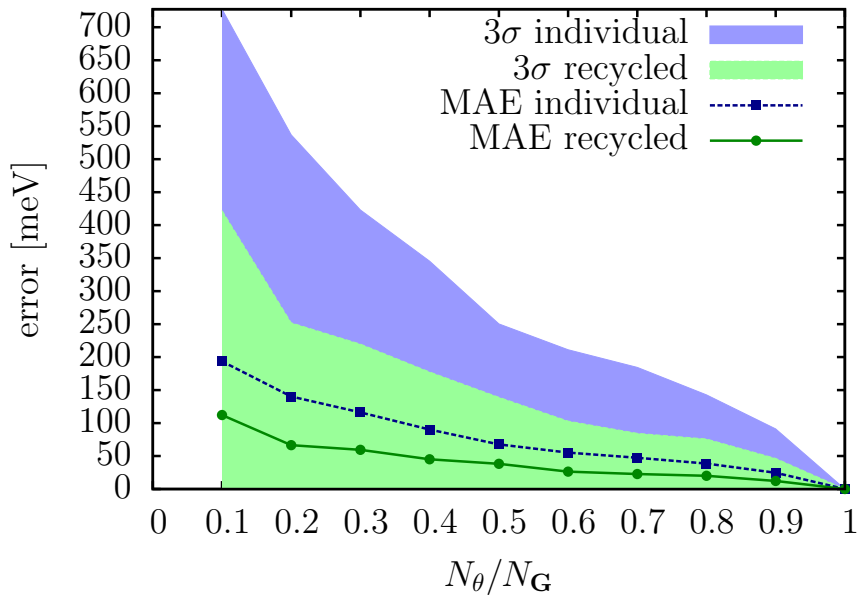


Figure 11.11: Mean absolute error (MAE) and 3σ for calculations with recycled unitary matrices and calculations without recycled (i.e. individual) basis transformation. Here $N_G = 449$.

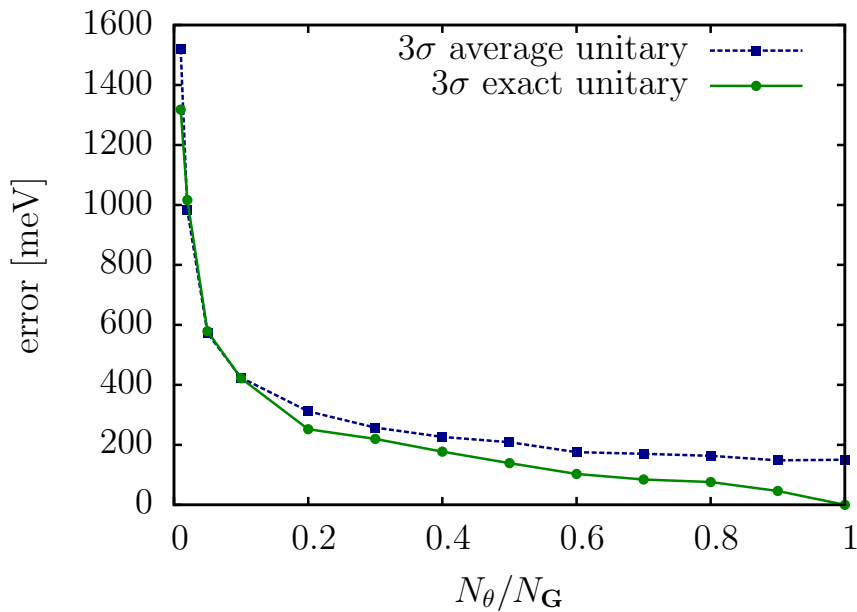


Figure 11.12: Comparison of 3σ of the random but exact unitary and the basis transformation which is only unitary in average, as described in Sec. 11.3.2

In Sec. 11.3.2 we introduced two methods to calculate the random unitary basis transformation. The first one relies on a QR decomposition of a random matrix and is denoted as *exact unitary*. The second one is based on a completely random matrix which is only unitary in average, termed *average unitary*. The Fig. 11.12 clearly shows, that the 3σ of the second approach (average unitary) can not outperform the first method for small N_θ/N_G , although it shows a similar performance for $N_\theta/N_G \leq 0.1$. It is also worth mentioning, that the first approach reveals a stronger increase in the error when varying N_θ/N_G from 1.0 to 0.5, while the error of the second approach grows only slightly from a plateau of about 200 meV.

11.3.4 Conclusion and Outlook

We presented an implementation of a random basis evaluation of electron-repulsion integrals in MP2. In particular we showed, that once a random basis is generated, it can be recycled for subsequent calculations in order to profit from the error cancellation of limited basis set sizes. The implementation relies on the most simple random number sampling, and the ratio $N_\theta/N_G = 0.5$ (i.e using only half as many basis vectors) introduces an error of about 17 meV/electron, if the QR decomposition strategy is used. Hence, the random basis transformations could be used for calculations on large systems, if only a relative error per electron is of interested. However, if a small absolute error is of interested, this method will bring rather no advantage.

A possible route for improvements could be to use importance sampling techniques, e.g., taking into account that the Coulomb kernel decays as $1/G^2$. Also, one could restrict the random basis approach to the large $|G|$ contributions, since they rarely contain physical information but cause the slow convergence with respect to the basis set size.

CHAPTER 12

Summary, Conclusion and Outlook

The principal aim of this thesis is to prove that developing low-scaling algorithms for many-body exchange-like contributions to the total energy is indeed possible. Exchange-like contributions are necessary to obey the symmetrization postulate for electrons but were also known as an obstacle for the development of efficient total energy codes. As a consequence, larger systems, involving several hundreds of correlated valence electrons, are now accessible. The result are two fully developed and ready-to-use algorithms to calculate the MP2 energy of periodic systems, parallelizable on thousands of CPUs. Four more algorithms are available either as concepts or as usable implementations with a few limitations. We will summarize the work in the following.

The LTMP2 algorithm (Sec. 10.1 or Ref. [41]) is the first proof that accurate MP2 calculations are possible with a quartic scaling complexity, both in principle and in practice. The main idea of the algorithm is to avoid the summation of all combinations of occupied-unoccupied pairs by a presummation over all unoccupied states to a few auxiliary states. This can be elegantly achieved in the Laplace transformed MP2 formulation.

The same strategy could be adapted (Sec. 10.2) to the second-order screened exchange (SOSEX) correction to the RPA. Pseudocode is available, serving as a guideline to reduce the scaling from N^5 to N^4 . Moreover, the code can be used to provide a general building block for other (higher-order) exchange-like diagrams, see (10.36).

We also presented the possibility to implement an algorithm that calculates the second-order exchange diagram with an only cubic scaling complexity (Sec. 10.3). Although we estimated the break point to be at unattractively large systems, the code could be useful in the not too distant future. Note, that this cubic scaling strategy also applies to SOSEX.

With the introduction of a real space Monte Carlo sampling of Feynman diagrams (Sec. 11.1), we switched to the stochastic strategies. Here, we presented new importance sampling techniques that drastically reduce the computational effort compared to the state of the art. Thus, providing a route to make the real space Monte Carlo method competitive to existing algorithms. The cubic scaling could open a path to large systems, in particular if only the relative error per electron is of interest.

Another stochastic strategy was pursued with stochastic orbitals (Sec. 11.2 or Ref [46]). This work is based on a publication by Neuhauser et al. [70] and introduces several improvements like correlated sampling. The code can be considered as an efficient

stochastic approach to calculate the second order exchange in cubic scaling, however, we also highlight the limitations of stochastic approaches.

Last but not least we mention an attempt to calculate the electron-repulsion integrals in a random basis. This was motivated by the fact that correlation energy methods often suffer from the slow convergence with respect to the basis set size, i.e. with respect to the number of plane-waves in VASP. Instead of the plane-wave basis we analyzed the effect of a random basis, introduced by a random unitary matrix. Since electron-repulsion integrals are the very ingredient for many correlation energy methods, the results could be interesting for the quantum chemistry and materials physics community.

In general, the presented methods form a basis for low-complexity calculations of higher-order exchange-like diagrams, allowing for applications on larger systems that could not be treated so far. More generally speaking, the developed strategies help to efficiently implement so called *vertex corrections* to total energies or quasiparticle energies, where "vertex corrections" refers to the scheme proposed by Hedin in Ref. [35].

However, one should not lose sight of the fact that even though developing low-scaling algorithms is important, developing economic total energy methods that correctly cover the essential physics is even more important for the electronic structure problem. In particular, the question arises, why the RPA, although neglecting higher-order exchange completely, is so successful in predicting material properties? Why is the exchange contribution in MP2 energy differences mostly very small but sometimes indispensable? Even if DFT has already solved many problems in the electronic structure problem, one can say without hesitation that there is still no clear perception as to how the correlation energy of materials can be reliably captured with reasonable computational effort.

Part III

Application of the Random Phase Approximation

CHAPTER 13

Ab initio phase diagram of PbSe crystals calculated with the RPA

Understanding the phase behavior of semiconductor materials is important for applications in solid state physics and nanoscience. Accurate experimental data is often difficult to obtain due to strong kinetic effects. In this work, we calculate the temperature-pressure phase diagram of lead selenide (PbSe) using the random phase approximation (RPA), an accurate wavefunction based many-body technique. We consider three crystalline phases, the low pressure B1 phase (NaCl-type), the intermediate B33 phase (CrB-type), and the high pressure B2 phase (CsCl-type). The electronic contributions to the free energy (at $T = 0$ K) are calculated in the Born-Oppenheimer approximation using the RPA, whereas phononic contributions are computed in the quasi-harmonic approximation using DFT and the PBEsol functional. At room temperature, we find transition pressures of 4.6 ± 0.3 GPa for the B1 \leftrightarrow B33 transition and 18.7 ± 0.3 GPa for the B33 \leftrightarrow B2 transition, in good agreement with experiments. In contrast to the interpretation of recent experiments, we observe a negative Clapeyron slope for both transitions. Gibbs free energy differences between competing structures have small gradients close to coexistence, consistent with pronounced hysteresis observed in experiments. The phase diagram presented in this work can serve as a reference for future studies of PbSe and should prove useful in the development of accurate and efficient force fields. This chapter largely follows the author's publication [77].

13.1 Introduction

Lead chalcogenides, PbX (X = S, Se, and Te), are widely studied semiconductor materials with applications in opto-electronics, sensors, and thermoelectrics [78]. PbX quantum dots are used as versatile building blocks for nanomaterials due to their narrow bandgap and strong interparticle interactions in self-assembled superlattices [79, 80]. The bandgap of these materials can be tuned over a wide range by applying external pressure [81, 82, 83, 84, 85]. A particularly sudden and dramatic change of the electrical and mechanical materials properties can be induced via structural transformations [86]. By controlling nanoscale morphology, semiconductors can even be trapped in high-pressure

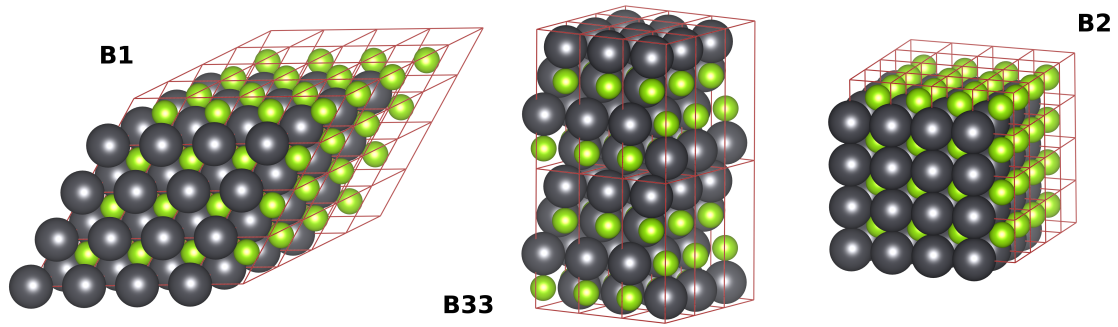


Figure 13.1: Supercells of the three considered phases B1, B33, and B2 of PbSe, as used for phonon calculations. Pb atoms are shown in gray, Se atoms in green color. Primitive cells are indicated by dark red lines.

crystal structures that are unstable in the bulk [87, 88, 89]. Controlling material properties of PbX via pressure-processing, however, requires knowledge of the structural stability and phase behavior of these materials.

The pressure-induced structural phase transitions of lead selenide (PbSe), which are the focus of this work, have been studied experimentally [90, 91, 92, 93] and computationally [83, 94, 95, 96, 85, 92, 93] for several decades. At ambient conditions, PbSe crystallizes in the semiconducting B1 phase (NaCl-type structure, $Fm\bar{3}m$, No. 225). At pressures of a few GPa, an intermediate orthorhombic semiconducting phase is observed; the metallic high pressure phase is B2 (CsCl-type, $Pm\bar{3}m$, No. 221). Several crystal structures have been suggested for the intermediate phase, including B16 (GeS-type, $Pnma$, No. 62), B27 (FeB-type, $Pnma$, No. 62), and B33 (CrB-type, $Cmcm$, No. 63) [91, 95, 96, 92, 93]. In this work, we report results for the B33 structure, since it is the structure with the highest symmetry and the free energy-volume curves are assumed to be very similar for all three possible intermediate structures.

One of the first accurate measurements of the transition pressures of PbSe was reported by Chattopadhyay et al. [90] using high pressure X-ray diffraction with synchrotron radiation. At room temperature, they report transition pressures for B1 \rightarrow B33 of approximately 4.5 GPa and for B33 \rightarrow B2 of approximately 16 GPa. A more recent room temperature X-ray diffraction study by Streltsov et al. [91] reports a measurable persistence of the B1 structure to at least 7.28 GPa, indicating that coexistence of the B1 and B33 phases can be observed over a broad pressure range. Strong hysteresis was also reported by Li et al. [92] who observed the onset of the B1 \rightarrow B33 transition at 4.8 GPa and 2.9 GPa in the forward and back directions, respectively, at room temperature. The onset of the B33 \rightarrow B2 transition was observed at 19.5 GPa in that study. Wang et al. [93] recently reported a temperature-pressure phase diagram for the B1 and B33 structures, displaying temperature dependent hysteresis and a positive Clapeyron slope: At room temperature the onset of the B1 \rightarrow B33 transition was found at 3.48 GPa, whereas at 1000 K the B33 \rightarrow B1 back-transition commenced at 6.12 GPa.

To our knowledge, available computational *ab initio* studies of the transition pressures

of PbSe are restricted to density functional theory (DFT) calculations at zero temperature, which ignore finite temperature effects. Furthermore, the published DFT results do not present a consistent picture. Depending on the choice of DFT functional, reported transition pressures range from 6.2 to 10.0 GPa for the B1 \leftrightarrow B33 transition and from 16.39 to 22.6 GPa for the B33 \leftrightarrow B2 transition [94, 95, 85, 92]. These different results directly reflect the problem of choosing the best DFT functional for a given material. Moreover, as pointed out by Skelton et al. [97], temperature plays an important role in lead chalcogenides and needs to be considered in *ab initio* investigations to obtain accurate results.

In this work, we present an *ab initio* study of the phase diagram of PbSe by employing the random phase approximation (RPA) [98, 99] for the electronic contributions (i.e., at $T = 0$ K) in order to reduce the variability associated with different DFT functionals. Applications of the RPA to solids are becoming increasingly popular, as RPA outperforms DFT in systematic benchmark studies [100, 101, 18]. In addition, low complexity implementations [69] of the RPA lend themselves to the study of large systems, including the B33 phase of PbSe studied here, which involves 56 valence electrons per primitive cell at a volume of approximately 200 \AA^3 . Nevertheless, the RPA is not exact and some shortcomings have been identified, motivating the research of systematic corrections to the RPA [18, 52, 102, 103, 104, 105, 106]. Still, as described in [107, 108] the corrected RPA methods provide only small quantitative changes to transition pressures, hence we expect no significant qualitative changes.

To treat finite temperature effects, we include phonon contributions to the free energy in the quasi-harmonic approximation using the PBEsol functional [32]. Following the strategy proposed in Ref. [109], the choice of PBEsol was made after comparing the pressure-volume curves calculated with the PBE [31], PBEsol [32], and SCAN [33] functionals with those obtained by RPA.

13.2 Theory and methods

At given pressure p and temperature T , the phase with the lowest molar Gibbs free energy g is thermodynamically stable. To obtain the relations $g(p, T)$ for the three crystal structures, we first calculate molar Helmholtz free energies $f(v, T)$ at several temperatures and molar volumes v . Interpolations were performed using the Birch-Murnaghan equation of state [22]. Gibbs free energies are then obtained via the Legendre transform

$$g = f + pv, \quad p = - \left(\frac{\partial f}{\partial v} \right)_T. \quad (13.1)$$

Helmholtz free energies are calculated as the sum of electronic and phononic contributions, $f = f_{\text{el}} + f_{\text{phon}}$, neglecting electron phonon interactions. More precisely, the Born-Oppenheimer approximation was assumed for electronic degrees of freedom and the quasi-harmonic approximation was used for lattice vibrations. The electronic contributions to the free energy were calculated within the RPA, as implemented in the Vienna ab

Table 13.1: Relaxed unit cells of the B33 phase (CrB-type, *Cmcm*, No. 63) for different volumes, containing 4 Pb atoms and 4 Se atoms. For the relaxation, the PBEsol functional was used with a $12 \times 4 \times 12$ k-point mesh and a plane wave cutoff of 700 eV.

Volume [\AA^3]	lattice parameters [\AA]	Pb Wyckoff site	Se Wyckoff site
168.37	$a = 3.8441$	4c, (0, 0.3826, 1/4)	4c, (0, 0.1270, 1/4)
	$b = 10.4987$		
	$c = 4.1719$		
195.68	$a = 4.0622$	4c, (0, 0.3792, 1/4)	4c, (0, 0.1300, 1/4)
	$b = 11.1456$		
	$c = 4.3218$		
222.98	$a = 4.2415$	4c, (0, 0.3717, 1/4)	4c, (0, 0.1342, 1/4)
	$b = 11.8782$		
	$c = 4.4258$		

 Table 13.2: List of explicitly treated valence electrons, core radii r_c , and energy cutoffs ENMAX for the PAW potentials.

Element	Valence	r_c [\AA]	ENMAX [eV]
for free energy calc. of electrons			
Pb	$5s^2 5p^6 5d^{10} 6s^2 6p^2$	2.3	317
Se	$4s^2 4p^4$	2.1	212
for free energy calc. of phonons			
Pb	$5s^2 5d^{10} 6s^2 6p^2$	2.5	238
Se	$4s^2 4p^4$	2.1	212

initio simulation package (VASP) [57, 11, 69]. For the phonon contributions, we computed harmonic force constants using large supercells of the B1, B33, and B2 phases, as illustrated in Fig. 13.1, with DFT and the PBEsol functional in VASP. Phonon free energies were then calculated with the phonopy program [110] in the quasi-harmonic approximation, which is a reasonable approach for lead chalcogenides [97]. For the intermediate B33 phase, relaxations of the unit cell shape and atom positions were performed for each considered cell volume. Due to its superior computational speed, the PBEsol functional was also used for these calculations. (Note, however, that RPA force calculations are already implemented in VASP [63]). All (free) energies and volumes are reported in units of meV and \AA^3 per PbSe, respectively.

Table 13.3: Computational parameters for the electronic contribution to the free energy (at $T = 0$ K).

Phase	$k_1 \times k_2 \times k_3$	ENCUT [eV]
PBEsol		
B1	$8 \times 8 \times 8$	550
B33	$12 \times 4 \times 12$	550
B2	$17 \times 17 \times 17$	550
RPA		
B1	$9 \times 9 \times 9$	450
B33	$9 \times 3 \times 9$	450
B2	$9 \times 9 \times 9$	450

13.3 Computational details

13.3.1 The crystal structures of B1, B33, and B2

The construction of primitive cells for the B1 and B2 crystal lattices is straightforward, since the volume is the only free parameter for these structures. For the B33 phase, the unit cell geometry and atom positions depend on the volume of the cell. Therefore, we performed lattice relaxations using the PBEsol functional at several volumes. As a starting point we took the experimentally measured lattice parameters given in Table 1 in Ref. [93]. Structural parameters of relaxed structures at three selected volumes can be found in Tab. 13.1.

13.3.2 Pseudopotentials, basis set and k-point meshes

All VASP calculations are based on the frozen core approximation and the projector augmented wave [10] method (PAW), using the potentials specified in Tab. 13.2.

The size of the plane wave basis is controlled by the kinetic energy cutoff (ENCUT flag in VASP). The k-point mesh is specified by three numbers ($k_1 \times k_2 \times k_3$), corresponding to a uniform sampling of the Brillouin zone in each direction of the reciprocal lattice. We applied the following criteria to determine the energy cutoff and the density of the k-point mesh. For all electronic free energy calculations using DFT, we required the total free energy to be converged to within 1 meV per PbSe. For all electronic free energy calculations based on the RPA, we only required the free energy *differences* to be converged within 1 meV per PbSe. The resulting energy cutoffs and k-point meshes can be found in Tab. 13.3. For phonon calculations, we built supercells containing 128 atoms for B1 and B2, and 144 atoms for B33, as illustrated in Fig. 13.1. To determine energy cutoffs and k-point meshes, we required a convergence of the zero point energy to within 1 meV per PbSe. Parameters used in phonon calculations can be found in Tab. 13.4.

Table 13.4: Computational parameters for the phonon contributions to the free energy. Supercells were constructed by replicating primitive cells n_i times along the respective lattice directions.

Phase	$k_1 \times k_2 \times k_3$	ENCUT	$n_1 \times n_2 \times n_3$	#atoms
B1	$2 \times 2 \times 2$	400	$4 \times 4 \times 4$	128
B33	$2 \times 1 \times 2$	500	$3 \times 2 \times 3$	144
B2	$3 \times 3 \times 3$	400	$4 \times 4 \times 4$	128

13.3.3 Error estimates

The transition pressure p_{XY} of a transition from phase X to phase Y (at fixed temperature) obeys the equation

$$p_{XY} = -\frac{f_X(v_X) - f_Y(v_Y)}{v_X - v_Y}, \quad (13.2)$$

where v_X and v_Y are the volumes of the phases X and Y at the transition pressure, respectively. Hence, we can estimate the error δp_{XY} of the transition pressure as

$$\delta p_{XY} \leq \frac{2\delta f}{|v_X - v_Y|}, \quad (13.3)$$

where δf is the error of the free energy due to unconverged basis sets and k-point grids. According to the convergence criteria described in Sec. 13.3.2, we can safely assume that $\delta f \leq 2 \text{ meV}$. Furthermore, we obtain a latent volume larger than 2 \AA^3 (see Fig. 13.4 and Tab. 13.5) for both transitions. We thus estimate a computational error of

$$\delta p_{XY} \leq \frac{4 \text{ meV}}{2 \text{ \AA}^3} \approx 0.3 \text{ GPa} \quad (13.4)$$

for both transitions.

13.4 Results

13.4.1 Comparison of DFT functionals with RPA

To select a DFT functional for phonon calculations, we first calculated electronic free energy-volume curves $f_{\text{el}}(v)$ using all three functionals and the RPA, as illustrated in Fig. 13.2. Pressure-volume relations (*i.e.*, equations of state) calculated from these data via $p = -\partial f_{\text{el}}/\partial v$ are shown in Fig. 13.3. Note that the calculated pressures originate only from the electronic contribution to the free energy (at $T = 0 \text{ K}$). As evident from Fig. 13.3, the PBEsol functional provides the overall best performance compared to RPA results. Accordingly, we chose the PBEsol functional for all DFT calculations.

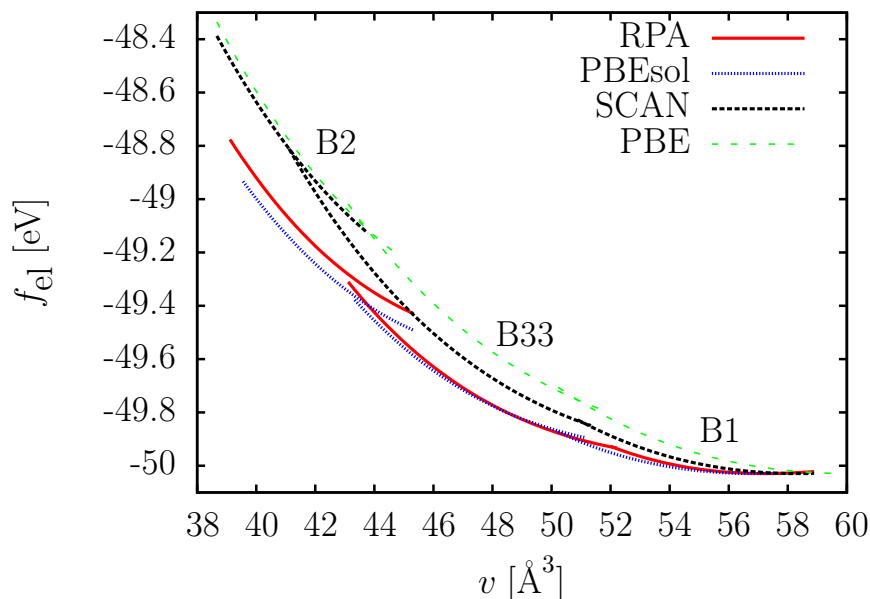


Figure 13.2: Electronic free energy-volume curves (at $T = 0$ K) for each phase calculated using three different DFT functionals and the RPA. The curves are shifted such that the minima of the free energy coincide for the B1 phase.

13.4.2 The temperature-pressure phase diagram

Total free energies $f = f_{\text{el}} + f_{\text{phon}}$ as a function of volume and temperature are shown in Fig. 13.4. The three crystal structures display conventional thermodynamic properties, including positive thermal expansion coefficients and increasing pressure with increasing temperature (at fixed volume). (Note that the latter implies that the entropy of each phase decreases with decreasing volume.) Gibbs free energies as a function of T and p are obtained from these data via the Legendre transform Eq. (13.1). The resulting temperature-pressure phase diagram of PbSe crystals is shown in Fig. 13.5. At room temperature, we find transition pressures of 4.6 ± 0.3 GPa for the B1 \leftrightarrow B33 transition and 18.7 ± 0.3 GPa for the B33 \leftrightarrow B2 transition. We provide free energy and volume differences of the B1 and B33 structures at three points along the coexistence curve in Tab. 13.5. As evident from Fig. 13.5, the RPA significantly stabilizes the intermediate B33 phase compared to PBEsol. The Clapeyron slope is clearly negative for both phase transitions. Interestingly, this result is in contrast to the experimentally measured phase diagram reported in Ref. [93], which shows broad hysteresis but suggests a positive Clapeyron slope.

The negative slope can be explained by softer phonon modes in the high pressure phases. In Fig. 13.6 we show the phonon density of states for all phases at volumes close to the phase transitions at $T = 300$ K. For the first transition (B1 \rightarrow B33, top panel in Fig. 13.6) the average phonon frequencies of both phases are equal within 0.1%, explaining why the transition pressure is largely independent of the temperature. The slightly negative

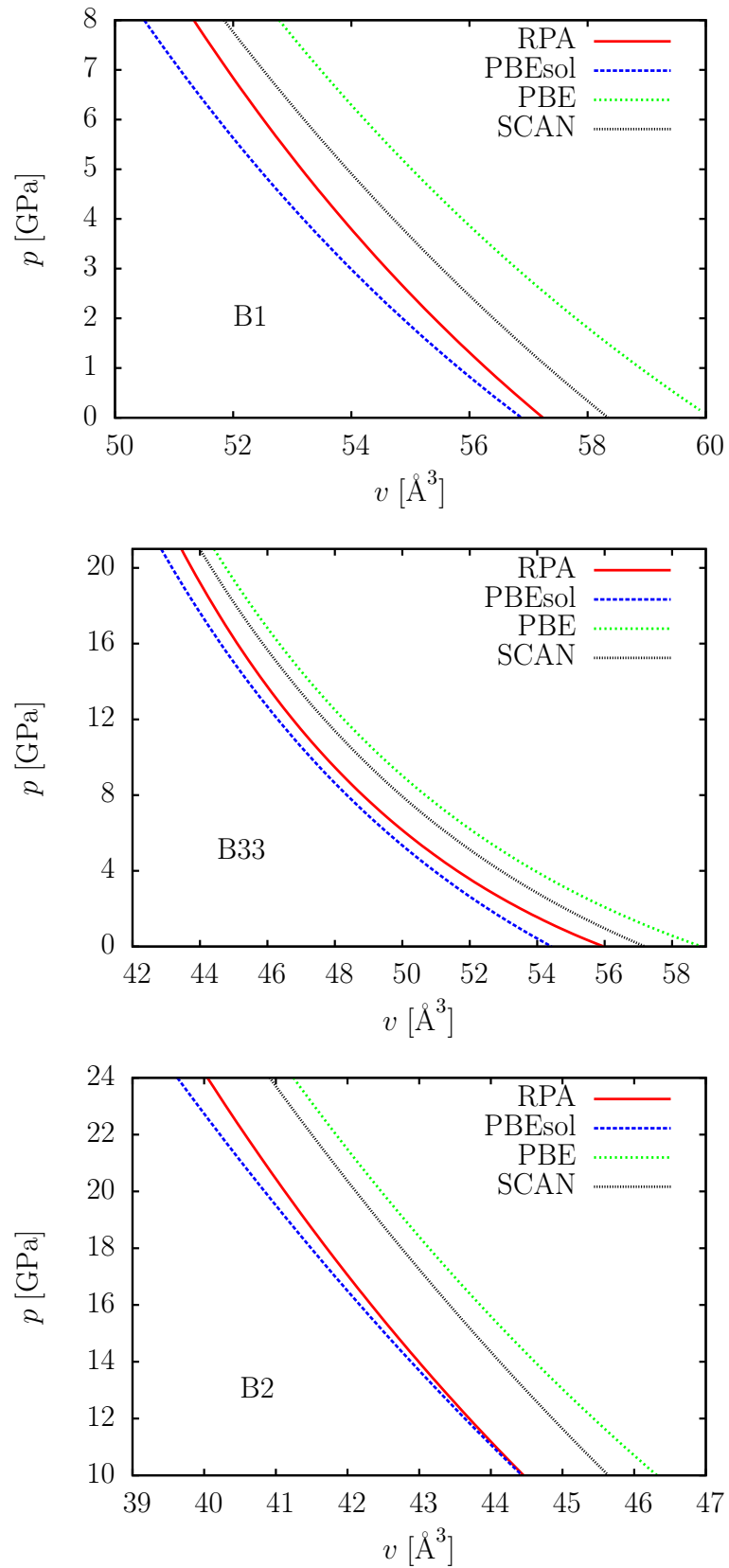


Figure 13.3: Pressure-volume relations calculated from the electronic free energy-volume curves ($T = 0$ K) shown in Fig. 13.2.

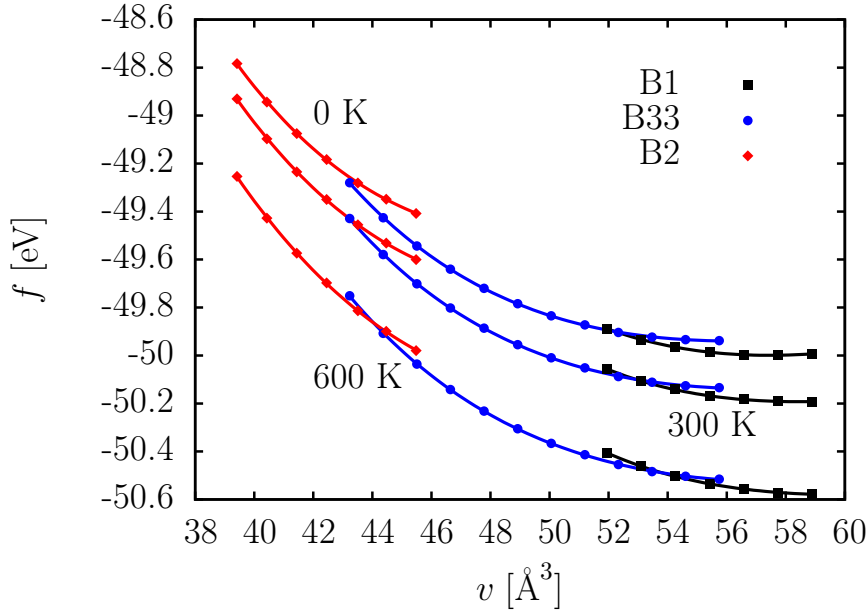


Figure 13.4: Free energy-volume curves of the B1, B33, and B2 structures, including electronic (RPA) and phononic (DFT/PBEsol) contributions, at three selected temperatures. This free energy-volume data set can also be found in the Supplemental information.

Clapeyron slope $\frac{dT}{dp} = \frac{\Delta v}{\Delta s} < 0$ signifies a larger entropy s for the B33 phase at higher temperature. This is related to a larger density of states at low frequencies in the B33 phase, caused by the presence of rather soft acoustic modes in the layered B33 structure. The transition from the B33 to the B2 phase is accompanied by a strong reduction of the average phonon frequencies, which implies a larger entropy s of the B2 phase at higher temperatures (bottom panel in Fig. 13.6). For this transition, the Clapeyron slope is clearly negative. The softer phonon modes in the B2 phase are mainly related to an *increase* of the nearest neighbor distances from 2.72 Å (B33 at $v = 44.37 \text{ Å}^3$) to 3.02 Å (B2 at $v = 42.45 \text{ Å}^3$), as the B2 phase is more densely packed than the B33 phase.

13.5 Discussion and Conclusion

We have calculated the temperature-pressure phase diagram of three crystal structures (B1, B33, B2) of PbSe using the *ab initio* method RPA. The RPA yields accurate free energy differences and thus provides a more accurate phase diagram of PbSe, compared to DFT results. By employing the RPA for the electronic free energy calculations at zero temperature, the computational error associated with the choice of DFT functional is reduced. The results presented in this work can serve as an accurate benchmark for the development of classical force fields that enable dynamic studies of transition mechanisms.

We observe pronounced temperature effects for both transitions, with transition pres-

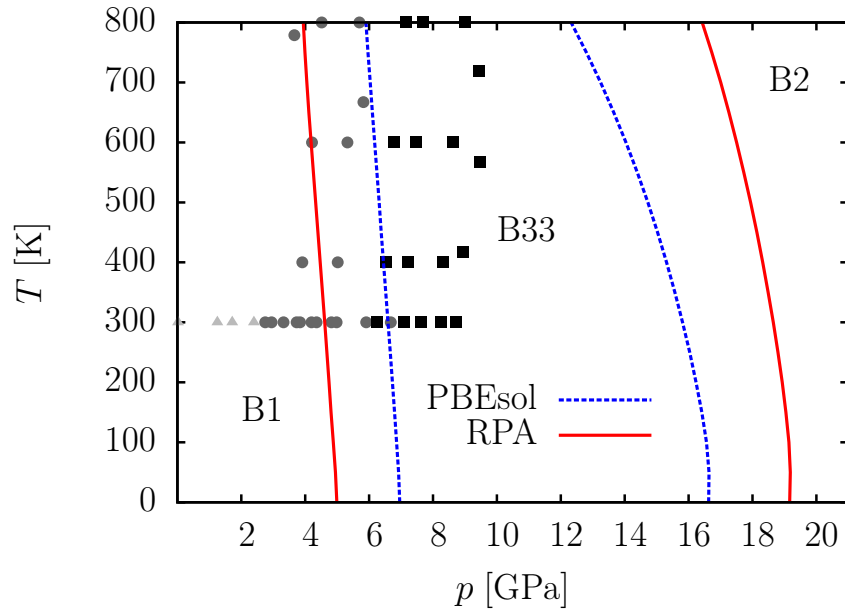


Figure 13.5: The temperature-pressure phase diagram of PbSe, obtained with pure DFT (blue curves) and the RPA (red curves). Experimental results from Ref. [93] are included: B1 (triangles), B33 (squares), and B1/B33 coexistence (circles). In contrast to Ref. [93] we find a negative Clapeyron slope for both phase transitions.

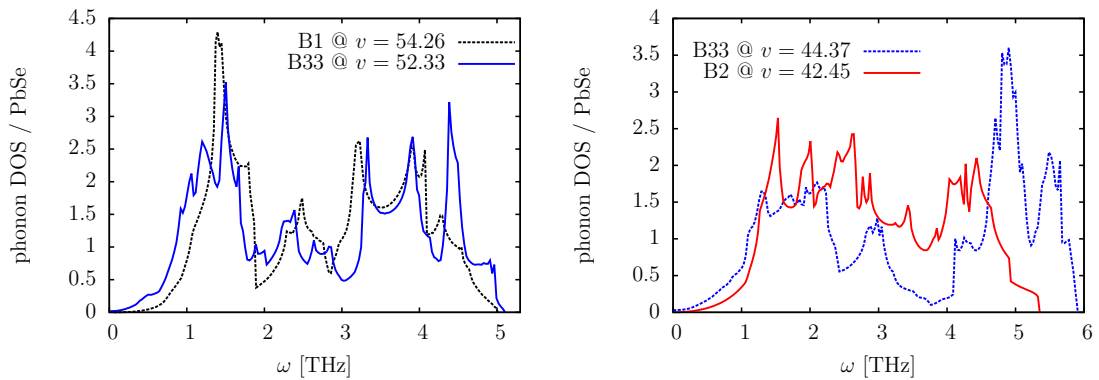


Figure 13.6: Phonon density of states (DOS) of the B1, B33, and B2 phases. The volumes are close to the transition volumes for the B1 \leftrightarrow B33 transition (top) and for the B33 \leftrightarrow B2 transition (bottom) at $T = 300$ K.

Table 13.5: Free energy and volume data of the B1 and B33 phases at coexistence. Here $p_{B1 \leftrightarrow B33} = -\Delta f / \Delta v$ is the transition pressure, v is the volume, $\Delta v = v_{B33} - v_{B1}$ is the volume difference, and $\Delta f = f_{B33} - f_{B1}$ is the free energy difference, calculated as the sum of the electronic free energy difference Δf_{el} and the phonon free energy difference Δf_{phon} .

$p_{B1 \rightarrow B33}$ [GPa]	no zero point vib.		$T = 0$ K		$T = 300$ K		$T = 800$ K	
	B1	B33	B1	B33	B1	B33	B1	B33
	53.16	50.92	53.30	51.06	53.99	51.90	55.66	53.51
Δv	-2.24		-2.24		-2.09		-2.16	
Δf_{el}	70		70		66		65	
Δf_{phon}	0		0		-6		-12	
Δf	70		70		60		53	

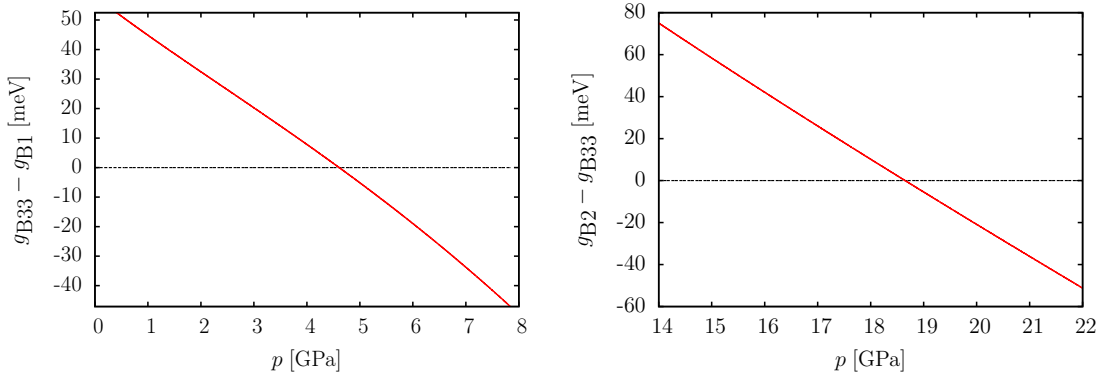


Figure 13.7: Gibbs free energy differences Δg per PbSe at $T = 300$ K for the B1 \leftrightarrow B33 and B33 \leftrightarrow B2 transitions. The small gradients of Δg (≈ 15 meV/GPa) are consistent with the experimentally observed hysteresis and broad coexistence ranges.

tures changing by approximately 20% when the temperature is increased from zero to 800 K. Our calculated transition pressures at room temperature (4.6 ± 0.3 GPa and 18.7 ± 0.3 GPa) lie well within the experimentally reported ranges of 2.9 to 7.28 GPa for the B1 \leftrightarrow B33 transition and 16 to 19.5 GPa for the B33 \leftrightarrow B2 transition. We find that the transition pressures *decrease* with increasing temperature, in apparent contradiction with experiments by Wang et al. [93]. However, we note that the scatter in the experimental data is substantial, with a fairly broad region of coexistence, so that a careful reassessment of the experimental data might be required.

While we have focused on PbSe in this work, it is instructive to consider the phase behavior of the other lead chalcogenides, PbS and PbTe. At ambient pressure, these materials display similar physical and electronic properties [111]; all three materials crystallize in the B1 structure, with typical trends of increasing unit cell dimension and

decreasing bulk modulus from PbS to PbTe. [97] The phase behavior at elevated pressure, however, depends on the chalcogen. Recent measurements of electrical resistance suggests a positive Clapeyron slope for the B1 to B33 transition of PbS. [112] PbTe, on the other hand, does not transform to the B33 structure but adopts the B27 structure as an intermediate. [113]

Experimental studies of structural phase transitions are often plagued by strong hysteresis. If transitions are initiated by nucleation followed by growth, classical nucleation theory (CNT) provides a means for estimating hysteresis widths. According to CNT, the free energy barrier to nucleation ΔG_{nuc} depends strongly on the molar free energy difference Δg between the two phases, $\Delta G_{\text{nuc}} \propto |\Delta g|^{-2}$. Small gradients of Δg in the vicinity of the transition point, as observed in this work (Fig. 13.7), thus result in large nucleation barriers and pronounced hysteresis. Furthermore, coexistence of crystal structures is often observed experimentally over a broad range of conditions, due to the powder-crystalline nature of experimental samples and kinetic effects associated with grain boundaries and other crystal defects. These experimental realities can complicate an accurate determination of coexistence curves and might well explain the discrepancy between this work and Ref. [93]. We expect that our calculations will provide useful guidance for future experiments. For instance, the observation of a negative Clapeyron slope $\frac{dT}{dp} = \frac{\Delta v}{\Delta s} < 0$ signifies a negative latent heat of transformation and a larger entropy s of the high-pressure phase. More experiments are likely needed to clarify the thermodynamic details of structural transformations in PbSe.

Part IV

Appendices

CHAPTER 14

Acknowledgments

I owe great thanks to my supervisor Georg Kresse. He was a great teacher and supporter for me. Initially inexperienced in this research field, he convinced me to venture into his group and awakened my enthusiasm for quantum many-body theory and computational materials physics. In many discussions we have developed more ideas than can be carried out within the framework of a doctoral thesis.

I also owe a lot to my colleagues. Solving problems at the whiteboard is not only fun, it is also usually much faster than if just thinking about it yourself. In particular I would like to mention Benjamin, Menno, and Felix.

The administrative team must not be forgotten either. I thank you for all the fast and professional help and support.

A big thank you also to my wife, Cornelia. Thanks to your own experience, you have always been at my side with help and advice. You were the best support during my work.

CHAPTER 15

List of publications and talks

15.1 Peer reviewed articles

- T. Schäfer, B. Ramberger, G. Kresse, *Quartic scaling MP2 for solids: A highly parallelized algorithm in the plane wave basis*, J. Chem. Phys. 146 (10), 104101, 2017
- T. Schäfer, B. Ramberger, G. Kresse, *Laplace transformed MP2 for three dimensional periodic materials using stochastic orbitals in the plane wave basis and correlated sampling*, J. Chem. Phys. 148 (6), 064103, 2018
- T. Schäfer, Z. Fan, M. Grünwald, G. Kresse, *Ab initio phase diagram of PbSe crystals calculated with the random phase approximation*, accepted in Phys. Rev. B., arXiv:1807.11415, 2018
- B. Ramberger, T. Schäfer, and G. Kresse, *Analytic Interatomic Forces in the Random Phase Approximation*, Phys. Rev. Lett. 118, 106403, 2017
- M. Bokdam, J. Lahnsteiner, B. Ramberger, T. Schäfer, and G. Kresse, *Assessing density functionals using many body theory for hybrid perovskites*, Physical Review Letters 119 (14), 145501, 2017

15.2 Contributed Talks

- American Physical Society March Meeting *March 2018, Los Angeles, USA*
Low-scaling MP2 for solids
- Austrian High Performance Computing Meeting *February 2018, Linz, Austria*
Parallelized and accurate algorithms for 3D materials
- ETSF Young Researchers Meeting *June 2017, Tarragona, Spain*
Quartic Scaling MP2 for Solids: A Highly Parallelized Algorithm in the Plane Wave Basis

- CECAM Workshop *May 2017, Toulouse, France*
Quartic Scaling MP2 for Solids: A Highly Parallelized Algorithm in the Plane Wave Basis
- 11th ViCoM Workshop *October 2016, Vienna, Austria*
Quartic scaling MP2 for periodic systems
- ViCoM Young Researchers' Meeting *September 2016, Vienna, Austria*
Quartic scaling MP2 for solids: A step towards vertex corrections

15.3 Poster presentations

- 16th International Congress of Quantum Chemistry *June 2018, Menton, France*
Low complexity algorithms for MP2 applied to 3D periodic materials
- ViCoM: From electrons to phase transitions *April 2018, Vienna, Austria*
Low complexity algorithms for MP2 applied to 3D periodic materials
- Total Energy and Force Methods *January 2018, Cambridge, UK*
Low complexity algorithms for MP2 applied to 3D periodic materials
- 13th ViCoM Workshop *October 2017, Stadtschlaining, Austria*
Low complexity algorithms for MP2 applied to 3D periodic materials
- Conference on Computational Physics (CCP) *July 2017, Paris, France*
High performance and low complexity algorithm for MP2 calculations in solids
- Austrian High Performance Computing Meeting *March 2017, Grundlsee, Austria*
High performance and low complexity algorithm for MP2 calculations in solids
- Autumn School on correlated electrons *September 2016, Jülich, Germany*
Highly parallelized MP2 for solids with quartic scaling
- 10th ViCoM Workshop *March 2016, Stadtschlaining, Austria*
MP2 exchange energy of large systems
- Total Energy and Force Methods *January 2016, Luxembourg, Luxembourg*
MP2 exchange energy of large systems

CHAPTER 16

Bibliography

- [1] M. Born and R. Oppenheimer. Zur Quantentheorie der Molekeln. *Ann. Phys.*, 389(20):457–484, 1927.
- [2] P. A M Dirac. A new notation for quantum mechanics. *Math. Proc. Cambridge Philos. Soc.*, 35(3):416–418, 1939.
- [3] A. March. Zur Elektronentheorie der Metalle. *Ann. Phys.*, 354(6):710–724, 1916.
- [4] A. Sommerfeld and H. Bethe. Elektronentheorie der Metalle. In *Aufbau Der Zusammenhängenden Mater.*, pages 333–622. Springer Verlag, 1933.
- [5] Felix Bloch. Über die Quantenmechanik der Elektronen in Kristallgittern. *Zeitschrift für Phys.*, 52(7-8):555–600, jul 1929.
- [6] P. A. M. Dirac. The Quantum Theory of the Electron. *Proc. R. Soc. A Math. Phys. Eng. Sci.*, 117(778):610–624, feb 1928.
- [7] Wolfgang Pauli. Noble lecture - Exclusion principle and quantum mechanics, 1946.
- [8] P. Focher, A. Lastrì, M. Covi, and G. B. Bachelet. Pseudopotentials and physical ions. *Phys. Rev. B*, 44(16):8486–8495, oct 1991.
- [9] David Vanderbilt. Soft self-consistent pseudopotentials in a generalized eigenvalue formalism. *Phys. Rev. B*, 41(11):7892–7895, apr 1990.
- [10] P. E. Blöchl. Projector augmented-wave method. *Phys. Rev. B*, 50(24):17953–17979, 1994.
- [11] G. Kresse and D. Joubert. From ultrasoft pseudopotentials to the projector augmented-wave method. *Phys. Rev. B*, 59(3):1758–1775, jan 1999.
- [12] Neil W. N. David Mermin Ashcroft. *Solid State Physics*, volume 9. Cengage Learning, Inc, 1966.

- [13] J. C. Slater. The Theory of Complex Spectra. *Phys. Rev.*, 34(10):1293–1322, nov 1929.
- [14] E. U. Condon. The Theory of Complex Spectra. *Phys. Rev.*, 36(7):1121–1133, oct 1930.
- [15] W. Pauli. Über den Zusammenhang des Abschlusses der Elektronengruppen im Atom mit der Komplexstruktur der Spektren. *Zeitschrift für Phys.*, 31(1):765–783, feb 1925.
- [16] V. Fock. Näherungsmethode zur Lösung des quantenmechanischen Mehrkörperproblems. *Zeitschrift für Phys.*, 61(1-2):126–148, 1930.
- [17] J. C. Slater. A simplification of the Hartree-Fock method. *Phys. Rev.*, 81(3):385–390, 1951.
- [18] Xinguo Ren, Patrick Rinke, Christian Joas, and Matthias Scheffler. Random-phase approximation and its applications in computational chemistry and materials science. *J. Mater. Sci.*, 47(21):7447–7471, 2012.
- [19] W. Heitler and F. London. Wechselwirkung neutraler Atome und homöopolare Bindung nach der Quantenmechanik. *Zeitschrift für Phys.*, 44(6-7):455–472, jun 1927.
- [20] Thomas Olsen and Kristian S. Thygesen. Static correlation beyond the random phase approximation: Dissociating H₂ with the Bethe-Salpeter equation and time-dependent GW. *J. Chem. Phys.*, 140(16):164116, apr 2014.
- [21] Irina V. Lebedeva, Alexander V. Lebedev, Andrey M. Popov, and Andrey A. Knizhnik. Comparison of performance of van der Waals-corrected exchange-correlation functionals for interlayer interaction in graphene and hexagonal boron nitride. *Comput. Mater. Sci.*, 128:45–58, 2017.
- [22] Francis Birch. Finite Elastic Strain of Cubic Crystals. *Phys. Rev.*, 71(11):809–824, jun 1947.
- [23] C W David. The Hamiltonian and Schrodinger Equation for Helium’s Electrons (Hylleraas). *Chem. Educ. Mater.*, 8, 2006.
- [24] Tosio Kato. On the eigenfunctions of many-particle systems in quantum mechanics. *Comm. Pure Appl. Math.*, 10:151–177, 1957.
- [25] P. Hohenberg and W. Kohn. Inhomogeneous Electron Gas. *Phys. Rev.*, 136(3B):B864–B871, nov 1964.
- [26] W. Kohn and L. J. Sham. Self-Consistent Equations Including Exchange and Correlation Effects. *Phys. Rev.*, 140(4A):A1133–A1138, nov 1965.

-
- [27] L H Thomas. The calculation of atomic fields. *Math. Proc. Cambridge Philos. Soc.*, 23(05):542, jan 1927.
- [28] Enrico Fermi. Un Metodo Statistico per la Determinazione di alcune Prioprietà dell'Atomo. *Rend. Accad. Naz. Lincei.*, 6:602–607, 1927.
- [29] R. P. Feynman, N. Metropolis, and E. Teller. Equations of State of Elements Based on the Generalized Fermi-Thomas Theory. *Phys. Rev.*, 75(10):1561–1573, may 1949.
- [30] L. Goerigk, A. Hansen, C. Bauer, S. Ehrlich, A. Najibi, and S. Grimme. A look at the density functional theory zoo with the advanced GMTKN55 database for general main group thermochemistry, kinetics and noncovalent interactions. *Phys. Chem. Chem. Phys.*, 19(48):32184–32215, 2017.
- [31] J. P. Perdew, K. Burke, and M. Ernzerhof. Generalized Gradient Approximation Made Simple. *Phys. Rev. Lett.*, 77(18):3865–3868, oct 1996.
- [32] Gábor I. Csonka, John P. Perdew, Adrienn Ruzsinszky, Pier H T Philipsen, Sébastien Lebègue, Joachim Paier, Oleg A. Vydrov, and János G. Ángyán. Assessing the performance of recent density functionals for bulk solids. *Phys. Rev. B*, 79(15):155107, apr 2009.
- [33] Jianwei Sun, Adrienn Ruzsinszky, and Johnp Perdew. Strongly Constrained and Appropriately Normed Semilocal Density Functional. *Phys. Rev. Lett.*, 115(3):1–6, 2015.
- [34] Jiří Klimeš, David R. Bowler, and Angelos Michaelides. Chemical accuracy for the van der Waals density functional. *J. Phys. Condens. Matter*, 22(2):022201, 2010.
- [35] L. Hedin. New Method for Calculating the One-Particle Green's Function with Application to the Electron-Gas Problem. *Phys. Rev.*, 139(3A):A796–A823, aug 1965.
- [36] G. W. Pratt. Generalization of Band Theory to Include Self-Energy Corrections. *Phys. Rev.*, 118(2):462–467, apr 1960.
- [37] R. D. Mattuck. *A guide to Feynman diagrams in the many-body problem*. Courier Corporation, 1976.
- [38] Chr Møller and M. S. Plesset. Note on an approximation treatment for many-electron systems. *Phys. Rev.*, 46(7):618–622, 1934.
- [39] E. Schrödinger. Quantisierung als Eigenwertproblem. *Ann. Phys.*, 385:437–490, 1926.
- [40] L. Rayleigh. *The Theory of Sound*. 2nd edition, 1894.

- [41] T. Schäfer, B. Ramberger, and G. Kresse. Quartic scaling MP2 for solids: A highly parallelized algorithm in the plane wave basis. *J. Chem. Phys.*, 146(10):104101, mar 2017.
- [42] W. Brauer. *Einführung in die Elektronentheorie der Metalle*. Geest & Portig K. G., 1972.
- [43] M. Marsman, A. Grüneis, J. Paier, and G. Kresse. Second-order Møller-Plesset perturbation theory applied to extended systems. I. Within the projector-augmented-wave formalism using a plane wave basis set. *J. Chem. Phys.*, 130(18):1–10, 2009.
- [44] J. Paier, R. Hirschl, M. Marsman, and G. Kresse. The PerdewBurkeErnzerhof exchange-correlation functional applied to the G2-1 test set using a plane-wave basis set. *J. Chem. Phys.*, 122(23):234102, jun 2005.
- [45] J. Almlöf. Elimination of energy denominators in Møller-Plesset perturbation theory by a Laplace transform approach. *Chem. Phys. Lett.*, 181(4):319–320, 1991.
- [46] T. Schäfer, B. Ramberger, and G. Kresse. Laplace transformed MP2 for three dimensional periodic materials using stochastic orbitals in the plane wave basis and correlated sampling. *J. Chem. Phys.*, 148(6):064103, feb 2018.
- [47] R. P. Feynman. Forces in Molecules. *Phys. Rev.*, 56(4):340–343, aug 1939.
- [48] David C Langreth and John P Perdew. Exchange-correlation energy of a metallic surface: Wave-vector analysis. *Phys. Rev. B*, 15(6):2884–2901, mar 1977.
- [49] R Kubo. The fluctuation-dissipation theorem. *Reports Prog. Phys.*, 29(1):306, jan 1966.
- [50] Judith Harl. *The linear response function in density functional theory*. Dissertation, University of Vienna, 2008.
- [51] E. K. U. Gross and Walter Kohn. Local density-functional theory of frequency-dependent linear response. *Phys. Rev. Lett.*, 55(26):2850–2852, dec 1985.
- [52] Andreas Grüneis, Martijn Marsman, Judith Harl, Laurids Schimka, and Georg Kresse. Making the random phase approximation to electronic correlation accurate. *J. Chem. Phys.*, 131(15):0–5, 2009.
- [53] Felix Alfred Hummel. *Density Functional Theory applied to liquid metals and the Adjacent Pairs Exchange correction to the Random Phase Approximation*. PhD thesis, 2015.
- [54] Guo P. Chen, Vamsee K. Voora, Matthew M. Agee, Sree Ganesh Balasubramani, and Filipp Furche. Random-Phase Approximation Methods. *Annu. Rev. Phys. Chem.*, 68(1):421–445, 2017.

-
- [55] Sandipan Banerjee, Jason N. Byrd, Robin Côté, H. Harvey Michels, and John A. Montgomery. Ab initio potential curves for the X2Sigma+_u and B2Sigma+_g states of Be2+: Existence of a double minimum. *Chem. Phys. Lett.*, 496(1-3):208–211, aug 2010.
- [56] Feng Liu, Stephen H. Garofalini, Dominic King-Smith, and David Vanderbilt. First-principles study of crystalline silica. *Phys. Rev. B*, 49(18):12528–12534, 1994.
- [57] G. Kresse and J. Hafner. Ab initio molecular dynamics for liquid metals. *Phys. Rev. B*, 47(1):558–561, jan 1993.
- [58] Judith Harl and Georg Kresse. Cohesive energy curves for noble gas solids calculated by adiabatic connection fluctuation-dissipation theory. *Phys. Rev. B - Condens. Matter Mater. Phys.*, 77(4):1–8, 2008.
- [59] Merzuk Kaltak, Jií Klimeš, and Georg Kresse. Low scaling algorithms for the random phase approximation: Imaginary time and laplace transformations. *J. Chem. Theory Comput.*, 10(6):2498–2507, 2014.
- [60] James J. Shepherd, Andreas Grüneis, George H. Booth, Georg Kresse, and Ali Alavi. Convergence of many-body wave-function expansions using a plane-wave basis: From homogeneous electron gas to solid state systems. *Phys. Rev. B - Condens. Matter Mater. Phys.*, 86(3):1–14, 2012.
- [61] Florian Göttl, Andreas Grüneis, Tomas Bučko, and Jürgen Hafner. Van der Waals interactions between hydrocarbon molecules and zeolites: Periodic calculations at different levels of theory, from density functional theory to the random phase approximation and Moller-Plesset perturbation theory. *J. Chem. Phys.*, 137(11), 2012.
- [62] David L. Freeman. Coupled-cluster expansion applied to the electron gas: Inclusion of ring and exchange effects. *Phys. Rev. B*, 15(12):5512–5521, jun 1977.
- [63] Benjamin Ramberger, Tobias Schäfer, and Georg Kresse. Analytic Interatomic Forces in the Random Phase Approximation. *Phys. Rev. Lett.*, 118(10):106403, mar 2017.
- [64] Jonathan E. Moussa. Cubic-scaling algorithm and self-consistent field for the random-phase approximation with second-order screened exchange. *J. Chem. Phys.*, 140(1), 2014.
- [65] Narbe Mardirossian, James D. McClain, and Garnet Kin-Lic Chan. Lowering of the complexity of quantum chemistry methods by choice of representation. (4):1–6, 2017.
- [66] Soohaeng Yoo Willow, Kwang S. Kim, and So Hirata. Stochastic evaluation of second-order many-body perturbation energies. *J. Chem. Phys.*, 137(20), 2012.

- [67] Soohaeng Yoo Willow, Kwang S. Kim, and So Hirata. Brueckner-Goldstone quantum Monte Carlo for correlation energies and quasiparticle energy bands of one-dimensional solids. *Phys. Rev. B - Condens. Matter Mater. Phys.*, 90(20):1–5, 2014.
- [68] Soohaeng Yoo Willow, Matthew R. Hermes, Kwang S. Kim, and So Hirata. Convergence Acceleration of Parallel Monte Carlo Second-Order Many-Body Perturbation Calculations Using Redundant Walkers. *J. Chem. Theory Comput.*, 9(10):4396–4402, oct 2013.
- [69] Merzuk Kaltak, Jí Klimeš, and Georg Kresse. Cubic scaling algorithm for the random phase approximation: Self-interstitials and vacancies in Si. *Phys. Rev. B - Condens. Matter Mater. Phys.*, 90(5):054115, aug 2014.
- [70] Daniel Neuhauser, Eran Rabani, and Roi Baer. Expeditious stochastic approach for MP2 energies in large electronic systems. *J. Chem. Theory Comput.*, 9(1):24–27, 2013.
- [71] B. P. Welford. Note on a Method for Calculating Corrected Sums of Squares and Products. *Technometrics*, 4(3):419–420, aug 1962.
- [72] Qinghui Ge, Yi Gao, Roi Baer, Eran Rabani, and Daniel Neuhauser. A guided stochastic energy-domain formulation of the second order Møller-Plesset perturbation theory. *J. Phys. Chem. Lett.*, 5(1):185–189, 2014.
- [73] Daniel Neuhauser, Roi Baer, and Dominika Zgid. Stochastic Self-Consistent Second-Order Green’s Function Method for Correlation Energies of Large Electronic Systems. *J. Chem. Theory Comput.*, 13(11):5396–5403, nov 2017.
- [74] Andreas Grüneis, Martijn Marsman, and Georg Kresse. Second-order MøllerPlesset perturbation theory applied to extended systems. II. Structural and energetic properties. *J. Chem. Phys.*, 133(7):074107, 2010.
- [75] A. Gruneis, G. H. Booth, M. Marsman, J. Spencer, A. Alavi, and G. Kresse. Natural Orbitals for Wave Function Based Correlated Calculations Using a Plane Wave Basis Set. *J. Chem. Theory Comput.*, 7(9):2780–2785, sep 2011.
- [76] M. L. Abrams and C. D. Sherrill. Full configuration interaction potential energy curves for the $X1\Sigma_g^+$, $B1\Delta_g$, and $B1\Sigma_g^+$ states of C₂: A challenge for approximate methods. *J. Chem. Phys.*, 121(19):9211–9219, nov 2004.
- [77] Tobias Schäfer, Zhaochuan Fan, Michael Grünwald, and Georg Kresse. Ab initio phase diagram of PbSe crystals calculated with the Random Phase Approximation. *Phys. Rev. B*, (accepted), 2018.
- [78] Dmitriy Khokhlov. *Lead chalcogenides: physics and applications*. CRC Press, 2002.

-
- [79] Tobias Hanrath, Joshua J. Choi, and Detlef-M. Smilgies. Structure/Processing Relationships of Highly Ordered Lead Salt Nanocrystal Superlattices. *ACS Nano*, 3(10):2975–2988, oct 2009.
- [80] William J. Baumgardner, Kevin Whitham, and Tobias Hanrath. Confined-but-Connected Quantum Solids via Controlled Ligand Displacement. *Nano Lett.*, 13(7):3225–3231, jul 2013.
- [81] J. M. Besson, William Paul, and A. R. Calawa. Tuning of PbSe lasers by hydrostatic pressure from 8 to 22 μ . *Phys. Rev.*, 173(3):699–713, sep 1968.
- [82] Su Huai Wei and Alex Zunger. Electronic and structural anomalies in lead chalcogenides. *Phys. Rev. B - Condens. Matter Mater. Phys.*, 55(20):13605–13610, may 1997.
- [83] Z Nabi, B Abbar, S. Mécabih, A. Khalfi, and N. Amrane. Pressure dependence of band gaps in PbS, PbSe and PbTe. *Comput. Mater. Sci.*, 18(2):127–131, 2000.
- [84] A. Svane, N. E. Christensen, M. Cardona, A. N. Chantis, M. Van Schilfgaarde, and T. Kotani. Quasiparticle self-consistent GW calculations for PbS, PbSe, and PbTe: Band structure and pressure coefficients. *Phys. Rev. B - Condens. Matter Mater. Phys.*, 81(24):1–10, 2010.
- [85] Full-text Html, P Bhambhani, K Kabra, B K Sharma, and G Sharma. High Pressure Study of Structural and Electronic Properties of PbSe. *J. Solid State Phys.*, 2014(2014):1–7, 2016.
- [86] Kaifu Bian, Zhongwu Wang, and Tobias Hanrath. Comparing the Structural Stability of PbS Nanocrystals Assembled in fcc and bcc Superlattice Allotropes. *J. Am. Chem. Soc.*, 134(26):10787–10790, jul 2012.
- [87] Tie Wang, Ruipeng Li, Zewei Quan, Welley Siu Loc, William A. Bassett, Hongwu Xu, Y. Charles Cao, Jiye Fang, and Zhongwu Wang. Pressure Processing of Nanocube Assemblies Toward Harvesting of a Metastable PbS Phase. *Adv. Mater.*, 27(31):4544–4549, aug 2015.
- [88] Michael Grünwald, Katie Lutker, A. Paul Alivisatos, Eran Rabani, and Phillip L. Geissler. Metastability in Pressure-Induced Structural Transformations of CdSe/ZnS Core/Shell Nanocrystals. *Nano Lett.*, 13(4):1367–1372, apr 2013.
- [89] Keren Jacobs, Juanita Wickham, and A. P. Alivisatos. Threshold Size for Ambient Metastability of Rocksalt CdSe Nanocrystals. *J. Phys. Chem. B*, 106(15):3759–3762, apr 2002.
- [90] T. Chattopadhyay, H. G. von Schnering, W. A. Grosshans, and W. B. Holzapfel. High pressure X-ray diffraction study on the structural phase transitions in PbS, PbSe and PbTe with synchrotron radiation. *Phys. B+C*, 139-140(C):356–360, may 1986.

- [91] S. V. Streltsov, A. Yu Manakov, A. P. Vokhmyanin, S. V. Ovsyannikov, and V. V. Shchennikov. Crystal lattice and band structure of the intermediate high-pressure phase of PbSe. *J. Phys. Condens. Matter*, 21(38):385501, 2009.
- [92] Yanchun Li, Gong Li, Chuanlong Lin, Xiaodong Li, and Jing Liu. Structure determination of the intermediate phase of PbSe using experiments and calculations. *J. Appl. Phys.*, 116(5):053502, aug 2014.
- [93] Shanmin Wang, Chengpeng Zang, Yongkun Wang, Liping Wang, Jianzhong Zhang, Christian Childs, Hui Ge, Hongwu Xu, Haiyan Chen, Duanwei He, and Yusheng Zhao. Revisit of Pressure-Induced Phase Transition in PbSe: Crystal Structure, and Thermoelastic and Electrical Properties. *Inorg. Chem.*, 54(10):4981–4989, 2015.
- [94] Rajeev Ahuja. High pressure structural phase transitions in IVVI semiconductors. *Phys. Status Solidi*, 235(2):341–347, 2003.
- [95] Y. Bencherif, A. Boukra, A. Zaoui, and M. Ferhat. High-pressure phases of lead chalcogenides. *Mater. Chem. Phys.*, 126(3):707–710, 2011.
- [96] Ferhat Demiray and Savas Berber. Ab initio investigation of B16(GeS), B27(FeB) and B33(CrB/TiI) phases of lead chalcogenides. *Phys. Scr.*, 88(1):015603, 2013.
- [97] Jonathan M. Skelton, Stephen C. Parker, Atsushi Togo, Isao Tanaka, and Aron Walsh. Thermal physics of the lead chalcogenides PbS, PbSe, and PbTe from first principles. *Phys. Rev. B - Condens. Matter Mater. Phys.*, 89(20):1–10, 2014.
- [98] P. Nozières and D. Pines. Correlation energy of a free electron gas. *Phys. Rev.*, 111(2):442–454, jul 1958.
- [99] Georg Kresse and Judith Harl. Accurate bulk properties from approximate many-body techniques. *Phys. Rev. Lett.*, 103(5):056401, jul 2009.
- [100] Judith Harl, Laurids Schimka, and Georg Kresse. Assessing the quality of the random phase approximation for lattice constants and atomization energies of solids. *Phys. Rev. B - Condens. Matter Mater. Phys.*, 81(11), 2010.
- [101] Joachim Paier, Xinguo Ren, Patrick Rinke, Gustavo E. Scuseria, Andreas Grüneis, Georg Kresse, and Matthias Scheffler. Assessment of correlation energies based on the random-phase approximation. *New J. Phys.*, 14(4):043002, 2012.
- [102] Thomas Olsen and Kristian S. Thygesen. Extending the random-phase approximation for electronic correlation energies: The renormalized adiabatic local density approximation. *Phys. Rev. B - Condens. Matter Mater. Phys.*, 86(8):1–4, 2012.
- [103] Thomas Olsen and Kristian S. Thygesen. Accurate ground-state energies of solids and molecules from time-dependent density-functional theory. *Phys. Rev. Lett.*, 112(20):1–5, 2014.

-
- [104] Patrick Bleiziffer, Marcel Krug, and Andreas Göring. Self-consistent Kohn-Sham method based on the adiabatic-connection fluctuation-dissipation theorem and the exact-exchange kernel. *J. Chem. Phys.*, 142(24), 2015.
- [105] Bastien Mussard, Dario Rocca, Georg Jansen, and G A. Dielectric Matrix Formulation of Correlation Energies in the Random Phase Approximation : Inclusion of Exchange Effects. 2016.
- [106] Maria Hellgren, Nicola Colonna, and Stefano De Gironcoli. Beyond the random phase approximation with a local exchange vertex. *Phys. Rev. B*, 98(4):1–12, 2018.
- [107] Niladri Sengupta, Jefferson E Bates, and Adrienn Ruzsinszky. From semilocal density functionals to random phase approximation renormalized perturbation theory: A methodological assessment of structural phase transitions. *Phys. Rev. B*, 97(23):235136, jun 2018.
- [108] Niraj K. Nepal, Adrienn Ruzsinszky, and Jefferson E. Bates. Rocksalt or cesium chloride: Investigating the relative stability of the cesium halide structures with random phase approximation based methods. *Phys. Rev. B*, 97(11):115140, mar 2018.
- [109] Menno Bokdam, Jonathan Lahnsteiner, Benjamin Ramberger, Tobias Schäfer, and Georg Kresse. Assessing Density Functionals Using Many Body Theory for Hybrid Perovskites. *Phys. Rev. Lett.*, 119(14):145501, oct 2017.
- [110] Atsushi Togo and Isao Tanaka. First principles phonon calculations in materials science. *Scr. Mater.*, 108:1–5, nov 2015.
- [111] Yi Zhang, Xuezhi Ke, Changfeng Chen, J. Yang, and P. R. C. Kent. Thermodynamic properties of PbTe, PbSe, and PbS: First-principles study. *Phys. Rev. B*, 80(2):024304, jul 2009.
- [112] Shanmin Wang, Jianzhong Zhang, Yi Zhang, Andrew Alvarado, Jeevake Attapattu, Duanwei He, Liping Wang, Changfeng Chen, and Yusheng Zhao. Phase-Transition Induced Elastic Softening and Band Gap Transition in Semiconducting PbS at High Pressure. *Inorg. Chem.*, 52(15):8638–8643, aug 2013.
- [113] G. Rousse, S. Klotz, A. M. Saitta, J. Rodriguez-Carvajal, M. I. McMahon, B. Couzinet, and M. Mezouar. Structure of the intermediate phase of PbTe at high pressure. *Phys. Rev. B*, 71(22):224116, jun 2005.